UNIVERSITY OF THESSALY
DEPARTMENT OF MECHANICAL AND INDUSTRIAL ENGINEERING

COMPUTATIONAL TECHNIQUES IN STRUCTURAL STABILITY OF THIN-WALLED CYLINDRICAL SHELLS

by

SOTIRIA HOULIARA, M.Sc.

DISSERTATION

Submitted to the Department of Mechanical and Industrial Engineering

in Partial Fulfillment

of the Requirements

for the Degree of

DOCTOR OF PHILOSOPHY

UNIVERSITY OF THESSALY, MARCH 2008

ACKNOWLEDGMENTS

I would like to express my sincere gratitude to my advisor, Dr. Spyros Karamanos, for his valuable support, guidance and friendship during the course of this research. Dr. Karamanos is an excellent mentor and it was a valuable experience to work with him. Furthermore, I am truly indebted to Dr. Nikolaos Aravas for his guidance and especially for his support that strongly facilitated the completion of this thesis. Also, I am grateful to the other members of the examining committee, namely Dr. Manolis Papadrakis, Dr. Charis Gantes, Dr. Demosthenes Talaslides, Dr. Philipos Perdikaris and Dr. Costas Papadimitriou for their valuable comments and suggestions.

At this point, I wish to express my sincere gratitude to the Public Benefit Foundation "Alexander S. Onassis" for the fellowships that awarded to me and facilitated greatly this work. These fellowships apart from the financial support constitute a great honor for me.

I am grateful to my very dear friends Kostas Zarogoulidis, Dimitris Skoulaxinos and Thodoris Papadopoulos, Vasileios Garas, Giannis Manolarakis and Thanasis Papageorgiou for their friendship, advices and encouragement during my undergraduate and postgraduate studies. It is a great experience to have them as my friends and just mentioning their names in this thesis is the least that I can to do to express my gratitude. Many thanks go to my fellow graduate students Danny Vasilikis, Patricia Pappa and George Varelis and especially to my office-mate and close friend Ioanna Charalambous-Moisidou, for their help and friendship.

I also wish to thank my very close friends Alexia Rorri and Maria Triantafyllou for their friendship, support and sincere advices. They are very special persons that constantly support and encourage me. Moreover, I am thankful to my friends Dida and Stefanos Papastergiou and Ioanna and Maria Kechagia.

Most of all, I am grateful and indebted to my parents, Dimitris and Paraskeui and my brother, Vasilis for their encouragement and help and mainly constant love.

Sotiria D. Houliara
Volos, March 2008

1

This thesis is dedicated to my dearest friends
Alexia Rorri, Maria Triantafyllou, Kostas Zarogoulidis,
Dimitris Skoulaxinos and Thodoris Papadopoulos.

2

ABSTRACT

The present study investigates the structural stability of thin-walled long cylinders subjected to structural loads (bending and axial compression) and pressure (internal or external). A numerical technique is employed that uses the ''tube-element'', a special-purpose finite element. Within this framework, two large-strain material models for the description of isotropic and transversely isotropic cylinders are developed. Bending loading is primarily considered, where buckling is associated with a highly nonlinear prebuckling state due to cross-sectional ovalization. Special emphasis is given on thin-walled elastic cylinders, and extensive numerical results are presented, concerning their buckling and postbuckling response, under uniform wrinkling conditions. Furthermore, the sensitivity of maximum moment on the presence of initial imperfections is also examined. The numerical results are compared with available bifurcation and postbuckling solutions presented elsewhere, and with analytical expressions developed for the purposes of the current study. The effects of anisotropy on buckling and postbuckling response are investigated. Finally, the stability of thin-walled inelastic metal cylinders under bending moments is also examined, using the aforementioned numerical technique, focusing on the determination of bifurcation moment and the localization of buckling deformations.

3

ΠΕΡΙΛΗΨΗ

Η εργασία αυτή έχει σαν κύριο στόχο την μελέτη της δομικής ευστάθειας λεπτότοιχων κυλινδρικών κελυφών, που υπόκεινται σε δομικά φορτία (κάμψη και αξονική συμπίεση) και πίεση. Έτσι στα πλαίσια της Διατριβής αναπτύχθηκε μία αριθμητική τεχνική για την προσομοίωση της συμπεριφοράς των κελυφών, στην οποία και ενσωματώθηκαν καταστατικά μοντέλα μεγάλων παραμορφώσεων.

Πιο αναλυτικά, στο πρώτο μέρος της Διατριβής παρουσιάζεται η υπολογιστική τεχνική που εφαρμόστηκε για την επίλυση του προβλήματος. Χρησιμοποιήθηκε πηγαίος κώδικας πεπερασμένων στοιχείων, ο οποίος αρχικά είχε αναπτυχθεί για σωληνωτά δομικά μέλη μεγάλου πάχους, και εδώ προσαρμόστηκε για την ανά

λυση λεπτότοιχων κελυφών. Βασικά στοιχεία της υπολογιστικής τεχνικής αποτελούν (α) το πεπερασμένο στοιχείο «σωλήνα» (tube-element), το οποίο έχει την δυνατότητα περιγραφής της παραμόρφωσης ενός επιμήκους σωληνωτού μέλους συνδυάζοντας την διαμήκη παραμόρφωση τύπου δοκού με την παραμόρφωση της διατομής του μέλους και (β) η χρησιμοποίηση ειδικών καταστατικών μοντέλων για την προσομοίωση της συμπεριφοράς του υλικού με έμφαση στα ανισότροπα ελαστικά υλικά. Τα ανωτέρω ενσωματώθηκαν σε μία μεθοδολογία μη γραμμικής ανάλυσης κατασκευών, η οποία βασίζεται σε μία Λαγκρανζιανή περιγραφή του παραμορφώσιμου στερεού με «ενσωματωμένες» συντεταγμένες και μία τροποποιημένη Newton-Raphson επίλυση των διακριτοποιημένων εξισώσεων ισορροπίας με τη μέθοδο μήκους-τόξου. Ιδιαίτερη έμφαση δίνεται επίσης στον προσδιορισμό διακλάδωσης της λύσης στην ελαστοπλαστική περιοχή, με την προσαρμογή της θεωρίας μοναδικότητας λύσης του Hill στην παρούσα αριθμητική τεχνική και διακριτοποίηση.

Η αποτελεσματικότητα της υπολογιστικής τεχνικής εξετάζεται στην επίλυση των «προτύπων» (benchmark) προβλημάτων ευστάθειας. Τα προβλήματα αυτά είναι η ευστάθεια κυκλικών ελαστικών κυλίνδρων σε αξονική συμπίεση υπό αξονομετρικές αρχικές ατέλειες, και η ευστάθεια και μεταλυγισμική συμπεριφορά μη-κυκλικών ελαστικών κυλίνδρων υπό αξονική συμπίεση. Και στα δύο προβλήματα, τα αριθμητικά αποτελέσματα της Διατριβής είναι σε εξαιρετική συμφωνία με ημι-αναλυτικές λύσεις, τόσο στο κρίσιμο φορτίο όσο και στην μεταλυγισμική συμπεριφορά και την ευαισθησία σε αρχικές ατέλειες.

Η ευστάθεια κυλινδρικών σωληνωτών μελών αποτελεί το βασικό πρόβλημα της Διατριβής. Στα πλαίσια, επομένως αυτής της μελέτης εξετάστηκε η κάμψη λεπτότοιχων ελαστικών ισότροπων κυλίνδρων υπό πίεση (εσωτερική ή εξωτερική), ένα πρόβλημα με σημαντική μη-

γραμμικότητα της προλυγισμικής κατάστασης, λόγω της «οβαλοποίησης» της κυλινδρικής διατομής. Προσδιορίζονται τα φορτία λυγισμού και οι αντίστοιχες «ιδιομορφές», καθώς και η μεταλυγισμική συμπεριφορά και η ευαισθησία σε αρχικές ατέλειες. Βασικό χαρακτηριστικό της διακλάδωσης είναι η συσχέτισή της με μία και μόνον μορφή λυγισμού. Επίσης, παρατηρείται μία μεγάλη ευαισθησία των αποτελεσμάτων. Τα αριθμητικά αποτελέσματα είναι σε πλήρη συμφωνία με ασυμπτωτικές λύσεις για την αρχική μεταλυγισμική συμπεριφορά, και επιπρόσθετα προσδιορίζουν πλήρως τον μεταλυγισμικό δρόμο ισορροπίας. Επίσης, εξετάζεται η ευαισθησία σε αρχικές ατέλειες, και τα αριθμητικά αποτελέσματα επαληθεύουν την γενική θεωρία του Koiter και την εκθετική σχέση «2/3». Τέλος, προτείνεται μία αναλυτική μεθοδολογία υπολογισμού του σημείου διακλάδωσης, η οποία καταλήγει σε σχέσεις κλειστής μορφής και είναι σε πολύ καλή συμφωνία με τα αριθμητικά αποτελέσματα.

Στην συνέχεια εξετάζεται ο λυγισμός και η μεταλυγισμική συμπεριφορά ανισότροπων ελαστικών κυλινδρικών κελυφών υπό κάμψη. Χρησιμοποιούνται καταστατικά μοντέλα για εγκαρσίως ισοτροπικά υλικά και τα αριθμητικά αποτελέσματα δείχνουν μία σημαντική επιρροή της ανισοτροπίας στο σημείο διακλάδωσης, καθώς και στην αντίστοιχη μορφή λυγισμού. Στην περίπτωση μεγάλης ανισοτροπίας κατά την αξονική διεύθυνση του κυλίνδρου, η μορφή λυγισμού έχει έντονο κυματοειδή χαρακτήρα κατά την εγκάρσια διεύθυνση, και στην περίπτωση αυτή, προσεγγιστική αναλυτική λύση κλειστής μορφής δεν δίνει καλά αποτελέσματα. Εξετάζεται επίσης αριθμητικά η ευαισθησία σε αρχικές ατέλειες, επαληθεύοντας την γενική θεωρία του Koiter και την εκθετική σχέση «2/3» για τον αρχικό μεταλυγισμικό δρόμο ισορροπίας.

Τέλος, αναλύεται το φαινόμενο της αστοχίας λεπτότοιχων κυλινδρικών μεταλλικών κελυφών υπό καμπτική ένταση. Αρχικά εξετάζεται η διακλάδωση λυγισμού με βάση την αριθμητική εφαρμογή της θεωρίας του Hill, σε μία κυματοειδή μορφή, ομοιόμορφη κατά μήκος του κυλίνδρου, καθώς και η ευαισθησία σε αρχικές ατέλειες. Επίσης, αποδείκνύεται αριθμητικά η μετέπειτα δημιουργία «τοπικής» ζώνης της μεταλυγισμικής κυματοειδούς παραμόρφωσης (buckling localization), η οποία συντελεί στην απότομη αστοχία του δομικού κυλινδρικού μέλους με τη μορφή τοπικής κύρτωσης ή ύβωσης.

6

Chapter 1

<u>INTRODUCTION</u>

Equation Chapter 1 Section 1

The structural analysis of cylindrical shells constitutes a classical problem of mechanics, with numerous applications in civil, aerospace, mechanical and marine structures. In particular, the nonlinear response and the loss of structural stability of thin-walled structures, as well as, their postbuckling behavior is a topic of both fundamental and applied research. In the past, this problem has caused significant controversy due to the unreasonably high analytical predictions of buckling loads, compared with the low buckling loads obtained from relevant experiments. This controversy remained a major issue of concern and dispute among structural engineers and researchers, until the early 40's. The works of von Karman et al. [1], [2] were a first major step towards understanding these discrepancies, pinpointing the sensitivity of the structure to deviations from the assumed initial ''perfect'' shape. The first rigorous confirmation of the influence of initial imperfections on the buckling load was given by Koiter [3], [4], [5]. In particular, Koiter was the first to relate the unstable postbuckling equilibrium path of a structure with its imperfection sensitivity. It is important to note that this imperfection sensitivity stems from the fact that the buckling (bifurcation) load is often associated with an infinite number of buckling modes. Other notable contributions on this subject were published by Kempner [6], [7], Kempner and Chen [8], Amazigo et al [9] and Budiansky and Hutchinson [10]. All the above works, underlined the important role of imperfection sensitivity, which was recognized as the major reason for the significant differences between analytical buckling predictions and experimental results. It was shown that, even small deviations from the perfect circular cylindrical geometry, result in a significant reduction of the theoretical buckling load.

The problem of circular cylinder under uniform axial compression, due to the above controversy, as well as because of its wide range of applications in structural engineering and mechanics, still remains a popular research topic. Therefore, a great number of relevant published works exists on this subject. For a concise presentation of those works related to imperfection sensitivity of cylindrical shells, the reader is referred to the books of Brush and Almroth [11] and Wempner and Talaslides [12]. Furthermore, the study of Teng [13] offers an extensive list of references for investigations of more practical problems. Finally, the recent book of Singer [14] contains an excellent literature review on this subject, with focus on experimental works.

8

On the other hand, the problem of non-circular cylinders under uniform axial compression has received less attention over the years. Non-circular cylinders are used to aerospace and mechanical engineering applications, due to either special external shapes or (internal) storage requirements. The response of these non-circular geometries has several similarities with the corresponding problem of circular cylinders. However, there are several stricking differences, which allow its separate investigation. More specifically, the shell has a variation of curvature in the hoop direction and the buckling load is associated with a singe mode, which makes these shells less sensitive on initial imperfections.

Bending of cylinders is another problem of particular engineering importance. Most of the work on this subject was motivated by the structural design of pipelines and was mainly focused on relatively thick cylinders. In recent years, the problem of buckling of cylinders has gain significant attention due to its applications in composite-material structures, as well as, in biomechanics and carbon nanotubes.

The present study is motivated by the need for an accurate prediction of the response of thin-walled cylinders subjected to axial compression, bending and pressure, using advanced numerical tools. Special emphasis is given on circular cylinders under structural loads (bending moments and uniform axial load) whereas issues of stability of non-circular cylinders are also examined. The analysis is numerical, using a special-purpose finite element technique. Analytical solutions for elastic cylinders are also reported.

Within this framework, the development of a rigorous numerical technique in order to investigate the stability of cylinders under structural loads and pressure, which uses the so-called ''tube-element'', is considered, as described in Chapter 2. The development of two material models for the description of large-strain transverse-isotropy and isotropy is presented. These constitutive models are incorporated in the finite element technique.

Using the above mentioned numerical techniques nonlinear equilibrium paths, bifurcation and limit points are calculated, whereas issues of postbuckling response and imperfection sensitivity are considered, as well. Chapters 3 to 7 cover applications of classical stability theory for cylinders subjected to axial compression, bending and pressure. In particular, Chapters 3 and 4 consider the case of uniform axial compression in both circular and non-circular cylinders. These problems are revisited for the purposes of this study and their numerical investigation constitutes a benchmark for the capabilities of the ''tube-element'', offering a verification of its accuracy and computational efficiency. The problem of elastic bending is examined in Chapters 5 and 6 for isotropic and anisotropic cylinders, respectively. In these Chapters a number of parameters that affect the bending response and stability are discussed. In addition, an attempt to develop an approximate solution for bifurcation is also described in both Chapters. The bending response of inelastic cylinders is examined in Chapter 7. Bifurcation in the inelastic range in the form of wrinkled buckling patterns is detected using a numerical implementation of

Institutional Repository - Library & Information Centre - University of Thessaly
12/07/2024 14:49:38 EEST - 18.189.193.27

the so-called "comparison solid" concept. Post-buckling response is calculated and imperfection sensitivity is examined. Special emphasis on buckling localization is also given. Finally, some important conclusions are summarized in Chapter 8.

10

Chapter 2

NUMERICAL FORMULATION

Equation Chapter 2 Section 2

In the present Chapter, a finite element technique is briefly presented, which simulates the nonlinear structural behavior of elastic and inelastic cylinders. It is a continuum-based formulation with finite-element discretization, through a special-purpose element, the so-called ''tube-element''. The technique is based on the large-strain formulation of Needleman [15] and was employed in [16] for the analysis of inelastic thick-walled cylinders, mainly motivated by the study of offshore pipelines and tubular members. Herein, this element formulation is further elaborated and enhanced for the stability analysis (buckling and postbuckling) of thin-walled cylinders. Emphasis is given on modelling of the anisotropic elastic material behavior, through the development of two large-strain constitutive models, which consider both the cases of hypoelasticity and hyperelasticity. Issues of the stability analysis of inelastic metal cylinders are also discussed, within the context of Hill's comparison solid. For the development of this numerical technique, some basic concepts of continuum mechanics that are necessary are shortly illustrated in the following.

2.1 Governing Equations

A Lagrangian formulation of the cylinder is adopted, as described in detail in [15]. Therefore, a net of coordinate lines embedded in and deforming with the continuum (curvilinear coordinate system) is employed. These coordinates are denoted by ξ^i $(i=1,2,3)$, so that:

$$\mathbf{x} = \mathbf{x}(\xi^1,\xi^2,\xi^3,t) \tag{2.1}$$

is the position vector of a material point (ξ^1,ξ^2,ξ^3) in the deformed configuration at time t. In particular, the position of the material point (ξ^1,ξ^2,ξ^3) at $t=0$ serves as a reference configuration, which is denoted by:

$$\mathbf{X} = \mathbf{X}(\xi^1,\xi^2,\xi^3) \tag{2.2}$$

In the sequel, $\mathbf{x}$ and $\mathbf{X}$ are the position vectors in the current (deformed) and the reference (undeformed) configuration, respectively.

At any material point, the covariant base vectors in the reference configuration are:

11

$$\mathbf{G}_i = \frac{\partial \mathbf{X}}{\partial \xi^i} \tag{2.3}$$

and in the current configuration are:

$$\mathbf{g}_i = \frac{\partial \mathbf{x}}{\partial \xi^i} \tag{2.4}$$

Furthermore, $\mathbf{G}^k$ and $\mathbf{g}^k$ denote the contravariant (reciprocal) base vectors in the reference and current configuration, respectively.

Deformation is described by the rate-of-deformation (stretch) tensor $\mathbf{d}$, which is the symmetric part of the velocity gradient. Therefore,

$$\mathbf{L} = \frac{\partial \mathbf{v}}{\partial \mathbf{x}} = \nabla_{\mathbf{x}} \mathbf{v} \tag{2.5}$$

$$\mathbf{d} = \frac{1}{2}(\mathbf{L} + \mathbf{L}^{\mathrm{T}}) \tag{2.6}$$

$$d_{pq} = \frac{1}{2}(v_{p/q} + v_{q/p}) \tag{2.7}$$

whereas $v_{i/j}$ are the components of the covariant derivative of the velocity vector in the current configuration, and can be written in the corresponding components in the reference configuration $V_{k/l}$. More specifically,

$$v_{p/q} = \mathbf{v}_{,q} \cdot \mathbf{g}_p = \frac{\partial \mathbf{v}}{\partial \xi^q} \cdot \mathbf{g}_p \tag{2.8}$$

$$V_{p/q} = \mathbf{v}_{,q} \cdot \mathbf{G}_p = \frac{\partial \mathbf{v}}{\partial \xi^q} \cdot \mathbf{G}_p \tag{2.9}$$

and from (2.8) and (2.9) one obtains

$$v_{p/q} = V_{k/q}(\mathbf{G}^k \cdot \mathbf{g}_p) \tag{2.10}$$

Therefore,

$$d_{pq} = \frac{1}{2}\Big(V_{k/q}(\mathbf{G}^k \cdot \mathbf{g}_p) + V_{k/p}(\mathbf{G}^k \cdot \mathbf{g}_q)\Big) \tag{2.11}$$

It is noted that the anti-symmetric part of $\mathbf{L}$ is the continuum spin $\boldsymbol{\omega}$, which expresses the average rotation of the material fibers at a specific material point.

Equilibrium is expressed through the principle of virtual work, considering an admissible displacement field $\delta \mathbf{u}$. For a continuum occupying the region V_0 and V in the reference and the deformed configuration, correspondingly, and with boundary B in the current configuration, the principle of virtual work is expressed as:

$$\int_{V_0} \delta U_{k/j}(\mathbf{G}^k \cdot \mathbf{g}_i)\, \tau^{ij} dV_0 = \int_B \delta \mathbf{u} \cdot \mathbf{t}\, dB_q + M\,\delta\theta \tag{2.12}$$

12

where $\mathbf{t}$ is the surface traction, M is the bending moment at the cylinder end, $\delta\theta$ is a variation of the end rotation, τ^{ij} are the contravariant components of the Kirchhoff stress tensor $\boldsymbol{\tau} = \tau^{ij}(\mathbf{g}_i \otimes \mathbf{g}_j)$, which is parallel to the Cauchy stress tensor $\boldsymbol{\sigma}$ ($\boldsymbol{\tau} = J\boldsymbol{\sigma}$, $J = \det(\mathbf{F})$) and

$$\delta U_{k/j} = \frac{\partial(\delta\mathbf{u})}{\partial\xi^j} \cdot \mathbf{G}_k \tag{2.13}$$

The contravariant components τ^{ij} of the Kirchhoff stress tensor with respect to the current deformed configuration, can be correlated to the contravariant components S^{ij} of the second Piola-Kirchhoff stress tensor with respect to the initial undeformed configuration. From continuum mechanics,

$$\boldsymbol{\tau} = \mathbf{F}\mathbf{S}\mathbf{F}^{\mathrm{T}} \tag{2.14}$$

therefore,

$$\tau^{ij}(\mathbf{g}_i \otimes \mathbf{g}_j) = \mathbf{F}[S^{ij}(\mathbf{G}_i \otimes \mathbf{G}_j)]\mathbf{F}^{\mathrm{T}} \tag{2.15}$$

and taking into account that for convected coordinates $\mathbf{g}_i = \mathbf{F}\mathbf{G}_i$ one results in $\tau^{ij} = S^{ij}$. Using this result, the principle of virtual work can also be expressed with respect to the components of the second Piola-Kirchhoff stress tensor as follows:

$$\int_{V_0} \delta U_{k/j}(\mathbf{G}^k \cdot \mathbf{g}_i) S^{ij} dV_0 = \int_B \delta\mathbf{u} \cdot \mathbf{t}\, dB_q + M\,\delta\theta \tag{2.16}$$

Furthermore, on the same basis one can show, that applying the expression

$$\dot{\mathbf{E}} = \mathbf{F}^{\mathrm{T}}\mathbf{d}\mathbf{F} \tag{2.17}$$

for the case of the convected coordinates, the rate of the covariant components $\dot{E}_{ij}$ of the Lagrange-Green strain tensor $\mathbf{E}$, expressed in the initial configuration, are equal to the covariant components d_{ij} of the rate-of-deformation tensor $\mathbf{d}$, expressed in the deformed configuration:

$$\dot{E}_{ij} = d_{ij} \tag{2.18}$$

Regarding the constitutive relations to be used in the present formulation, hypoelastic and hyperelastic relationships are considered. In the case of hypoelasticity the rate of the contravariant components of Kirchhoff stress $\boldsymbol{\tau}$ are related to the covariant components of the rate-of-deformation tensor $\mathbf{d}$ as follows:

$$\dot{\tau}^{ij} = R^{ijkl} d_{kl} \tag{2.19}$$

where R^{ijkl} are the components of $\mathbf{R}$, a fourth order tensor, with respect to the current base vectors.

Alternatively, in the framework of a hyperelastic constitutive model that employs a quadratic free energy function, the components S^{ij} of the second Piola-Kirchhoff stress tensor $\mathbf{S}$, with

13

respect to the reference base, are related to the components of Lagrange-Green strain tensor $\mathbf{E}$ (also expressed with respect to the reference base) as follows:

$$S^{ij} = D_e^{ijkl} E_{kl} \tag{2.20}$$

where $\mathbf{D_e}$ is a fourth order rigidity tensor that depends exclusively on the material properties and it is independent of the deformation, when a quadratic function for the free energy is considered. Differentiation of (2.20) results in the following rate equation:

$$\dot{S}^{ij} = D_e^{ijkl} \dot{E}_{kl} \tag{2.21}$$

These two constitutive models will be discussed in the subsequent sections.

2.2 Elastic Material Behavior

A major part of this study concerns the stability of elastic cylinders. In the following, constitutive models employed to describe elastic material response are presented for both isotropic and anisotropic elastic response with special emphasis on transversely isotropic material behavior. An isotropic material possesses no preferred directions, and its properties are the same in all directions. Furthermore, in the present study a particular anisotropic case, the transverse isotropy is considered, where the material possesses at every point a single preferred direction. The anisotropy axis in the undeformed and deformed configurations is demonstrated in Fig. 1. The anisotropy axis in the initial configuration is aligned in the axial direction of the undeformed cylinder, which is the direction of the covariant base vector $\mathbf{G}_2$. Therefore, the corresponding direction unit vector is expressed as follows:

$$\mathbf{N} = \frac{1}{\|\mathbf{G}_2\|} \mathbf{G}_2 \tag{2.22}$$

In the deformed (current) configuration, the direction of anisotropy axis is assumed in the direction of the local covariant base vector $\mathbf{g}_2$, so that the corresponding direction unit vector is:

$$\mathbf{n} = \frac{1}{\|\mathbf{g}_2\|} \mathbf{g}_2 \tag{2.23}$$

where $\|\mathbf{G}_2\|$ and $\|\mathbf{g}_2\|$ are the magnitudes of vectors $\mathbf{G}_2$ and $\mathbf{g}_2$, respectively.

An example of such a material is a composite material, which consists of a matrix reinforced by fibers arranged in parallel straight lines. These materials are employed in a variety of industrial applications and recently for the description of biomechanical materials (e.g. soft tissues).
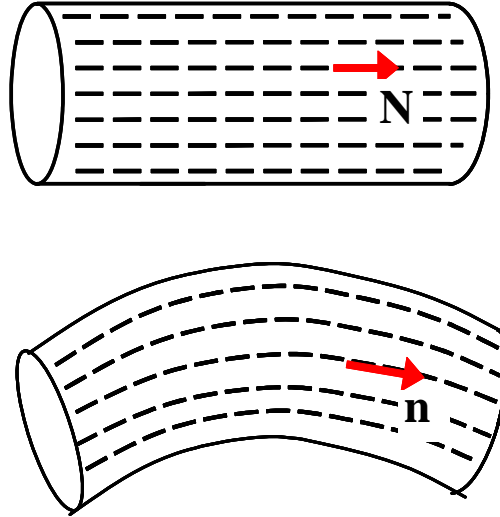
14

Fig. 1 Axis of transverse isotropy in the reference and current configuration

2.2.1 Hypoelastic Constitutive Model

A material is characterized as hypoelastic if an objective stress rate tensor is related to the rate-of-deformation tensor. Constitutive equations which model transversely isotropic materials, for finite elastic strains are presented in this section. Furthermore, the appropriate simplifications that lead to the case of isotropy are indicated.

From continuum mechanics, the rate of change of the unit vector $\mathbf{n}$ in a deformable body is given by the following expression,

$$\dot{\mathbf{n}} = \boldsymbol{\omega}_\alpha \, \mathbf{n} \tag{2.24}$$

where the second order tensor $\boldsymbol{\omega}_\alpha$ is given by the following expression

$$\boldsymbol{\omega}_\alpha = \boldsymbol{\omega} + \mathbf{d}(\mathbf{n} \otimes \mathbf{n}) - (\mathbf{n} \otimes \mathbf{n})\mathbf{d} \tag{2.25}$$

and $\boldsymbol{\omega}$ is the continuum spin.

Thus the following hypoelastic constitutive equation is considered

$$\overset{\square}{\boldsymbol{\tau}} = \mathbf{D_e} \, \mathbf{d} \tag{2.26}$$

where $\overset{\square}{\boldsymbol{\tau}}$ is a rate of Kirchhoff stress, which is co-rotational with the anisotropy direction vector $\mathbf{n}$, defined by (2.23),

$$\overset{\square}{\boldsymbol{\tau}} = \dot{\boldsymbol{\tau}} + \boldsymbol{\tau}\boldsymbol{\omega}_\alpha - \boldsymbol{\omega}_\alpha \boldsymbol{\tau} \tag{2.27}$$

and $\mathbf{D_e}$ is the fourth-order elastic rigidity tensor. The components $\hat{D}_e^{ijkl}$ of tensor $\mathbf{D_e}$ in a Cartesian system, defined by the following orthonormal vectors,

15

$$\mathbf{e}_1 = \frac{1}{\|\mathbf{g}^1\|}\mathbf{g}^1 \tag{2.28}$$

$$\mathbf{e}_2 = \mathbf{n} \tag{2.29}$$

$$\mathbf{e}_3 = \mathbf{e}_1 \times \mathbf{e}_2 \tag{2.30}$$

are given in the following matrix form [17], [18]:

$$
\begin{array}{c}
 \\
\begin{array}{cccccc}
\mathbf{11} & \mathbf{22} & \mathbf{33} & \mathbf{12} & \mathbf{13} & \mathbf{23}
\end{array} \\
\begin{array}{c}
\mathbf{11} \\ \mathbf{22} \\ \mathbf{33} \\ \mathbf{12} \\ \mathbf{13} \\ \mathbf{23}
\end{array}
\begin{bmatrix}
A_{11} & \lambda & \lambda_2 & 0 & 0 & 0 \\
\lambda & A_{22} & \lambda & 0 & 0 & 0 \\
\lambda_2 & \lambda & A_{11} & 0 & 0 & 0 \\
0 & 0 & 0 & \mu & 0 & 0 \\
0 & 0 & 0 & 0 & (1/2)(A_{11}-\lambda_2) & 0 \\
0 & 0 & 0 & 0 & 0 & \mu
\end{bmatrix}
\end{array}
\tag{2.31}
$$

and $\mathbf{n}$ is given by equation (2.23). It can be readily shown that tensor $\overset{\square}{\boldsymbol{\tau}}$ is objective.

The five constants $A_{11}, A_{22}, \lambda, \lambda_2, \mu$ designate the five independent effective properties of the media. These properties can be related to the engineering properties of the material through the following identities [18], [19]:

$$
\begin{aligned}
A_{11} &= K_{13} + \mu_{13} \\
A_{22} &= E_{22} + 4\mu_{13}\nu_{21}^2 \\
\lambda &= 2K_{13}\nu_{21} \\
\lambda_2 &= K_{13} - \mu_{13} \\
\mu &= \mu_{12}
\end{aligned}
\tag{2.32}
$$

where

$$K_{13} = \frac{1}{2}\frac{E_{11}}{1-\nu_{13}-2\nu_{12}\nu_{21}} \tag{2.33}$$

$$\mu_{13} = \frac{1}{2}\frac{E_{11}}{1+\nu_{13}} \tag{2.34}$$

It is noted that, in the above equations E_{11}, E_{22} are the uniaxial moduli and they are directly measurable from a tensile test, μ_{12} is a shear modulus and ν_{21}, ν_{13} are Poisson's ratios. In the notation ν_{ij} a convention is employed so that the first index i refers to the coordinate of the imposed stress or strain and the second index j refers to the response direction. Therefore, transverse isotropy can be described by five independent material constants, namely $E_{11}, E_{22}, \mu_{12}, \nu_{21}$ and ν_{13}.

Tensor $\mathbf{D_e}$, in this local Cartesian system defined in the deformed configuration, is expressed as follows

$$\mathbf{D_e} = \hat{D}_e^{pqrs}\left(\mathbf{e}_p \otimes \mathbf{e}_q \otimes \mathbf{e}_r \otimes \mathbf{e}_s\right) \tag{2.35}$$

16

Subsequently, the components D_e^{ijkl} of tensor $\mathbf{D_e}$ can be written in terms of the embedded coordinates ξ^i, through the standard tensor transformation

$$D_e^{ijkl} = \hat{D}_e^{pqrs}\left(\mathbf{g}^i \cdot \mathbf{e}_p\right)\left(\mathbf{g}^j \cdot \mathbf{e}_q\right)\left(\mathbf{g}^k \cdot \mathbf{e}_r\right)\left(\mathbf{g}^l \cdot \mathbf{e}_s\right) \qquad (2.36)$$

Using the definition of Jaumann stress rate

$$\overset{\nabla}{\boldsymbol{\tau}} = \dot{\boldsymbol{\tau}} - \boldsymbol{\omega}\boldsymbol{\tau} + \boldsymbol{\tau}\boldsymbol{\omega} \qquad (2.37)$$

the stress rate $\overset{\square}{\boldsymbol{\tau}}$, co-rotational with the anisotropy direction vector $\mathbf{n}$, can be related to $\overset{\nabla}{\boldsymbol{\tau}}$ as follows

$$\overset{\nabla}{\boldsymbol{\tau}} = \overset{\square}{\boldsymbol{\tau}} + \boldsymbol{\tau}\left(\boldsymbol{\omega} - \boldsymbol{\omega}_\alpha\right) - \left(\boldsymbol{\omega} - \boldsymbol{\omega}_\alpha\right)\boldsymbol{\tau} \qquad (2.38)$$

where

$$\boldsymbol{\omega} - \boldsymbol{\omega}_\alpha = \left(\mathbf{n} \otimes \mathbf{n}\right)\mathbf{d} - \mathbf{d}\left(\mathbf{n} \otimes \mathbf{n}\right) \qquad (2.39)$$

Equivalently,

$$\overset{\nabla}{\boldsymbol{\tau}} = \mathbf{D_e}\mathbf{d} + \boldsymbol{\tau}\left[\left(\mathbf{n} \otimes \mathbf{n}\right)\mathbf{d} - \mathbf{d}\left(\mathbf{n} \otimes \mathbf{n}\right)\right] - \left[\left(\mathbf{n} \otimes \mathbf{n}\right)\mathbf{d} - \mathbf{d}\left(\mathbf{n} \otimes \mathbf{n}\right)\right]\boldsymbol{\tau} \qquad (2.40)$$

Using simple tensor algebra, one can write

$$\left(\mathbf{n} \otimes \mathbf{n}\right)\mathbf{d} = \frac{1}{\left\|\mathbf{g}_2\right\|^2} d_{kl}\delta_2^k\left(\mathbf{g}_2 \otimes \mathbf{g}^l\right) \qquad (2.41)$$

and

$$\mathbf{d}\left(\mathbf{n} \otimes \mathbf{n}\right) = \frac{1}{\left\|\mathbf{g}_2\right\|^2} d_{kl}\,\delta_2^l\,\left(\mathbf{g}^k \otimes \mathbf{g}_2\right) \qquad (2.42)$$

where δ_m^k is Kronecker's delta. Furthermore, using equations (2.41) and (2.42), one readily obtains

$$\boldsymbol{\tau}\left(\mathbf{n} \otimes \mathbf{n}\right)\mathbf{d} = \frac{1}{\left\|\mathbf{g}_2\right\|^2}\delta_2^k\,\tau^{im}\,g_{m2}g^{jl}\left(\mathbf{g}_i \otimes \mathbf{g}_j\right)d_{kl} \qquad (2.43)$$

$$\mathbf{d}\left(\mathbf{n} \otimes \mathbf{n}\right)\boldsymbol{\tau} = \frac{1}{\left\|\mathbf{g}_2\right\|^2}\tau^{mj}\delta_2^l\,g_{m2}g^{ik}\left(\mathbf{g}_i \otimes \mathbf{g}_j\right)d_{kl} \qquad (2.44)$$

$$\left(\mathbf{n} \otimes \mathbf{n}\right)\mathbf{d}\boldsymbol{\tau} = \frac{1}{\left\|\mathbf{g}_2\right\|^2}\tau^{jl}\delta_2^k\,\delta_2^i\left(\mathbf{g}_i \otimes \mathbf{g}_j\right)d_{kl} \qquad (2.45)$$

$$\boldsymbol{\tau}\mathbf{d}\left(\mathbf{n} \otimes \mathbf{n}\right) = \frac{1}{\left\|\mathbf{g}_2\right\|^2}\tau^{ik}\delta_2^l\,\delta_2^j\left(\mathbf{g}_i \otimes \mathbf{g}_j\right)d_{kl} \qquad (2.46)$$

Therefore, equation (2.40) can be written as follows

$$\overset{\nabla}{\boldsymbol{\tau}} = \left(\mathbf{D_e} + \mathcal{A}\right)\mathbf{d} \qquad (2.47)$$

where the components of fourth-order order tensor $\mathcal{A}$, using (2.43)-(2.46), are

17

$$\mathcal{A}^{ijkl} = \frac{1}{\|\mathbf{g}_2\|^2} \left\{ g_{2m} \left(\delta_2^k \tau^{im} g^{jl} + \delta_2^l \tau^{jm} g^{ik} \right) - \left(\tau^{jl} \delta_2^i \delta_2^k + \tau^{ik} \delta_2^j \delta_2^l \right) \right\} \tag{2.48}$$

From continuum mechanics, the convected stress rate, defined as:

$$\overset{\circ}{\boldsymbol{\tau}} = \dot{\tau}^{ij} \left(\mathbf{g}_i \otimes \mathbf{g}_j \right) \tag{2.49}$$

is related to the Jaumann stress rate through the following expression:

$$\overset{\circ}{\boldsymbol{\tau}} = \overset{\triangledown}{\boldsymbol{\tau}} - \mathcal{L}\mathbf{d} \tag{2.50}$$

where $\mathcal{L}$ is the geometric rigidity fourth-order tensor, with components:

$$\mathcal{L}^{ijpq} = \frac{1}{2} [g^{ip} \tau^{jq} + g^{jp} \tau^{iq} + g^{iq} \tau^{jp} + g^{jq} \tau^{ip}] \tag{2.51}$$

Using (2.50) and (2.47), one finds:

$$\overset{\circ}{\boldsymbol{\tau}} = \left(\mathbf{D}_e + \mathcal{A} - \mathcal{L} \right) \mathbf{d} = \mathbf{R}\mathbf{d} \tag{2.52}$$

where $\mathbf{R}$ is a fourth order tensor, with components equal to:

$$R^{ijkl} = D_e^{ijkl} + \mathcal{A}^{ijkl} - \mathcal{L}^{ijkl} \tag{2.53}$$

In component form, equation (2.52) is written as follows:

$$\dot{\tau}^{ij} = \left(D_e^{ijkl} + \mathcal{A}^{ijkl} - \mathcal{L}^{ijkl} \right) d_{kl} \tag{2.54}$$

The rigidity tensor components in equation (2.53) will be used in the linearized equilibrium equation (2.12), to be discussed in a subsequent section. At this point it is pointed out, that the main advantage of this hypoelastic model is that the stress rate $\overset{\square}{\boldsymbol{\tau}}$ is always expressed co-rotationally with the anisotropy direction vector $\mathbf{n}$ at the current configuration. In other words, the constitutive equation ''follows'' the current orientation of the anisotropy axis.

The hypoelastic material model has a simpler form when the elastic material response is isotropic. In such a case, the continuum spin $\boldsymbol{\omega}$, expressing the average rotation of the material fibers at a specific material point, can be used in equation (2.27) instead of $\boldsymbol{\omega}_\alpha$, and in this case the co-rotational rate $\overset{\square}{\boldsymbol{\tau}}$ becomes the Jaumann stress rate $\overset{\triangledown}{\boldsymbol{\tau}}$:

$$\overset{\triangledown}{\boldsymbol{\tau}} = \dot{\boldsymbol{\tau}} - \boldsymbol{\omega}\boldsymbol{\tau} + \boldsymbol{\tau}\boldsymbol{\omega} \tag{2.55}$$

and

$$\overset{\triangledown}{\boldsymbol{\tau}} = \mathbf{D}_e \mathbf{d} \tag{2.56}$$

where the rigidity tensor $\mathbf{D}_e$ in equation (2.56) now depends on two material constants, namely the Young's modulus E and the Poisson's ratio ν. It is noted that this simplification is obtained if the following assumptions are adopted in (2.31):

$$A_{11} = A_{22} \tag{2.57}$$

$$\lambda = \lambda_{22} \tag{2.58}$$

18

$$\mu = \frac{1}{2}(A_{11} - \lambda_2) \qquad (2.59)$$

With respect to the current basis, the components D_e^{ijkl} of the rigidity tensor $\mathbf{D_e}$ have the following form:

$$D_e^{ijkl} = \frac{E}{2(1+\nu)}[g^{jq}g^{ip} + g^{iq}g^{jp} + \frac{2}{1-2\nu}g^{ij}g^{pq}] \qquad (2.60)$$

whereas matrix $\mathcal{L}$ is given by equation (2.51), as well. Therefore, equation (2.54) for elastic isotropic response is reformed as:

$$\dot{\tau}^{ij} = \left(D_e^{ijkl} - L^{ijkl}\right)d_{kl} = R^{ijkl}d_{kl} \qquad (2.61)$$

2.2.2 Hyperelastic Constitutive Model

The main assumption in hyperelasticity is the existence of a Helmholtz free-energy function Ψ, also referred to as strain-energy function, which is defined per unit reference volume. Herein, the Helmholtz free-energy function Ψ is considered a function of the Lagrange-Green strain tensor $\mathbf{E}$, and the general form of a constitutive equation in hyperelasticity can be expressed by:

$$\mathbf{S} = \rho_0 \frac{\partial \Psi(\mathbf{E})}{\partial \mathbf{E}} \qquad (2.62)$$

where $\mathbf{S}$ is the second Piola-Kirchhoff stress tensor, $\mathbf{E}$ is the Lagrange-Green strain tensor ($2\mathbf{E} = \mathbf{F}^T\mathbf{F} - \mathbf{I}$) and ρ_0 is the mass density in the initial configuration. The rate form of this hyperelastic constitutive model is obtained by differentiation of (2.62), so that:

$$\dot{\mathbf{S}} = \mathbf{D_e}\dot{\mathbf{E}} \qquad (2.63)$$

with $\mathbf{D_e}$ given by:

$$\mathbf{D_e} = \rho_0 \frac{\partial^2 \Psi(\mathbf{E})}{\partial \mathbf{E}\partial \mathbf{E}} \qquad (2.64)$$

In this study the free energy $\Psi(\mathbf{E})$ is expressed through a quadratic function of the components of $\mathbf{E}$ ([19], [20], [21]), as follows:

$$\rho_0 \Psi(\mathbf{E}) = \frac{1}{2}(\mathbf{D_e}\mathbf{E}) \cdot \mathbf{E} \qquad (2.65)$$

so that a linear constitutive equation between $\mathbf{S}(\mathbf{E})$ and $\mathbf{E}$ and their rates will be obtained. It is mentioned that in this way tensor $\mathbf{D_e}$ depends on the material constants only, and may include any type of material anisotropy.

In the special case of transversely isotropic materials, tensor $\mathbf{D_e}$ can be expressed in a Cartesian system in the undeformed configuration as follows:

19

$$\mathbf{D_e} = \hat{D}_e^{pqrs}\left(\overline{\mathbf{e}}_p \otimes \overline{\mathbf{e}}_q \otimes \overline{\mathbf{e}}_r \otimes \overline{\mathbf{e}}_s\right) \tag{2.66}$$

where the components $\hat{D}_e^{pqrs}$ are given by (2.31)-(2.33) with respect to the Cartesian system, defined in the reference configuration by the following orthonormal vectors:

$$\overline{\mathbf{e}}_1 = \frac{1}{\|\mathbf{G}^1\|}\mathbf{G}^1 \tag{2.67}$$

$$\overline{\mathbf{e}}_2 = \mathbf{N} \tag{2.68}$$

$$\overline{\mathbf{e}}_3 = \overline{\mathbf{e}}_1 \times \overline{\mathbf{e}}_2 \tag{2.69}$$

Subsequently, the components of D_e^{ijkl} of tensor $\mathbf{D_e}$ can be written in terms of the embedded coordinates, defined in the initial configuration, through the tensor transformation

$$D_e^{ijkl} = \hat{D}_e^{pqrs}\left(\mathbf{G}^i \cdot \overline{\mathbf{e}}_p\right)\left(\mathbf{G}^j \cdot \overline{\mathbf{e}}_q\right)\left(\mathbf{G}^k \cdot \overline{\mathbf{e}}_r\right)\left(\mathbf{G}^l \cdot \overline{\mathbf{e}}_s\right) \tag{2.70}$$

It is mentioned that, in the case of transversely isotropy, $\mathbf{D_e}$ can be expressed in a general tensor notation as follows [19], [20], [21]:

$$\mathbf{D_e} = 2a\mathbf{I} \otimes \mathbf{I} + 2b\mathbf{J} + 2c\mathbf{A} \otimes \mathbf{A} + d\mathbf{P} + e(\mathbf{I} \otimes \mathbf{A} + \mathbf{A} \otimes \mathbf{I}) \tag{2.71}$$

where $\mathbf{I}$ is the second-order identity tensor, $\mathbf{J}$ is the fourth-order identity tensor, the orientation tensor $\mathbf{A}$ is defined as:

$$\mathbf{A} = \mathbf{N} \otimes \mathbf{N} \tag{2.72}$$

the components of tensor $\mathbf{P}$ are defined as:

$$P_{ijkl} = \frac{1}{2}(A_{ik}\delta_{jl} + A_{il}\delta_{jk} + \delta_{ik}A_{jl} + \delta_{il}A_{jk}) \tag{2.73}$$

with respect to a Cartesian system,

and a, b, c, d, e are related to the five independent elastic constants of the transversely isotropic material $E_{11}, E_{22}, \mu_{12}, \nu_{21}$ and ν_{13} as follows [19]:

$$a = \frac{1}{2}(K_{13} - \mu_{13}) \tag{2.74}$$

$$b = \mu_{13} \tag{2.75}$$

$$c = \frac{1}{2}(E_{22} - \mu_{13} - 2\mu_{12} + (1 - 2\nu_{21})^2 K_{13}) \tag{2.76}$$

$$d = 2(\mu_{12} - \mu_{13}) \tag{2.77}$$

$$e = \mu_{13} - (1 - 2\nu_{21})K_{13} \tag{2.78}$$

with K_{13}, μ_{13} given by (2.33) and (2.34), respectively.

One should note that this hyperelastic material modeling refers always to the initial configuration and, therefore, it does not ''follow'' the local anisotropy axis throughout the deformation history. However, it is applicable to the more general cases of anisotropy (e.g.

orthotropy), where the anisotropy axes and their orientation in the deformed (current) configuration can not be defined through a hypoelastic model.

In the framework of hyperelasticity with quadratic free energy functions, the special case of isotropy can be described in the same basis as above. In such a case, the fourth-order tensor $\mathbf{D}_e$ obtains a more simple form as:

$$\mathbf{D}_e = \lambda \mathbf{I} \otimes \mathbf{I} + 2\mu \mathbf{J} \tag{2.79}$$

where the so-called Lame constants λ, μ are given in terms of the physical parameters E, ν as follows:

$$\begin{aligned} \lambda &= \frac{E\nu}{1 - \nu - 2\nu^2} \\ \mu &= \frac{1}{2}\frac{E}{1+\nu} \end{aligned} \tag{2.80}$$

Note

In the present work, and for the purposes of conducting an extensive parametric study, the local components $\hat{D}_e^{ijkl}$ of tensor $\mathbf{D}_e$ (2.31) are reformed in a more convenient manner. It is reminded that the axis of anisotropy is directed along axis 2, which corresponds to the longitudinal direction of the cylinder (Fig. 1). More specifically, the following equations are assumed for the five independent material constants (A_{11}, A_{22}, λ_2, λ and μ).

$$\tfrac{1}{2}\left(A_{11} - \lambda_2\right) = \mu \tag{2.81}$$

$$\lambda_2 = \lambda \tag{2.82}$$

In such a case, from expressions (2.81) and (2.82), one trivially obtains:

$$A_{11} = \lambda + 2\mu \tag{2.83}$$

It is further assumed that:

$$A_{22} = SA_{11} \tag{2.84}$$

where S is a parameter that indicates the level of anisotropy. Therefore, the components $\hat{D}_e^{ijkl}$ of tensor $\mathbf{D}_e$ in a local Cartesian system are now given by:

$$
\begin{array}{c}
\begin{array}{cccccc} \mathbf{11} & \mathbf{22} & \mathbf{33} & \mathbf{12} & \mathbf{13} & \mathbf{23} \end{array} \\
\begin{array}{c} \mathbf{11} \\ \mathbf{22} \\ \mathbf{33} \\ \mathbf{12} \\ \mathbf{13} \\ \mathbf{23} \end{array}
\begin{bmatrix}
\lambda + 2\mu & \lambda & \lambda & 0 & 0 & 0 \\
\lambda & S(\lambda + 2\mu) & \lambda & 0 & 0 & 0 \\
\lambda & \lambda & \lambda + 2\mu & 0 & 0 & 0 \\
0 & 0 & 0 & \mu & 0 & 0 \\
0 & 0 & 0 & 0 & \mu & 0 \\
0 & 0 & 0 & 0 & 0 & \mu
\end{bmatrix}
\end{array} \tag{2.85}
$$

21

Clearly, if $S=1$, the material is isotropic elastic, and λ and μ become the well-known Lamé constants.

Using the above three independent material constants λ, μ, S and assuming uniaxial stress states in the direction of axes 1 and 2, one obtains the uniaxial moduli E_{11}, E_{22} and the corresponding Poisson's ratios $v_{12}, v_{13}, v_{21}, v_{23}$:

$$E_{11} = \lambda \frac{4(1-S) - 4S\frac{\mu}{\lambda}(2+3\frac{\mu}{\lambda})}{\frac{\lambda}{\mu}(1-S) - 4S(1+\frac{\mu}{\lambda})} \tag{2.86}$$

$$E_{22} = \lambda \frac{S(3+2\frac{\mu}{\lambda}) - \frac{\lambda}{\mu}(1-S)}{1+\frac{\lambda}{\mu}} \tag{2.87}$$

$$v_{12} = \frac{2}{4S(1+\frac{\mu}{\lambda}) - \frac{\lambda}{\mu}(1-S)} \tag{2.88}$$

$$v_{13} = \frac{\frac{\lambda}{\mu}(1-S) - 2S}{\frac{\lambda}{\mu}(1-S) - 4S(1+\frac{\mu}{\lambda})} \tag{2.89}$$

$$v_{21} = \frac{1}{2(1+\frac{\mu}{\lambda})} = v_{23} \tag{2.90}$$

Using (2.86) and (2.87) a dependent variable $\bar{q}$ can be introduced, that expresses the ratio of the longitudinal uniaxial moduli E_{22} over the hoop moduli E_{11}.

$$\bar{q}^2 = \frac{E_{22}}{E_{11}} = S - \frac{\frac{\lambda}{\mu}(1-S)}{4(1+\frac{\mu}{\lambda})} \tag{2.91}$$

From (2.91), one concludes that the E_{22}/E_{11} ratio depends on the level of anisotropy S and the λ/μ ratio. Employing (2.91) the corresponding values of $\bar{q}^2 = E_{22}/E_{11}$ are shown graphically in Fig. 2 in terms of S for three different values of λ/μ ratio.

22
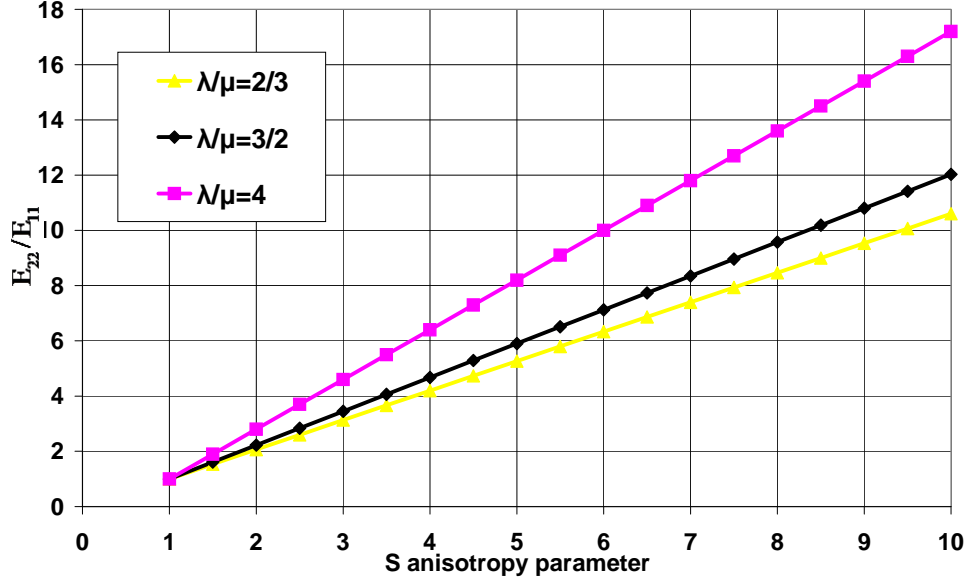
Fig. 2 Values of E_{22}/E_{11} in terms of S

2.3 Inelastic Constitutive Model

To model inelastic material behavior, J_2 flow theory of plasticity with isotropic hardening is adopted. The hypoelastic constitutive equations relate the Jaumann rate of Kirchhoff stress to the rate-of-deformation. The deviatoric Kirchhoff stress is defined as:

$$\mathbf{s} = \boldsymbol{\tau} - \frac{1}{3}(\boldsymbol{\tau}\cdot\mathbf{I})\mathbf{I} \tag{2.92}$$

with contravariant components (on the current basis vectors)

$$s^{ij} = \tau^{ij} - \frac{1}{3}g^{ij}g_{kl}\tau^{kl} \tag{2.93}$$

The von Mises (effective) stress is defined as:

$$Y = \sqrt{3J_2} = \sqrt{\frac{3}{2}\mathbf{s}\cdot\mathbf{s}} = \sqrt{\frac{3}{2}g_{ik}g_{jl}s^{ij}s^{kl}} \tag{2.94}$$

where J_2 is the second invariant of $\mathbf{s}$.

Yielding occurs when

$$Y = Y_{max} \quad \text{and} \quad \dot{Y} > 0 \tag{2.95}$$

where Y_{max} is equal to the maximum value of Y throughout the deformation history but not less than $Y_{max,0}$, which is the initial yielding value for the case of uniaxial tension. If at least one of the conditions of (2.95) is violated elastic behavior occurs and the constitutive equations are the ones described in section 2.2.1 (isotropic material behavior). Furthermore, it is assumed that

23

the rate-of-deformation tensor $\mathbf{d}$ is decomposed in an additive manner to an elastic and a plastic part

$$\mathbf{d} = \mathbf{d}^e + \mathbf{d}^p \tag{2.96}$$

Furthermore, it is assumed that the material obeys the normality rule imposed by the Drucker's stability postulate. Upon yielding the plastic part $\mathbf{d}^p$ of the rate-of-deformation tensor is:

$$\mathbf{d}^p = \frac{3}{2} \frac{\dot{d}_p}{Y} \mathbf{s} \tag{2.97}$$

where it can be easily shown that the equivalent plastic strain d_p is equal to

$$d_p = \int_0^t \sqrt{\frac{2}{3} \mathbf{d}^p \cdot \mathbf{d}^p} \, dt \tag{2.98}$$

The above equation indicates that d_p is a monotonically increasing parameter that offers a measure of the total plastic deformation. Based on this observation, it is assumed that Y_{max} is also a monotonically increasing function of d_p, where $d_p = 0$ and $Y_{max} = Y_{max,0}$ at initial yielding. The function can be found from a standard calibration procedure using a uniaxial stress-strain curve, as outlined at the end of this section. During elastoplastic loading, $Y = Y_{max}$ and therefore:

$$\dot{Y} = \dot{Y}_{max} \qquad \text{and} \qquad \dot{Y} = \frac{dY_{max}}{dd_p} \dot{d}_p \tag{2.99}$$

It can be shown that the differentiation of (2.94) gives:

$$\dot{Y} = \frac{3}{2Y} \mathbf{s} \cdot \overset{\triangledown}{\boldsymbol{\tau}} \tag{2.100}$$

The hypoelastic constitutive equation relates the Jaumann rate of Kirchhoff stress to the elastic part of rate-of-deformation tensor $\mathbf{d}^e = \mathbf{d} - \mathbf{d}^p$ as follows:

$$\overset{\triangledown}{\boldsymbol{\tau}} = \mathbf{D}_e \mathbf{d}^e \tag{2.101}$$

where $\mathbf{D}^e$ is the elastic rigidity matrix and for the case of isotropic elasticity is given by (2.60).

Using (2.101) and (2.97)-(2.100), and after some manipulations the following equation is obtained:

$$\overset{\triangledown}{\boldsymbol{\tau}} = \mathbf{D} \mathbf{d} \tag{2.102}$$

where $\mathbf{D}$ is the fourth-order elastic-plastic rigidity tensor whose contravariant components with respect to the current basis are:

$$D^{ijkl} = D_e^{ijkl} - \frac{3G}{Y^2} \frac{1}{1 + (H/3G)} s^{ij} s^{kl} \tag{2.103}$$

24

where D_e^{ijkl} components are given by (2.60) and $H = \dfrac{dY_{\max}}{dd_p}$. Consequently, the convected rate

of Kirchhoff stress $\overset{\circ}{\boldsymbol{\tau}}$ is found to be:

$$\overset{\circ}{\boldsymbol{\tau}} = (\mathbf{D} - \mathcal{L})\mathbf{d} = \mathbf{R}\,\mathbf{d} \tag{2.104}$$

where the contravariant components of tensor $\mathcal{L}$ are computed from (2.51).

It can be easily checked that the components of tensor $\mathbf{R}$ exhibit the symmetries $R^{ijkl} = R^{jikl} = R^{ijlk}$ (due to symmetry of $\overset{\circ}{\boldsymbol{\tau}}$ and $\mathbf{d}$) and the nontrivial symmetry $R^{ijkl} = R^{klij}$.

To complete the development of the constitutive equations, the function $Y_{\max}(d_p)$ must be appropriately defined from the uniaxial tension stress-strain curve. It is assumed that the uniaxial curve $\hat{\sigma}$ versus $\hat{\varepsilon}$ is known, where $\hat{\sigma}$ is the nominal strain and $\hat{\varepsilon}$ is the nominal strain. If P is the applied load, L_0, L are the initial and current bar lengths, respectively, so that $\Delta L = L - L_0$ and A_0, A are the initial and current cross-sectional areas, respectively, the following are obtained:

axial nominal stress

$$\hat{\sigma} = \frac{P}{A_0} \tag{2.105}$$

axial nominal strain

$$\hat{\varepsilon} = \frac{\Delta L}{L_0} \tag{2.106}$$

axial Cauchy stress

$$\sigma = \frac{P}{A} = \hat{\sigma}\frac{A_0}{A} \tag{2.107}$$

axial Kirchhoff stress

$$\tau = \frac{V}{V_0}\sigma = \frac{L}{L_0}\hat{\sigma} = (1 + \hat{\varepsilon})\hat{\sigma} \tag{2.108}$$

deviatoric Kirchhoff stress components

$$s_{11} = \frac{2}{3}\tau$$
$$s_{22} = s_{33} = -\frac{1}{3}\tau \tag{2.109}$$
$$s_{ij} = 0, \quad i \neq j$$

plastic rate-of-deformation stress components

$$d_{11}^{p} = d_{11}^{p}$$

$$d_{22}^{p} = d_{33}^{p} = -\frac{1}{2}d_{11}^{p} \qquad (2.110)$$

$$d_{ij}^{p} = 0, \quad i \neq j$$

total rate-of-deformation in the axial direction

$$d_{11} = \frac{dL/L}{dt} \qquad (2.111)$$

elastic part of rate-of-deformation in the axial direction

$$d_{11}^{e} = \frac{\dot{\tau}}{E} \qquad (2.112)$$

plastic deformation parameter

$$\dot{d}_{p} = d_{11}^{p} \qquad (2.113)$$

furthermore, the von Mises stress is

$$Y = \tau = (1 + \hat{\varepsilon})\hat{\sigma} \qquad (2.114)$$

from

$$d_{11}^{p} = d_{11} - d_{11}^{e} \qquad (2.115)$$

and therefore,

$$\dot{d}_{p} = \frac{dL}{dt}\frac{1}{L} - \frac{\dot{\tau}}{E} \qquad (2.116)$$

Integration of this quantity gives:

$$d_{p} = \ln(1 + \hat{\varepsilon}) - (1 + \hat{\varepsilon})\frac{\hat{\sigma}}{E} \qquad (2.117)$$

Expressions (2.105)-(2.108), (2.114) and (2.117) provide $Y_{\max}$ and d_{p} in terms of the ''engineering'' values of stress $\hat{\sigma}$ and strain $\hat{\varepsilon}$.

2.4 Linearization of Equilibrium Equations

The numerical solution of the nonlinear equilibrium equations is based on the linearization of principle of virtual work (2.12) and (2.16). For this purpose, the principle of virtual work is considered at a ''nearby'' configuration $\mathbf{x}'$:

$$\int_{V_0} \delta U'_{k/j}(\mathbf{G}^{k} \cdot \mathbf{g}'_{i})\tau'^{ij}dV_0 = \int_{B'_q} \delta\mathbf{u}' \cdot \mathbf{t}'dB'_q + M'\delta\theta' \qquad (2.118)$$

This configuration corresponds to stress tensor $\boldsymbol{\tau}'$, boundary traction $\mathbf{t}'$ and bending moment M'. The increment of displacement $\Delta\mathbf{u}$, is defined as:

$$\Delta\mathbf{u} = \mathbf{x}' - \mathbf{x} = \int_{t_x}^{t_{x'}} \dot{\mathbf{x}}dt \qquad (2.119)$$

26

The covariant base vectors at the nearby configuration are expressed as:

$$\mathbf{g}_i{}' = \frac{\partial \mathbf{x}'}{\partial \xi^i} = \frac{\partial \mathbf{x}}{\partial \xi^i} + \frac{\partial (\Delta \mathbf{u})}{\partial \xi^i} = \mathbf{g}_i + \frac{\partial (\Delta \mathbf{u})}{\partial \xi^i} \tag{2.120}$$

Moreover,
$$\tau'^{\,ij} = \tau^{ij} + \int_{t_x}^{t_{x'}} \dot{\tau}^{ij} dt \tag{2.121}$$

Assuming a hypoelastic material behavior in the form of expression (2.104), which includes the case of plasticity, expression (2.121) is written as follows:

$$\tau'^{\,ij} = \tau^{ij} + \int_{t_x}^{t_{x'}} R^{ijpq} d_{pq} dt \tag{2.122}$$

where the values of $t_x, t_{x'}$ express the ''time-like'' parameter t in the two configurations, $\mathbf{x}$ and $\mathbf{x}'$ respectively.

After some straightforward calculations the principle of virtual work (2.12) can be written linearized in the following linearized form

$$\int_{V_0} \delta U_{i/j} \mathcal{D}^{ijpq} \Delta U_{p/q} dV_0 = \int_B \delta \mathbf{u} \cdot \left(\mathbf{t} + \Delta \mathbf{t} \right) dB_q + \left(M + \Delta M \right) \delta \theta - \int_{V_0} \delta U_{i/j} \hat{\sigma}^{\,ji} dV_0 \tag{2.123}$$

In the above equation, Δt and ΔM are the increments of the surface traction and bending moment, respectively. Furthermore, $\delta U_{p/q}$ is defined by (2.13), and similarly:

$$\Delta U_{p/q} = \frac{\partial (\Delta \mathbf{u})}{\partial \xi^q} \cdot \mathbf{G}_p \tag{2.124}$$

where $\Delta \mathbf{u}$ are the incremental displacements, whereas $\hat{\sigma}^{\,ij}$ are the components of the nominal stress tensor defined as follows:

$$\hat{\boldsymbol{\sigma}} dV_0 = \mathbf{F}^{-1} \boldsymbol{\sigma} dV$$
$$\hat{\boldsymbol{\sigma}} = J\mathbf{F}^{-1} \boldsymbol{\sigma} \tag{2.125}$$

where $\mathbf{F}$ is the deformation gradient and $J = \det(\mathbf{F})$, and finally:

$$\hat{\sigma}^{\,ij} = \tau^{ij} (\mathbf{g}_i \cdot \mathbf{G}^j) \tag{2.126}$$

In addition, the fourth-order tensor components $\mathcal{D}^{ijpq}$ are equal to:

$$\mathcal{D}^{ijpq} = (\mathbf{G}^i \cdot \mathbf{g}_k) R^{kjmq} (\mathbf{g}_m \cdot \mathbf{G}^p) + \tau^{jq} G^{ip} \tag{2.127}$$

where tensor $\mathbf{R}$ is defined by (2.104).

Equation (2.123) is the linearized form of the principle of virtual work, based on hypoelastic material behavior, which includes plasticity effects. In the case of hypoelasticity, the linearized principle of virtual work is given by the same expression (2.123), where in equation (2.127) tensor components R^{ijkl} are replaced by tensor components D_e^{ijkl} given by (2.70).

2.5 Galerkin Discretization

The numerical solution is based on the finite element discretization of linearized equilibrium equations described in the previous section. Using appropriate shape functions, the incremental displacement field can be written as:

$$\Delta\mathbf{u} = [\mathbf{N}]\Delta\hat{\mathbf{U}} \tag{2.128}$$

in which $[\mathbf{N}]$ is the interpolation matrix that contains shape functions and $\Delta\hat{\mathbf{U}}$ contains the increments of nodal degrees of freedom. Using the same functions for the virtual displacements,

$$\delta\mathbf{u} = [\mathbf{N}]\delta\hat{\mathbf{U}} \tag{2.129}$$

Covariant differentiation of equations (2.128) and (2.129), and using the following equations

$$\Delta U_{p/q} = \frac{\partial(\Delta\mathbf{u})}{\partial\xi^q} \cdot \mathbf{G}_p$$

$$\delta U_{p/q} = \frac{\partial(\delta\mathbf{u})}{\partial\xi^q} \cdot \mathbf{G}_p \tag{2.130}$$

one results in:

$$grad(\Delta\mathbf{u}) = \left\{\Delta U_{k/l}\right\} = [\mathbf{B}]\Delta\hat{\mathbf{U}} \tag{2.131}$$

$$grad(\delta\mathbf{u}) = \left\{\delta U_{k/l}\right\} = [\mathbf{B}]\delta\hat{\mathbf{U}} \tag{2.132}$$

where $[\mathbf{B}]$ contains the derivatives of the elements of the interpolation matrix.

Furthermore, the traction component normal to any shell lamina is imposed to be zero at any stage of deformation $\tau^{33} = 0$, following classical shell theory.

On account of the symmetry of the Kirchhoff stress, and because $\tau^{33} = 0$, the five-component column vector of stress components $\boldsymbol{\tau}$ is written as:

$$\boldsymbol{\tau} = \begin{bmatrix} \tau^{11} \\ \tau^{22} \\ \tau^{12} \\ \tau^{23} \\ \tau^{31} \end{bmatrix} \tag{2.133}$$

Applying the condition that $\dot{\tau}^{33} = 0$ (since $\tau^{33} = 0$ at all times) the constitutive equation in terms of the convected rate of Kirchhoff stress (hypoelasticity) can be written in matrix form as:

$$\dot{\boldsymbol{\tau}} = [\mathbf{R}]\mathbf{d} \tag{2.134}$$

in which

$$\dot{\boldsymbol{\tau}} = \begin{bmatrix} \dot{\tau}^{11} \\ \dot{\tau}^{22} \\ \dot{\tau}^{12} \\ \dot{\tau}^{23} \\ \dot{\tau}^{31} \end{bmatrix} \qquad \mathbf{d} = \begin{bmatrix} d_{11} \\ d_{22} \\ d_{12} \\ d_{23} \\ d_{31} \end{bmatrix} \tag{2.135}$$

28

and $[\mathbf{R}]$ is a 5x5 matrix, containing the components of the appropriate rigidity tensor.

On the basis of the symmetries of the components R^{ijpq}, it can be shown that matrix $[\mathbf{R}]$ is symmetric. Another auxiliary matrix $[\mathbf{C}]$ (9x9) is defined so that:

$$C_{IJ} = \tau^{j(I)q(J)}G^{i(I)p(J)} \tag{2.136}$$

with the relations between the indices given by:

$$
\begin{array}{ccc}
I,J & i \text{ or } p & j \text{ or } q \\
1 & 1 & 1 \\
2 & 2 & 1 \\
3 & 3 & 1 \\
4 & 1 & 2 \\
5 & 2 & 2 \\
6 & 3 & 2 \\
7 & 1 & 3 \\
8 & 2 & 3 \\
9 & 3 & 3
\end{array} \tag{2.137}
$$

This arrangement is consistent with that of gradient components in (2.131).

$$
\{\Delta U_{p/q}\} = \begin{bmatrix}
\Delta U_{1/1} \\
\Delta U_{2/1} \\
\Delta U_{3/1} \\
\Delta U_{1/2} \\
\Delta U_{2/2} \\
\Delta U_{3/2} \\
\Delta U_{1/3} \\
\Delta U_{2/3} \\
\Delta U_{3/3}
\end{bmatrix} \tag{2.138}
$$

It can be readily verified that $[\mathbf{C}]$ is symmetric (because $\tau^{jk}G^{il} = \tau^{kj}G^{li}$).

Recalling that the mixed components of the deformation gradient with respect to the reference base vectors are written as follows,

$$F_{\cdot j}^{i} = \mathbf{F} \cdot (\mathbf{G}^{i} \otimes \mathbf{G}_{j}) = (\mathbf{F}\mathbf{G}_{j}) \cdot \mathbf{G}^{i} = \mathbf{G}^{i} \cdot \mathbf{g}_{j} \tag{2.139}$$

a 5x9 matrix $[\mathbf{W}]$ containing these components is introduced:

$$
[\mathbf{W}] = \begin{bmatrix}
F_{.1}^{1} & F_{.1}^{2} & F_{.1}^{3} & 0 & 0 & 0 & 0 & 0 & 0 \\
0 & 0 & 0 & F_{.2}^{1} & F_{.2}^{2} & F_{.2}^{3} & 0 & 0 & 0 \\
F_{.2}^{1} & F_{.2}^{2} & F_{.2}^{3} & F_{.1}^{1} & F_{.1}^{2} & F_{.1}^{3} & 0 & 0 & 0 \\
0 & 0 & 0 & F_{.3}^{1} & F_{.3}^{2} & F_{.3}^{3} & F_{.2}^{1} & F_{.2}^{2} & F_{.2}^{3} \\
F_{.3}^{1} & F_{.3}^{2} & F_{.3}^{3} & 0 & 0 & 0 & F_{.1}^{1} & F_{.1}^{2} & F_{.1}^{3}
\end{bmatrix} \tag{2.140}
$$

Moreover, another 5x5 matrix $[\mathcal{D}]$ is introduced,

29

$$[\mathcal{D}] = [\mathbf{W}]^{\mathrm{T}}[\mathbf{R}][\mathbf{W}] + [\mathbf{C}] \tag{2.141}$$

Using the matrices and column vectors defined above, the linearized form of the principal of virtual work (2.123) can be written as:

$$\delta \hat{\mathbf{U}}^{\mathrm{T}} \left(\int_{V_0} [\mathbf{B}]^{\mathrm{T}}[\mathcal{D}][\mathbf{B}] dV_0 \right) \Delta \hat{\mathbf{U}} = \delta \hat{\mathbf{U}}^{\mathrm{T}} \left(\int_{B_q} [\mathbf{N}]^{\mathrm{T}} \mathbf{t}' dB_q - \int_{V_0} [\mathbf{B}]^{\mathrm{T}}[\mathbf{W}]^{\mathrm{T}} \boldsymbol{\tau} dV_0 \right) \tag{2.142}$$

Requiring that (2.142) holds for arbitrary virtual displacements $\delta \hat{\mathbf{U}}$, the following set of equations is obtained:

$$[\mathbf{K}] \Delta \hat{\mathbf{U}} = \mathbf{F}_{\mathrm{ext}} - \mathbf{F}_{\mathrm{int}} \tag{2.143}$$

where $[\mathbf{K}]$ is the incremental stiffness matrix

$$[\mathbf{K}] = \int_{V_0} [\mathbf{B}]^{\mathrm{T}}[\mathcal{D}][\mathbf{B}] dV_0 \tag{2.144}$$

and $\mathbf{F}_{\mathrm{ext}}, \mathbf{F}_{\mathrm{int}}$ are the external and internal load vectors respectively.

$$\mathbf{F}_{\mathrm{ext}} = \int_{B_q} [\mathbf{N}]^{\mathrm{T}} \mathbf{t}' dB_q \tag{2.145}$$

$$\mathbf{F}_{\mathrm{int}} = \int_{V_0} [\mathbf{B}]^{\mathrm{T}}[\mathbf{W}]^{\mathrm{T}} \boldsymbol{\tau} dV_0 \tag{2.146}$$

After assembling the stiffness matrices and load vectors of all elements, using the above relations, the system of equations for the displacement increment is solved. Upon computing the displacement increment, the corresponding increments of strains and stresses are calculated and thus an estimate for the nearby state of equilibrium is obtained. The iterative procedure is continued until equilibrium is achieved ($\mathbf{F}_{\mathrm{ext}} = \mathbf{F}_{\mathrm{int}}$).

2.6 ''Tube-Element''-Description

In the past, several attempts have been reported to apply ''pipe'' or ''elbow'' elements for modelling of elongated cylinders, as alternatives to shell elements. These elements combine longitudinal (beam-type) deformation of the cylinder's axis with cross-sectional deformation of the cylinder wall, and have been employed for the analysis of tubes and pipelines. Such elements been shown to be quite effective for the modelling of tubular members, pipelines, elbows and piping systems. Among other advantages of those elements over shell elements, one should underline the more convenient application of boundary conditions and kinematic constraints, as well as the clearest interpretation of numerical results.

The first attempt to combine the longitudinal deformation of the tube axis with cross-sectional ovalization was described in the studies of Bathe and Almeida [22], [23] for linear analysis and in a subsequent work of Bathe et al [24], where some nonlinear capabilities were investigated.

Militello and Huespe [25] proposed a further improvement of the above element including warping deformation, but keeping the inextentionality condition, which implies that the circumference length of the cylinder does not change during deformation. Hermite polynomials were used to ensure inter-element continuity. In a more recent paper, Yan et al [26] have proposed an enhanced ''pipe-elbow element'', which further improves the above concepts and capabilities. Their element included warping deformation, and accounted for a certain degree of cross-sectional extentionality and for non-symmetric cross-sectional deformation. Moreover, the contribution of pressure on the stiffness matrix (i.e. the ''pressure stiffness'' effects) was considered. This element was used for the numerical calculation of limit plastic response of tubes.

Hibbit et al [27] have developed an elbow element for the elastic and elastic-plastic analysis of initially straight and bent tubes under pressure and structural loads. The element is incorporated in the Finite Element program ABAQUS. It is based on the Koiter–Sanders linear shell kinematics and on a discrete Kirchhoff concept, imposed through a penalty formulation. Cross-sectional warping is included and the corresponding deformation parameters are discretized through the use of trigonometric functions up to the 6th degree. Finally, the element accounts for pressure effects rigorously.

A nonlinear ''tube-element'' is presented in this section, which is employed for the purposes of this study in simulating the behavior of cylinders (initially straight or bent) subjected to bending within the plane of the cylinder. This ''tube-element'' combines longitudinal (beam-type) with cross-sectional deformation. Isoparametric beam finite element concept is used to describe longitudinal deformation and three nodes are defined along the cylinder's axis (Fig. 3). Geometry and displacements are interpolated using quadratic polynomials. Bending is applied about axis x_1 (i.e. $x_2 - x_3$ is the plane of bending) and each node possesses three degrees of freedom (two translational and one rotational), which define its position and orientation.

A reference line is chosen within the cross-section at node (k) and a local Cartesian coordinate system is defined, so that the $\overline{\mathbf{x}}, \overline{\mathbf{y}}$ axes define the cross-sectional plane. The orientation of node (k) is defined by the position of three orthonormal vectors $\mathbf{e}_x^{(k)}, \mathbf{e}_y^{(k)}$ and $\mathbf{e}_z^{(k)}$. For in-plane (ovalization) deformation, fibers initially normal to the reference line remain normal to the reference line. Furthermore, those fibers may rotate in the out-of-plane direction by angle $\gamma(\theta)$. Using quadratic interpolation in the longitudinal direction, the position vector $\mathbf{x}(\theta, \zeta, \rho)$ of an arbitrary point at the deformed configuration is:

$$\mathbf{x}(\theta, \zeta, \rho) = \sum_{\kappa=1}^{3} \left[\left(\mathbf{x}^{(k)} + \mathbf{r}^{(k)}(\theta) + \rho \mathbf{n}^{(k)}(\theta) + \rho \gamma(\theta) \mathbf{e}_z^{(k)} \right) N^{(k)}(\zeta) \right] \qquad (2.147)$$

31

where $\mathbf{x}^{(k)}$ is the position vector of node (k), $\mathbf{r}^{(k)}(\theta)$ is the position of the reference line at a certain cross-section relative to the corresponding node (k), $\mathbf{n}^{(k)}(\theta)$ is the ''in-plane'' outward normal of the reference line at the deformed configuration and $N^{(k)}(\zeta)$ is the corresponding Lagrangian quadratic polynomial.
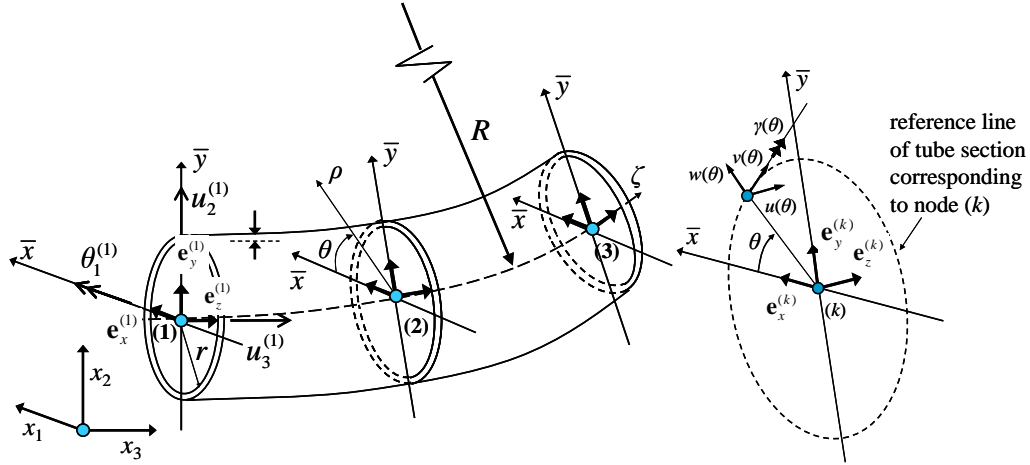

Fig. 3 Tube element and deformation parameters; $x_2 - x_3$ is the plane of bending

The position of the reference line $\mathbf{r}^{(k)}(\theta)$ at the deformed cross-section corresponding to node (k) is

$$\mathbf{r}^{(k)}(\theta) = x_r(\theta)\mathbf{e}_x^{(k)} + y_r(\theta)\mathbf{e}_y^{(k)} + z_r(\theta)\mathbf{e}_z^{(k)} \qquad (2.148)$$

where

$$x_r(\theta) = \left[r + w(\theta)\right]\cos\theta - v(\theta)\sin\theta$$
$$y_r(\theta) = \left[r + w(\theta)\right]\sin\theta + v(\theta)\cos\theta \qquad (2.149)$$
$$z_r(\theta) = u(\theta)$$

are the components of $\mathbf{r}^{(k)}(\theta)$ with respect to the cross-section vector triplet (Fig. 3). In the above expressions, $w(\theta), v(\theta)$ and $u(\theta)$ are displacements of the reference line in the radial, tangential and out-of-plane (axial) direction, respectively, whereas, angle rotation $\gamma(\theta)$ corresponds to the material out-of-plane fiber rotation (Fig. 3). For an extensive presentation of ring analysis, the reader is referred to the book by Brush and Almroth [11].

The deformation functions $w(\theta), v(\theta), u(\theta)$ and $\gamma(\theta)$ are discretized as follows:

32

$$w(\theta) = a_0 + a_1 \sin\theta + \sum_{n=2,4,6,...} a_n \cos n\theta + \sum_{n=3,5,7,....} a_n \sin n\theta$$

$$v(\theta) = -a_1 \sin\theta + \sum_{n=2,4,6,...} b_n \sin n\theta + \sum_{n=3,5,7,....} b_n \cos n\theta$$

$$u(\theta) = \sum_{n=2,4,6,...} c_n \cos n\theta + \sum_{n=3,5,7,....} c_n \sin n\theta \qquad (2.150)$$

$$\gamma(\theta) = \sum_{n=0,2,4,6,...} \gamma_n \cos n\theta + \sum_{n=1,3,5,7,....} \gamma_n \sin n\theta$$

Coefficients α_n, b_n refer to in-plane cross-sectional deformation ("ovalization" parameters) and c_n, γ_n refer to out-of-plane cross-sectional deformation ("warping" parameters). In the above expressions, symmetry with respect to the $x_2 - x_3$ plane is considered because of in-plane bending and only half of the tube is analyzed ($-\pi/2 \le \theta \le \pi/2$).

The outward unit vector $\mathbf{n}^{(k)}(\theta)$, normal to the reference line can be written as:

$$\mathbf{n}^{(k)}(\theta) = n_x \mathbf{e}_x^{(k)} + n_y \mathbf{e}_y^{(k)} \qquad (2.151)$$

where

$$n_x = \frac{(dy_r/d\theta)}{(ds_r/d\theta)}$$

$$n_y = -\frac{(dx_r/d\theta)}{(ds_r/d\theta)} \qquad (2.152)$$

and

$$\frac{dy_r}{d\theta} = -[r + w(\theta) + v'(\theta)]\sin\theta + [w'(\theta) - v(\theta)]\cos\theta$$

$$\frac{dx_r}{d\theta} = -[r + w(\theta) + v'(\theta)]\cos\theta - [w'(\theta) - v(\theta)]\sin\theta \qquad (2.153)$$

$$\frac{ds_r}{d\theta} = \sqrt{r^2 + 2r[v'(\theta) + w(\theta)] + [v'(\theta) + w(\theta)]^2 + [w'(\theta) - v(\theta)]^2}$$

The position vector expressed through (2.147) can be written alternatively as follows

$$\mathbf{x}(\theta, \zeta, \rho) = \sum_{k=1}^{3} \left[\left(\mathbf{x}^{(k)} + (x_r + \rho n_x)\mathbf{e}_x^{(k)} + (y_r + \rho n_y)\mathbf{e}_y^{(k)} + (z_r + \rho\gamma)\mathbf{e}_z^{(k)} \right) N^{(k)}(\zeta) \right] \quad (2.154)$$

and differentiating this expression with respect to the time variable and omitting higher order terms the following for the velocity vector is obtained:

$$\dot{\mathbf{x}} = \mathbf{v}(\theta, \zeta, \rho) = \sum_{k=1}^{3} \left[\dot{\mathbf{x}}^{(k)} + (\dot{x}_r + \rho\dot{n}_x)\mathbf{e}_x^{(k)} + (\dot{y}_r + \rho\dot{n}_y)\mathbf{e}_y^{(k)} + (\dot{z}_r + \rho\dot{\gamma})\mathbf{e}_z^{(k)} + \right.$$
$$\left. + (y_r + \rho n_y)\dot{\mathbf{e}}_y^{(k)} + (z_r + \rho\gamma)\dot{\mathbf{e}}_z^{(k)} \right) N^{(k)}(\zeta) \right] \qquad (2.155)$$

Equation (2.155) can be rewritten in terms of incremental displacements:

$$\Delta\mathbf{u}(\theta, \zeta, \rho) = \sum_{k=1}^{3} [(\Delta\mathbf{u}^{(k)} + (\Delta x_r + \rho\Delta n_x)\mathbf{e}_x^{(k)} + (\Delta y_r + \rho\Delta n_y)\mathbf{e}_y^{(k)} +$$
$$+ (\Delta z_r + \rho\Delta\gamma)\mathbf{e}_z^{(k)} + (y_r + \rho n_y)\Delta\mathbf{e}_y^{(k)}) N^{(k)}(\zeta)] \qquad (2.156)$$

33

Considering vector $\Delta\hat{\mathbf{U}}$, which contains the increments of nodal degrees of freedom of the ''tube-element'' as follows:

$$\Delta\hat{\mathbf{U}} = \begin{bmatrix} \vdots \\ \Delta u_2^{(k)} \\ \Delta u_3^{(k)} \\ \Delta\theta_1^{(k)} \\ \Delta a_0^{(k)} \\ \Delta a_1^{(k)} \\ \vdots \\ \Delta b_2^{(k)} \\ \Delta b_3^{(k)} \\ \vdots \\ \Delta\gamma_0^{(k)} \\ \Delta\gamma_1^{(k)} \\ \vdots \\ \Delta c_2^{(k)} \\ \Delta c_3^{(k)} \\ \vdots \end{bmatrix} \qquad (2.157)$$

the incremental displacements in equation (2.156) can be written in the form of equation (2.128), so that matrix $[\mathbf{N}]$ is defined.

The covariant base vectors, tangential to the coordinate lines (θ, ζ, ρ), can by calculated by differentiation with respect to the local coordinates of the position vector as follows:

$$\mathbf{g}_1 = \mathbf{g}_\theta = \frac{\partial\mathbf{x}}{\partial\theta} = \sum_{k=1}^3\left[\left(\frac{d\mathbf{r}^{(k)}(\theta)}{d\theta} + \rho\frac{d\mathbf{n}^{(k)}(\theta)}{d\theta} + \rho\frac{d\gamma(\theta)}{d\theta}\mathbf{e}_z^{(k)}\right)N^{(k)}(\zeta)\right] \qquad (2.158)$$

$$\mathbf{g}_2 = \mathbf{g}_\zeta = \frac{\partial\mathbf{x}}{\partial\zeta} = \sum_{k=1}^3\left[\left(\mathbf{x}^{(k)} + \mathbf{r}^{(k)}(\theta) + \rho\mathbf{n}^{(k)}(\theta) + \rho\gamma(\theta)\mathbf{e}_z^{(k)}\right)\frac{N^{(k)}(\zeta)}{d\zeta}\right] \qquad (2.159)$$

$$\mathbf{g}_3 = \mathbf{g}_\rho = \frac{\partial\mathbf{x}}{\partial\rho} = \sum_{k=1}^3\left[\left(\mathbf{n}^{(k)}(\theta) + \gamma(\theta)\mathbf{e}_z^{(k)}\right)N^{(k)}(\zeta)\right] \qquad (2.160)$$

Considering the covariant base vectors in the reference configuration $\mathbf{G}_1, \mathbf{G}_2, \mathbf{G}_3$, appropriate differentiation of (2.156) and the definition of vector $\Delta\hat{\mathbf{U}}$, matrix $[\mathbf{B}]$ is formed to be used in equation (2.131).

In this study, the numerical results are obtained through the implementation of the described nonlinear ''tube-element'', exploring issues of stability, post-buckling response and imperfection sensitivity, considering a number of parameters that affect the structural response of thin-walled cylinders.

34

2.7 Tracing of Unstable Equilibrium Paths

The nonlinear governing equations are solved through an incremental Newton-Raphson numerical procedure, enhanced to enable the tracing of unstable equilibrium paths. For the purposes of the present study an ''arc-length'' path follower technique is implemented. Path follower techniques in structural mechanics were originally introduced by Riks [28], [29], and Wempner [30], and modified by Crisfield [31] in a more efficient form. These methods enable Newton-Raphson step-by-step solution algorithms to overcome limit points (maximum loads/moments), which may be characterized by ''snap-through'' or ''snap-back'' behavior in the load-deflection equilibrium path (Fig. 4).

To illustrate the above ''continuation techniques'', the set of discretized equilibrium equations can be written as:

$$\mathbf{g}(\mathbf{u}, \lambda) = \mathbf{q}_i(\mathbf{u}) - \lambda \mathbf{q}_{ef} = 0 \qquad (2.161)$$

where vector $\mathbf{q}_i(\mathbf{u})$ expresses the internal forces, which are functions of the displacements $\mathbf{u}$, vector $\mathbf{q}_{ef}$ is a fixed external loading vector, which is kept fixed, and the scalar λ is a ''load-level'' parameter that multiplies $\mathbf{q}_{ef}$.

(a)   **(b)**
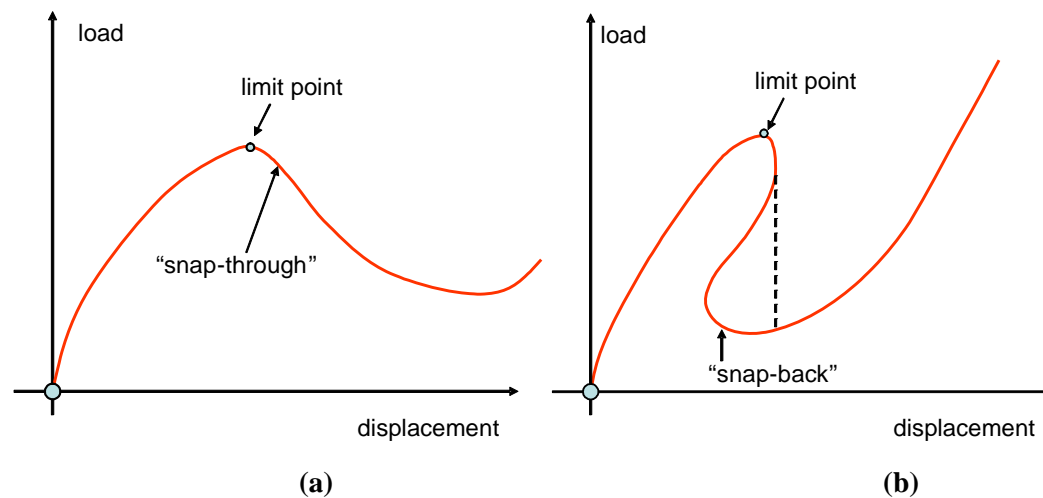
Fig. 4 ''Snap-through'' and ''snap-back'' behavior in load/displacement curves.

The major limitation of employing a load-control marching scheme that specifies the value of λ is that at or beyond a limit point, there is no intersection between the equilibrium path of (2.161) and the line λ=constant. Furthermore, the adoption of a displacement-control marching scheme would allow tracing of a path in the form of Fig. 4a, but may fail to follow the path shown in Fig. 4b. Various forms of arc-length methods have stemmed from [28], [29], [30], aiming at the determination of the equilibrium path through the intersection of (2.161) with a ''hyper-plane'' in the space of incremental load and displacements. In this methodology, the

35

load increment $\Delta\lambda$ is considered as an extra unknown. Towards this purpose, an additional equation is introduced, prescribing the "radius" of the "hyper-plane" to be used, for the intersection with the equilibrium path. More specifically, if Δl is a prescribed constant which expresses the fixed "radius" of the desired intersection, then the following constrain equation is employed

$$\Delta l = \sqrt{(\Delta\mathbf{u} + \delta\mathbf{u})^{\mathrm{T}}(\Delta\mathbf{u} + \delta\mathbf{u}) + (\Delta\lambda + \delta\lambda)^2 \psi \mathbf{q}_{\mathrm{ef}}^{\mathrm{T}} \mathbf{q}_{\mathrm{ef}}} \qquad (2.162)$$

where $\delta\mathbf{u}$ is the correction to the incremental displacements $\Delta\mathbf{u}$, $\delta\lambda$ is the correction of the load increment $\Delta\lambda$ and ψ is a scaling parameter that varies between 0 and 1.

In Fig. 5, starting form point (1) on the path, the method provides point (2) as the intersection of the path with an "arc" of radius Δl about point (1) (Fig. 5). It is noted that vector $\Delta\mathbf{u}$ and the scalar quantity $\Delta\lambda$ are incremental (not iterative) quantities from the last converged equilibrium state [point(1)].

The main essence of the arc-length methods is that the load parameter λ becomes now an extra variable. Hence, together with the n displacement variables $\Delta\mathbf{u}$, there is an additional unknown $\Delta\lambda$, so that a total of $n+1$ variables exist, and $n+1$ equations, namely n equilibrium equations of (2.161) and one constraint equation from (2.162) are to be solved. An efficient method to solve those equations within a Newton-Raphson methodology has been proposed by Crisfield [31].

The present nonlinear study is based on the implementation of the above arc-length method in the Newton-Raphson step-by-step numerical solution. When bending is examined, the marching scheme is controlled by the non-dimensional arc-length parameter Δl defined as:

$$\Delta l = \sqrt{\frac{\Delta\mathbf{u}^{\mathrm{T}}\Delta\mathbf{u}}{\Delta\mathbf{u}_{\mathrm{r}}^{\mathrm{T}}\Delta\mathbf{u}_{\mathrm{r}}} + \psi\left(\frac{\Delta M}{\Delta M_r}\right)^2} \qquad (2.163)$$

which comes from (2.162) and is a combination of bending moment increment ΔM with the increment of some "selected" degrees of freedom $\Delta\mathbf{u}$, where ΔM_r is a normalization moment, and $\Delta\mathbf{u}_{\mathrm{r}}$ are normalization displacements, both obtained from a preliminary load-control small step. In proportion, when axial compression is examined expression (2.163) is reformed as:

$$\Delta l = \sqrt{\frac{\Delta\mathbf{u}^{\mathrm{T}}\Delta\mathbf{u}}{\Delta\mathbf{u}_{\mathrm{r}}^{\mathrm{T}}\Delta\mathbf{u}_{\mathrm{r}}} + \psi\left(\frac{\Delta P}{\Delta P_0}\right)^2} \qquad (2.164)$$

where ΔP is the load increment and ΔP_0 is a normalization load parameter. It has been recognized that the success of the method depends in the appropriate selection of degrees of freedom in vector $\Delta\mathbf{u}$. In general, convergence near and beyond the limit point is facilitated when monotonically increasing degrees of freedom are included in vector $\Delta\mathbf{u}$.

In this work, for cases where buckling instability is due to bending loads, the incremental values the two translational degrees of freedom at each node (k) of the ''tube-element'' $\Delta u_2^{(k)}$, $\Delta u_3^{(k)}$ are employed to form the vectors of incremental displacements $\Delta\mathbf{u}$ and reference displacements $\Delta\mathbf{u}_r$ in (2.163) and the value of ψ is taken equal to 1 (spherical arc-length).

When axial compression of cylinders is examined, all the degrees of freedom are considered (translational, rotational, ovalization and warping) in forming the incremental displacement vector $\Delta\mathbf{u}$ and the reference displacement vector $\Delta\mathbf{u}_r$, to trace post-buckling equilibrium paths. In these cases the implementation of cylindrical arc-length procedure ($\psi=0$) has been found to facilitate convergence near the bifurcation point.

Finally, to enable the incremental analysis to follow the post-buckling path at the bifurcation point, a very small initial imperfection of the tube is imposed, in both cases (bending and axial compression). The initial imperfection is considered in the shape of the first instability mode, obtained by an appropriate eigenvalue analysis at the bifurcation stage. The imperfection is a small fraction (e.g. 10^{-6}) of the shell thickness, but it is yet sufficient to improve convergence near the buckling point and ''trigger'' bifurcation.

$$\Delta l = \sqrt{(\Delta\mathbf{u} + \delta\mathbf{u})^{\mathrm{T}}(\Delta\mathbf{u} + \delta\mathbf{u}) + (\Delta\lambda + \delta\lambda)^2 \psi \mathbf{q}_{ef}^{\mathrm{T}} \mathbf{q}_{ef}}$$
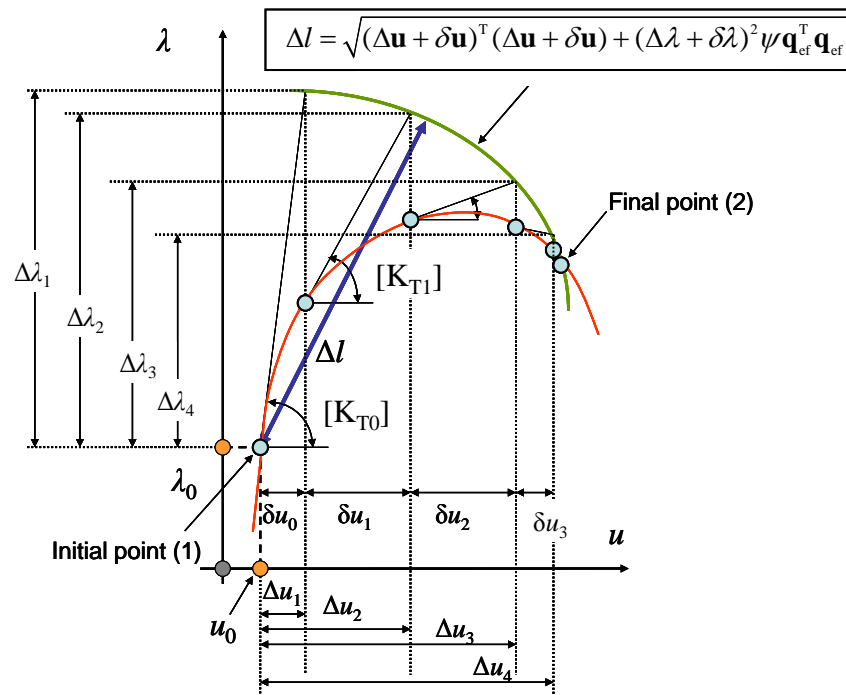
Fig. 5 Schematic representation of arc-length procedure

37

2.8 Bifurcation in the Inelastic Range

Detection of bifurcation in the inelastic regime is described in this section based on the so-called ''comparison solid'' concept, introduced in the work of Hill [32].

For the case of hypoelastic constitutive modeling the general form of an elastic-plastic material model with smooth yield surface is considered, as follows:

$$\dot{\tau}^{ij} = R^{ijkl} d_{kl} \tag{2.165}$$

which, using (2.18), can be written as:

$$\dot{\tau}^{ij} = R^{ijkl} \dot{E}_{kl} \tag{2.166}$$

When the material response is elastic (including elastic unloading) components R^{ijkl} are equal to:

$$R^{ijkl} = D_e^{ijkl} - \mathcal{L}^{ijkl} \qquad \text{for} \quad m^{ij} \dot{E}_{ij} \leq 0 \tag{2.167}$$

whereas for plastic loading

$$R^{ijkl} = D_e^{ijkl} - \mathcal{L}^{ijkl} - \frac{1}{g} m^{ij} m^{kl} \qquad \text{for} \quad m^{ij} \dot{E}_{ij} \geq 0 \tag{2.168}$$

where g depends on the deformation history and the current state of stress and tensor **m** is normal to the yield surface.

Bifurcation is associated with loss of uniqueness of incremental solution. It is supposed that at the current state of stress and deformation, a load increment is imposed. Loss of uniqueness means that at least two incremental solutions exist, namely $\dot{\mathbf{u}}_a$ and $\dot{\mathbf{u}}_b$. The corresponding increments of Green-Lagrange tensor are $\dot{\mathbf{E}}_a$ and $\dot{\mathbf{E}}_b$, and the corresponding increments of Kirchhoff stress are $\dot{\boldsymbol{\tau}}_a$ and $\dot{\boldsymbol{\tau}}_b$. Form the equilibrium equations (2.12) one can readily show that loss of uniqueness is equivalent to the following condition

$$H = \int_{V_0} (\hat{\tau}^{ij} \hat{E}_{ij} + \tau^{ij} \hat{u}_i^k \hat{u}_{k/j}) dV_0 = 0 \tag{2.169}$$

where functional H depends on the current stress state τ^{ij} and

$$\hat{\mathbf{u}} = \dot{\mathbf{u}}_b - \dot{\mathbf{u}}_a \tag{2.170}$$

$$\hat{\mathbf{E}} = \dot{\mathbf{E}}_b - \dot{\mathbf{E}}_a \tag{2.171}$$

$$\hat{\boldsymbol{\tau}} = \dot{\boldsymbol{\tau}}_b - \dot{\boldsymbol{\tau}}_a \tag{2.172}$$

The question on whether plastic loading or elastic unloading occurs for stress points on the yield surface causes a difficulty in evaluating functional H in equation (2.169). To overcome this difficulty, Hill [32] introduced the so-called ''comparison solid'', a fictitious solid with moduli L_C^{ijkl} equal to the elastic moduli (2.167) when the current stress is within the yield surface and equal to the elastic-plastic moduli (2.168) when the current state is on the yield surface.

38

It can be shown [33], that in any case,

$$L_C^{ijkl} \hat{E}_{ij} \hat{E}_{kl} \le \hat{\tau}^{ij} \hat{E}_{ij} \tag{2.173}$$

Therefore, introducing the quadratic functional

$$F = \int_{V_0} (L_C^{ijkl} \hat{E}_{ij} \hat{E}_{kl} + \tau^{ij} \hat{u}_{/j}^k \hat{u}_{k/j}) dV_0 \tag{2.174}$$

and using (2.169) and (2.173) one may readily conclude that in any case

$$F \le H \tag{2.175}$$

Therefore, the condition

$$F > 0 \tag{2.176}$$

is a sufficient condition for uniqueness of solution. Furthermore, the non-positive definiteness of F (i.e. $F = 0$) constitutes an approximate condition for loss of uniqueness and provides upper-bound estimates of the buckling load.

In the present work, an implementation of the above concept is incorporated in the finite element technique, considering the following quadratic functional:

$$F = \int_V (L_C^{ijkl} \Delta E_{ij} \Delta E_{kl} + \tau^{ij} \Delta U_{/j}^k \Delta U_{k/j}) dV \tag{2.177}$$

where

$$\tau^{ij} \Delta U_{/j}^k \Delta U_{k/j} = \tau^{ij} G^{mk} \Delta U_{m/j} \Delta U_{k/j} \tag{2.178}$$

$$\Delta E_{pq} = \frac{1}{2} \Big[(\mathbf{G}^k \cdot \mathbf{g}_p) \Delta U_{k/q} + (\mathbf{G}^k \cdot \mathbf{g}_q) \Delta U_{k/p} \Big] \tag{2.179}$$

Subsequently, following the discretization described in detail in section 2.5, the quadratic functional F can be written in the following discretized form

$$F = \frac{1}{2} \Delta \hat{\mathbf{U}}^T [K_C] \Delta \hat{\mathbf{U}} \tag{2.180}$$

where

$$[K_C] = \int_{V_0} [\mathbf{B}]^T [\mathcal{D}_C] [\mathbf{B}] dV_0 \tag{2.181}$$

$$[\mathcal{D}_C] = [\mathbf{W}]^T [\mathbf{L}_C] [\mathbf{W}] + [\mathbf{C}] \tag{2.182}$$

and $[\mathbf{L}_C]$ is the constitutive matrix with moduli L_C^{ijkl} as defined above. Therefore, the positive definiteness of functional F is equivalent to the positive definiteness of matrix $[K_C]$.

Using J_2 flow theory of plasticity, matrix $[K_C]$ can be evaluated using the corresponding elastic and inelastic moduli. More specifically, if the stress state is within the yield surface then R^{ijkl} are equal to the elastic moduli

$$R^{ijkl} = D_e^{ijkl} - \mathcal{L}^{ijkl} \tag{2.183}$$

where

39

$$D_e^{ijkl} = \frac{E}{2(1+\nu)}\left(g^{jl}g^{ik} + g^{il}g^{jk} + \frac{2}{1-2\nu}g^{ij}g^{kl} \right) \qquad (2.184)$$

and

$$\mathcal{L}^{ijkl} = \frac{1}{2}\left[g^{ik}\tau^{jl} + g^{jk}\tau^{il} + g^{il}\tau^{jk} + g^{jl}\tau^{ik} \right] \qquad (2.185)$$

On the other hand, if the stress state is on the yield surface R^{ijkl} are equal to

$$R^{ijkl} = \left(D_e^{ijkl} - \mathcal{L}^{ijkl} \right) - \frac{1}{q}s^{ij}s^{kl} \qquad (2.186)$$

where

$$q = \frac{Y^2}{3G}\left(1 + \frac{H}{3G} \right) \qquad (2.187)$$

and Y is the effective von Mises stress and $H = \dfrac{dY_{\max}}{dd_p}$, d_p is defined by (2.188).

It has been recognized that in order to obtain accurate predictions of bifurcation in the inelastic range, a material model more elaborate than the J$_2$ flow plasticity model. This observation was denoted in early works on axially compressed cylinders [34], [35] where analytical works based on J$_2$ flow plasticity provided buckling load predictions, which were quite high compared with available experimental data. On the other hand, it has been demonstrated that bifurcation predictions that employ the moduli of J$_2$ deformation theory of plasticity are much closer to experimental data. A recent series of experiments on axially-loaded very-thick cylindrical shells that buckle well into the plastic range, together with analytical predictions using J$_2$ flow and J$_2$ deformation theory moduli, have been reported by Bardi and Kyriakides [36]. The reason for the good agreement of deformation theory predictions with test data, as opposed to the poor predictions of flow theory, is that plastic strain increments based on deformation theory are not normal to the von Mises yield surface and this makes the material behaviour significantly ''softer'' when abrupt changes in the direction of the stress path occurs at the buckling stage.

To evaluate matrix $[K_C]$ in the framework of a J$_2$ deformation theory of plasticity, the corresponding elastic and inelastic moduli should be considered. More specifically, the elastic moduli are those indicated by equations (2.183), and the inelastic moduli are

$$R^{ijkl} = \left(D_s^{ijkl} - \mathcal{L}^{ijkl} \right) - \frac{1}{q_s}s^{ij}s^{kl} \qquad (2.189)$$

where

$$D_s^{ijkl} = \frac{E_s}{2(1+\nu_s)}\left(g^{jl}g^{ik} + g^{il}g^{jk} + \frac{2}{1-2\nu_s}g^{ij}g^{kl} \right) \qquad (2.190)$$

and

$$q_s = (1+\nu_s)\frac{h_s}{E_s} + \frac{2}{3}Y^2$$

$$\frac{\nu_s}{E_s} = \frac{\nu}{E} + \frac{1}{2}\left(\frac{1}{E_s} - \frac{1}{E}\right) \tag{2.191}$$

$$\frac{1}{h_s} = \left(\frac{3}{2Y}\right)^2\left(\frac{1}{E_s} - \frac{1}{E}\right)$$

In the above expressions E_t, E_s are the tangent modulus and the secant modulus, respectively, and Y is the effective von Mises stress.

In the framework of the present step-by-step Newton-Raphson solution procedure, at the end of each loading step (i.e. after convergence is achieved), matrix $[K_C]$ is formed using J_2 deformation theory moduli and its positive definiteness is examined through its eigenvalues. Bifurcation occurs when the smallest eigenvalue of $[K_C]$ becomes equal to zero. The eigenmode that corresponds to the first zero eigenvalue is the buckling mode. This instability mode is imposed subsequently as an initial imperfection for the analysis of the imperfect cylinder, as described in Chapter 7.

Chapter 3

THIN-WALLED ELASTIC CYLINDERS UNDER AXIAL COMPRESSION – EFFECTS OF AXISYMMETRIC INITIAL IMPERFECTIONS

In the earlier Chapter the numerical technique employed for the purposes of this study were briefly discussed with special emphasis on the ''tube-element'' and constitutive modeling issues. In the following, this technique is employed for the buckling strength of elastic circular cylinders under axial compression, in the presence of axisymmetric initial imperfections. This problem can be considered as a benchmark for the capabilities of the ''tube-element'', offering a verification of its accuracy and computational efficiency, as the obtained numerical results are in very good agreement with semi-analytical results reported elsewhere.

Equation Chapter 3 Section 3

3.1 Introduction

The circular cylindrical shell under axial compression constitutes one of the most classical and challenging problems in structural mechanics. This problem has caused significant controversy in the 40's and 50's, as great discrepancies between theoretically predicted and experimentally observed buckling loads were reported. It is now generally accepted that the poor correlation between theory and tests is due, to a large extent, to the significant imperfection sensitivity of the cylinder buckling load. Imperfection sensitivity expresses a measure of the effect of small deviations from the assumed shape on the buckling load and for elastic structures it is directly related to the initial postbuckling behavior.

A major contribution towards understanding of the role of initial imperfections on buckling strength of circular cylinders was given by von Karman and Tsien [37]. In this landmark study, it was shown that the postbuckling structural capacity drops sharply, immediately after the bifurcation point. Using simple models to simulate the shell behavior, it was suggested that for these structures in the presence of initial imperfections buckling would occur at remarkably lower load values compared to the critical loads of the corresponding perfect structures.

Another rigorous confirmation of the dominant role of initial imperfections on the buckling load, was given by Koiter [3]. The initial postbuckling behavior was examined in an asymptotic sense and a perturbation technique, which relies on the principle of stationary potential energy,

42

was adopted. Similar results were derived by Budiansky and Hutchinson [10] and Budiansky [38], writing the field equations in variational form through the principle of virtual work. Subsequent studies that correlated the reductions in the buckling strength of shells (cylindrical and spherical) with assumed initial imperfections were reported by Cohen [39], Fitch [40] and Fabian [41]. It is mentioned that an overview of imperfection sensitivity in isotropic shells was given in a review paper by Hutchinson and Koiter [42].

Furthermore, special mention should be made in another study of Koiter [4], where upper bounds to the loads at which non-axisymmetric bifurcation from axisymmetric state occurs, were determermined. Axisymmetric imperfection amplitudes of just one shell thickness were found to reduce the bifurcation load to a fifth of the classical load. In contradiction to the general theory [3], this particular study [4] was not based on the restrictive assumption that the amplitude of the initial imperfection is small.

In the present Chapter, infinitely long cylindrical shells with axisymmetric initial imperfections are analyzed. Non-axisymmetric modes and bifurcations along the equilibrium path are identified by the implementation of the ''tube-element''. The body of this Chapter includes a summary of the numerical results and their interpretation, whereas a direct comparison of the obtained results with the corresponding given by Koiter [4] is offered for the case of isotropic cylinders. Finally, results for transversely isotropic cylinders are also reported, illustrating the effects of the anisotropy level on the buckling strength of imperfect cylinders.

3.2 Axisymmetric Buckling of Perfect Elastic Cylinders

The circular cylindrical shell under uniform compression has served as a reference in many studies of shell buckling. In this section a brief presentation of the analytical expressions that describe the axisymmetric bucking of cylinders is given. When a cylindrical shell is uniformly compressed buckling (axisymmetric or asymmetric) occurs at a critical stress, which is determined by the following expression [11], [43]:

$$\sigma_{cr} = \frac{E}{\sqrt{3(1-\nu^2)}}\frac{t}{r} \tag{3.1}$$

where E is the Young's modulus, ν is the Poisson's ratio, t is the shell thickness and r is the cylinder radius. It is important to note that this buckling load corresponds to an infinite number of instability modes (axisymmetric or not). Specializing in the case of axisymmetric buckling, where no dependence of deformation with respect to hoop coordinate exists, the length L_{hw} of the half-waves into which the shell buckles is equal to:

$$L_{hw} = \pi\left(\sqrt[4]{\frac{r^2 t^2}{12(1-\nu^2)}}\right) \tag{3.2}$$

43

It is noted that for metals Poisson's ratio ν is equal to 0.3 and therefore $L_{hw} = 1.73\sqrt{rt}$

For orthotropic cylindrical shells the critical load that corresponds to axisymmetric buckling can also be determined for a perfect cylinder [11]:

$$\sigma_{cr} = \frac{1}{\sqrt{3}} \frac{t}{r} \sqrt{C_{11}C_{22} - C_{21}^2} \tag{3.3}$$

whereas, the corresponding buckling wavelength is determined by:

$$L_{hw} = \pi \sqrt[4]{\frac{C_{11}C_{44}r^2}{C_{11}C_{22} - C_{21}^2}} \tag{3.4}$$

with the parameters C_{ij} given by:

$$C_{11} = \frac{E_{11}}{1 - \nu_{12}\nu_{21}} \tag{3.5}$$

$$C_{22} = \frac{E_{22}}{1 - \nu_{12}\nu_{21}} \tag{3.6}$$

$$C_{21} = \frac{\nu_{21}E_{22}}{1 - \nu_{12}\nu_{21}} \tag{3.7}$$

$$C_{44} = C_{11}\frac{t^3}{12} \tag{3.8}$$

3.3 Non-Axisymmetric Bifurcation of Imperfect Cylinders - Semi-Analytical Solution

In this section the study of Koiter [4] is rewritten in a systematic manner, for the sake of completeness. Buckling behavior can be readily studied through the quasi-shallow equations suggested by Donnell [44], [45], which give accurate results for cylindrical shells, whose deformation components in the deformed configuration are rapidly varying functions of the circumferential coordinate.

The nonlinear set of equations for quasi-shallow shells as originally introduced by Donnell [44], [45], is given above:

$$
\begin{aligned}
& N_{x,x} + N_{xs,s} = 0 \\
& N_{xs,x} + N_{s,s} = 0 \\
& D\nabla^4 w + \frac{1}{r}N_s - (N_x w_{,xx} + 2N_{xs}w_{,xs} + N_s w_{,ss}) = 0
\end{aligned} \tag{3.9}
$$

where

$$\nabla^4 w \equiv w_{,xxxx} + w_{,xxss} + w_{,ssss} \tag{3.10}$$

$$D = \frac{Et^3}{12(1 - \nu^2)} \tag{3.11}$$

and s is a circumferential coordinate ($s = r\theta$).

44

Considering a small axisymmetric initial imperfection denoted by $w^*(x)$ and assuming that the unloaded shell, which includes w^*, is stress-free, the following strain-displacements relations for the imperfect shell are obtained:

$$\varepsilon_x = u_{,x} + \frac{1}{2}\left[(w+w^*)_{,x}\right]^2 - \frac{1}{2}\left(w^*_{,x}\right)^2 = u_{,x} + \frac{1}{2}w^2_{,x} + w_{,x}w^*_{,x}$$

$$\varepsilon_s = v_{,s} + \frac{w}{r} + \frac{1}{2}w^2_{,s} \tag{3.12}$$

$$\gamma_{xs} = u_{,s} + v_{,x} + w_{,x}w_{,s} + w^*_{,x}w_{,s}$$

and the third equation in (3.9) can be replaced by:

$$D\nabla^4 w + \frac{1}{r}N_s - [N_x(w+w^*)_{,xx} + 2N_{xs}w_{,xs} + N_s w_{,ss}] = 0 \tag{3.13}$$

which is in accordance with the expressed equilibrium for a slightly crooked column.

Linearization of the equilibrium equations is performed by introducing the following displacements u, v, w

$$u \rightarrow u_0 + u_1$$

$$v \rightarrow v_0 + v_1 \tag{3.14}$$

$$w \rightarrow w_0 + w_1$$

where $\{u_0, v_0, w_0\}$ correspond to equilibrium configuration (prebuckling) and $\{u_1, v_1, w_1\}$ is an infinitesimally small increment of displacements in addition to the prebuckling displacements. For axisymmetric configurations on the primary path, $u_0 = u_0(x), v_0 = 0, w_0 = w_0(x)$. Introduction of these terms into the equilibrium equations and simplification by neglecting higher order terms, results in the following linearized expression of equilibrium:

$$N_{x1,x} + N_{xs1,s} = 0$$

$$N_{xs1,x} + N_{s1,s} = 0 \tag{3.15}$$

$$D\nabla^4 w_1 + \frac{1}{r}N_{s1} - \left(N_{x0}w_{1,xx} + N_{s0}w_{1,ss} + w''_0 N_{x1} + w^{*''} N_{x1}\right) = 0$$

where:

$$N_{x1} = C\left(e_{xx1} + v e_{ss1}\right)$$

$$N_{s1} = C\left(e_{ss1} + v e_{xx1}\right) \tag{3.16}$$

$$N_{xs1} = C\left(\frac{1-v}{2}\right)e_{xs1}$$

and

$$e_{xx1} = u_{1,x} + w'_0 w_{1,x} + w^{*'} w_{1,x}$$

$$e_{ss1} = v_{1,s} + \frac{1}{r}w_1 \tag{3.17}$$

$$e_{xs1} = u_{1,x} + u_{1,s} + w'_0 w_{1,s} + w^{*'} w_{1,s}$$

45

($'$) prime denotes differentiation with respect to x.

Expressions (3.15)-(3.17) can be reduced to three linear homogeneous equations with variable coefficients N_{x0}, N_{s0}, N_{xs0} and w^*. The three equations can now be further reduced to two by introducing a stress function $f(x,s)$ for which:

$$
\begin{aligned}
N_{x1} &= f_{,ss} \\
N_{s1} &= f_{,xx} \\
N_{xs1} &= -f_{,xs}
\end{aligned}
\tag{3.18}
$$

For geometric compatibility, from (3.17) the following is imposed

$$
e_{xx1,ss} + e_{ss1,xx} - e_{xs1,xs} = \frac{1}{r} w_{1,xx} - w_0'' w_{1,ss} - w^{*''} w_{1,ss}
\tag{3.19}
$$

and using (3.16) an expression in terms of f and w_1 is obtained:

$$
\nabla^4 f - Et \left[\frac{1}{r} w_{1,xx} - w_0'' w_{1,ss} - w^{*''} w_{1,ss} \right] = 0
\tag{3.20}
$$

Finally, the third equation in (3.15) becomes

$$
D\nabla^4 w_1 + \frac{1}{r} f_{,xx} - \left[N_{x0} w_{1,xx} + N_{s0} w_{1,ss} + w_0'' f_{,ss} + w^{*''} f_{,ss} \right] = 0
\tag{3.21}
$$

The last two expressions form two equations in the unknown functions f and w_1, and constitute an eigenvalue problem, the solution of which determines the critical load. Due to axisymmetric initial configuration, $u_0 = u_0(x)$, $v_0 = 0$, $w_0 = w_0(x)$ and $N_{xs0} = 0$, there is no dependence of the hoop variable s ($\partial(.)/\partial s = 0$). Therefore, the non-linear equations (3.9) and (3.21) are now written:

$$
N_{x0}' = 0
\tag{3.22}
$$

$$
D w_0^{(4)} + \frac{1}{r} N_{s0} - N_{x0} \left(w_0'' + w^{*''} \right) = 0
\tag{3.23}
$$

and represent a system of non-linear equations in terms of u_0, w_0. From (3.22), N_{x0} is independent of x and considering end conditions, one obtains:

$$
N_{x0} = \frac{P}{2\pi r} = \sigma_L \cdot t
\tag{3.24}
$$

Furthermore, the constitutive relations are given by:

$$
\begin{aligned}
N_{x0} &= C \left(\varepsilon_{x0} + v \varepsilon_{s0} \right) \\
N_{s0} &= C \left(\varepsilon_{s0} + v \varepsilon_{x0} \right)
\end{aligned}
\tag{3.25}
$$

and the non-linear kinematics (3.12) are:

$$
\begin{aligned}
\varepsilon_{x0} &= u_{0,x} + \frac{1}{2} w_{0,x}^2 \\
\varepsilon_{s0} &= \frac{w_0}{r}
\end{aligned}
\tag{3.26}
$$

46

Combining (3.25) and (3.26) one obtains:

$$\varepsilon_{x0} = \frac{N_{x0}}{C} - v\varepsilon_{s0}$$

$$N_{s0} = C\left[\varepsilon_{s0} + v\left(\frac{N_{x0}}{C} - v\varepsilon_{s0}\right)\right] = \frac{Etw_0}{r} - v\sigma_L t \tag{3.27}$$

and substituting into (3.22) leads to the expression:

$$Dw_0^{(4)} + \left(\sigma_L t\right)w_0'' + \left(\frac{Et}{r^2}\right)w_0 = \sigma_L t\left(\frac{v}{r} - w^{*''}\right) \tag{3.28}$$

Expression (3.28) determines the nonlinear prebuckling equilibrium configuration.

In the following, we assume that axisymmetric initial imperfection $w^*(x)$ has the form:

$$w^*(x) = -\xi t \cos\frac{2mx}{r} \tag{3.29}$$

where m is a wavelength parameter, ξ denotes the amplitude of the deviation of the middle surface as a fraction of the shell thickness, r is the cylinder radius. The minus sign in (3.29) signifies that the imperfect shell bulges inward at $x = 0$. Introduction of (3.29) into (3.28) gives:

$$Dw_0^{(4)} + \left(\sigma_L t\right)w_0'' + \frac{Et}{r^2}w_0 = \sigma_L \frac{t}{r}\left(v - 4m^2\xi\frac{t}{r}\cos\frac{2\pi x}{\alpha}\right) \tag{3.30}$$

A solution of the following form is assumed

$$w_0(x) = vr\frac{\sigma_L}{E} + B\cos\frac{2mx}{r} \tag{3.31}$$

where B is a constant expressed by:

$$B = -\xi\frac{4\lambda g^2}{4g^4 + 1 - 4\lambda g^2} \tag{3.32}$$

and λ and g are non-dimensional load and wavelength parameters, respectively, defined by the expressions

$$\lambda = \frac{\sigma_L}{\sigma_{L,cr}} \tag{3.33}$$

$$g^2 = \frac{m^2}{\sqrt{3(1-v^2)}}\left(\frac{t}{r}\right) \tag{3.34}$$

$$\sigma_{L,cr} = \frac{E}{\sqrt{3(1-v^2)}}\left(\frac{t}{r}\right) \tag{3.35}$$

Quantity $\sigma_{L,cr}$ is the classical value of the critical stress for the corresponding perfect cylinder.

Therefore,

$$N_{x0} = -\sigma_L t$$

$$N_{s0} = E\left(\frac{t}{r}\right) B \cos\frac{2mx}{r}$$

$$w_0(x) = v r \frac{\sigma_L}{E} + B \cos\frac{2mx}{r} \tag{3.36}$$

$$w^*(x) = -\xi t \cos\frac{2mx}{r}$$

and introducing constant k and function Φ

$$k = \frac{4\rho^4 + 1}{4\rho^4 + 1 - 4\lambda\rho^2}$$

$$k - 1 = \frac{4\lambda\rho^2}{4\rho^4 + 1 - 4\lambda\rho^2} \tag{3.37}$$

$$\Phi = \frac{\sqrt{3(1-v^2)}}{Et^3} f \tag{3.38}$$

equations (3.20) and (3.21) may be written

$$\nabla^4\Phi + \frac{C}{rt^2}\left[-w_{1,xx} + 4c\xi kg^2 \cos\frac{2mx}{r} w_{1,ss}\right] = 0 \tag{3.39}$$

$$\nabla^4 w_1 + \frac{4c}{r}\left[\Phi_{,xx} - 4c\xi kg^2\left(\cos\frac{2mx}{r}\right)\Phi_{,ss} + \frac{\lambda}{t}w_{1,xx} + \frac{c\xi}{t}(k-1)\cos\frac{2mx}{r}w_{1,ss}\right] = 0 \tag{3.40}$$

These equations constitute the linearized stability problem. Non-trivial solutions of the homogeneous equations exist only for discrete values of the load parameter λ. The resulting minimum eigenvalue represents an upper bound for the actual critical load. These variable-coefficient equations can be solved numerically. It is noted that only even-ordered derivatives appear in (3.39) and (3.40), and that the coefficients are functions of the axial coordinate x alone. Therefore, as indicated by Koiter [3] it is reasonable to assume the existence of solutions which are functions of s through a factor $\cos(ns)$, where n is an integer. Koiter followed a numerical procedure and employed a Galerkin method, introducing a solution of the form:

$$w_1(x,s) = W(x)\cos(ns) \tag{3.41}$$

The displacement $W(x)$ employed by Koiter [3] was in the form:

$$W(x) = \sum_{j=1} C_j \cos[(2j-1)mx/r] \tag{3.42}$$

so the existence of an asymmetric buckling pattern with nodal lines where the circumferential tensile stresses attain their maximum is possible. The axial period of such a mode is thus twice the period of the axisymmetric equilibrium configuration.

Furthermore, the imperfection wavelength parameter g was taken equal to:

$$g = \frac{1}{\sqrt{2}} \tag{3.43}$$

48

so that the axisymmetric deviation (3.29) coincides with the axisymmetric buckling mode of a perfect cylindrical shell. Indeed, for the axisymmetric buckling of axially compressed cylinders the buckling half-wavelength [43] is

$$L_0 = \left(\frac{\pi^4}{12\left(1 - v^2\right)} \right)^{1/4} \sqrt{rt} \tag{3.44}$$

and from (3.29) one results in

$$\frac{\pi}{L_0} = \frac{m}{\left(r/2\right)} \tag{3.45}$$

whereas the definition of constant g in (3.33) leads to

$$m^2 = \sqrt{3\left(1 - v^2\right)} \left(\frac{r}{t} \right) g^2 \tag{3.46}$$

Combing (3.44)-(3.46) one obtains that g is equal to $1/\sqrt{2}$.

Koiter [4] presented results of the critical value of the applied load for an imperfect cylinder over the classical critical load of the corresponding perfect cylinder for various values of the imperfection amplitude ξ. For initially imperfect cylindrical shells, the critical loads were found to be markedly reduced, for example for imperfection amplitude that is only half of the cylinder wall thickness, the critical load P_{cr} is reduced to less than 30% of the corresponding value of the perfect shell $P_{cr,0}$. Despite the fact that from the engineering point-of-view this problem concerns the idealized case of axisymmetric imperfections, this study [3] provides a rigorous demonstration of the fact that small initial imperfections can substantially reduce the load carrying capacity of cylindrical shells. In the following, the above problem is revisited using our numerical tools.

3.4 Numerical Results

For the purposes of this study, an elastic thin-walled cylinder ($r/t = 100$) is examined under axial compression with axisymmetric imperfections. The axisymmetric imperfection shape is obtained from an appropriate bifurcation analysis. In such a case, the hoop dependence of cross-sectional deformations functions $w(\theta), v(\theta), u(\theta)$ and $\gamma(\theta)$ is omitted in equations (2.150). The ''tube-element'' allows a convenient application of this axisymmetry; the only non-zero coefficients that are employed in the numerical analysis are a_0 and γ_0. In the context of an initial numerical analysis, an axisymmetric buckling mode is obtained (Fig. 6), and it is imposed as an imperfection in a subsequent analysis. The imperfection amplitude $\xi = W_0 / t$ is defined as the total wave height W_0, normalized by the cylinder thickness t (Fig. 7). Following

the study of Koiter [4], only a tube portion corresponding to twice the period of the axisymmetric equilibrium configuration is examined, applying the appropriate boundary conditions.
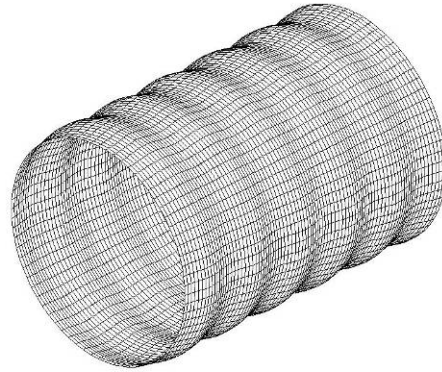
Fig. 6 Axisymmetric buckling mode
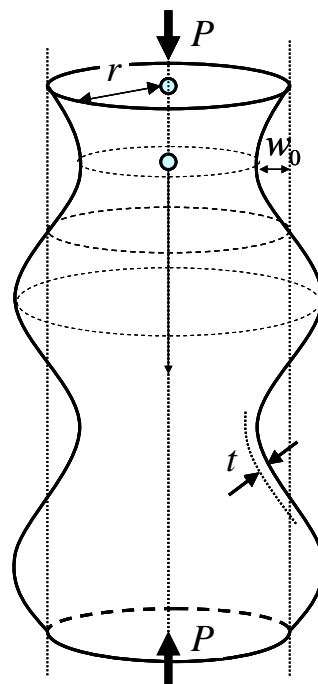
Fig. 7 Amplitude of the initial imperfection ($\xi = W_0 / t$)

In the context of the present study a comparison between hypoelastic and hyperelastic material modeling is also conducted. Therefore, for the same specific imperfection amplitudes ($\xi = 0.1$, 0.5 and 1.0) and for a 16th degree expansion in (2.150), numerical results are reported for

50

various anisotropy levels in Fig. 8-Fig. 10. The numerical results indicate insignificant differences between the two material models.
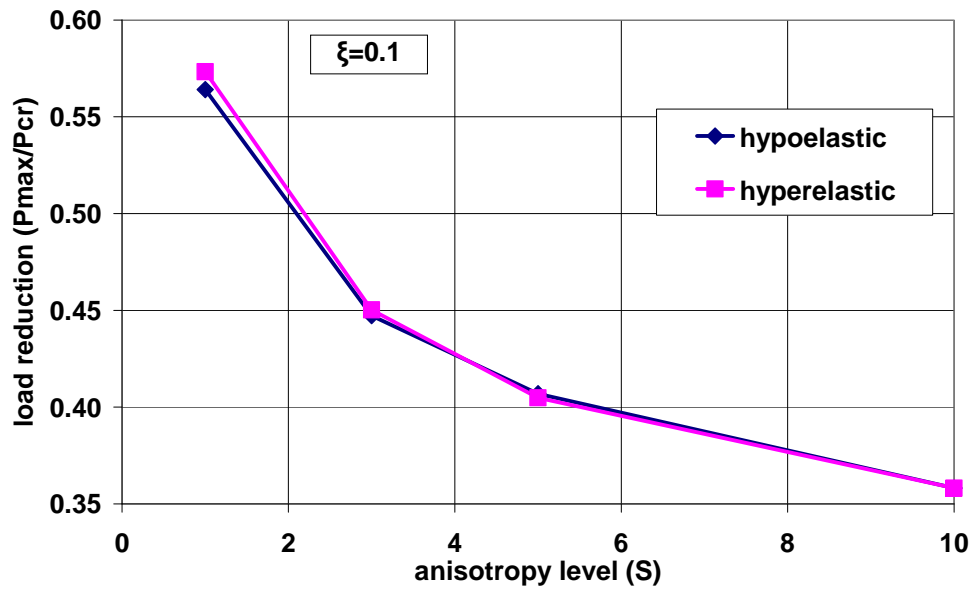
Fig. 8 Comparison of hypoelastic and hyperelastic material models with respect to anisotropy level for ξ =0.1 (r/t =100)
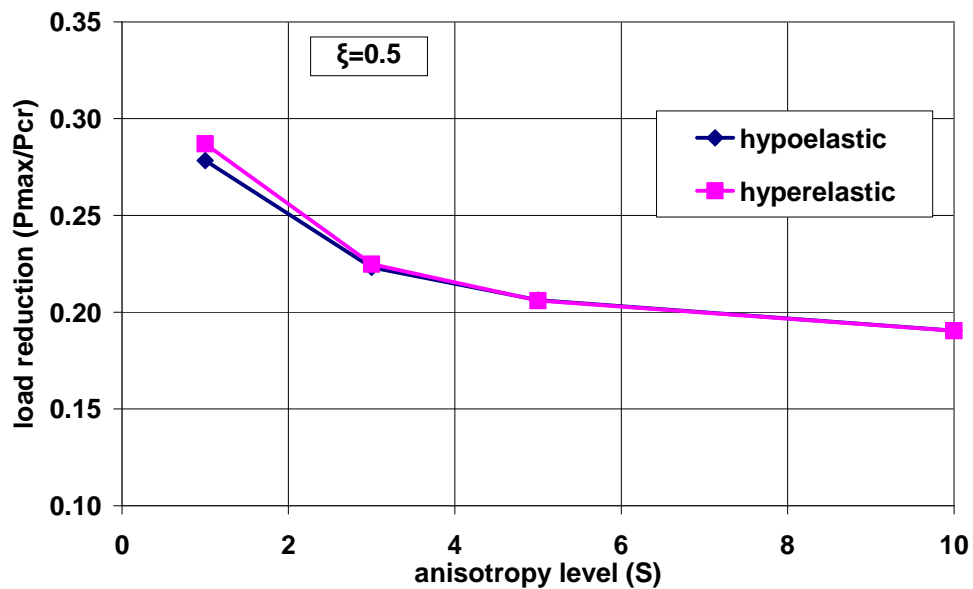
Fig. 9 Comparison of hypoelastic and hyperelastic material models with respect to anisotropy level for ξ =0.5 (r/t =100)

51
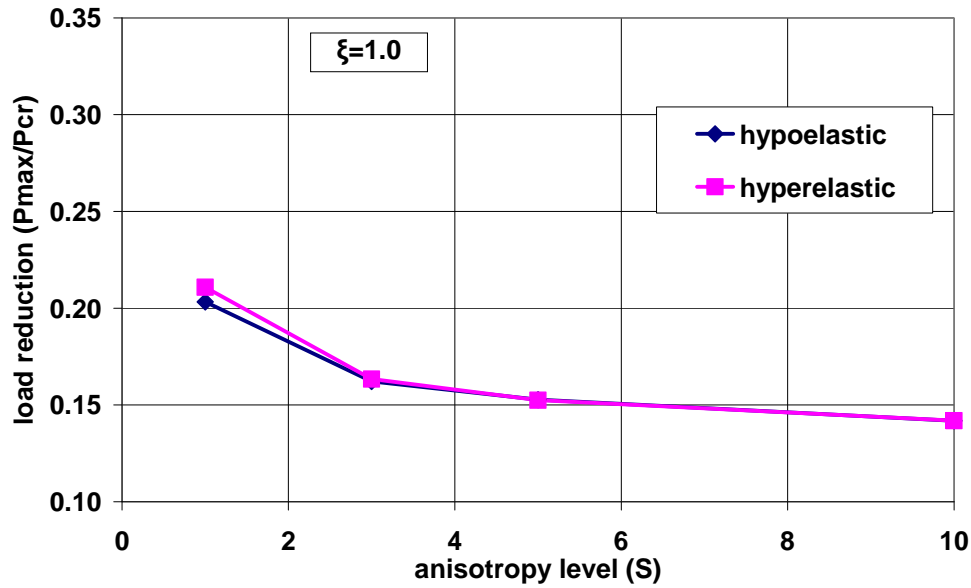
Fig. 10 Comparison of hypoelastic and hyperelastic material models with respect to anisotropy level for $\xi = 1.0$ **(** $r / t = 100$**)**

In the following, parametric study is conducted to determine the number of Fourier coefficients for the ovalization a_n, b_n and warping c_n, γ_n parameters that are necessary for this analysis. The convergence of the results is verified by increasing the number of terms in the trigonometric series (2.150) until the required accuracy was achieved, as it is depicted in Fig. 11. The results show that a 10th degree expansion for $w(\theta), v(\theta), c(\theta)$ and $\gamma(\theta)$ is found to be adequate to provide satisfactory convergence for the load reduction factor (P_{max} / P_{cr}), and this is verified by a direct comparison of the obtained numerical results and the results reported in [3]. Moreover, for the purposes of this study a cylindrical arc-length algorithm ($\psi = 0$) is adopted, which monitors the increments of all the degrees of freedom of the ''tube-element'', and 23 equally spaced integration points around the half-circumference are employed.
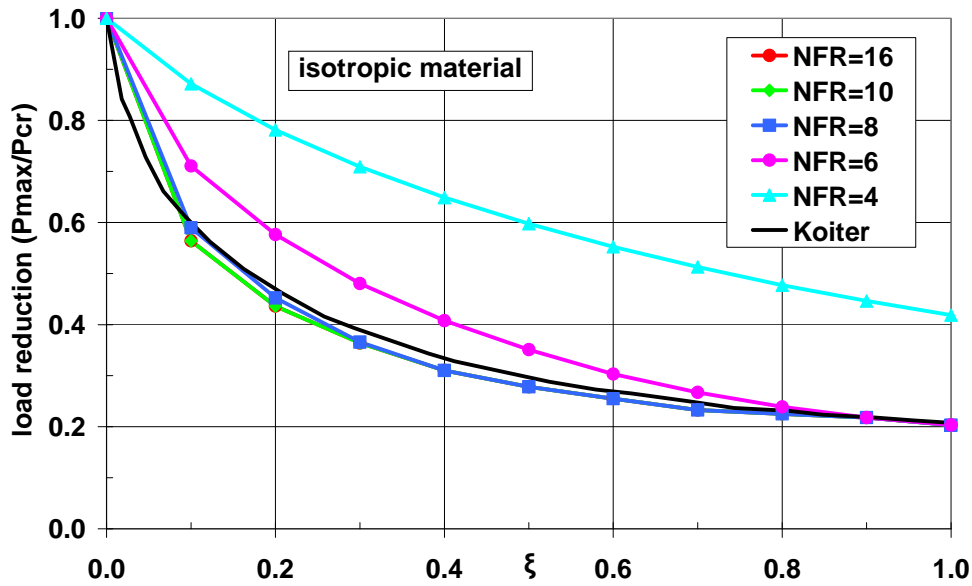
Fig. 11 Convergence study for the expansion of the Fourier coefficients, comparison with the results reported in [3] (r/t =100)

Transversely isotropic cylinders are also considered, adopting the parameterization of anisotropy through the anisotropy parameter S. Therefore, in the following figures (Fig. 12-Fig. 14) the asymmetric buckling modes obtained for a transversely isotropic cylinder (S =5) are depicted with respect to the amplitude of the initial imperfection ξ, together with the number of n waves along the hoop direction. It is noted that in those Figures for visualization purposes the buckling patterns are properly magnified.
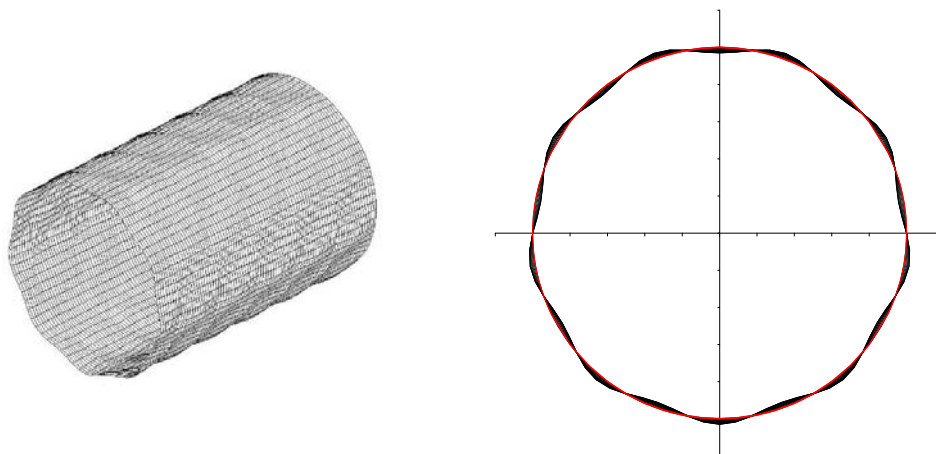
Fig. 12 Non-axisymmetric buckling mode (S =5, ξ =0.1, n =9, r/t =100)

53
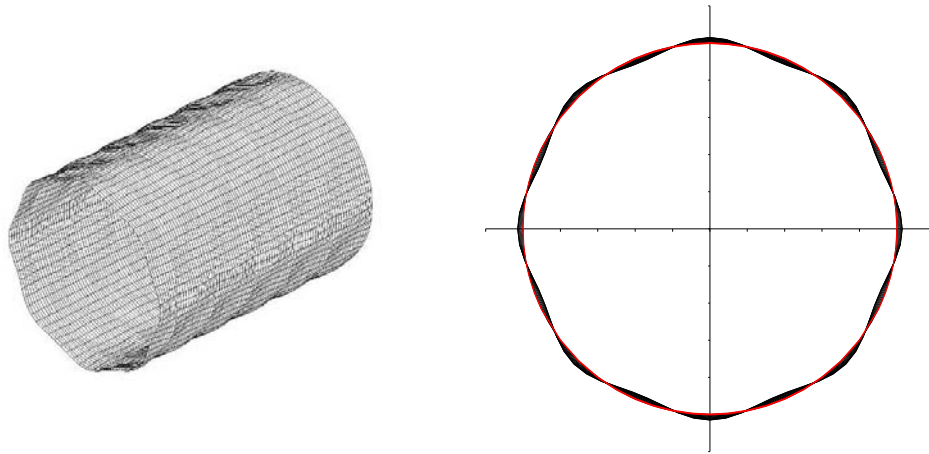
Fig. 13 Non-axisymmetric buckling mode (S =5, ξ =0.5, n =8, r/t =100)
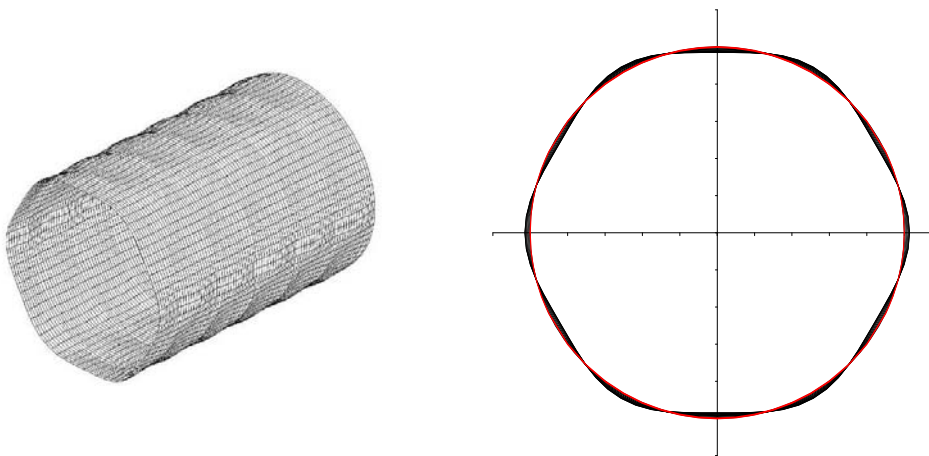
Fig. 14 Non-axisymmetric buckling mode (S =5, ξ =1.0, n =6, r/t =100)
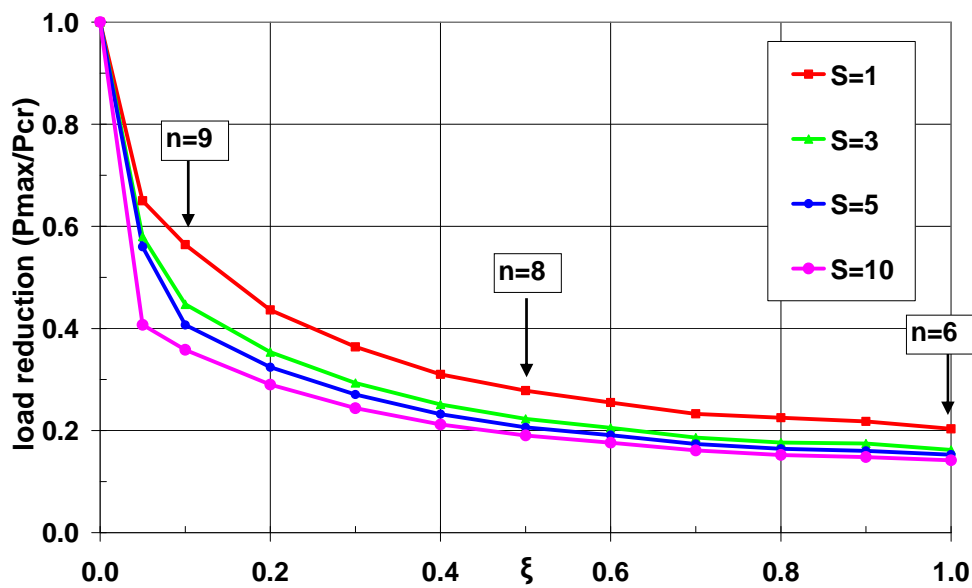
Fig. 15 Load reduction factors for various levels of anisotropy; formation of n waves along the circumference (hypoelastic model, r/t =100)

54

In Fig. 15 the load reduction factor is given with respect to the imperfection amplitude ξ for various levels of anisotropy. The load reduction is more drastic as the anisotropy level increases. Moreover, for the particular cases with imperfection amplitudes $\xi = 0.1, 0.5, 1.0$ the number of waves n along the circumferential direction is given. It is noted that this number is independent of the level of anisotropy S but it is affected by the initial imperfection amplitude ξ. It was also found that the value of buckling wavelength is affected by the presence of anisotropy, and it increases with increasing level of anisotropy.

55

Chapter 4

THIN-WALLED NON-CIRCULAR ELASTIC CYLINDERS UNDER AXIAL COMPRESSION

Non-circular cylinders of small or large eccentricities are used to aerospace and mechanical engineering applications, due to either special external shapes or (internal) storage requirements. The problem of non-circular cylinders under axial compression has several similarities with the corresponding problem of circular cylinders under axial compression. However, there are several stricking differences, which refer to imperfection sensitivity and postbuckling response and allow its separate investigation.

In the following, buckling and postbuckling response of non-circular elastic cylinders under uniform axial compression is examined numerically, using large-strain hypoelastic and hyperelastic constitutive models, and the numerical results are compared with a semi-analytical asymptotic solution. Imperfection sensitivity issues are also discussed, and the influence of the level of anisotropy on the buckling characteristics is investigated. It is mentioned, that non-circular cylinders under uniform axial compression, due to the variation of hoop curvature around the cylinder, can serve as a reference problem for the stability of bent cylinders, to be examined extensively in the subsequent Chapters.

Equation Chapter (Next) Section 4

4.1 Introduction

In this section, a brief review of the relevant literature for the axial compression of non-circular elastic cylinders is presented focusing mainly on the studies of isotropic cylinders. Important contributions on buckling of anisotropic cylinders are reported, as well. It should be noted that although the number of studies dealing with the behavior of non-circular cylinders is constantly increasing over the years, this number is rather limited compared to the vast literature in the topic of circular cylinders under axial compression.

The elastic stability of non-circular cylinders under axial compression constituted a structural mechanics problem for which a specific discrepancy between theoretical and experimental results was observed. In contrast to the circular cylinder case and despite the fact that initial postbuckling response was calculated to be unstable [46], [47], ultimate loads higher than initial buckling load have been observed in experiments for non-circular cylinders with moderate-to-

56

large eccentricities. Circular cylinders under axial compression exhibit buckling, which is associated with an infinite number of modes, occurs instantaneously over the entire circumference of the shell and it is accompanied by a very pronounced drop in the load-bearing capability of the shell. Thus, for the circular shell, the initial buckling results immediately in collapse. On the other hand, in the case of non-circular cylinders, experiments have shown that initial buckling occurs in the region of the minimum curvature of the circumference and is accompanied by a relatively little initial drop in the load-bearing capability. Subsequently, buckling patterns gradually propagate outside the regions of maximum curvature in the circumference and this allows the non-circular cylinder to use some reserved strength. This behavior is more noticeable, as the eccentricity of the non-circular cross-section is increasing. For highly-eccentric cross-sections, the initial postbuckling path was found less sensitive to imperfections. This behavior is reasonable, constituting a smooth transition from the significant imperfection sensitivity of the circular cylinder to the flat plate buckling behavior.

  Numerical studies [47]-[52] for non-circular cylinders under uniform axial compression have confirmed the experimental observations regarding the strong buckling stress dependence on the amount of cross-sectional eccentricity. From these experimental observations it was assumed that a reasonable estimate of this critical stress for thin-walled shells of moderate eccentricities can be obtained from the corresponding buckling stress of an axially compressed circular cylinder, which has a radius equal to the maximum radius r_{max} of hoop curvature of the non-circular cylinder. Therefore, the critical stress σ_{cr} can be obtained by the following expression:

$$\sigma_{cr} = \sqrt{3(1-v^2)}\,\frac{Et}{r_{max}} \tag{4.1}$$

For the particular case of non-circular cylinders of elliptic shape r_{max} is the radius of curvature at the ends of the minor axis of the ellipse, defined by:

$$r_{max} = A^2/B \quad (A > B) \tag{4.2}$$

where A is used for the length of the semi-major axis of the non-circular cross-section and B for the length of the semi-minor axis (Fig. 16). Buckling initiates in the region of minimum curvature at the ends of the minor axis, which was also confirmed by numerical results [47]-[52]. It is noted that from expressions (4.1) and (4.2) it can be readily concluded that the buckling load of a non-circular cylinder is lower than that of an equivalent circular cylinder with the same perimeter. Furthermore, for a given value of cylinder perimeter, the buckling load decreases, as cross-sectional eccentricity increases.
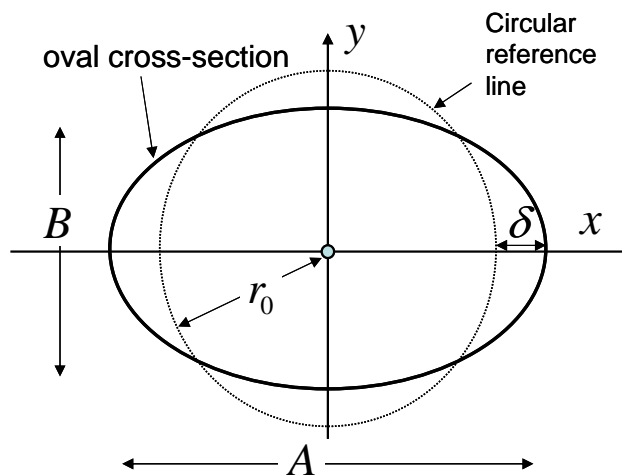
Fig. 16 Non-circular elliptic geometry

The early numerical results of the initial postbuckling behavior presented by Kempner and Chen in their early studies [7], [48], [49] indicated a significant and sharp drop in the load displacement path when the buckling load was attained similar to the one appeared in circular cylinders. However, this was not verified by experiments [46], [47] and subsequent theoretical studies [50], [51], [52]. Initial postbuckling behavior of infinitely long oval cylinders was examined by Hutchinson [50] within the context of Koiter's postbuckling theory [3]. Hutchinson [50] reported negative values for the Koiter's initial postbuckling coefficient b (Appendix-(11)), and concluded that non-circular cylinders are imperfection sensitive for all but the most highly eccentric cross-sections. In the subsequent studies of Kempner and Chen [51], [52] a more accurate formulation was adopted as proposed in [50], and the results showed that the postbuckling curve of an oval cylinder is characterized by a less drastic drop in the load-displacement path compared with circular cylinders, especially for highly-eccentric shells. Analogous conclusions for the buckling and postbuckling response were drawn in the study of Almroth et al [53]. Other theoretical studies were reported by Bushnell [54] and Semenyuk [55], which aimed at the calculation of the buckling load of simply supported elliptical cylinders, considering edge effects.

Sun [56] and Firer and Sheinman [57], [58] investigated the anisotropic response of non-circular cylinders under axial compression based on Donnell type kinematic relations. In these studies, buckling and postbuckling behavior of non-circular shells was examined with emphasis on the effect of fiber orientation in angle-ply laminated shell configurations. Sun [56] extended Hutchinson's asymptotic analysis [50] to include oval cylinders made of anisotropic composite laminates, and concluded that the buckling load and the initial postbuckling behavior, as expressed through the value of coefficient b, are significantly affected by the wall laminate structure.

58

The significant effect of the fiber orientation in angle-ply laminated cylinders has also been verified in the works of Firer and Sheinman [57], [58]. In these works non-circular cylinders were studied and edge conditions were considered. Isotropic cylinders were also considered as a special case, and previous results in isotropic cylinders [50] were verified.

Soldatos [59], [60] dealt with the buckling of axially compressed laminated oval cylinders subjected to simply supported boundary conditions, and pointed out the significant effect of the laminate configuration on the buckling and postbuckling behavior. For an up-to-date extensive review on the subject of mechanics of non-circular cylinders the reader is referred to the review paper of Soldatos [61].

In the current study, numerical results are presented for non-circular (elliptic) cylinders with moderate values of eccentricity ($B/A > 0.9$), focusing on buckling, postbuckling and imperfection sensitivity. These results are obtained through an appropriate implementation of the ''tube-element'' in the numerical technique, as described in the next section.

4.2 Modeling of Non-Circular Geometries

In this section, modelling of non-circular cross-sections is described in the framework of the ''tube-element'' formulation. Non-circular cross-sections can be expressed through an appropriate definition of the radial and tangential initial deviations from a circular reference line of radius r_{ref}, denoted as $\bar{w}(\theta)$ and $\bar{v}(\theta)$

The elliptic cross-section obeys the following parametric equation (Fig. 16):

$$(x/A)^2 + (y/B)^2 = 1 \tag{4.3}$$

where A and B denote the semi-major axis and the semi-minor axis, respectively ($A > B$). This equation can be rewritten in a simple parametric form, as follows:

$$
\begin{aligned}
x &= A\cos\theta \\
y &= B\sin\theta
\end{aligned}
\tag{4.4}
$$

where θ is a parameter, which can be interpreted as a hoop angular coordinate ($-\pi \le \theta \le \pi$).

Considering elliptic cross-sections at which the horizontal and the vertical deviations of the circular reference geometry of radius r_{ref}, δ_H and δ_V, respectively, are equal,

$$\delta_H = \delta_V = \delta \tag{4.5}$$

one obtains:

$$A = r_{ref} + \delta \tag{4.6}\backslash$$

$$B = r_{ref} - \delta \tag{4.7}$$

Next, equation (4.6) is replaced in equation (4.4):

<div align="center">59</div>

$$x = (r_{ref} + \delta)\cos\theta$$
$$y = (r_{ref} - \delta)\sin\theta \tag{4.8}$$

and after some straight forward calculations, it can be shown that (4.8) can be reformed as:

$$x = (r_{ref} + \delta\cos 2\theta)\cos\theta + \delta\sin 2\theta\sin\theta$$
$$y = (r_{ref} + \delta\cos 2\theta)\sin\theta - \delta\sin 2\theta\sin\theta \tag{4.9}$$

From simple circular ring kinematics [11], the coordinates of a point on the undeformed elliptic cross-section are given by

$$x = [r_{ref} + \overline{w}(\theta)]\cos\theta - \overline{v}(\theta)\sin\theta$$
$$y = [r_{ref} + \overline{w}(\theta)]\sin\theta + \overline{v}(\theta)\sin\theta \tag{4.10}$$

Therefore, combining (4.9) and (4.10) the in-plane initial deviations from circular geometry $\overline{w}(\theta), \overline{v}(\theta)$ are found equal to:

$$\overline{w}(\theta) = \delta\cos 2\theta$$
$$\overline{v}(\theta) = -\delta\cos 2\theta \tag{4.11}$$

and from equations (2.150) one readily obtains

$$a_2 = -b_2 = \delta \tag{4.12}$$

where δ is a parameter that defines the ellipse eccentricity ratio B/A ($B/A = (r_{ref} - \delta)/(r_{ref} + \delta)$). In conclusion, imposing initial values of a_2, b_2 according to (4.12) while all the other coefficients's initial values are equal to zero, the elliptic geometric is accurately described.

Another type of non-circular geometry is the consideration of a cylinder with an ''oval'' cross-section. Again, deviations $\overline{w}(\theta)$ and $\overline{v}(\theta)$ from a reference circular cross-section should be defined. In this case, deviations $\overline{w}(\theta)$ and $\overline{v}(\theta)$ are assumed as follows:

$$\overline{w}(\theta) = \delta\cos 2\theta$$
$$\overline{v}(\theta) = -\frac{\delta}{2}\cos 2\theta \tag{4.13}$$

so the following expression is adopted, which satisfies the first-order inextentionality condition:

$$a_2 = -2b_2 = \delta \tag{4.14}$$

The above inextentionality condition means that the circumference length of the oval cylinder is equal to the corresponding length of the equivalent circular cylinder, within a first order approximation.

Therefore, ''tube-element'' formulation allows the examination of non-circular geometries, in general. For the purposes of this study both elliptic and oval cross-sections were examined and the differences between these non-circular cross-sections were found negligible, especially for cylinders of moderate eccentricities.

4.3 Numerical Results

Numerical results for non-circular elliptic cylinders of various eccentricities are presented, with special emphasis on cylinders of moderate eccentricities ($B/A > 0.9$). For consistency with previous studies in isotropic cylinders, the values of stresses are normalized by the following stress σ_N.

$$\sigma_N = \frac{\sqrt{E_{11}E_{22}}\,t}{r_{max}}\sqrt{3(1-\nu_{12}\nu_{21})} \tag{4.15}$$

where E_{11} and E_{22} refer to hoop and longitudinal elastic modulus, respectively, ν_{12} and ν_{21} are Poisson's ratios (section 2.2) and r_{max} is the radius of curvature at the ends of the minor axis. In isotropic cylinders, this normalization stress σ_N results in the critical stress of an elliptic cylinder.

The shortening of the cylinder is expressed by the dimensionless parameter $\bar{\varepsilon} = K\varepsilon$, where ε is the axial strain of the cylinder and K is a geometric parameter proportional to the radius of curvature at the ends of minor axis r_{max}, defined as:

$$K = \frac{r_{max}}{t}\sqrt{3(1-\nu_{12}\nu_{21})} \tag{4.16}$$

Furthermore, the value of the axial half-wavelength L_{hw} is normalized by $(r_{max}t)^{1/2}$. Based on the equivalent radius r_0, which is defined as the radius of the circle with exactly the same perimeter as the elliptic cross-section, another non-dimensional parameter q, is introduced, denoted by:

$$q = (12(1-\nu_{12}\nu_{21}))^{1/4}\sqrt{r_0/t} \tag{4.17}$$

Calculations were conducted with both hypoelastic and hyperelastic constitutive models resulting in identical buckling and postbuckling response. Equilibrium paths were traced through the cylindrical arc-length algorithm ($\psi = 0$), which monitors the increments of all the degrees of freedom of the ''tube-element'', as described in section 2.7. To trace the secondary postbuckling path a slight initial imperfection is imposed, with amplitude W_0 equal to 10^{-7} times the cylinder thickness t ($\xi = W_0/t$). The imperfection shape is considered in the form of the buckling mode, obtained by an eigenvalue analysis just prior to bifurcation, as described in section 3.4 for circular cylinders.

A parametric study is conducted to determine the number of Fourier coefficients for the ovalization a_n, b_n and warping c_n, γ_n parameters that are necessary for this analysis, as in the previous Chapter. The convergence of the results is verified by increasing the number of terms in the trigonometric series (2.150) until the required accuracy was achieved. The results show that a 8th degree expansion for relatively thick cylinders (Fig. 17) and a 16th degree expansion

for thinner shells (Fig. 18) are adequate to provide satisfactory convergence not so much for ther the load reduction factor (P_{max}/P_{cr}) but for the postbuckling equilibrium path. This feature can be correlated with the abrupt changes in the shell configuration that take place in thin-walled structures. Furthermore, for the purposes of this study 23 equally spaced integration points around the half-circumference are employed.
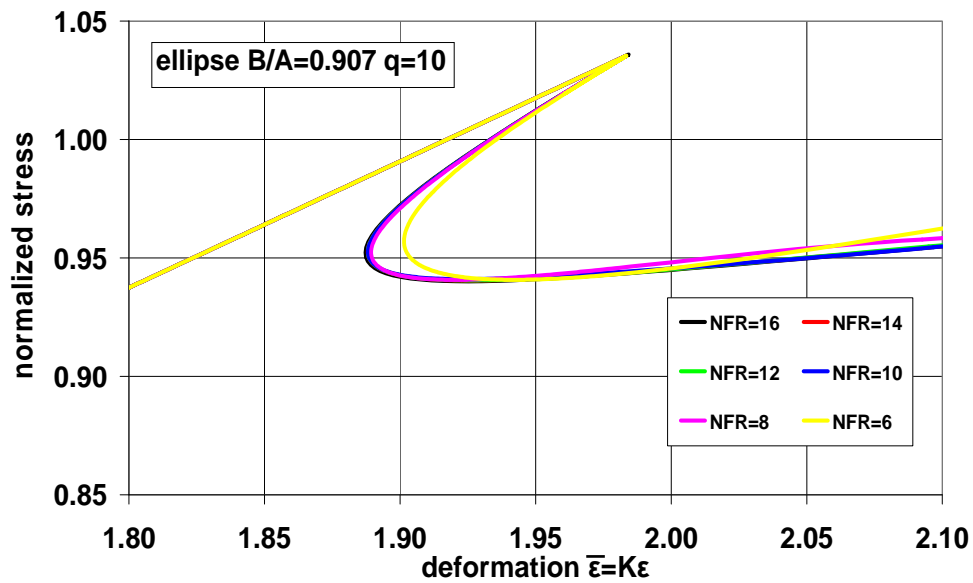
Fig. 17 Effect of the degree of trigonometric expansion used in equation (2.150) (B/A =0.907, r_o/t =30, S =1)
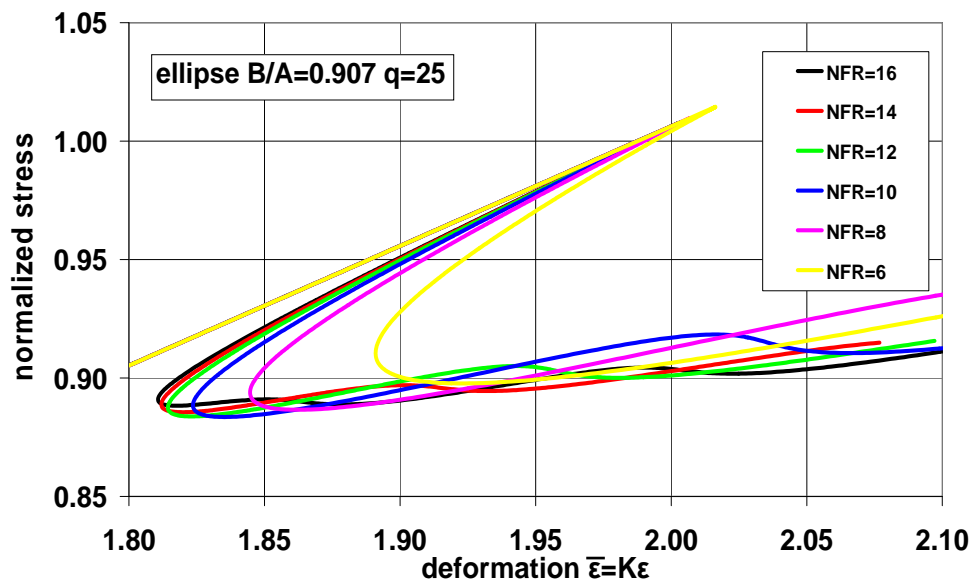
Fig. 18 Effect of the degree of trigonometric expansion used in equation (2.150) (B/A =0.907, r_o/t =190, S =1)
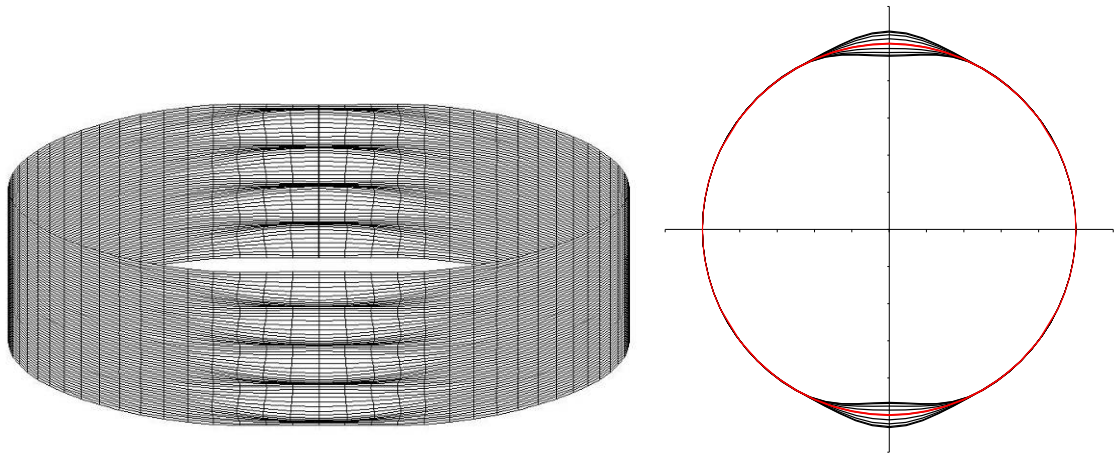
Fig. 19 Buckling mode for an elliptic isotropic cylinder (B/A =0.907, r_o/t =190, S =1)
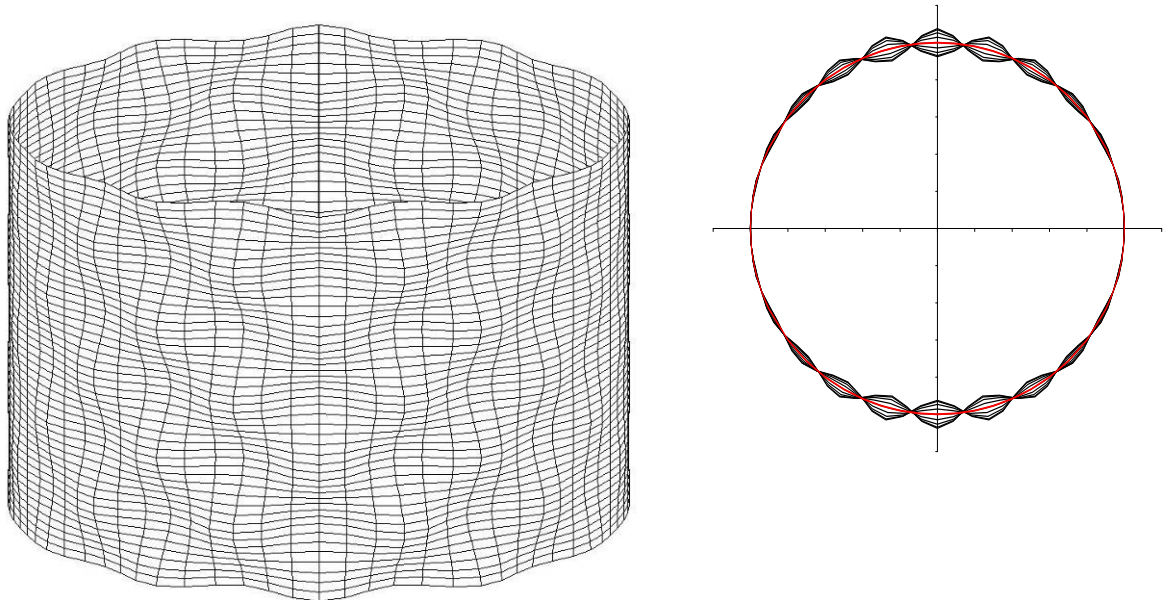
Fig. 20 Buckling mode for a transversely isotropic elliptic cylinder (B/A =0.907, r_o/t =190, S =5)

The buckling modes of a thin-walled elliptic cylinder with small eccentricity are shown in Fig. 19 and Fig. 18, considering two values of the anisotropy parameter S . It is noted that the buckling load of a non-circular cylinder subjected to axial compression is associated with only one instability mode as opposed to the case of circular shells, where buckling load is characterized by an infinite number of modes. This difference relies on the ovalized initial configuration and the variation of the hoop curvature along the cross-section. This is also responsible for the ''local'' character of buckling in the circumferential direction, especially for the case of isotropic cylinders. When anisotropy effects are negligible, a smooth buckle at each

63

end of the minor axis is developed (Fig. 19). On the other hand, the buckling shape of anisotropic cylinders is characterized by multiple short-length waves within the hoop direction, which are located in more extended part of the circumference (Fig. 20). These multiple wave configurations in the hoop direction explain the significant variation of the buckling wavelengths with respect to the level of anisotropy. For the case of isotropic cylinders the axial wavelength of the buckling mode of an elliptic cylinder is very close to the wavelength of the axisymmetric buckling mode of a circular cylinder with radius r_{max} ($L_{hw} = \pi[12(1-\nu^2)]^{-1/4}(r_{max}t)^{1/2}$), and approaches this value for thinner cylinders. The numerical results verify these observations; for an elliptic with $r_o/t = 190$ and $S = 1$ and 5 the corresponding half wavelengths are calculated equal to $1.74\sqrt{r_B t}$, and $5.80\sqrt{r_B t}$, respectively.

The efficiency and the capabilities of the ''tube-element'' are investigated through the comparison of the present numerical results with observations presented elsewhere [50]. These results (Fig. 21-Fig. 26) illustrate that a non-circular isotropic cylinder under axial compression undergoes snap-back bifurcation, but not a complete collapse. The buckling response of perfect and imperfect elliptical cross-sections with relatively large minor-to-major axis ratio $B/A = 0.907$ (i.e. small eccentricity) is depicted in Fig. 21-Fig. 24 for two different values of the q parameter. The results show that imperfect cylinders buckle at load level below the critical load of a perfect elliptical cylinder, in the form of a snap-back buckling, but can still sustain further load increase. More specifically, the buckling response of a relatively thick cylinder is depicted in Fig. 21 and Fig. 22, where q is equal to 10 ($r_0/t = 30$), and the case of a thinner cylinder is examined in Fig. 23 and Fig. 24, with $q = 25$ ($r_0/t = 190$). For comparison purposes the geometric parameters B/A and q are similar to the ones considered by Hutchinson [50], although in that study only initial postbuckling was examined and no numerical results of the full non-linear equilibrium path were presented.
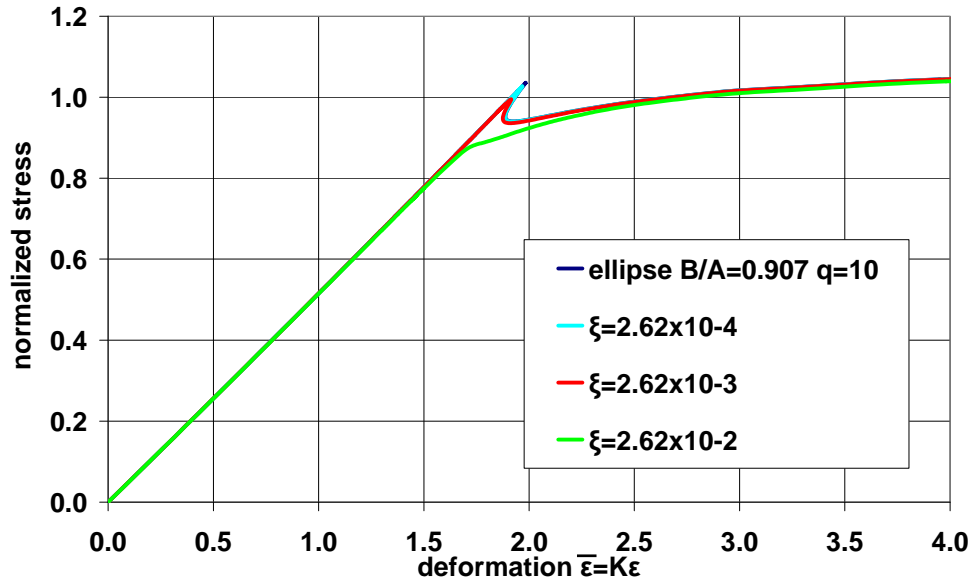
Fig. 21 Numerical results of the load-deflection path of an isotropic elliptic cylinder
(B/A =**0.907,** q =**10,** S =**1**)
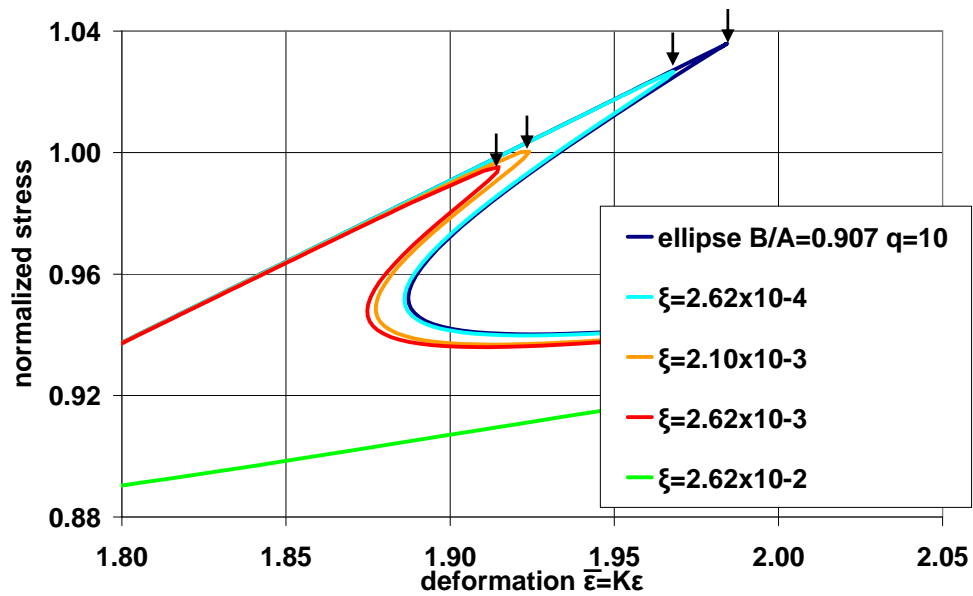
Fig. 22 Detail of the bifurcation point for an isotropic elliptic cylinder; arrows (↓) indicate maximum load points (B/A =**0.907,** q =**10,** S =**1**)

65
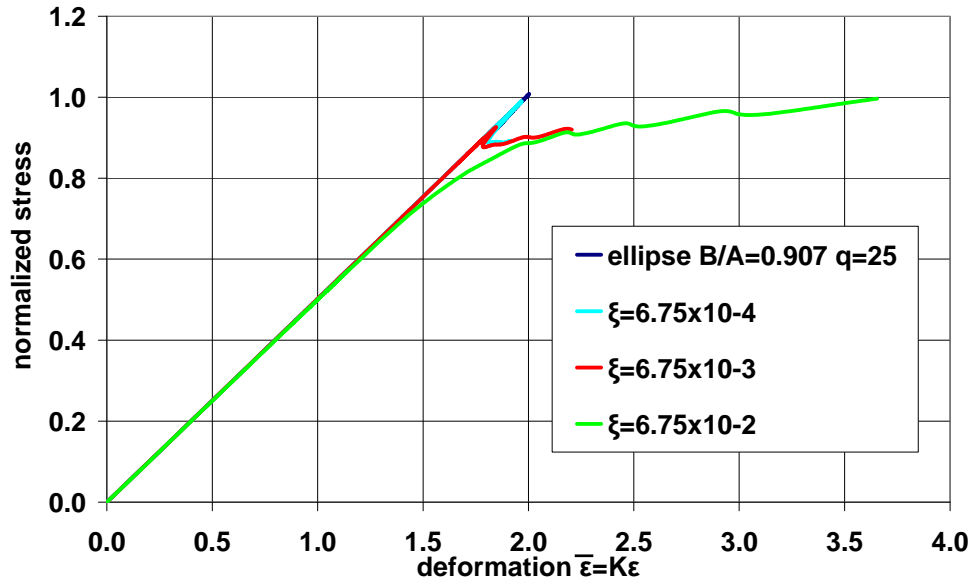
Fig. 23 Numerical results of the stress-deformation curve of an isotropic elliptic cylinder
(B/A =**0.907,** q =**25,** S =**1**)
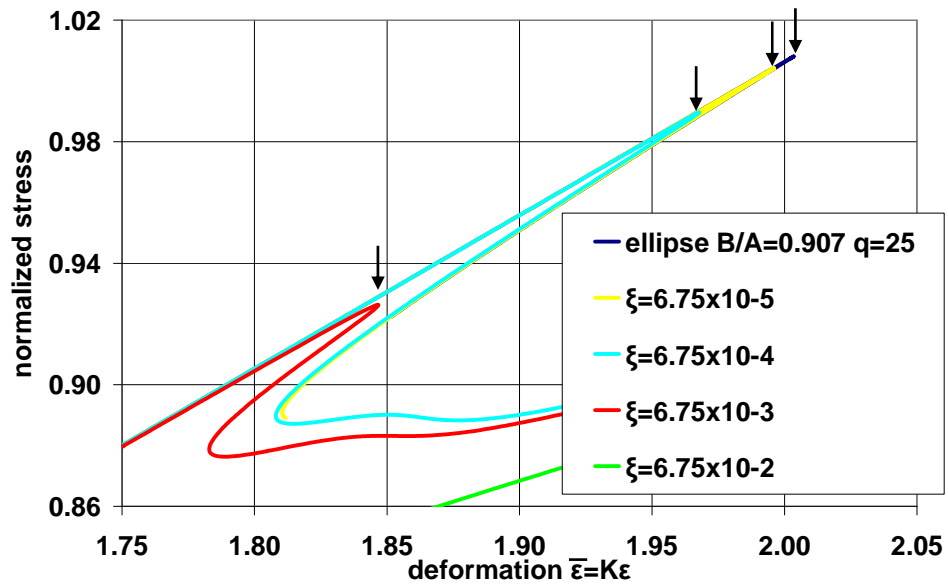
Fig. 24 Detail of the bifurcation point for an elliptic cylinder, arrows (↓) indicate maximum load points (B/A =0.907, q =25, S =1)

66
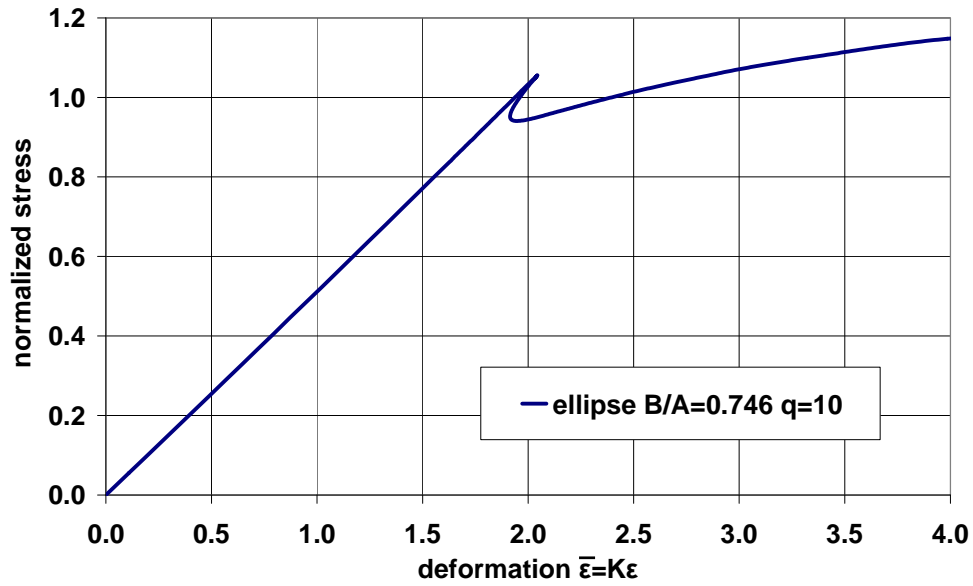
Fig. 25 Numerical results of the stress-deformation curve of an elliptic cylinder (B/A =0.746, r_0/t =30, S =1)
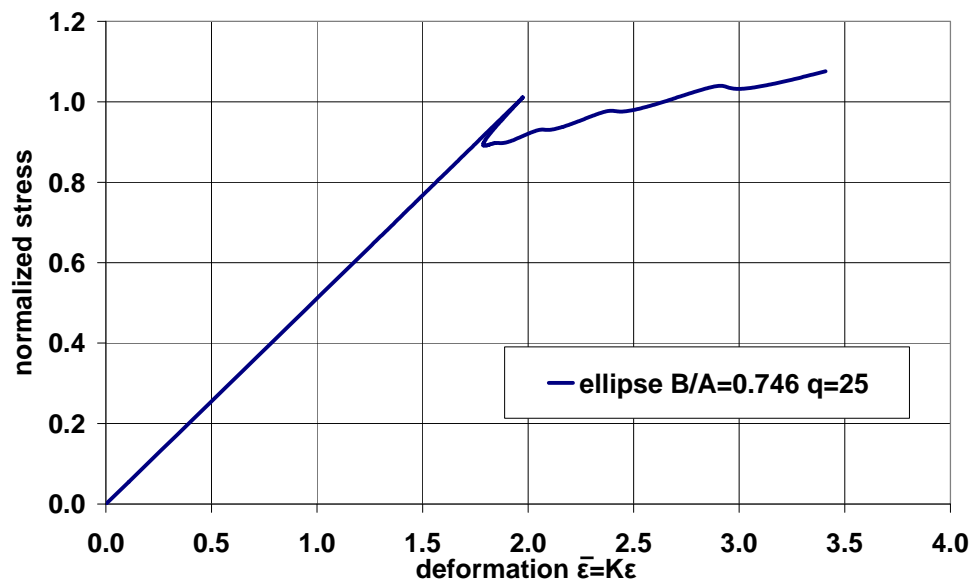
Fig. 26 Numerical results of the stress-deformation curve of an elliptic cylinder (B/A =0.746, r_0/t =190, S =1)

Results for two values of the q parameter (q =10 and 25) are also presented in Fig. 25 and Fig. 26, for a more eccentric cross-section (B/A =0.746). In these Figures, a similar response is obtained, which verifies that the postbuckling structural capacity of non-circular geometries exceeds the initial bifurcation load.

67

Based on the numerical results, one may observe that for thinner cylinders (e.g. q =25), in addition to the first sharp load reduction the postbuckling curve has a ''wavy'' form, with local limit points, which correspond to a kind of secondary buckling, as reported in [53].

In the following, the response of transversely isotropic imperfect cylinders is illustrated for different values of the imperfection amplitude ξ. The numerical results show that an increase of the imperfection amplitude ξ results in a reduction of the maximum load carrying capacity.
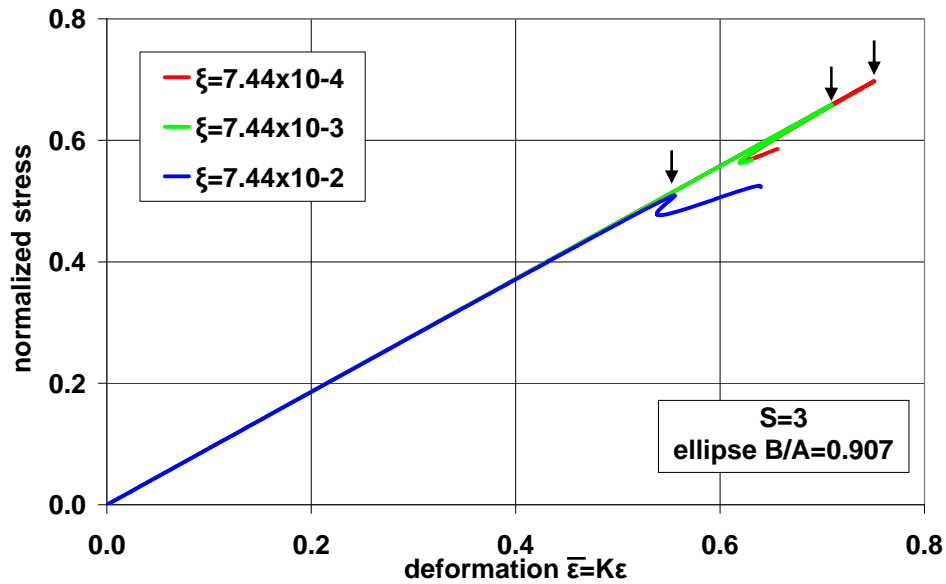
Fig. 27 Load-displacement path for an imperfect elliptic cylinder; arrows (↓) indicate maximum load points (B/A =0.907, r_0/t =190, S =3)
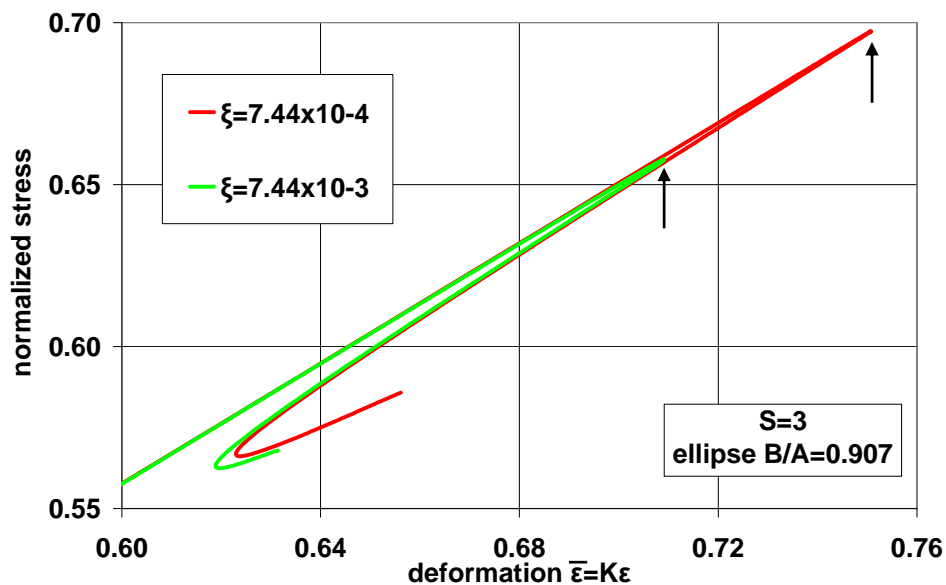
Fig. 28 Detail of the bifurcation point for an imperfect elliptic cylinder; arrows (↑) indicate maximum load points (B/A =0.746, r_0/t =190, S =3)

68

Numerical results for imperfection sensitivity numerical are also presented for both isotropic and transversely isotropic cylinders. The case of isotropic cylinders is considered first, to allow for a direct comparison of the present numerical results with results reported in [50]. Applying Koiter's postbuckling theory [3] (Appendix), Hutchinson [50] examined the character of the postbuckling behavior in the initial stages after bifurcation for isotropic shell structures. Assuming a sinusoidal variation of the buckling mode in the axial direction of the cylinder, Hutchinson calculated the value of coefficient b in equation (11) of the Appendix for characteristic values of B/A ratios and different values of the geometric parameter q. It is noted that for axial compression loading the parameter ρ in this expression, which indicates the non-linearity of the pre-buckling state, is equal to unity.

Numerical results for the maximum load parameter $\lambda = P_{\max}/P_{cr}$, in terms of initial imperfection amplitude ξ, are compared with the asymptotic expression (11) (Appendix), using the values of coefficient b directly from [50]. This comparison is shown in Fig. 29 and Fig. 30 for q =10 and 25, respectively, and for B/A =0.907. The comparison indicates a very good agreement of the present numerical technique and the asymptotic expression of [50], and offers a verification of the efficiency of the numerical formulation in describing accurately the nonlinear response of non-circular axially-loaded cylinders
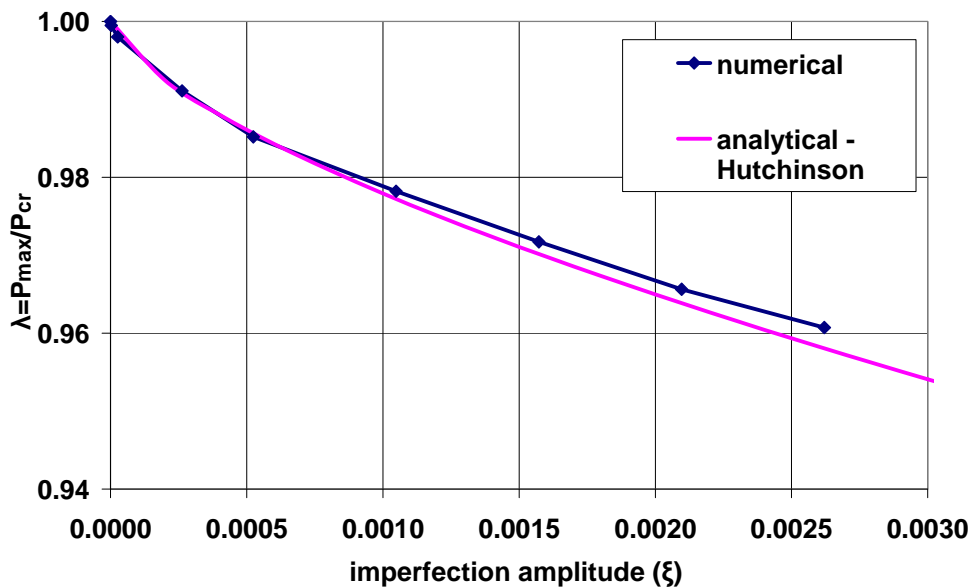
Fig. 29 $P_{\max}/P_{cr}$ **vs imperfection amplitude for** B/A **=0.907 and** q **=10; direct comparison of the present numerical results and the asymptotic solution [50]**

69
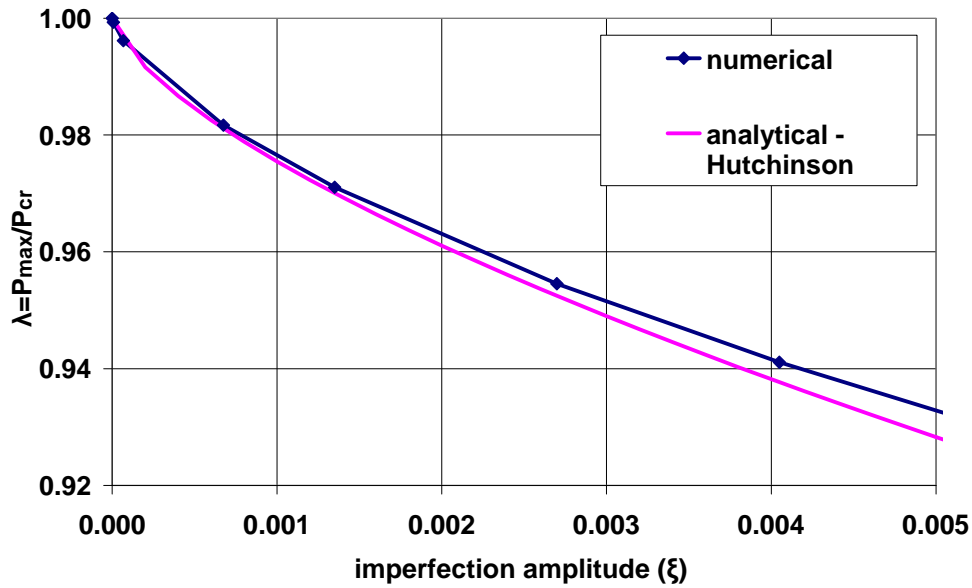
Fig. 30 $P_{\max}/P_{cr}$ **vs imperfection amplitude for** B/A **=0.907 and** q **=25; direct comparison of the**

present numerical results and the asymptotic solution [50]

In the case of transverse isotropy, an analogous comparison is not available due to the lack of asymptotic solutions for the value of b. However, numerical results have been obtained and are depicted in Fig. 31 for B/A =0.907 and q =25. These results clearly show the load reduction, as expressed by the ratio $P_{\max}/P_{cr}$, with respect to imperfection amplitude for different levels of anisotropy; even small geometrical imperfections may cause a considerable reduction of the buckling load. This reduction is affected by the presence of anisotropy, and it is found less drastic, when anisotropy is more pronounced. Finally, it is noted that using a standard curve fitting procedure in the results of Fig. 31, an exponential expression of the following form

$$\frac{P_{\max}}{P_{cr}} = 1 - C\xi^{2/3} \qquad (4.18)$$

is obtained, which follows the ''2/3'' exponential rule and fits the numerical results.

70
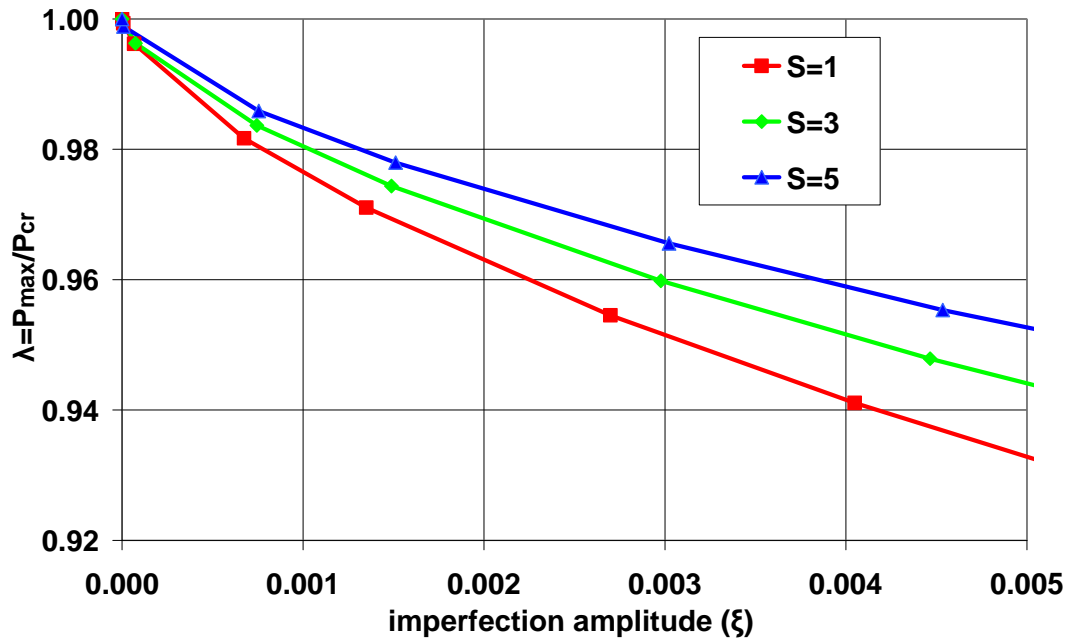
Fig. 31 P/P_{cr} **vs imperfection amplitude for different values of anisotropy parameter**

S (B/A =**0.907**, q =**25**)

71

Chapter 5

THIN-WALLED ELASTIC ISOTROPIC CYLINDERS UNDER BENDING AND PRESSURE

In the previous Chapter, structural stability of thin-walled non-circular elastic cylinders under axial compression was examined, considering both isotropic and transversely isotropic cylinders. In the present Chapter the stability of thin-walled isotropic cylinders subjected to bending moments is investigated, mainly numerically. In addition, using a simplified formulation, closed-form expressions are developed for ovalization and bifurcation instabilities, which are compared with the numerical results. Furthermore, aspects of uniform wrinkling-bifurcation are illustrated using a simple mechanical model, which considers the ovalized prebuckling state and the effects of pressure. Special emphasis is given on the effects of a slight initial curvature along the cylinder. Finally, using the nonlinear numerical tools, the stability of the secondary equilibrium path in the vicinity of the bifurcation point and the role of initial imperfections in the reduction of the critical load are examined.

Equation Chapter 5 Section 5

5.1 Ovalization Instability

The main characteristic of cylinder response under bending is the distortion (ovalization) of its cross-section due to the inward stress components σ_V of the longitudinal bending stresses (Fig. 32). The ovalization mechanism results in loss of stiffness in the form of limit point instability, referred to as ''ovalization instability'' or Brazier effect [62].

Next, a brief presentation of previous publications is given, which adopts closed-form expressions for the moment-curvature and ovalization-curvature relationships. The validity of those expressions is examined through rigorous finite element results.

72
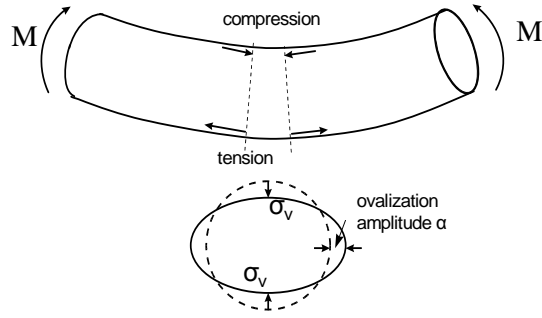
Fig. 32 Ovalization mechanism

5.1.1 Introduction

According to classical beam theory solution of the cylinder flexure problem, neglecting nonlinear geometry effects, a linear relation between bending moment and curvature is obtained:

$$M = EIk \tag{5.1}$$

which can be written in a non-dimensional form as follows:

$$m = \kappa\pi \tag{5.2}$$

where the values of moment M and curvature k are normalized by M_e and k_N respectively, where:

$$M_e = \frac{Ert^2}{\sqrt{1-v^2}} \quad , \qquad k_N = \frac{t}{r^2\sqrt{1-v^2}} \tag{5.3}$$

so that

$$m = \frac{M}{M_e}, \qquad\qquad \kappa = \frac{k}{k_N} \tag{5.4}$$
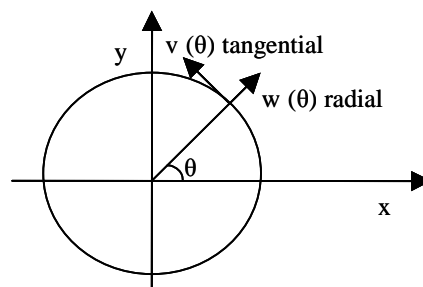
Fig. 33 Cross-sectional displacements

Brazier [62] enhanced solution (5.2) including nonlinear kinematic terms, responsible for the ovalization of the cross-section, which were assumed to be inextentional. In [62] a doubly

73

symmetric trigonometric solution for the cross-sectional ovalization displacements (Fig. 33) was obtained, which is described by:

$$v(\theta) = -\frac{k^2 r^5 (1-\nu^2)}{2t^2}\sin 2\theta = -\frac{\kappa^2 r}{2}\sin 2\theta$$
$$w(\theta) = \frac{k^2 r^5 (1-\nu^2)}{t^2}\cos 2\theta = \kappa^2 r \cos 2\theta \tag{5.5}$$

resulting in the closed-form nonlinear expressions for the moment-curvature in terms of applied curvature.

$$m = \pi\kappa(1-\frac{3}{2}\kappa^2) \tag{5.6}$$

Furthermore, expressing ovalization in terms of the non-dimensional parameter ζ, defined as follows:

$$\zeta = \frac{D_1 - D_2}{2D} \tag{5.7}$$

and from Fig. 32 one obtains:

$$\zeta = \frac{\alpha}{r} \tag{5.8}$$

where D_1 and D_2 are the cylinder diameters normal and parallel to the plane of bending and a is the ovalization amplitude, a closed-form expression for the ovalization-curvature relationship is obtained:

$$\zeta = \kappa^2 \tag{5.9}$$

Imposing stationary value of equation (5.6), one can calculate the value of limit moment, its corresponding curvature, and the cylinder flattening (ovalization). Ovalization at the limit point is found equal to about 22% of the radius (Fig. 34) and the corresponding values of moment and curvature are m_{Br} =0.987 and κ_{Br} =0.471, respectively.
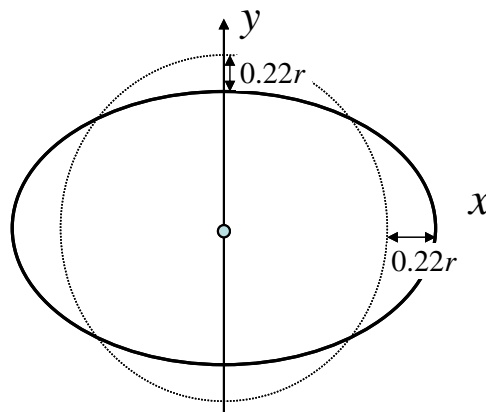
Fig. 34 Flattening of the cross-section at ovalization limit point according to Brazier solution

74

Wood [63] examined the flexure of a uniformly pressurized, long, circular and initially straight cylinder under bending, using an energy formulation. According to this study, the ovalization displacements were considered as additional (small perturbation) to the initial displacements due to pressure and the bending solution. The additional displacements were assumed to be inextentional, as in Brazier's work. Employing a Rayleigh-Ritz technique and minimizing the total potential energy, the resulting displacements for the cross-section were obtained, as follows:

$$v(\theta) = -A_2 \sin(2\theta) + A_3 \sin(3\theta)$$
$$w(\theta) = 2A_2 \cos(2\theta) + 3A_3 \cos(3\theta)$$

(5.10)

where

$$\frac{2A_2}{r} = \frac{\kappa^2}{1-f}\left(1 + \frac{2-v}{2}\frac{f}{1-v^2}\left(\frac{t}{r}\right)^2\right)$$

$$\frac{3A_3}{r} = \frac{-\kappa^3}{8-3f}\frac{v}{1-v^2}\frac{t}{r}$$

(5.11)

In the above equations, the pressure level is normalized by p_e, which is the elastic buckling pressure:

$$p_e = \frac{E}{4(1-v^2)}\left(\frac{t}{r}\right)^3$$

(5.12)

so that the normalized pressure is:

$$f = \frac{p}{p_e}$$

(5.13)

The cross-sectional displacements (5.10) include higher-order terms compared to (5.5). For small values of t/r, it is possible to neglect those higher-order terms and the following equations are obtained:

$$m = \kappa\pi\left(1 - \frac{3}{2}\kappa^2\frac{1}{1-f}\right)$$

(5.14)

$$\zeta = \frac{\kappa^2}{1-f}$$

(5.15)

The ovalization limit moment and the corresponding curvature can be calculated from (5.14) as follows:

$$\frac{dm}{d\kappa} = 0$$

(5.16)

so that

$$\kappa_{ov} = 0.471\sqrt{1-f}$$

(5.17)

and from (5.14)

75

$$m_{ov} = 0.987\sqrt{1-f} \tag{5.18}$$

Setting $f = 0$ in the above relations for κ_{ov}, m_{ov} the corresponding values of Brazier [15] are obtained ($m_{Br} = 0.987$ and $\kappa_{Br} = 0.471$).

Reissner [64] investigated ovalization instability of initially straight and curved cylinders. Until that publication, motivated by the stress analysis of pipe elbows, initially curved cylinders have been examined for linear response only, in order to determine elastic flexibility and stress intensity factors, extending the classical von Karman linear solution [65]. In that work, Reissner [64] presented for the first time a unified treatment of the two problems (i.e. nonlinear bending of straight and curved cylinders), which, until then, have been considered separately. Based on a vectorial consideration of equilibrium in a cylinder cross-section, Reissner [64] examined the nonlinear problem of bending of initially straight and curved tubes, considering the effects of pressure. In the first part of this work, Reissner demonstrated that the results of Brazier [62] and Wood [63] for initially straight cylindrical shells may be considered as a first approximation of the cylinder bending problem. Higher order terms were included for the moment-curvature path, improving the third degree equations (5.6) and (5.14). Retaining terms up to the fifth power of curvature κ, Reissner resulted in the following relation for the moment-curvature path:

$$m = \kappa\pi\left(1 - \frac{3}{2}\kappa^2\frac{1}{1-f} - \frac{3}{2}\kappa^4\frac{1}{(1-f)^2}\right) \tag{5.19}$$

Keeping only two terms on the right hand side of equation (5.19), one readily results in (5.14).

According to (5.19) limit moment m_{ov} and the corresponding curvature κ_{ov} are calculated as follows:

$$\frac{dm}{d\kappa} = 0 \tag{5.20}$$

which results in,

$$\kappa_{ov} = 0.415\sqrt{1-f} \tag{5.21}$$

and from (5.19), one obtains:

$$m_{ov} = 0.909\sqrt{1-f} \tag{5.22}$$

which are somewhat different from the values of equations (5.17) and (5.18).

Moreover, Reissner [64] presented a simple expression for the analysis of cylinders with slight initial curvature. Assuming that the order of magnitude of initial curvature κ_{in} ($\kappa_{in} = k_{in}/k_N$) is the same as the ovalization curvature κ_{ov} for the corresponding initially straight cylinders, the following simple expressions for the cross-section displacements $w(\theta)$, $v(\theta)$ were obtained:

76

$$w(\theta) = \frac{\kappa r(\kappa + \kappa_{in})}{1 - f}\cos 2\theta$$

$$v(\theta) = -\frac{\kappa r(\kappa + \kappa_{in})}{2(1 - f)}\sin 2\theta$$

(5.23)

It can be readily verified that these displacements satisfy the first-order ''inextentionality'' condition ($w(\theta) + v'(\theta) = 0$). This inextentionality condition means that the circumference length of the cylinder does not change along the deformation path, within a first order approximation. Those equations resulted in closed-form moment-curvature and ovalization-curvature expressions that account for pressurized cylinders of slight initial curvature:

$$m = \kappa\pi\left(1 - \frac{3(\kappa + \kappa_{in})(2\kappa + \kappa_{in})}{4(1 - f)}\right)$$

(5.24)

$$\zeta = \frac{\kappa_{in}\kappa + \kappa^2}{1 - f}$$

(5.25)

Negative and positive values of κ_{in} corresponds to opening and closing moments, respectively (Fig. 35). The ovalization curvature κ_{ov} can be found by imposing:

$$\frac{dm}{d\kappa} = 0$$

(5.26)

and it is equal to:

$$\kappa_{ov} = \frac{1}{6}\left(\sqrt{8(1 - f) + 3\kappa_{in}^2} - 3\kappa_{in}\right)$$

(5.27)

In the case of initially straight cylinders ($\kappa_{in} = 0$), the above equations (5.24) and (5.25) result in equations (5.14) and (5.15), correspondingly.
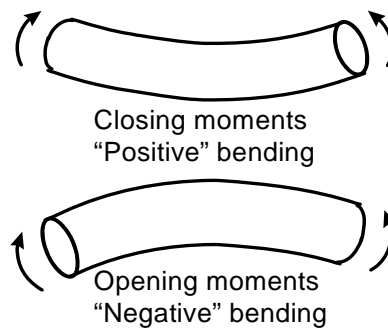
Fig. 35 Loading conditions in initially curved cylinders

Following those notable publications, several researchers have addressed the problem of nonlinear ovalization using more advanced analytical tools. Reissner [66] examined in detail the ovalization instability of initially straight tubes, considering two independent variables,

77

namely the rotation of the cross-section reference line $\beta(\theta)$, and a stress function $\psi(\theta)$, where θ is the hoop coordinate. For circular cross-section, the formulation resulted in a system of two nonlinear differential equations in terms of β and ψ. The moment-curvature path ($m-\kappa$), included terms up to the fifth power of the curvature κ, which constitutes an enhanced form of the third-degree $m-\kappa$ expression of Brazier [62]. In a subsequent paper, Reissner and Weinitschke [67] presented an integral formulation for the ovalization instability of circular initial straight cylinders and an iterative numerical solution method. Results for deformation and stress beyond the limit point were also reported.

Axelrad [68], [69] presented a nonlinear formulation for the ovalization instability of cylindrical members under bending based on a nonlinear flexible shell theory. Results were reported for initially straight and bent cylindrical shells, including the effects of pressure. For initially straight cylinders, the formulation was identical to the one developed by Reissner [66]. A description of this formulation and some characteristic results can be found in the works of Axelrad [70], [71] and in the work of Axelral and Emmerling [72].

Thurston [73] used a modified Newton's method to solve the governing equations proposed by Reissner [66] and calculated the ultimate moment and the corresponding curvature for initially straight cylinders. Those values correlated very well with the analytical results presented by Axelrad [69], [70]. Boyle [74] re-examined the instability of initially bent cylinders, considering a similar nonlinear shell theory. The solution was compared with simplified closed-form moment-curvature expressions, and was in very good agreement with the results of Axelrad [69]. In a more recent work, Karamanos [75] investigated ovalization instability of long thin-walled initially straight and bent cylinders. Using a nonlinear finite element formulation, results over a wide range of initial curvature values were presented. The efficiency and accuracy of analytical expressions introduced elsewhere with respect to the numerical results were discussed.

5.1.2 Analytical Energy Solution

The case of pressurized initially straight or bent circular cylinders is briefly examined for the sake of completeness from a unified yet simple formulation, using a variational approach. The energy formulation includes the effects of pressure and initial curvature in ovalization instability. The total potential energy, in the case of pressurized bending, is the sum of the above quantities:

$$\Pi = U_L + U_C + V_P - W_P - M\,k \qquad (5.28)$$

where, U_L is the longitudinal bending strain energy, U_C is the cross-sectional (hoop) deformation strain energy, V_P is the pressure potential and W_p is the second-order of hoop pressure stress $\sigma_p = pr/t$.

From beam theory, the longitudinal part U_L is expressed in terms of stress σ_x and the strain ε_x in the direction of tube axis as follows.

$$U_L = \frac{1}{2}\int_A \sigma_x \varepsilon_x dA = \frac{E}{2}\int_A \varepsilon_x^2 dA = \frac{Etr}{2}\int_0^{2\pi} \varepsilon_x^2 d\theta \tag{5.29}$$

The strain ε_x in the direction of the cylinder axis is given by the following expression directly from ring theory:

$$\varepsilon_x = ky + \frac{u_n}{R} = k[(r+w)\sin\theta + v\cos\theta] + \frac{1}{R}[v\cos\theta + w\sin\theta] \tag{5.30}$$

where $1/R = k_{in}$ is the initial curvature of the cylindrical shell, k is the applied curvature, r and t are the radius and the thickness of the cylinder cross-section respectively, y is the distance from the neutral axis, u_n is the displacement in the direction of the plane of bending and k is the longitudinal applied curvature. In the above expressions $w(\theta)$ and $v(\theta)$ are the displacements of the reference line in the radial and tangential direction respectively (Fig. 36).
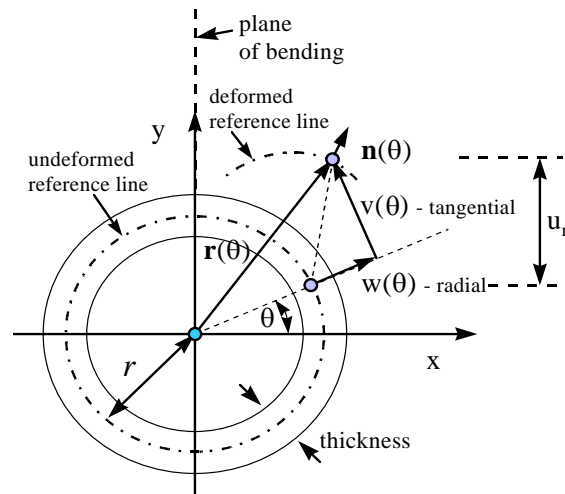
Fig. 36 Cross-sectional ovalization (in-plane) deformation parameters

The total curvature $1/R'$ of the cylinder at the deformed configuration is:

$$\frac{1}{R'} = k + \frac{1}{R} \tag{5.31}$$

Referring to the hoop strain energy U_C, a ring-theory formulation is adopted, based on the Bernoulli assumption (i.e. plane sections remain plane and normal to the deformed cross-

79

sectional mid-thickness reference line) as described in Brush and Almroth [11]). Every point has an axial hoop strain equal to:

$$\varepsilon_\theta = \varepsilon_{\theta 0} + k_\theta \rho = \left[\frac{1}{r}(v'+w) \right] + \left[\frac{1}{r^2}(v'-w'') \right] \rho \tag{5.32}$$

where ( )$'$ denotes differentiation with respect to θ, ρ is the material coordinate in the radial direction (through the thickness). Assuming inextentionality of in-plane displacements, $\varepsilon_{\theta 0}$ is set equal to zero, which results in:

$$w(\theta) + v'(\theta) = 0 \tag{5.33}$$

Therefore the hoop strain energy U_C can be expressed as follows:

$$U_C = \frac{1}{2} \int\int_{A_\theta} \sigma_\theta \varepsilon_\theta r\, d\theta d\rho = \frac{1}{2} \frac{Er}{(1-v^2)} \int\int_{A_\theta} \varepsilon_\theta^2 d\theta d\rho = \frac{Et^3}{24(1-v^2)r^3} \int_0^{2\pi} (v'+v''')d\theta \tag{5.34}$$

To express the work due to pressure a ring is considered in plane-strain conditions that correspond to a cross-section of the cylinder. For pressure loading, the pressure at each point on the ring surface remains normal to the surface as the ring deforms. Therefore, a ring subjected to uniform internal or external pressure constitutes a conservative system. It is a closed system and the potential energy of the applied pressure is the product of the pressure p times the change of the area enclosed by the surface of the ring. It is readily shown that the potential energy due to pressure is:

$$U_{press} = p\Delta A = p\frac{1}{2}\int_0^{2\pi}(2rw+v^2-vw'+v'w+w^2)d\theta \tag{5.35}$$

In the following, external pressure corresponds to positive values of p and internal pressure is expressed by negative values of p.

The work of stress σ_p, due to pressure is expressed as follows:

$$\int_V \sigma\,\overline{\varepsilon}_{\theta 0} dV = \iint_{A_\theta} \frac{pr}{t}\overline{\varepsilon}_{\theta 0} r\,d\theta d\rho = \int_0^{2\pi} \frac{pr}{t}\overline{\varepsilon}_{\theta 0} rt\,d\theta = \frac{1}{2}p\int_0^{2\pi}(v-w')^2 d\theta \tag{5.36}$$

where $\sigma_p = \dfrac{pr}{t}$ (from elementary strength of materials and $\overline{\varepsilon}_{\theta 0}$ is the second order hoop normal strain.

$$\overline{\varepsilon}_{\theta 0} = \frac{1}{2}\left(\frac{v-w'}{r}\right)^2 \tag{5.37}$$

Subsequently, a simple Ritz discretization with trigonometric functions is considered to obtain analytical closed-form solution for the ovalization-curvature relationship and the moment-curvature equilibrium path. For simplicity, only one trigonometric doubly symmetric term is assumed for $w(\theta)$ and $v(\theta)$:

80

$$w(\theta) = a\cos 2\theta \quad \text{and} \quad v(\theta) = -\frac{a}{2}\sin 2\theta \tag{5.38}$$

where a is ovalization amplitude (Fig. 32).

It is noted that assumption (5.38) satisfies the condition of inextentionality. Inserting all the above equations in the expression of potential energy (5.28) one results in the following equation:

$$\Pi = \frac{Etr}{2}(k^2 r^2 \pi + \frac{5a^2}{8R'^2}\pi - \frac{3}{2}\frac{kra}{R'}\pi) + \frac{3}{8}\frac{\pi Et^3 a^2}{(1-v^2)r^3} - \frac{3}{2}a^2 p\pi - Mk \tag{5.39}$$

The above expression refers to both initially straight and curved cylinders.

Neglecting quadratic terms in the expression of U_L, one results in a simpler expression for the potential energy. The total curvature $1/R'$ is expressed as:

$$\frac{1}{R'} = k + k_{in} \tag{5.40}$$

and equation (5.39) results in:

$$\Pi(a,k) = \frac{Etr}{2}(k^2 r^2 \pi - \frac{3}{2}k(k+k_{in})ra\pi) + \frac{3}{8}\frac{\pi Et^3 a^2}{(1-v^2)r^3} - \frac{3}{2}a^2 p\pi - Mk \tag{5.41}$$

Solutions for the ovalization parameter a in terms of the applied curvature k yield directly from the minimization of Π in terms of a. Consideration of equilibrium ($\partial\Pi/\partial a = 0$) leads to the ovalization-curvature relationship:

$$a = \frac{\kappa r(\kappa + \kappa_{in})}{1-f} \tag{5.42}$$

so that:

$$\zeta = \frac{\alpha}{r} = \frac{\kappa(\kappa + \kappa_{in})}{1-f} \tag{5.43}$$

Inserting the value of ovalization amplitude α, as described in (5.42), in the expression of potential energy and enforcing equilibrium ($\partial\Pi/\partial k = 0$), an expression for the bending moment is obtained:

$$m = \kappa\pi(1 - \frac{3(\kappa + \kappa_{in})(2\kappa + \kappa_{in})}{4(1-f)}) \tag{5.44}$$

From expression (5.44) the ovalization curvature is obtained and it is found equal to:

$$\kappa_{ov} = \frac{1}{6}\left(\sqrt{8(1-f) + 3\kappa_{in}^2} - 3\kappa_{in}\right) \tag{5.45}$$

In addition, the ovalization moment m_{ov} is obtained from equation (5.44) for $\kappa = \kappa_{ov}$.

The moment-curvature relation (5.44) is identical with the one presented by Reissner [64]. In that work, this expression was obtained through an analytical formulation based on nonlinear kinematics and assuming a small initial curvature of the cylinder, whereas in the present study

81

it is obtained through an energy formulation. Furthermore, setting $\kappa_{in} = 0$ in expression (5.44), the closed-form expression (5.14) of Wood [63] is obtained. Specialization of (5.44) to the case of non-pressurized initially straight cylinders results in equation (5.6), which was first presented in Brazier [15] .

It is also possible to obtain closed-form expressions for the longitudinal stress σ_x. Inserting the value of ovalization amplitude from (5.43) in the inextentional discretization of the displacements $w(\theta)$ and $v(\theta)$ one obtains:

$$w(\theta) = r \frac{\kappa(\kappa + \kappa_{in})}{1 - f} \cos 2\theta \quad \text{and} \quad v(\theta) = -r \frac{\kappa(\kappa + \kappa_{in})}{2(1 - f)} \sin 2\theta \tag{5.46}$$

and using the expression (5.30) for the longitudinal strain ε_x, a closed-form expression is obtained for the longitudinal stress $\sigma_x = E\varepsilon_x$, as follows.

$$\frac{\sigma_x}{\sigma_e} = \kappa \left((1 - \frac{3(\kappa + \kappa_{in})^2}{4(1 - f)}) \sin\theta + \frac{(\kappa + \kappa_{in})^2}{4(1 - f)} \sin 3\theta \right) \tag{5.47}$$

where $\sigma_e = \frac{E}{\sqrt{1 - \nu^2}} \left(\frac{t}{r} \right)$ is a ''reference'' stress used for normalization purposes only.

Expression (5.47) is identical with the one presented by Reissner [64].

Furthermore, employing the above simplified formulation, it is possible to obtain analytical expressions for the radii of curvature at the deformed cross-section. Using the following expression for the hoop curvature:

$$\frac{1}{r_\theta} = \frac{1}{r} + k_\theta \tag{5.48}$$

where r, r_θ are the radiis of curvature before and after the deformation, respectively, and k_θ is the change of curvature in the hoop direction, and applying ring-theory [11], the following expressions are obtained:

$$\frac{1}{r_\theta(\theta)} = \frac{1}{r} + \frac{v'(\theta) - w''(\theta)}{r^2} \tag{5.49}$$

and using (5.43), (5.46) and (5.49) one readily obtains:

$$\frac{1}{r_\theta(\theta)} = \frac{1}{r} + \frac{3\kappa^2 \cos 2\theta + 3\kappa\kappa_{in} \cos 2\theta}{r(1 - f)} \tag{5.50}$$

Summarizing, the above described energy formulation results in the following closed-form expressions in terms of the applied curvature κ, considering the effects of initial curvature κ_{in} and pressure f.

Radial displacement

$$w(\theta) = \frac{\kappa r(\kappa + \kappa_{in})}{1 - f} \cos 2\theta \tag{5.51}$$

82

Tangential displacement

$$v(\theta) = -\frac{\kappa r(\kappa + \kappa_{in})}{2(1-f)}\sin 2\theta \qquad (5.52)$$

Ovalization-curvature

$$\zeta = \frac{\kappa(\kappa + \kappa_{in})}{1-f} \qquad (5.53)$$

Moment-curvature

$$m = \kappa\pi(1 - \frac{3(\kappa + \kappa_{in})(2\kappa + \kappa_{in})}{4(1-f)}) \qquad (5.54)$$

Longitudinal stresses

$$\frac{\sigma_x}{\sigma_e} = \kappa\left((1 - \frac{3(\kappa + \kappa_{in})^2}{4(1-f)})\sin\theta + \frac{(\kappa + \kappa_{in})^2}{4(1-f)}\sin 3\theta\right) \qquad (5.55)$$

Curvature in the hoop direction at the deformed configuration

$$\frac{1}{r_\theta(\theta)} = \frac{1}{r} + \frac{3\kappa(\kappa + \kappa_{in})}{r(1-f)}\cos 2\theta \qquad (5.56)$$

The presented energy formulation considers the case of circular cylinders, and the majority of the cases examined in this study concern this case. However, it is possible to include a stress-free initial ovality of the cylinder cross section in the above formulas. The initial ovality of the cross-section is assumed inextentional, in accordance with (5.38) and is expressed in the following form:

$$w_0(\theta) = a_0\cos 2\theta \quad \text{and} \quad v_0(\theta) = -\frac{a_0}{2}\sin 2\theta \qquad (5.57)$$

where a_0 is the initial ovalization amplitude additional to ovalization amplitude a and the initial ovalization parameter ζ_0 is defined by $\zeta_0 = \alpha_0/r$

Reconsideration of (5.41) and similar minimization of Π results in the following formulas:
Radial displacement

$$w(\theta) = \left(\frac{\zeta_0 f}{1-f} + \frac{\kappa r(\kappa + \kappa_{in})}{1-f}\right)\cos 2\theta \qquad (5.58)$$

Tangential displacement

$$v(\theta) = -\left(\frac{\zeta_0 f}{2(1-f)} + \frac{\kappa r(\kappa + \kappa_{in})}{2(1-f)}\right)\sin 2\theta \qquad (5.59)$$

Ovalization-curvature

$$\zeta = \frac{\zeta_0 f}{1-f} + \frac{\kappa(\kappa + \kappa_{in})}{1-f} \qquad (5.60)$$

Moment-curvature

83

$$m = -\zeta_0 \pi \frac{3(2\kappa + \kappa_{in})}{4(1-f)} + \kappa\pi\left(1 - \frac{3(\kappa + \kappa_{in})(2\kappa + \kappa_{in})}{4(1-f)}\right) \tag{5.61}$$

Longitudinal stresses

$$\frac{\sigma_x}{\sigma_e} = -\zeta_0 \frac{\kappa - 2f\kappa - f\kappa_{in}}{4(1-f)}(3\sin\theta - \sin 3\theta) + \kappa\left((1 - \frac{3(\kappa + \kappa_{in})^2}{4(1-f)})\sin\theta + \frac{(\kappa + \kappa_{in})^2}{4(1-f)}\sin 3\theta\right)$$

$$\tag{5.62}$$

Curvature in the hoop direction at the deformed configuration

$$\frac{1}{r_\theta(\theta)} = \frac{1}{r} + \frac{3\zeta_0(1-2f)}{r(1-f)}\cos 2\theta + \frac{3\kappa(\kappa + \kappa_{in})}{r(1-f)}\cos 2\theta \tag{5.63}$$

which correspond to (5.51)-(5.56) for $\zeta_0 = 0$.

5.1.3 Numerical Results

In this section the analytical closed-form expressions obtained by the energy formulation (5.58)-(5.63) are compared with numerical results from the nonlinear finite element formulation of Chapter 2, as well as results from previous researchers. The numerical results corresponding to ovalization instability are obtained under the assumption that bifurcation (buckling) into a wrinkled state does not occur. In all cases, pressure-if present-is applied first and then keeping the pressure level constant, bending load is gradually increased. For the purposes of such an analysis a cross-sectional analysis that employs only one ''tube-element'' is required, considering only in-plane cross-sectional deformation (displacements $w(\theta)$ and $v(\theta)$) and neglecting warping (displacement $c(\theta)$ and rotation $\gamma(\theta)$).

The cylinder material is isotropic elastic and its behavior is described by the large-strain hypoelastic constitutive model, incorporated in the nonlinear finite element technique as described in Chapter 2. Results obtained from the hyperelastic model have been found to be very similar. For consistency purposes (with the bifurcation analysis, as it is going to be discussed in a following paragraph) a 16th degree expansion is used for the number of cross-sectional parameters although convergence can be easily obtained by using less terms, due to the absence of bifurcation. Furthermore, 19 equally spaced integration points around the half-circumference are employed, and five and two Gauss points are used in the radial direction (through the thickness) and in the longitudinal direction, respectively. Values of moment, curvature and pressure are normalized by M_e, k_N, p_e, respectively, as described before (5.3), (5.12). Results are presented for tubes with r/t equal to 120. However, it was found that using the described normalization the numerical results are independent of the r/t ratio.

84

First, the case of initially straight cylinders (κ_{in}=0) is examined. The accuracy of the above closed-form expressions [(5.58)-(5.63)] is examined through their comparison with numerical results, as it is depicted in Fig. 37 and Fig. 38. In Fig. 39 the influence of pressure on the $m-\kappa$ path is demonstrated. It can be seen that the presence of external pressure (f >0) reduces the moment capacity, whereas there is a beneficial effect of internal pressure (f <0). The $\zeta-\kappa$ relationship for different values of pressure is shown in Fig. 40. The numerical results indicate that the presence of internal pressure reduces cross-sectional ovalization.

The closed-form expression (5.55) for the longitudinal stresses of initially straight cylinders in terms of curvature and pressure compares well with the numerical results, as shown in Fig. 41 and Fig. 42. It has to be pointed out that stress distribution is no longer linear with respect to the distance with the neutral axis. Three cases are depicted referring to internal, external and no pressure, respectively. The comparison of stress distributions is conducted at the point on the primary path that corresponds to the maximum value of moment (the ovalization limit point stage), as calculated through the finite element analysis.

(a)

85

(b)

(c)
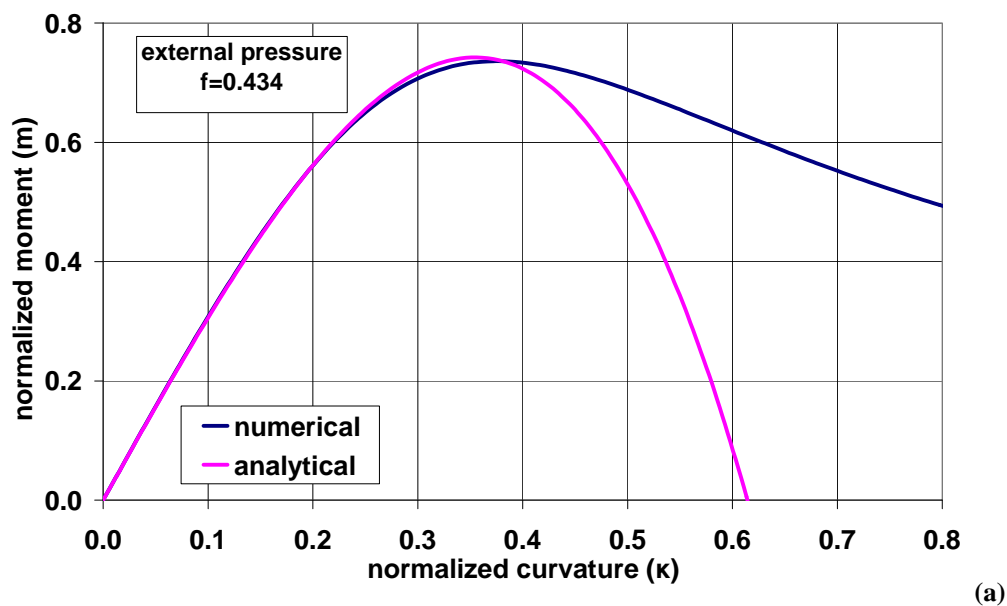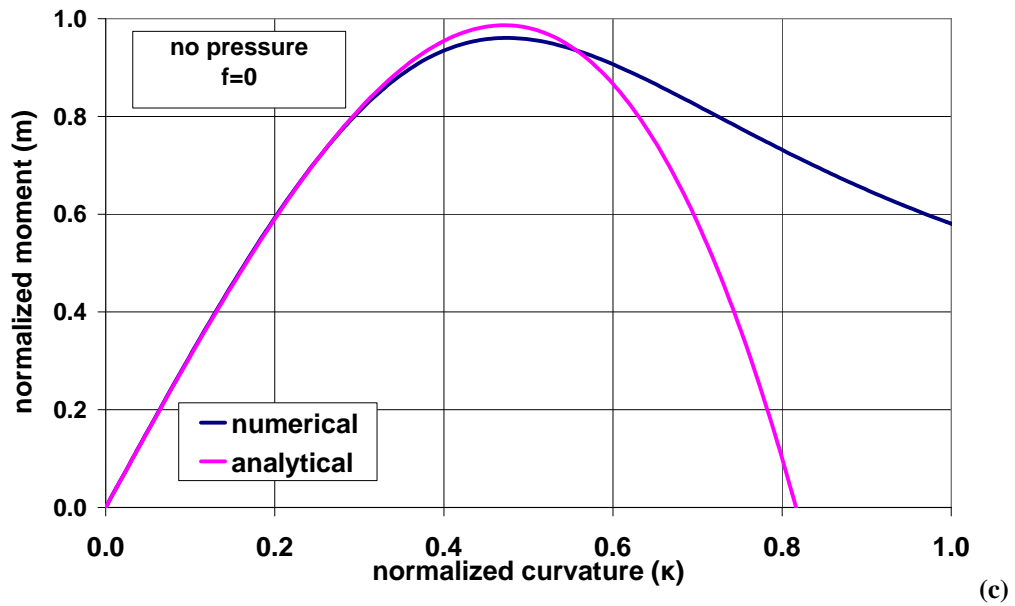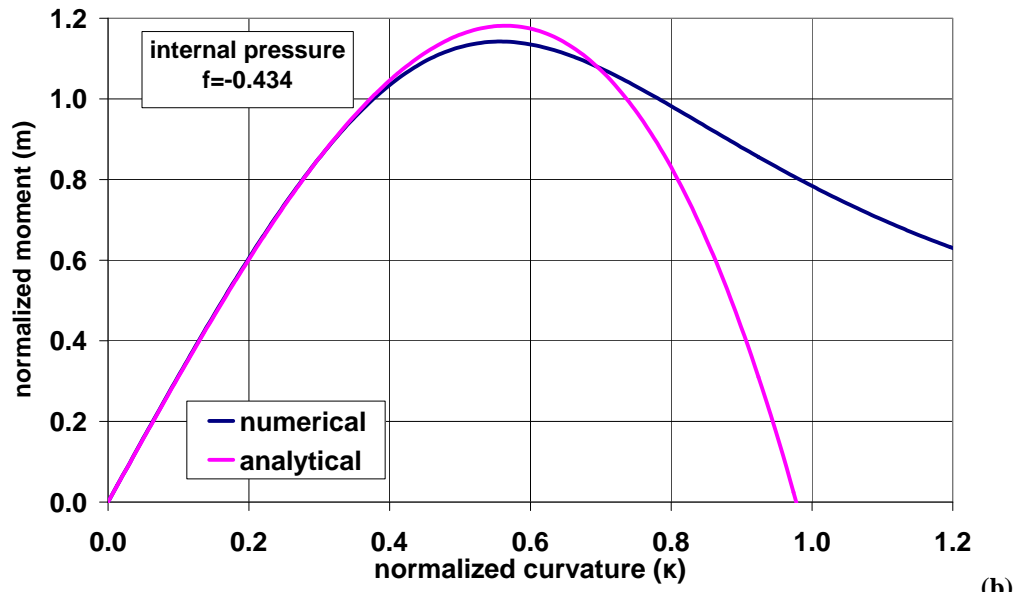
Fig. 37 $m - \kappa$ **paths for cross-sectional analysis with respect to pressure** f **(** $r/t = 120, \kappa_{in} = 0$ **)**

86
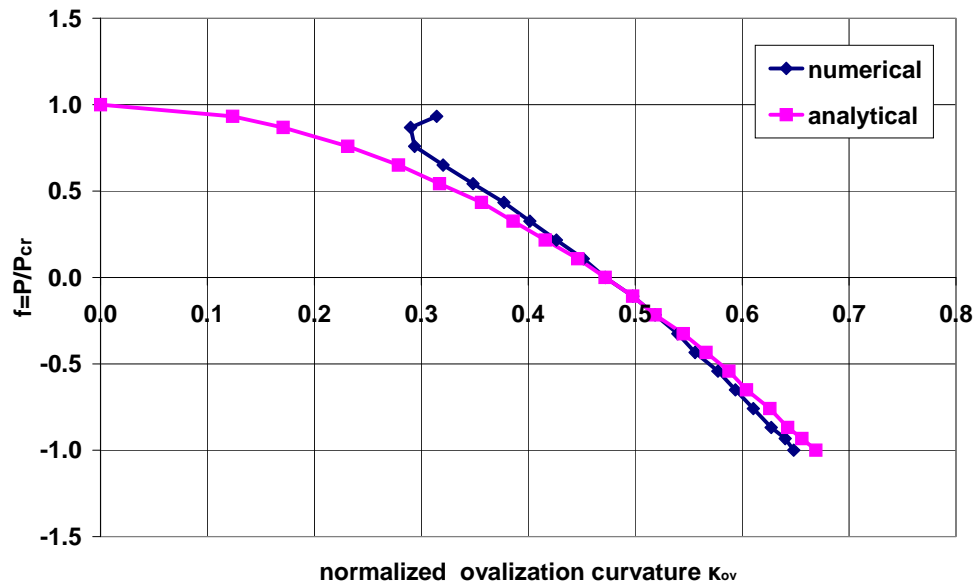
(a)
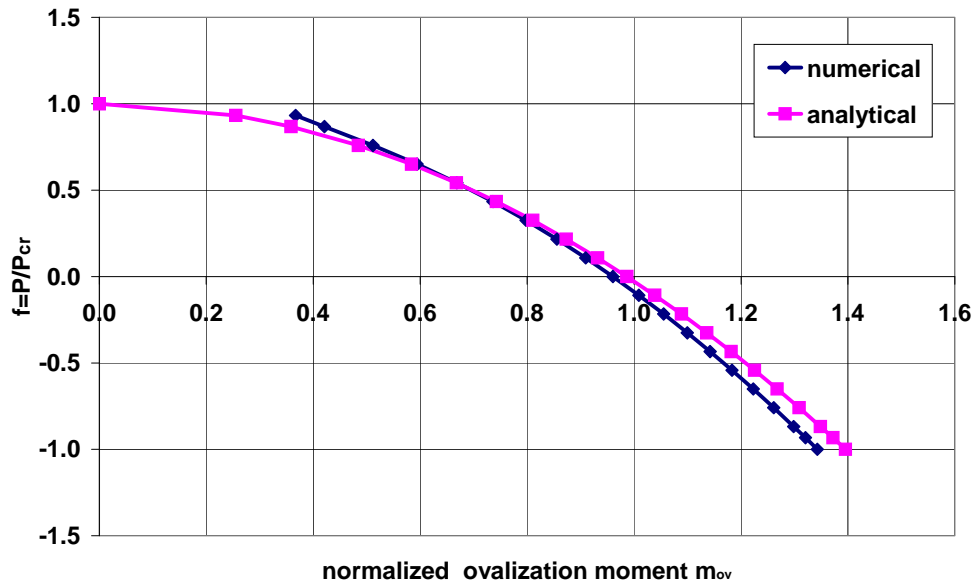
(b)

Fig. 38 Variation of κ_{ov} and m_{ov} with respect to the pressure level f (r/t =120, κ_{in} =0)

87
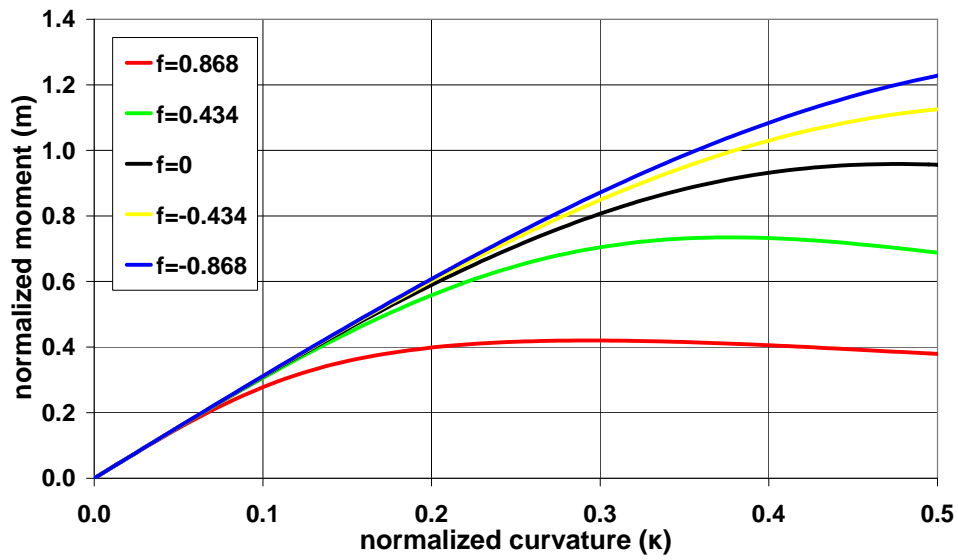
Fig. 39 Analytical results of $m-\kappa$ **equilibrium paths considering pressure effects (** r/t **=120,** κ_{in} **=0)**
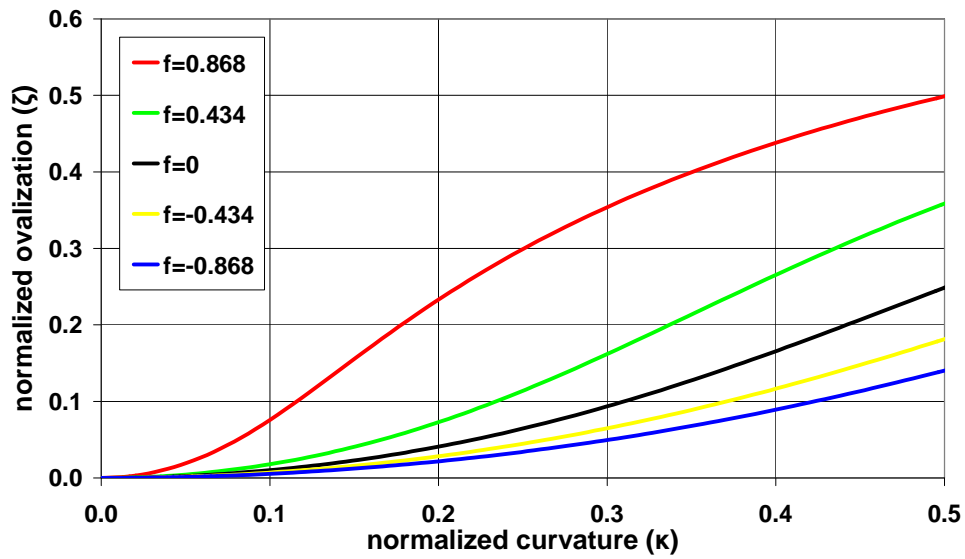
Fig. 40 Analytical results of $\zeta-\kappa$ **paths considering pressure effects (** r/t **=120,** κ_{in} **=0)**

88

The case of initially bent cylinders is examined next. The analytical expressions are compared with numerical results. The moment-curvature path from equation (5.54) is quite close to the numerical results in the cases of closing moments. For comparison purposes, some results of the two-dimensional analysis of non-pressurized initially bent cylinders are also included in the following diagrams

The moment-curvature of unpressurized initially bent cylinders is shown in Fig. 43. The initial curvature is small compared to the critical curvature. It is reminded that negative and positive values of κ_{in} correspond to opening and closing moments, respectively (Fig. 35). For these values of initial curvature analytical results compare fairly well with the numerical results, especially for closing moments, whereas, for higher values of initial curvature, numerical and analytical results compare qualitatively, as it is depicted in Fig. 44.

The analytical expression (5.19) for the moment-curvature path included higher order terms than expressions (5.6), (5.14). Nevertheless, equation (5.19) describes ovalization less accurately, as compared with numerical results. This observation confirms Calladine's [76] remark that Brazier [62] was ''lucky in being able to obtain good results for the maximum bending moment by using a power series, which was so crudely truncated''. A comparison between the aforementioned moment-curvature relations (5.6), (5.14) and (5.19) for an initially straight unpressurized cylinder is given in Fig. 45. This comparison results in the observation that including higher order terms in the ovalization analysis (e.g. [64]) the ovalization mode is described less accurately than neglecting these terms [62].
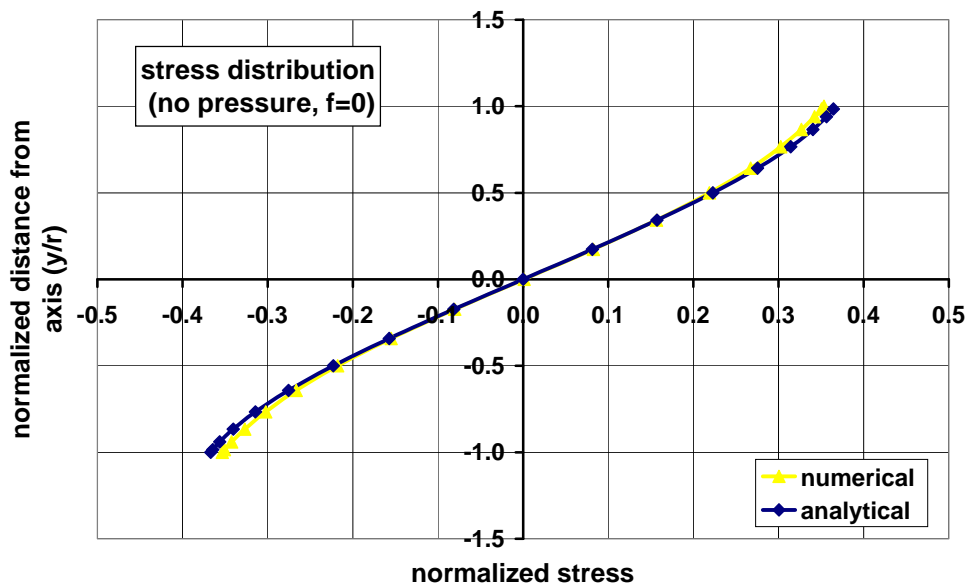
Fig. 41 Longitudinal stress distributions at the ovalization limit point ($r/t =120, \kappa_{in} =0, f =0$)

89
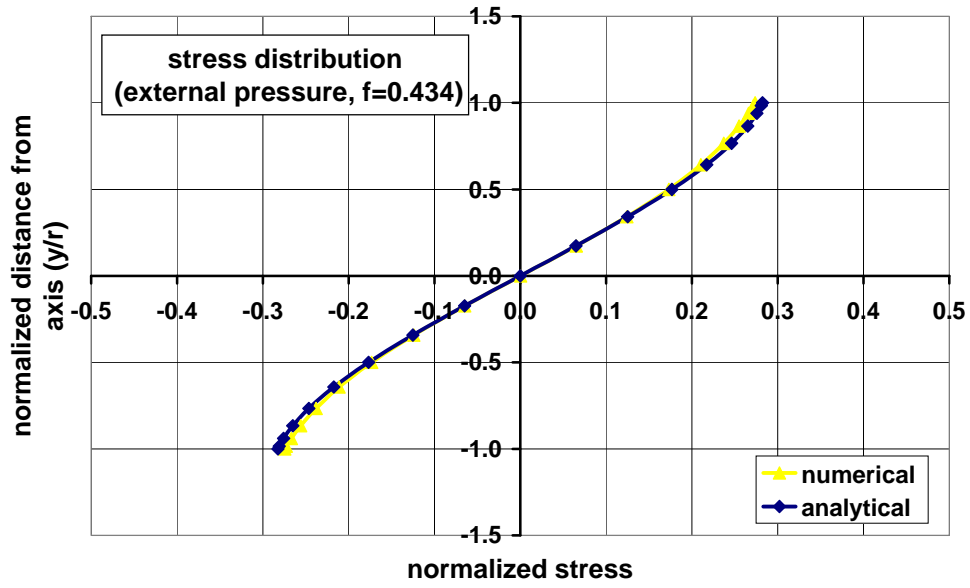
(a)
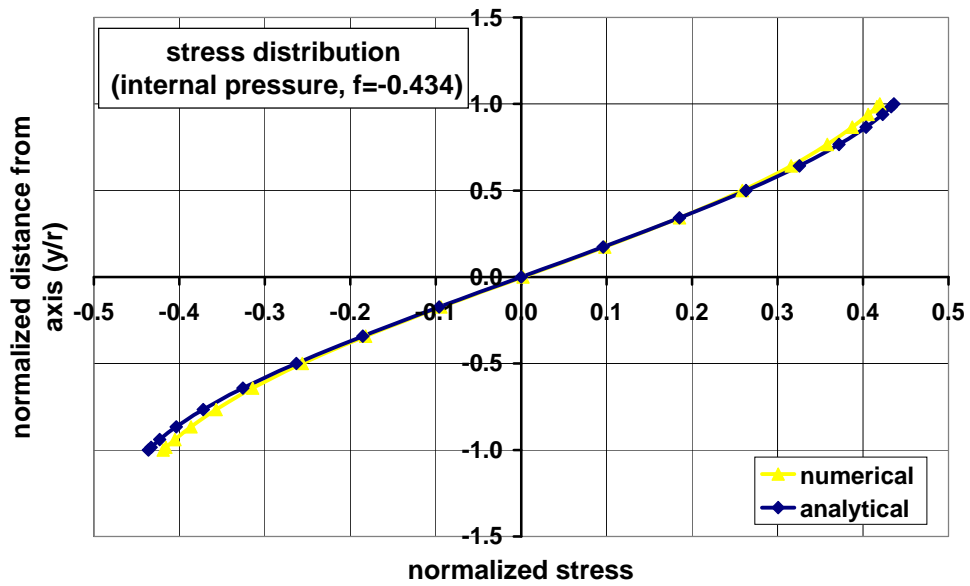
(b)

Fig. 42 Longitudinal stress distributions at the ovalization limit point for pressurized bending

($r/t = $**120,** $\kappa_{in} = $**0**)
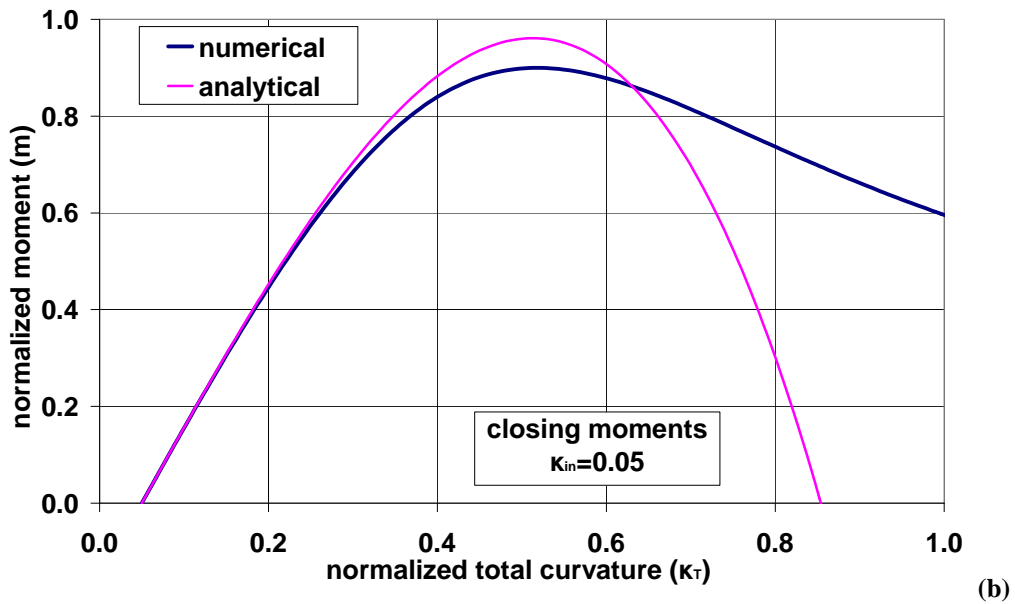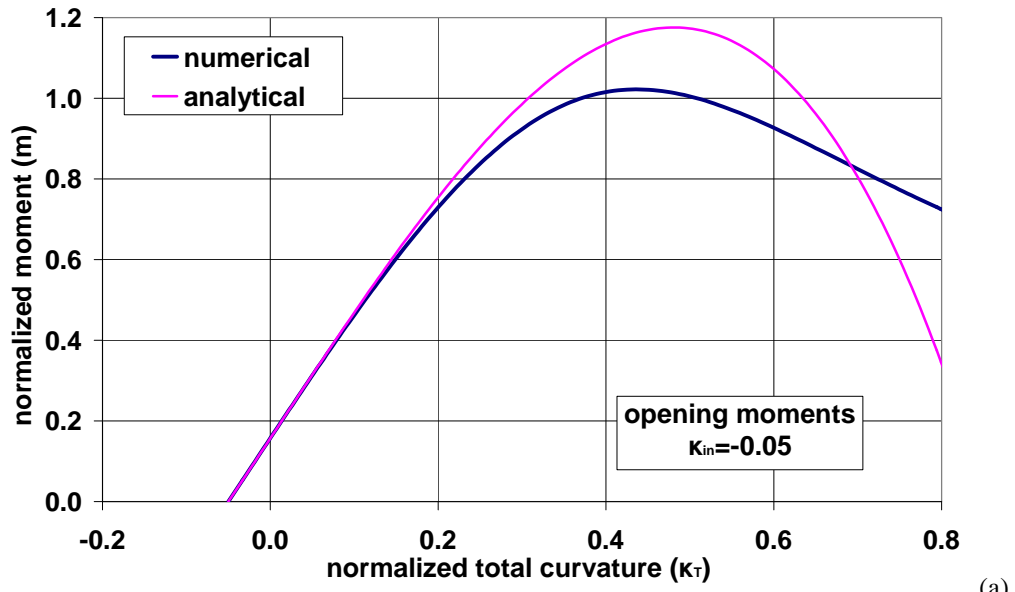
Fig. 43 $m - \kappa$ paths for slightly initially bent cylinders ($r/t = 120$, $f = 0$)

91
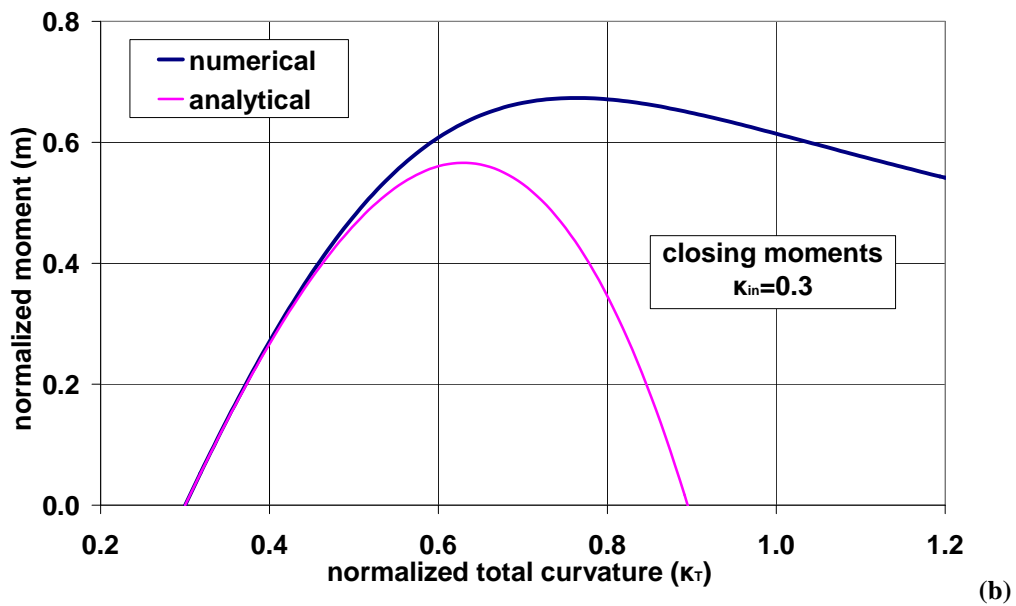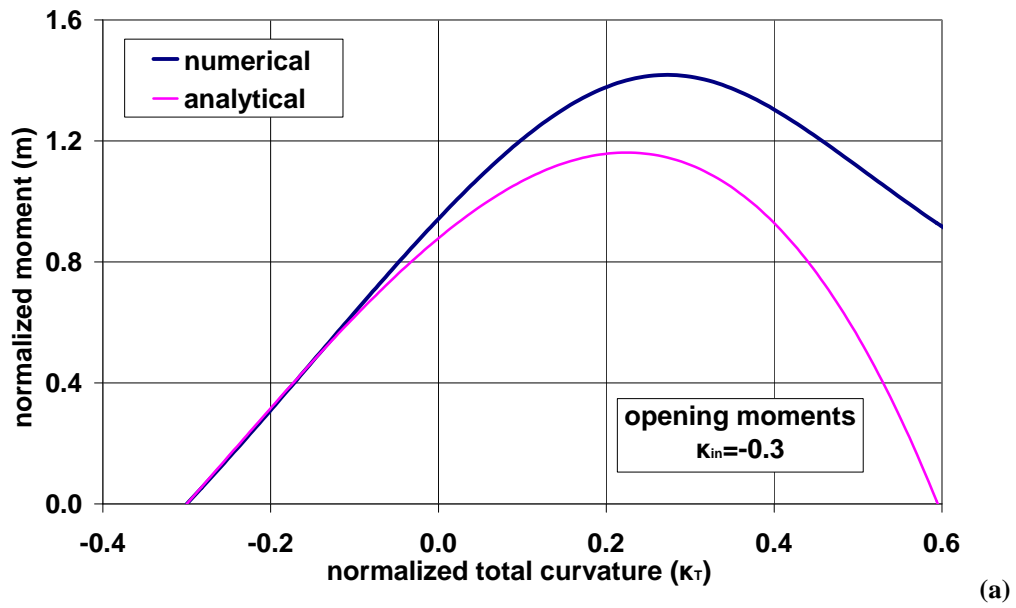
Fig. 44 Moment-curvature paths for initially bent cylinders;(a) opening moments, (b) closing moments (r/t =120, f =0)

92
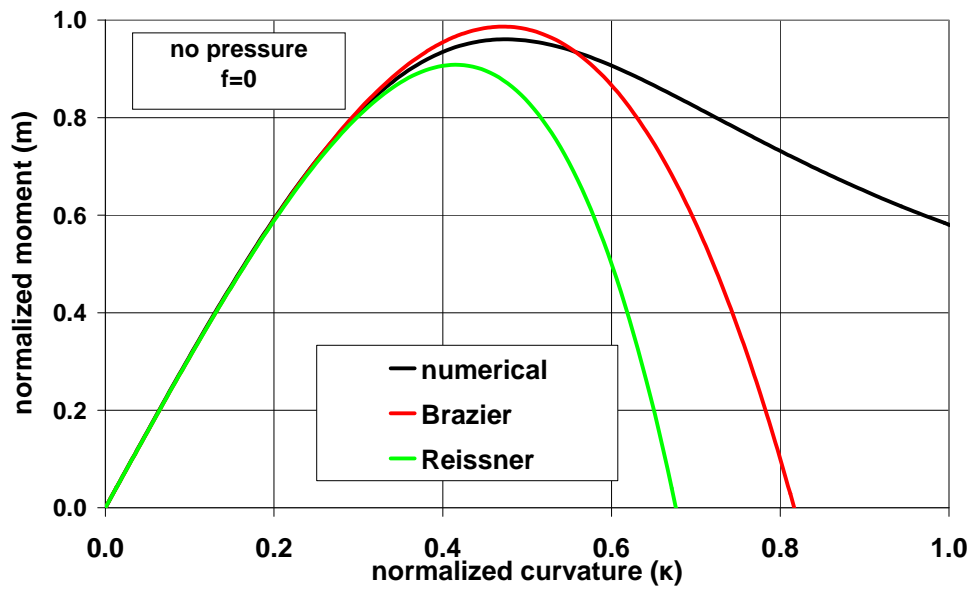
Fig. 45 Moment-curvature paths of initially straight cylinder; comparison of numerical results with the expressions presented by [62], [64] ($r/t = 120$, $\kappa_{in} = 0$, $f = 0$)
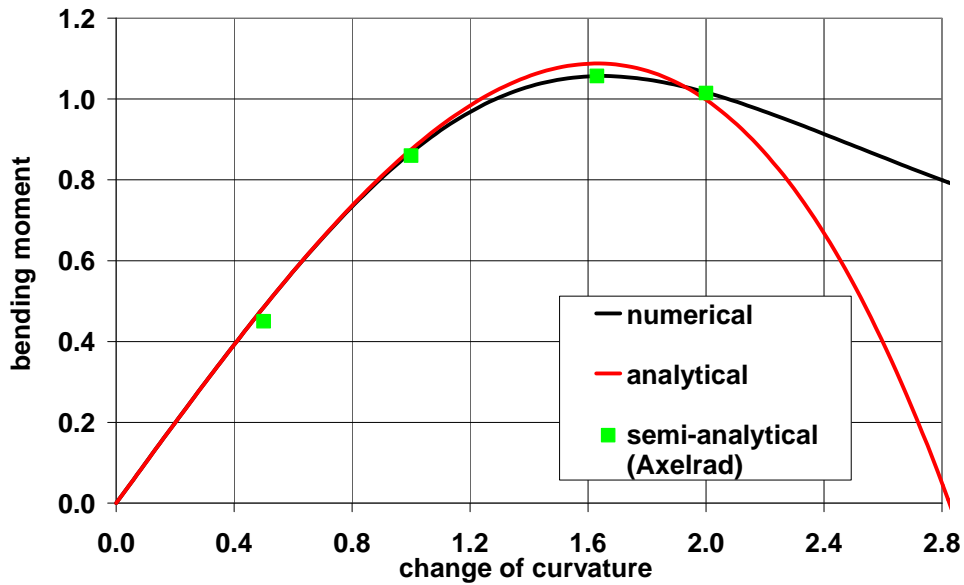
Fig. 46 Moment-curvature paths; comparison of numerical results with results given in [70]

93

Apart from the simplified analytical closed-form expression (5.54) and the numerical results, the comparison to a semi-analytical solution, presented by Axelrad [69], [70], is also depicted. In Fig. 46 the solution of Axelrad [69], [70] is compared with the numerical results and a very good agreement is found.

Using the above analytical and numerical results, the ovalization phenomenon is illustrated in a clear and elegant manner, and some observations can be drawn as follows:

Due to the nonlinear effects of ovalization, the cylinder becomes more flexible; the ''lever-arm' between total tension and total compression decreases so that bending resistance is reduced.

At a certain point, the above mechanism becomes dominant, and causes moment reduction, despite the fact that stresses continue to increase due to increasing curvature; at this point, the moment-curvature diagram exhibits a limit point and the corresponding limit moment is called ''ovalization moment'' or ''limit moment''; the corresponding curvature is called ovalization or limit curvature, respectively.

Using the normalization described by (5.3), (5.12), the normalized results are independent of the radius-to-thickness ratio r/t value.

5.2 Bifurcation Instability

Thin-walled elastic cylinders subjected to bending, apart from ovalization, fail because of buckling, a bifurcation-type of instability in the form of wrinkles (Fig. 47). In the present study, bifurcation on the ovalized primary path into a uniformly wrinkled state is described. It is important to note that buckling problem is associated with a highly nonlinear pre-buckling state, where the compression zone of the cylindrical shell wall has a double and opposite curvature in the longitudinal and in the hoop direction.
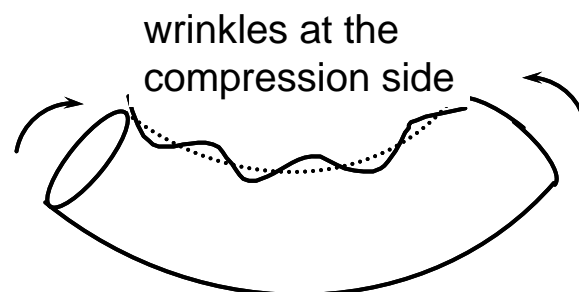
Fig. 47 Development of buckles at the compression side

94

5.2.1 Introduction

In an early publication, Seide and Weingarten [77] investigated bifurcation of initially straight circular cylinders under bending, assuming a linear (non-deformed) pre-buckling state, and a Ritz-type bifurcation solution in terms of trigonometric functions. Their numerical results indicated that the critical (buckling) moment M_{cr} of a cylinder corresponds to a nominal bending stress $\sigma_{cr} = M_{cr}/(\pi r^2 t)$, which is quite close to the buckling stress of the cylinder under uniform compression, thus the following equations may offer a good approximation for the buckling moment and the corresponding bending stress:

$$M_{cr} = 1.813 \frac{E t^2 r}{\sqrt{(1 - v^2)}} \tag{5.64}$$

$$\sigma_{cr} = \frac{E}{\sqrt{3(1 - v^2)}} \left(\frac{t}{r} \right) \tag{5.65}$$

Applying the normalization adopted in this study, equation (5.64) is written as:

$$m_{cr} = 1.831 \tag{5.66}$$

Kempner and Chen [52], considering the DMV shell equations and assuming a linear pre-buckling state, examined bifurcation instability of circular and oval cylinders under bending, in the presence of axial force. Furthermore, Koiter-Budiansky initial post-buckling theory was employed to investigate post-buckling behavior, in terms of trigonometric functions in the longitudinal direction, and an asymptotic approximation of the secondary path was obtained. The initial post-buckling analysis of [52] indicated a symmetric bifurcation point, and an initially unstable secondary equilibrium path.

However, it was shown in the previous sections that the maximum moment may not exceed the ovalization limit moment. Therefore, critical moment given by (5.66) is unreasonably high compared to $m_{Br} = 0.987$. This significant discrepancy is due to the fact that the bifurcation solutions in [52], [77] neglect cross-sectional ovalization on the pre-buckling state and, therefore, they predict an unrealistic value of buckling moment. The nonlinear effects of the ovalized pre-buckling configuration on bifurcation instability were considered by Axelrad [78]. Axelrad assumed that bifurcation occurs when the maximum compressive bending stress value reaches the critical stress value for a uniformly compressed circular tube of radius equal to the local radius of the ovalized shell at the "critical" point. By consequence, expression (5.65) may be applicable in a local sense, replacing the initial hoop curvature $1/r$ with the current circumferential curvature at the location where buckling initiates. Using the same concept, Emmerling [79] computed the bifurcation bending moment and curvature of initially oval cylinders under bending and pressure.

95

Stephens et al [80], using a finite-difference discretization of shell stability equations, investigated bifurcation of finite-length, initially-straight cylinders under bending, considering pre-buckling ovalization, as well as end-effects, and calculated bifurcation moments for different levels of pressure. The buckling moment of long cylinders was calculated close to Brazier ovalization limit moment ($m_{Br} = 0.987$). Fabian [41] examined buckling of thin elastic initially straight cylinders under bending and pressure (internal or external), through a perturbation of the nonlinear DMV shallow-shell equations. Results from the linearized (first-order) stability problem indicated that bifurcation occurs on the primary path before the ovalization limit point, regardless the level of pressure. Subsequently, using Koiter-Budiansky initial post-buckling theory, as adopted in [40] for nonlinear pre-buckling state, and assuming a trigonometric variation of stresses and displacements in the longitudinal direction, an asymptotic approximation of the post-buckling path was obtained.

Ju and Kyriakides [81] reported few numerical results for bending buckling of initially straight non-pressurized elastic cylinders (D/t =200) using the nonlinear Sander's shell equations and discretization in terms of trigonometric functions. The results verified that bifurcation occurs before ovalization point and it is attained on the primary path. In addition, an unstable post-buckling path was observed. In a recent paper Karamanos [75] examined instabilities of non-pressurized elastic cylindrical shells with r/t =120, with emphasis on the effects initial curvature. Furthermore, it was concluded that, depending on the initial curvature value and the direction of bending load, buckling may occur before or after the limit point of the primary ovalization path. It was also found that depending on the hoop curvature and longitudinal stress variation, buckling may occur at various locations around the cross-section. The investigation described in [75] is further enhanced herein, where imperfection sensitivity and initial post-buckling behavior issues are examined. In addition, aspects of bifurcation are illustrated using a simple mechanical model, which considers the ovalized pre-buckling configuration and pressure effects.

It is worth mentioning that in the recent years, this problem of elastic stability has received significant attention due to its applications in nanomechanics, more specifically, several attempts have been reported to apply shell stability concepts in order to simulate the structural stiffness and explain the buckling and post-buckling response of carbon nanotubes subjected to bending loads [82], [83], [84].

5.2.2 Numerical Results

The majority of the numerical results refer to initially circular cylinders, but some results of initially ovalized cylinders are depicted, as well. The values of moment, curvature, ovalization

96

and pressure are normalized as described by equations (5.3) and (5.12). Furthermore, the value of half-wave length L_{hw} is normalized by $L_0 = \sqrt{rt}\left[\pi^4 / 12\left(1-v^2\right)\right]^{1/4}$, so that $s = L_{hw} / L_0$, where L_0 is the half-wavelength of an axisymmetrically-deformed elastic cylinder subjected to uniform axial compression [43].

The results are obtained mainly by the implementation of the hypoelastic model (section 2.2.1). Some cases have also been re-examined using the hyperelastic model (section 2.2.2). The comparison resulted in the conclusion that for the case of bending there is negligible difference between the two constitutive models regarding buckling and post-buckling response.

A preliminary parametric study is conducted, to determine the number of cross-sectional parameters to be used. This investigation leads to the conclusion that a 16th degree expansion is adequate for the cases of interest, and determines the ''earliest'' bifurcation point upon primary ovalization path. Therefore, in Fig. 48 the effects of the degree of trigonometric expansion are illustrated. Regarding the number of integration points in the circumferential direction, 19 equally spaced integration points around the half-circumference are employed. Five and two Gauss points are used in the radial direction (through the thickness) and in the longitudinal direction, respectively.

In Fig. 49 the bending response of two non-pressurized initial straight cylinders with $r/t=20$ and 720 is illustrated, where bifurcation occurs before limit point ($\kappa_{cr} < \kappa_{ov}$). The path denoted as ''uniform ovalization'' corresponds to a cross-sectional bending analysis (two-dimensional analysis), as described in paragraph 5.3.
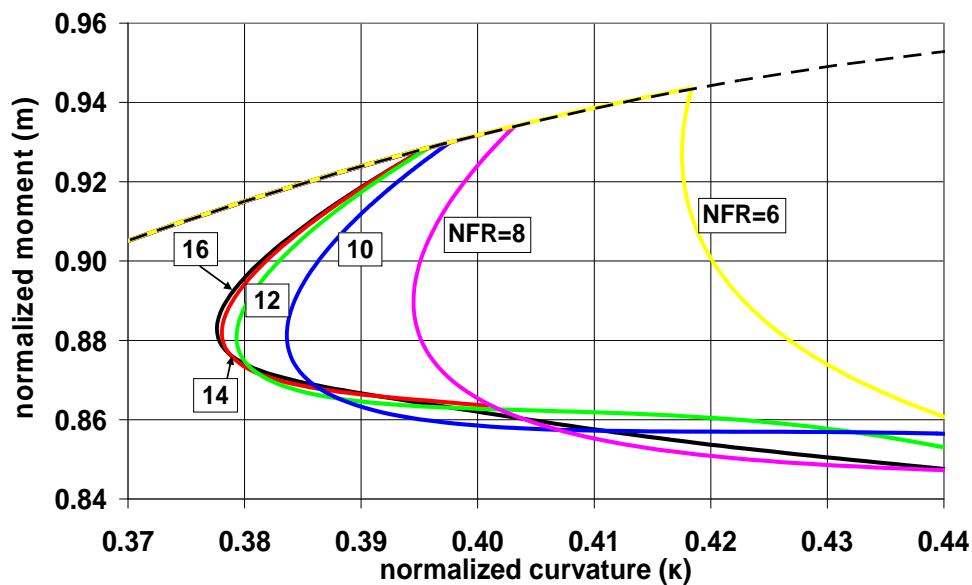
Fig. 48 Numerical results for the degree of trigonometric expansion used in equation (2.150)
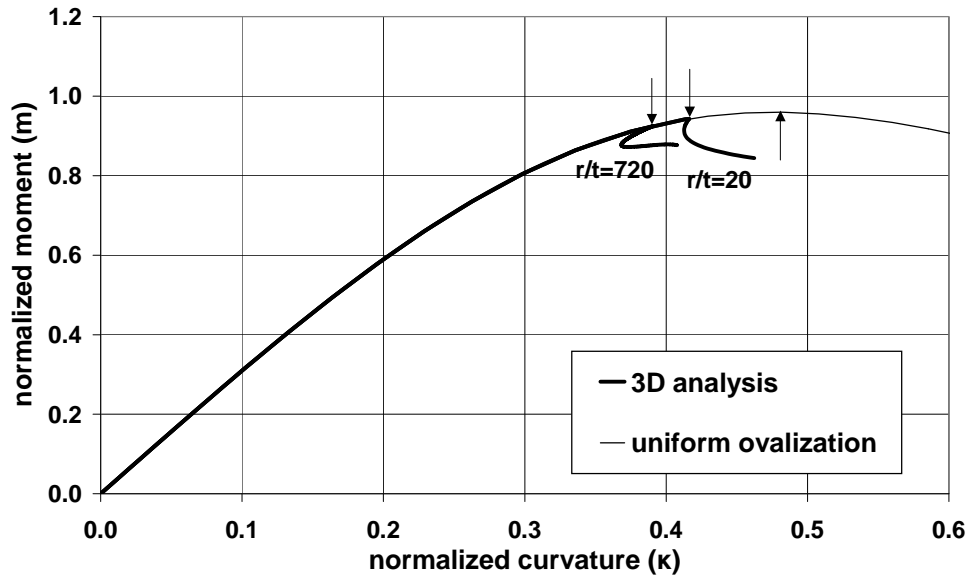
**Fig. 49 Numerical results of initially straight cylinders in the absence of pressure; arrows (↓)
denote bifurcation points, arrow (↑) denotes the limit point on the primary path**

Fig. 50 shows the dependence of the buckling point on the r/t ratio. Thin-walled cylinders (i.e. cylinders with large values of r/t ratio) buckle at lower values of curvature and moment (κ_{cr} and m_{cr}). In all cases, the initial post-buckling behavior is unstable, characterized by a ''snap-back'' immediately after bifurcation, which is reminiscent of the initial post-buckling path of circular or oval cylinders under uniform axial compression. The ''snap-back'' of the post-bifurcation path is sharper for thinner cylindrical shells (Fig. 50).

The pre-buckling (just prior to bifurcation) and post-buckling configurations of deformed cylinders for zero pressure (r/t=120) are depicted in Fig. 51. Note that for visualization purposes, the post-buckling displacements are magnified. Upon bifurcation, the compressed part of the tube surface exhibits a periodic wavy pattern. Another important observation concerns the ''local'' character of buckling in the circumferential direction. More specifically, buckling occurs within a zone around the critical point, referred to as buckling zone. In the present case (κ_{in}=0, f=0, ζ_0=0), the buckling zone is located in the vicinity of $\theta = \pi/2$ and its size depends on the cylinder's r/t ratio. Numerical calculations have shown that the size of the buckling zone decreases with increasing values of r/t ratio. In Fig. 51 the size of the buckling zone, defined as the distance between the two ''nodal points'' A and B is equal to $0.69\,r$ for a cylinder with r/t=120. Note that for cylinders with r/t=20 and r/t=720, the corresponding size is calculated equal to $1.22\,r$ and $0.52\,r$ respectively.

The shape of Fig. 51 also indicates that post-buckling configuration is associated with an inward post-buckling displacement of the ''buckling zone'', which is uniform along the

98

cylinder, and this is in agreement with experimental observations from uniformly compressed circular and oval cylinders.
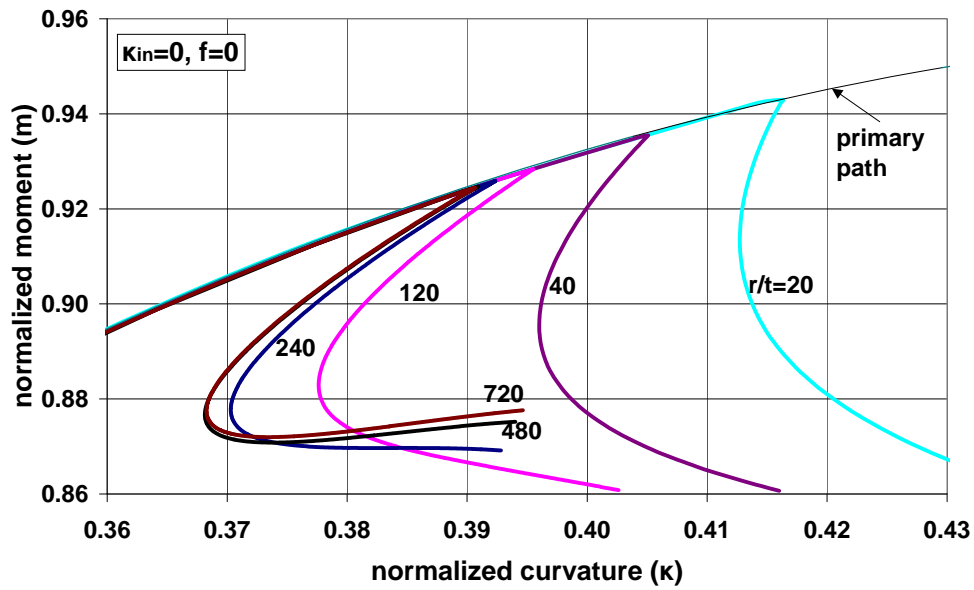
Fig. 50 Numerical results of $m-\kappa$ paths (f =0, κ_{in} =0); effect of r/t ratio on the bifurcation point
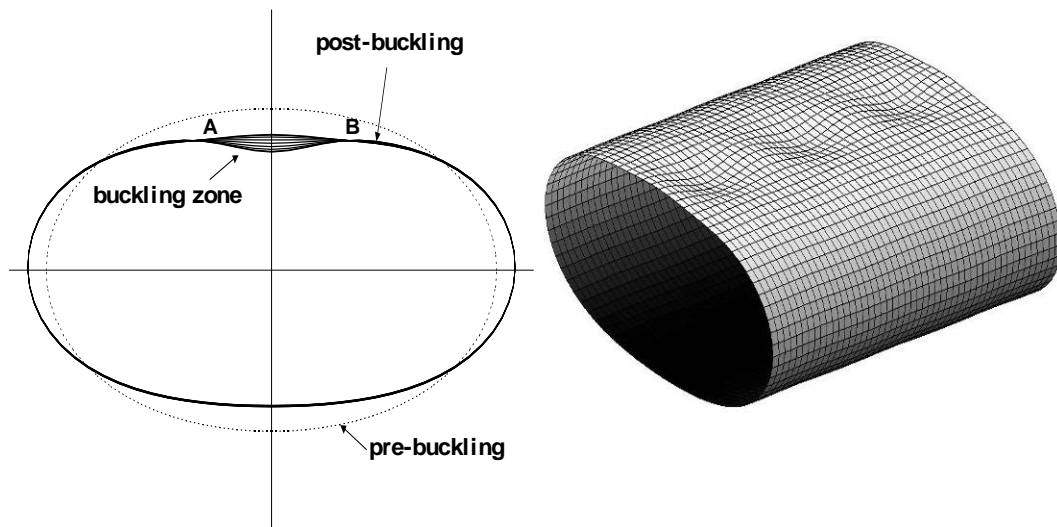
Fig. 51 Pre-buckling and post-buckling shapes of a cylinder cross-section (f =0, κ_{in} =0, r/t =120)

99

The response of initially straight cylinders with $r/t = 120$, for different pressure levels is shown in Fig. 52 and Fig. 53, where the thick lines corresponds to paths with buckling and the thin lines represent uniform ovalization response. In all cases, bifurcation occurs before a limit point is reached on the primary path, whereas the initial post-buckling path is unstable, exhibiting a ''snap-back'' immediately after bifurcation.
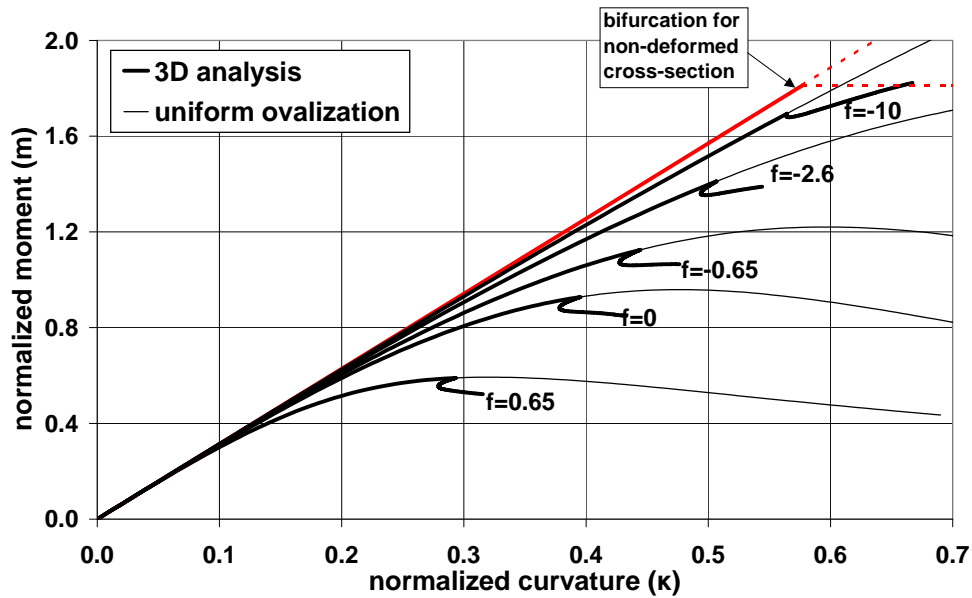
Fig. 52 Numerical results of $m - \kappa$ paths with respect to the level of pressure ($\kappa_{in} = 0$, $r/t = 120$)
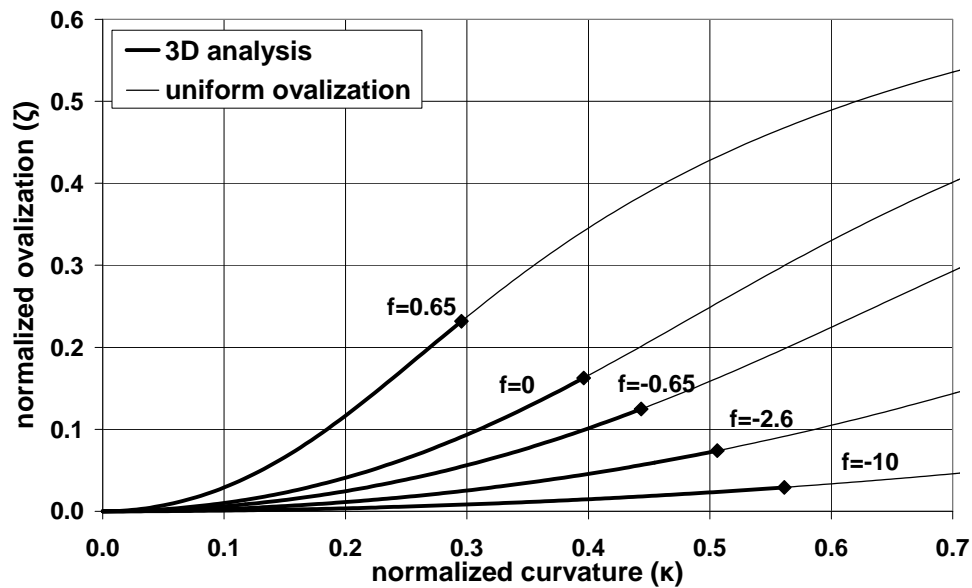
Fig. 53 Numerical results of $\zeta - \kappa$ paths with respect to the level of pressure; points (♦) define bifurcation points numerically calculated ($\kappa_{in} = 0$, $r/t = 120$)

100

The presence of external pressure results in a significant increase of cross-sectional ovalization (flattening) and causes a significant reduction of the buckling moment m_{cr} and the corresponding critical curvature κ_{cr}. On the other hand, internal pressure alleviates cross-sectional ovalization and increases both the m_{cr} and κ_{cr} values. For high levels of internal pressure (e.g. $f = -10$), ovalization is negligible, the pre-buckling $m - \kappa$ path is quasi-linear and the m_{cr} value approaches the buckling moment computed from (5.64) under the assumption of undeformed cylinder cross-section ($m_{cr} = 1.813$), as shown in Fig. 52. Moreover, Fig. 54 shows the variation of ovalization limit moment m_{ov} and critical moment m_{cr} with respect to the pressure level f.
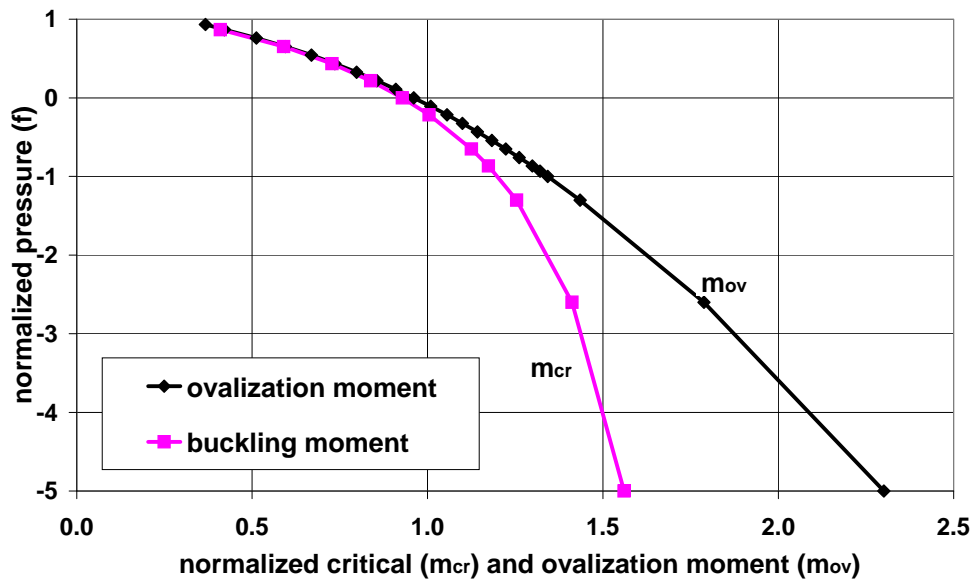
Fig. 54 Numerical results for the variation of critical and ovalization moments with respect to the pressure level f (κ_{in}=0, r/t=120)

101
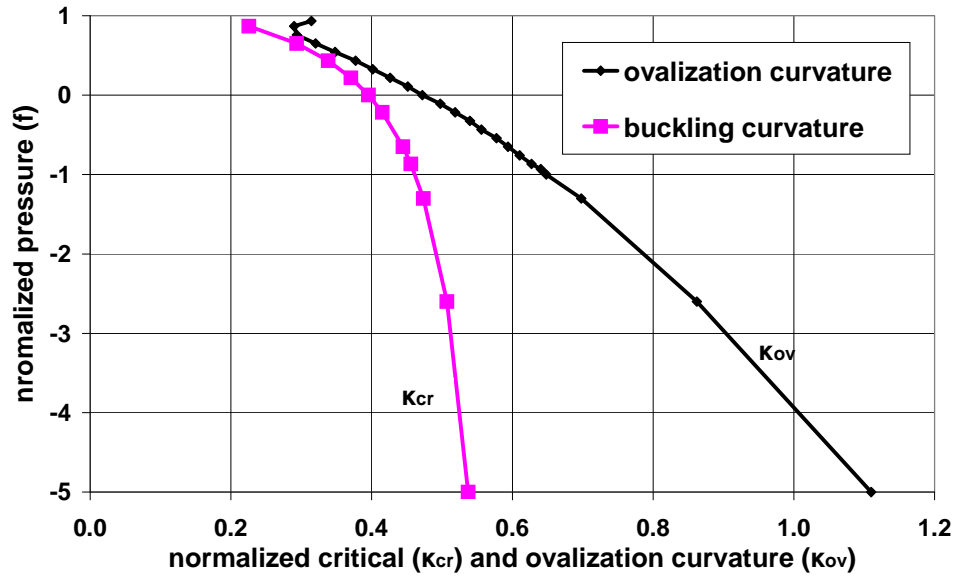
Fig. 55 Numerical results for the variation of critical and ovalization curvatures with respect to the pressure level f (κ_{in} =0, r/t =120)
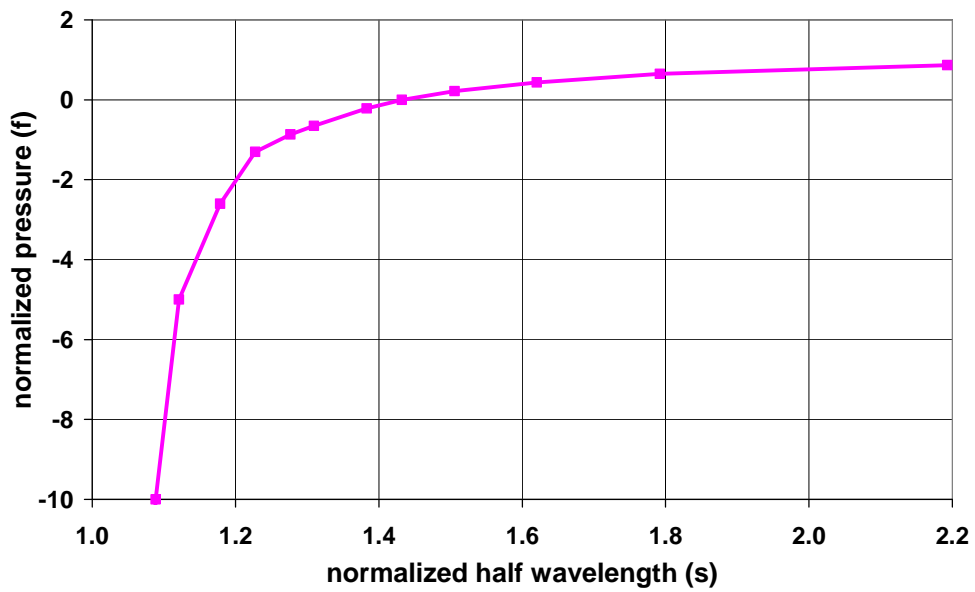
Fig. 56 Numerical results of the dependence of buckling half-wavelength on pressure level f

(κ_{in} =0, r/t =120)

102

Furthermore, the dependence of the corresponding normalized curvature values (κ_{ov} and κ_{cr}) on the pressure level f is depicted in Fig. 55, and indicates that, with increasing external pressure, the bifurcation point approaches the ovalization limit point.

The dependence of buckling half-wavelength on the level of pressure is plotted in Fig. 56. The value of s for large values of internal pressure ($f \rightarrow -\infty$) approaches unity ($s \rightarrow 1$), which means that for high internal pressure the buckling wavelength becomes equal to the axisymmetric-buckling wavelength of a similar elastic cylinder subjected to uniform axial compression. On the other hand, for external pressure values close to p_{cr} ($f \rightarrow 1$) the half wavelength value approaches infinity ($s \rightarrow -\infty$). In this case, the ovalization mechanism, accentuated by the presence of high external pressure, governs cylinder's response.

In Fig. 57, the elastic deformation energy of the cylinder per unit length is plotted in terms of curvature for an initially non-pressurized straight cylinder ($f = 0$, $\kappa_{in} = 0$). The energy is normalized by the product of M_e and k_N. The diagram is initially monotonically increasing and exhibits a negative 'jump' at the bifurcation curvature. This discontinuity is more pronounced for a thin-walled cylinder ($r/t = 720$), shown in the detail of Fig. 57. Beyond this point, it continues to increase monotonically. The reason for this discontinuity is the ''snap-back'' of the initial post-bifurcation path immediately after buckling. It is noted that experimental measurements, as well as molecular dynamics simulations in elastic carbon nanotubes, have shown a similar ''kink'' on the elastic deformation energy diagram [84].

The bending response of circular initially slightly bent cylinders ($\kappa_{in} = \pm 0.20$) in terms of the pressure level (f) is shown in Fig. 58-Fig. 61. Negative and positive values of κ_{in} correspond to opening and closing bending moments respectively (Fig. 35). For these values of initial curvature, buckling occurs before the ovalization limit moment, regardless the level of pressure, and the post-buckling path is also characterized by a ''snap-back''. The numerical calculations also show that the ''buckling zone'' is located around $\theta = \pi/2$ for both closing and opening moments. In Fig. 58 and Fig. 60 it is indicated that the presence of external pressure accentuates cross-sectional ovalization and therefore, reduces the moment capacity m_{cr} and the corresponding critical curvature κ_{cr}. On the other hand, there is a beneficial effect of internal pressure on the m_{cr} and κ_{cr} values, due to the significant reduction of cross-sectional ovalization, as shown in Fig. 59 and Fig. 61.
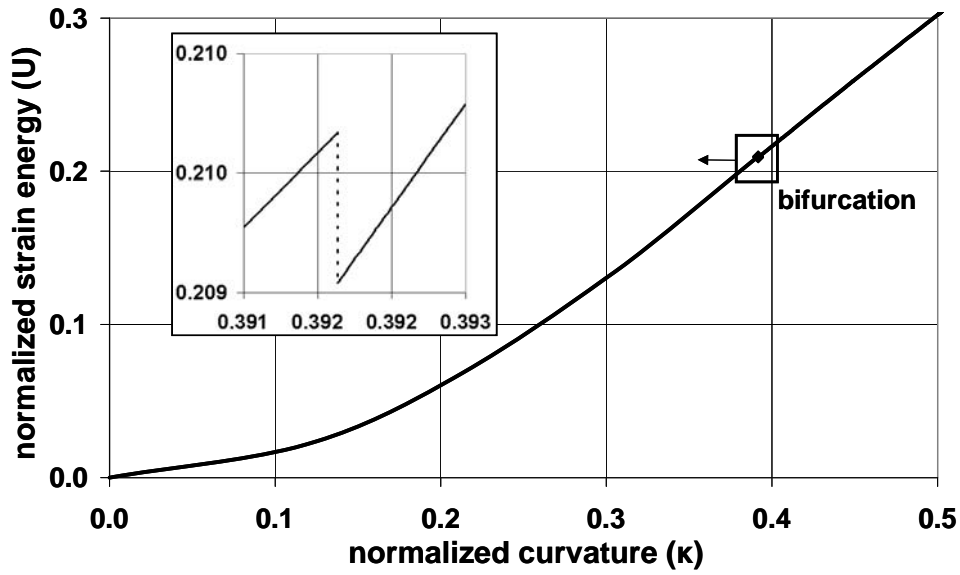
Fig. 57 Numerical results of the normalized strain energy curve in terms of applied curvature; point on the curve (♦) denotes bifurcation (r/t =720, κ_{in} =0, f =0)
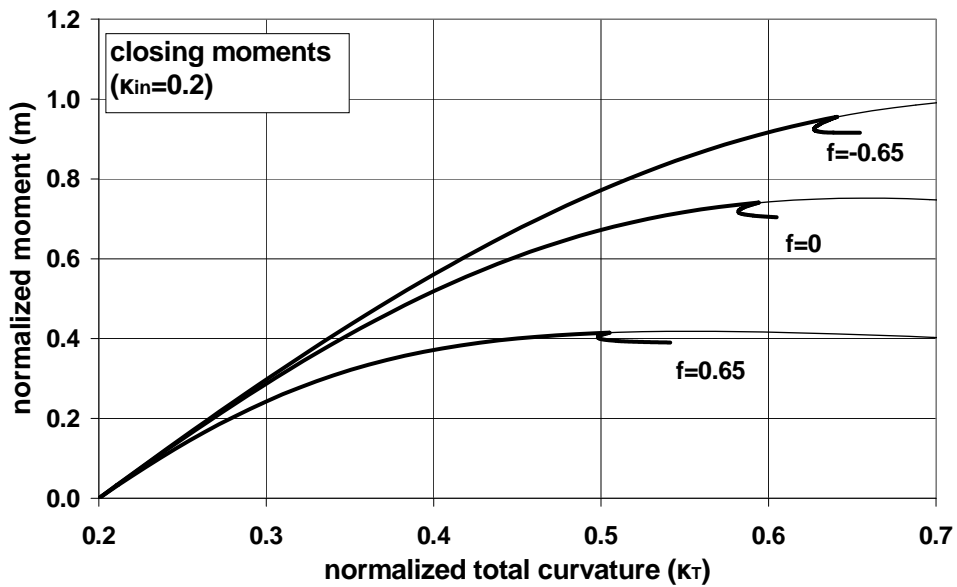

Fig. 58 Response of an initially bent cylinder for closing moments for three different levels of pressure (r/t =120, κ_{in} =0.2); thick lines corressonds to paths with buckling and thin lines to uniform ovalization paths respectively (numerical results)
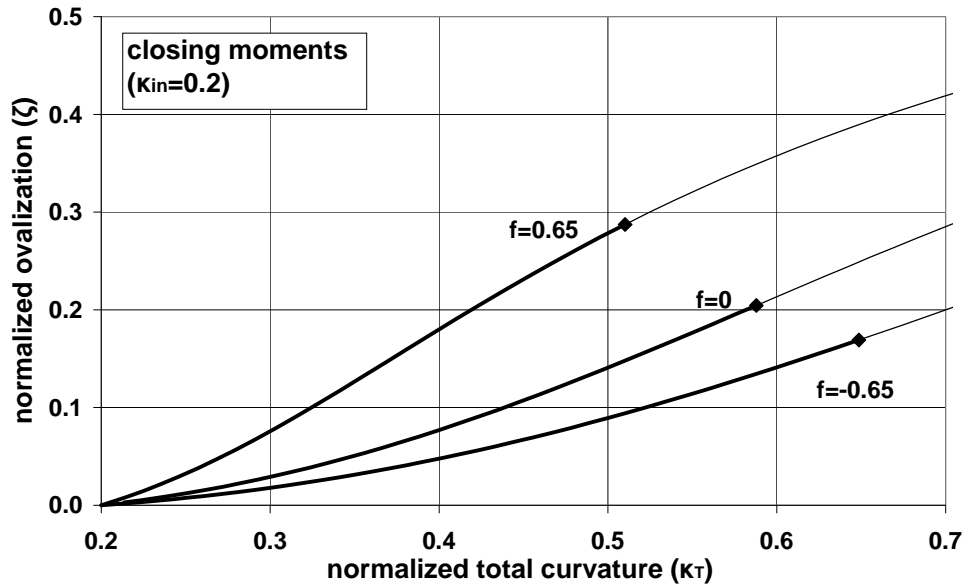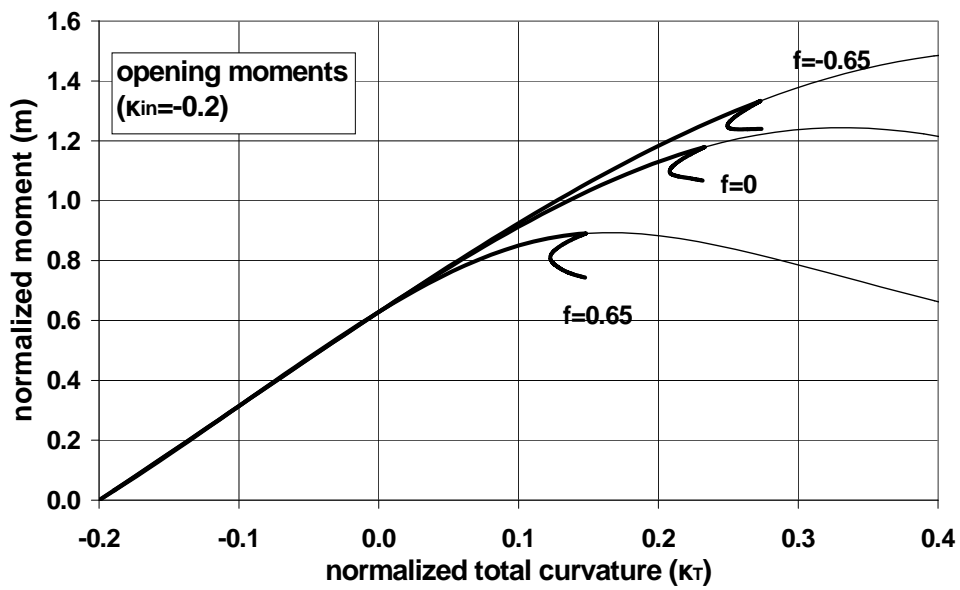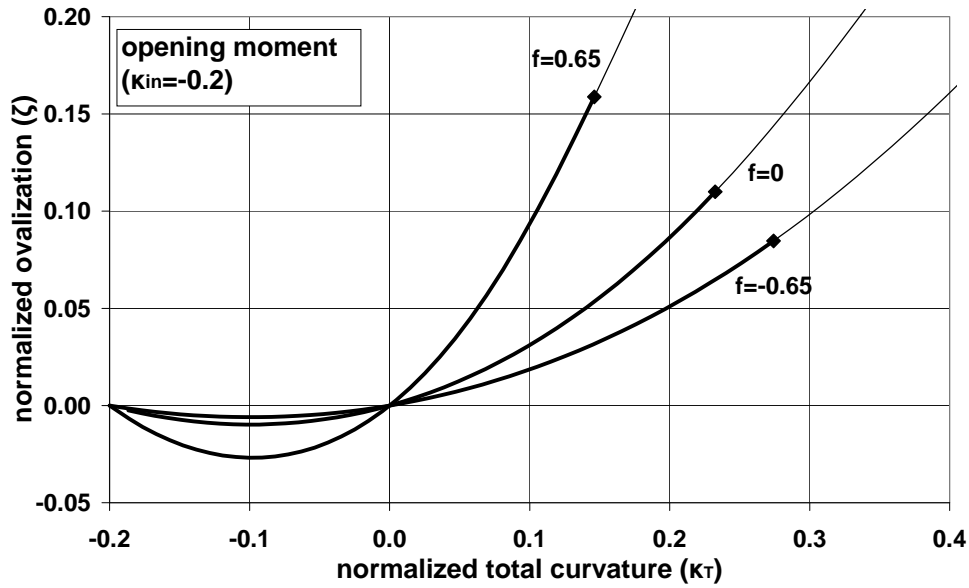
Fig. 59 Ovalization of an initially bent cylinder for closing moments for three different levels of pressure (r/t =120, κ_{in} =0.2); thick lines correspond to paths with buckling and thin lines to uniform ovalization paths respectively and points (♦) denote bifurcation (numerical results)

Fig. 60 Response of an initially bent cylinder under opening moments for three different levels of pressure (r/t =120, κ_{in} =-0.2); thick lines correspond to paths with buckling and thin lines to uniform ovalization paths, respectively (numerical results)

105

Fig. 61 Ovalization of an initially bent cylinder for opening moments for three different levels of pressure (r/t =120, κ_{in} =-0.2); thick lines correspond to paths with buckling and thin lines to uniform ovalization paths, respectively, whereas points (♦) denote bifurcation (numerical results)

It is noted that, in the case of opening moments (Fig. 60), the cylinder initially exhibits reverse ovalization (negative values of ζ), so that the diameter on the plane of bending lengthens and the other principal diameter shortens ('bulging' ovalization) until the total curvature of the cylinder becomes about half the initial curvature value ($\kappa_T \simeq -|\kappa_{in}|/2$). Subsequently, ''bulging'' ovalization decreases and, beyond the curvature where the cylinder becomes straight ($\kappa_T = \kappa + \kappa_{in} = 0$), cross-sectional ''flattening'' occurs until buckling. The fact that all $\kappa - \zeta$ curves pass through the origin ($\kappa_T = \zeta = 0$) can be verified from the simplified ovalization-curvature expression (5.43).

The response of circular cylinders with more pronounced initial curvature (κ_{in} =1.030) under closing bending moments is shown in Fig. 62 and Fig. 63. The numerical results indicate that bifurcation occurs well beyond limit point instability, for three different pressure levels, so that ovalization instability governs cylinder's response. In addition, the secondary path under external pressure (f =0.65) follows closely the primary equilibrium path. A closer view of the secondary path for f =0.65 around bifurcation is shown in the detail of Fig. 62. The ovalization response of these pressurized cylinders (κ_{in} =1.030), plotted in Fig. 63, indicates that bucking occurs at large values of cross-sectional flattening ($\zeta_{cr} > 0.35$). The ''flattened'' cross-sectional shapes of the buckled cylinder configurations (Fig. 64), show that the periodic wavy pattern

106

also occurs within a small portion of the cylinder circumference, verifying the ''local'' character of buckling also observed in Fig. 51. Nevertheless, the $\theta = \pi/2$ location may not be critical in all cases. In the absence of pressure (f =0) the critical point is located at about $\theta \approx \pi/3$ (Fig. 64a and Fig. 64b). In the presence of external pressure (f =0.65) the numerical results indicated that the buckling zone is located at the ''extrados'' of the cross-section ($\theta = -\pi/2$), as shown in Fig. 64c. This is explained by the compressive longitudinal stresses at $\theta = -\pi/2$, depicted in the detail of Fig. 65, in conjunction with the flat shape of the ovalized cross-section at this location.
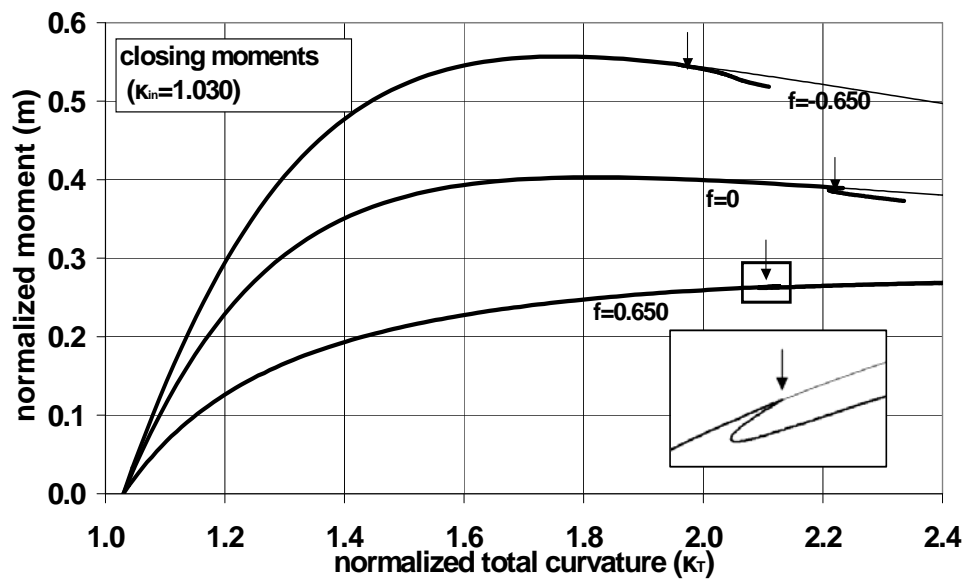
Fig. 62 Numerical results of the response of an initially bent cylinder under closing moments (κ_{in} =1.030) for three different levels of pressure f (r/t =120); thick lines correspond to paths with buckling and thin lines to uniform ovalization paths respectively whereas arrows (↓) denote bifurcation

107
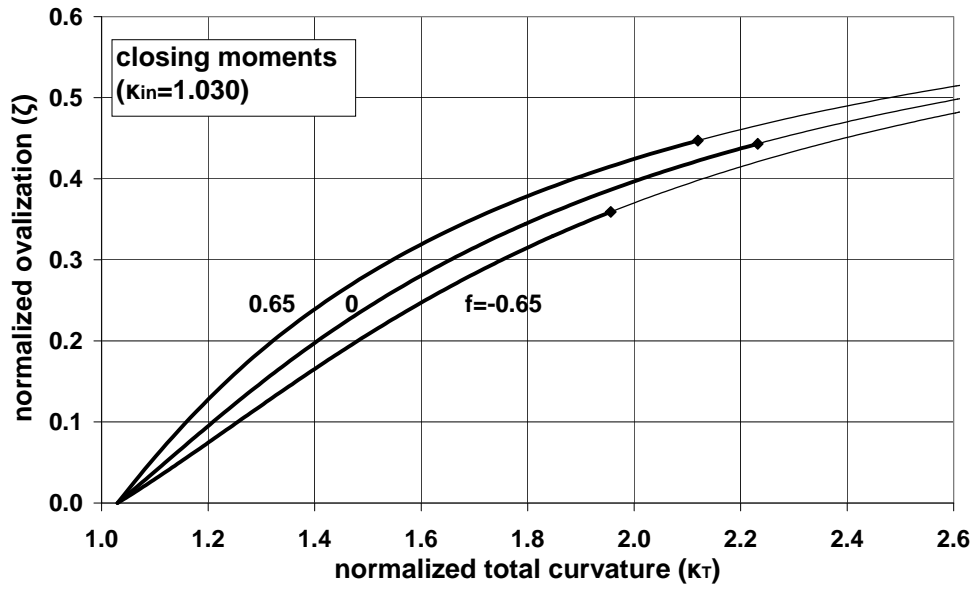
Fig. 63 Ovalization analysis of initially bent cylinders (κ_{in} =1.030); thick lines correspond to buckling paths and thin lines to uniform ovalization paths, points (♦) denote bifurcation
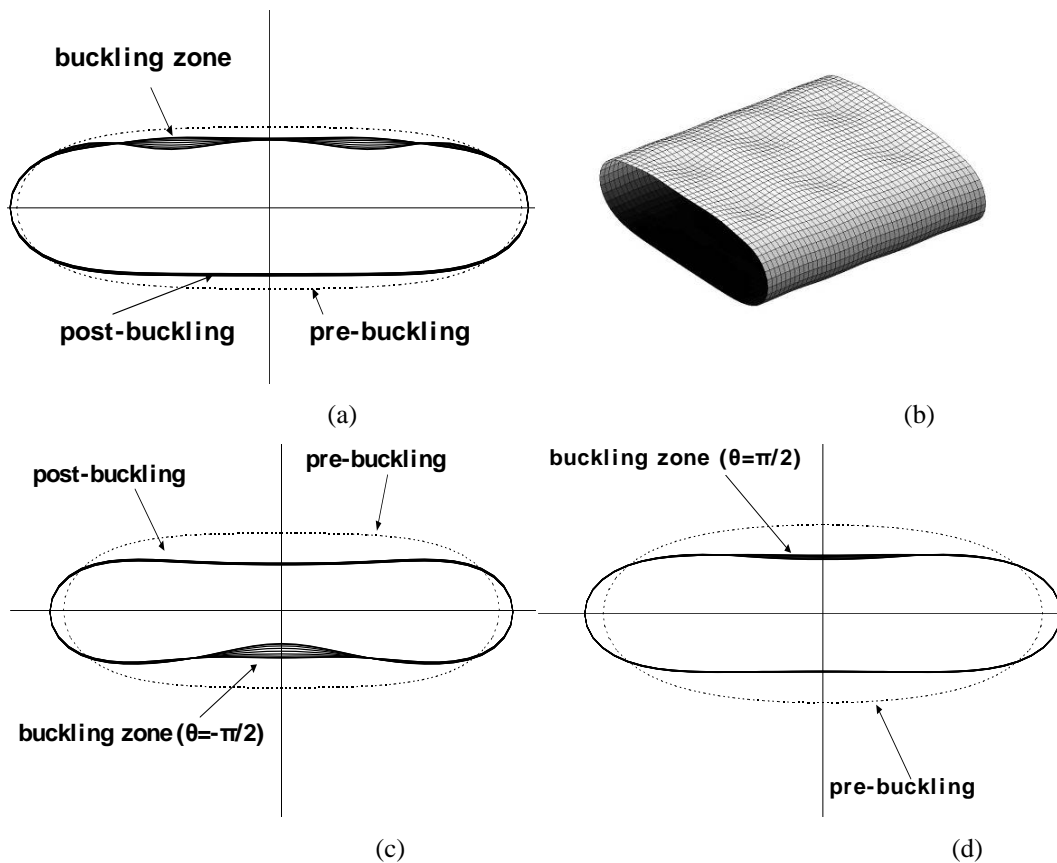

(a)

(b)

(c)

(d)

Fig. 64 Pre-buckling and post-buckling shapes (κ_{in} =1.030, r/t =120); (a) and (b) f =0, critical point at $\theta = \pi/3$; (c) f =0.65, critical point at $\theta = -\pi/2$; (d) f =-0.65, critical point at $\theta = \pi/2$
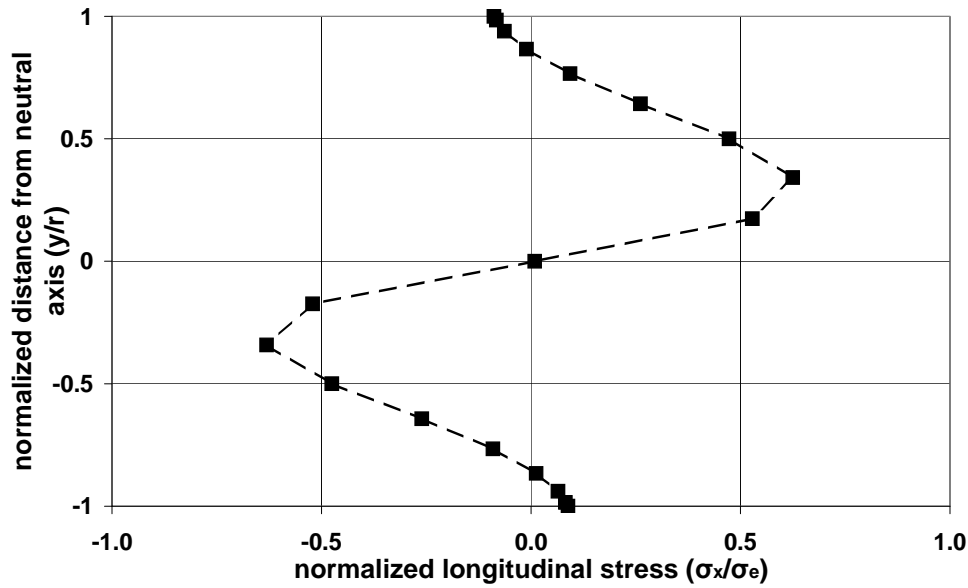
108

Fig. 65 Finite element results of the variation of longitudinal stresses at cross-section of an initially curved cylinder (r/t =120, κ_{in} =1.030, f =0.65).

The response of an initially curved cylinder subjected to opening bending moments (κ_{in} =-1.374) is shown in Fig. 66 for different pressure levels. In all three cases buckling occurs before a limit point is reached. Furthermore, buckling occurs before the cylinder becomes straight (κ_T <0), as also shown in Fig. 67, and the corresponding post-buckling cylinder response exhibits a very sharp ''snap-back''. The buckled cylinder cross-sections within a half-wavelength are depicted in Fig. 68, and show that for the three different pressure levels considered, the buckling zone is no longer in the vicinity of $\theta=\pi/2$. Also note that the externally pressurized case corresponds to the most pronounced bulging ovalization.

Finally, the effects of initial cross-sectional ovality on the buckling moment are examined, considering a relatively small stress-free doubly-symmetric out-of-roundness of the cylinder cross-section, which is assumed constant along the cylinder. Expressions (5.57) correspond to a ''first-order inextentional'' ovalization deformation ($w_0(\theta)+v_0{}'(\theta)=0$) and the ovalization parameter has an initial value ζ_0 equal to a_0/r . The effects of such an imperfection on the bending response of an initially straight cylinder (κ_{in} =0) are shown in Fig. 69 for zero pressure (f =0), and for relatively small initial ovality $|\zeta_0| \le 0.1$. Positive values of initial ovalization correspond to ''initial flattening'' of the cylinder cross-section, whereas negative values refer to ''initial bulging''. The results of Fig. 70a demonstrate that the orientation of the initial out-of-roundness may be quite important, especially in the presence of external pressure (f >0). In particular, reverse initial ovality, combined with external pressure, results in a post-buckling

path that follows closely the primary equilibrium path (Fig. 70b). In Fig. 70, all the $m - \kappa$ curves, regardless the pressure level, pass through a common point A ($m_A = 0.945$ and $\kappa_A = 0.306$) located before the bifurcation point. Furthermore, at this value of curvature the corresponding cross-sectional ovalization is zero (point A in Fig. 71). The above values of m_A and κ_A can be also be verified by the simplified analytical ovalization solution presented above; requiring $\zeta + \zeta_0 = 0$ and $\kappa_{in} = 0$ in (5.60) and (5.61), one readily obtains $\kappa = \left|\zeta_0\right|^{1/2}$ and $m = \pi \left|\zeta_0\right|^{1/2}$, and that for $\zeta_0 = -0.1$ those values are very close to m_A and κ_A.

(a)

(b)

110

(c)
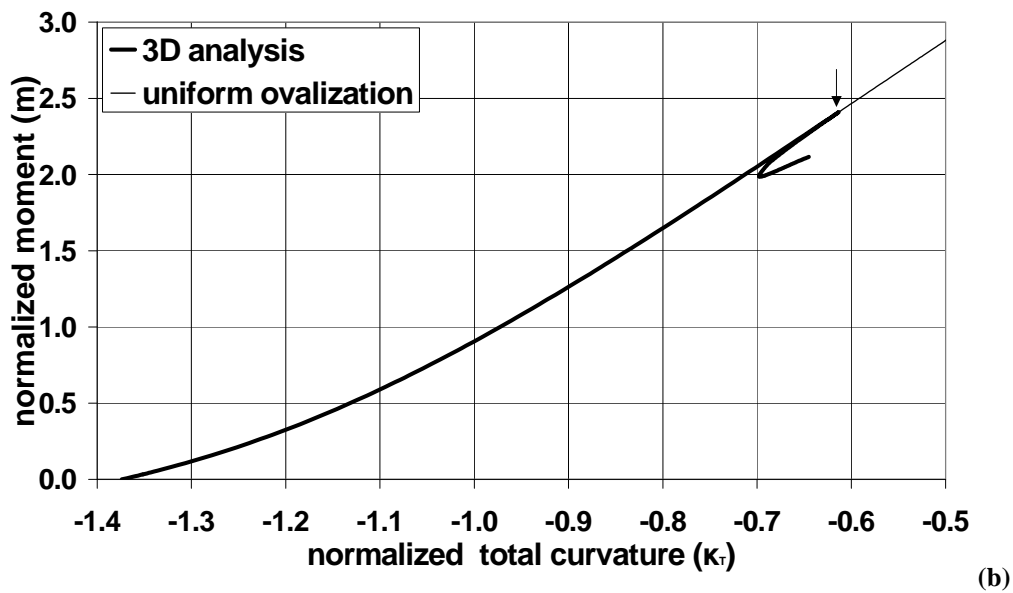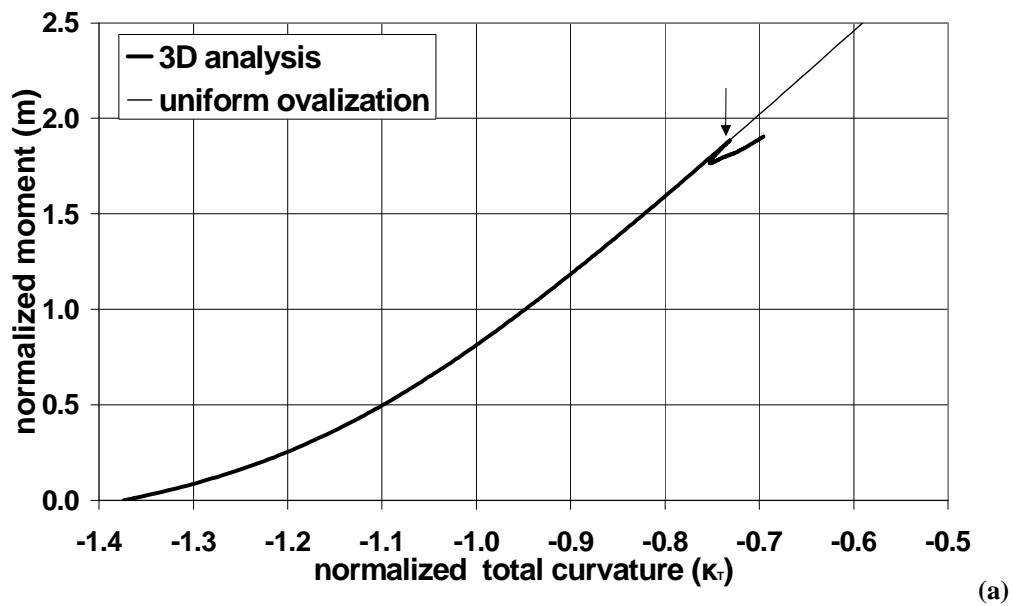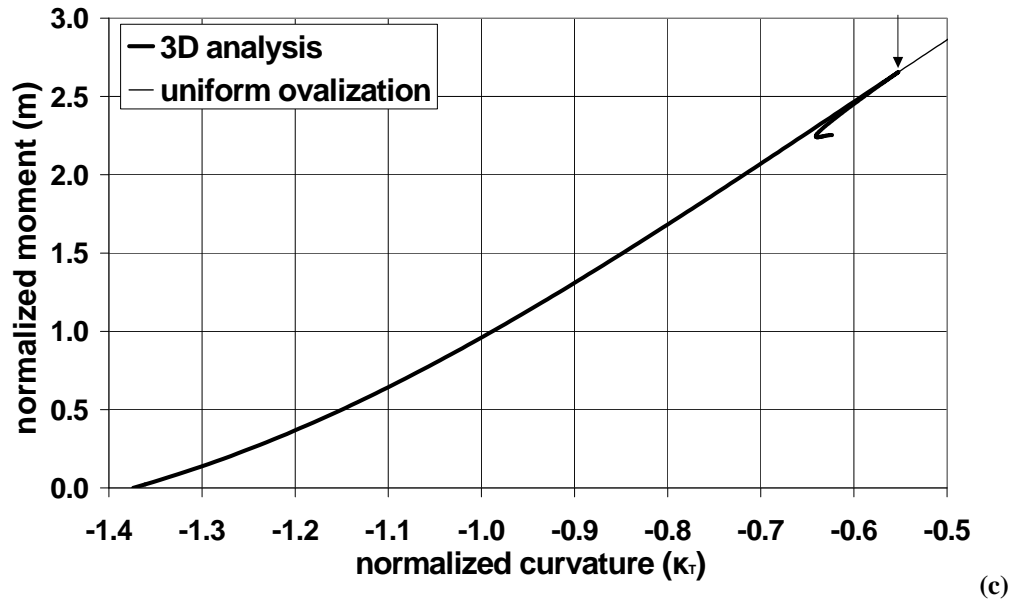
Fig. 66 Finite element results of the response of initially curved cylinders (κ_{in} =-1.374) for reverse bending and for three different pressure levels f in which arrows (↓) denote bifurcation; (a) f =0.5, (b) f =0, (c) f =-0.5 (r/t =120)
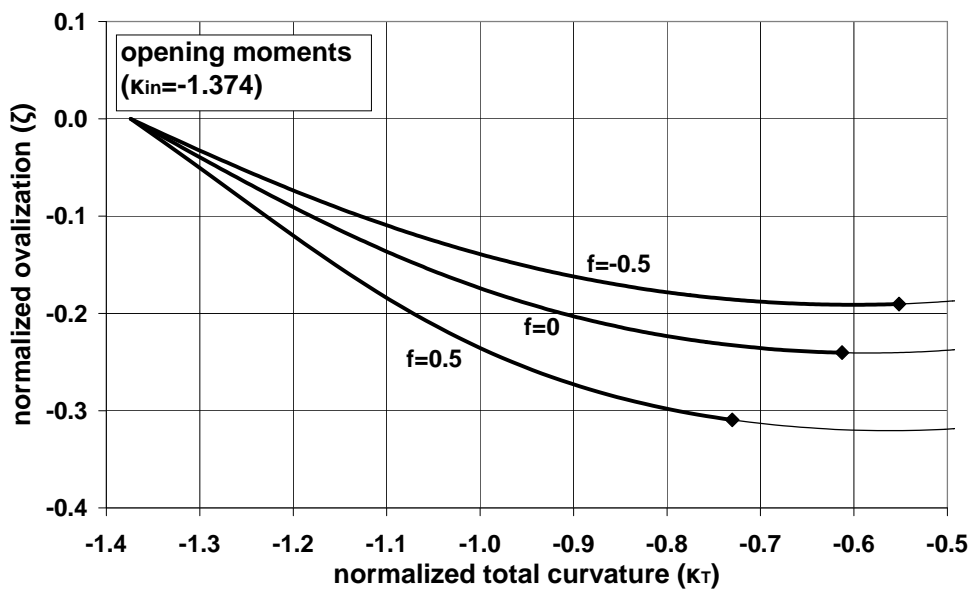

Fig. 67 Finite element results of ovalization analysis for an initially bent cylinder (κ_{in} =-1.374); thick lines correspond to paths with buckling and thin lines to uniform ovalization paths respectively (r/t =120).

111
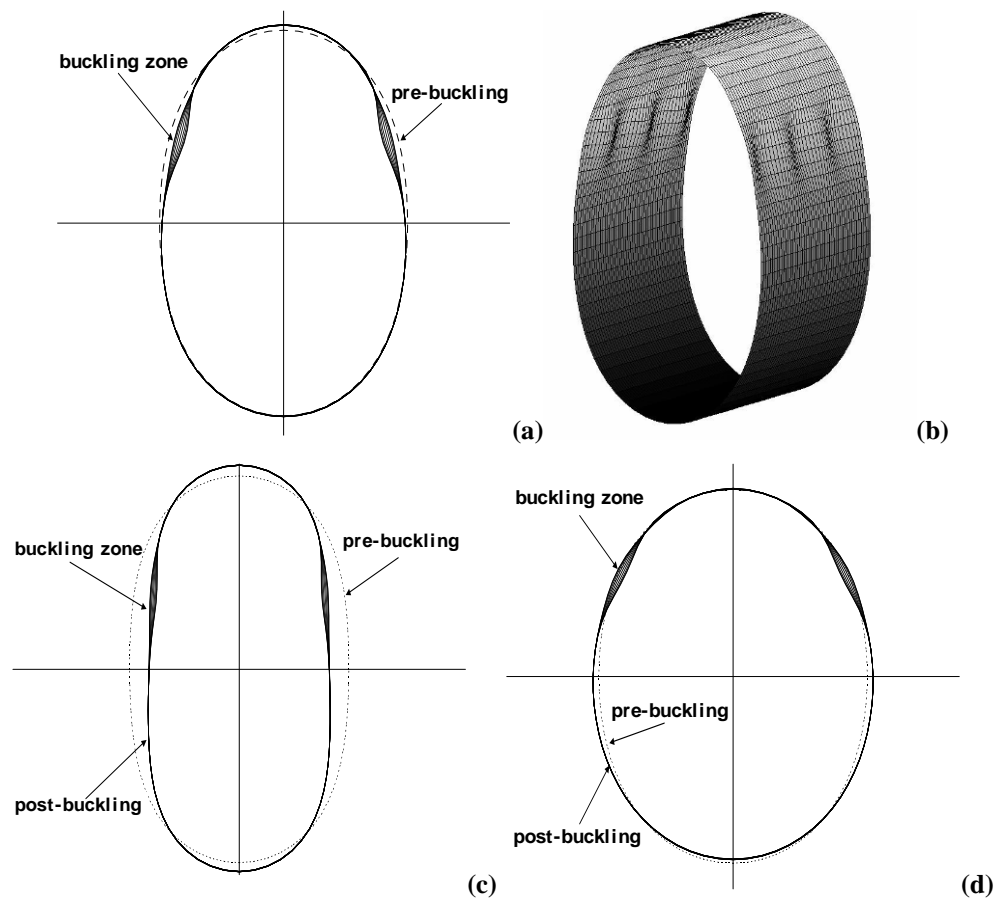
Fig. 68 Pre-buckling and post-buckling shapes; (a) and (b) f =0, critical point at $\theta \approx \pi/6$, **(c)** f =0.5, critical point at $\theta \approx \pi/6$, **(d)** f =-0.5, critical point at $\theta \approx 40^0$; (κ_{in} =-1.374, r/t =120).
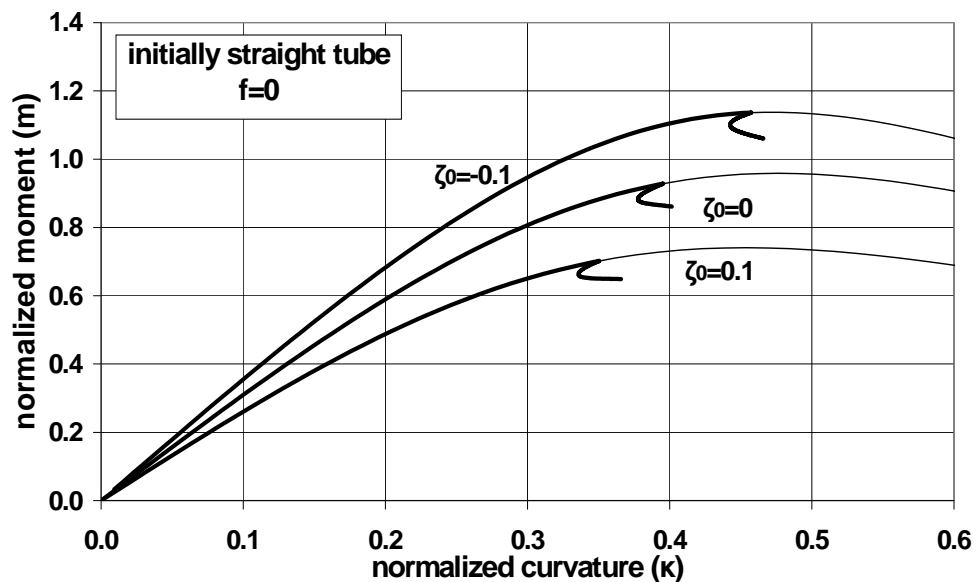

Fig. 69 Numerical results in initially ovalized cylinders; thick lines correspond to paths with buckling and thin lines to uniform ovalization paths respectively (r/t =120, κ_{in} =0, f =0)
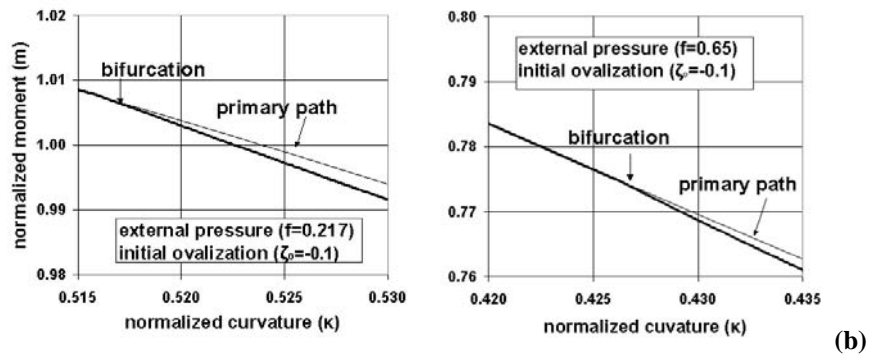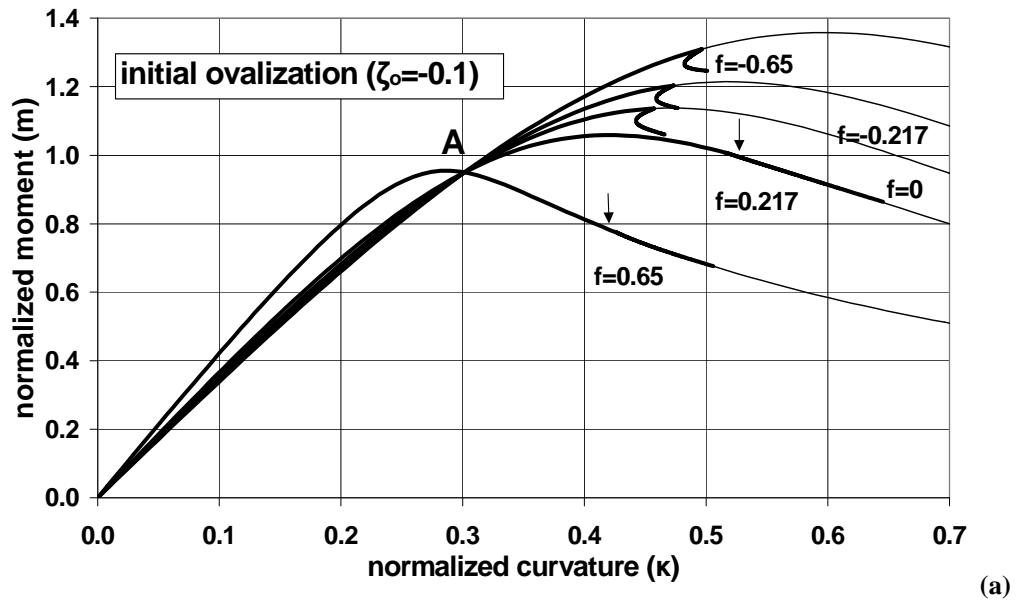
112

Fig. 70 Numerical results of initially ''bulged'' cylinders (ζ_0 =-0.1); thick lines correspond to buckling paths and thin lines to uniform ovalization paths, arrows (↓) denote bifurcation(r/t =120)
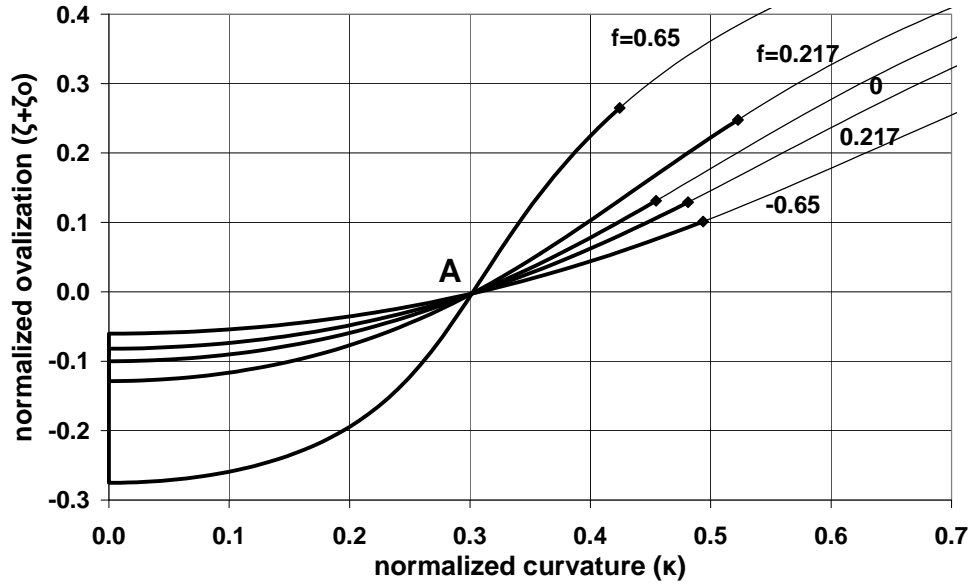
113

Fig. 71 Numerical results of initially ''bulged'' cylinders (ζ_0 =-0.1); thick lines correspond to buckling paths and thin lines to uniform ovalization paths (r/t =120, κ_{in} =0).

5.2.3 Simplified Analytical Solution

Simplified bifurcation analysis for shells have been proposed in previous works (e.g. [78], [79]), based on the assumption that buckling is fully determined by the stress and deformation inside the zone of the initial buckle, and that stresses and curvatures inside that zone are constant. Under this assumption, an expression similar to (5.65) can be obtained, which governs shell instability at each point around the circumference. The local character of buckling around the cross-section, shown in Fig. 51, Fig. 64 and Fig. 68, provides good evidence for the validity of the above assumption. In the present work, this concept is outlined, and it is further enhanced to obtain closed-form analytical expressions for the bifurcation curvature κ_{cr} and moment m_{cr}, as well as for the corresponding buckling wavelength ($s = L_{hw}/L_0$).

<u>Linearized Shell Equations</u>

Local coordinates *X* and *Y* are defined on the buckling zone area, denoting the distances from the center of the buckling zone, in the longitudinal and the hoop direction respectively (Fig. 72). Starting from the nonlinear DMV equations

$$\frac{Et^3}{12(1-v^2)}\nabla^4 W - \frac{1}{R_x}N_x - \frac{1}{R_y}N_y + 2N_{xy}\frac{\partial^2 W}{\partial X \partial Y} = p(X,Y) \qquad (5.67)$$

$$\frac{1}{Et}\nabla^4 F - \frac{1}{R_x}\left(\frac{\partial^2 W}{\partial Y^2}\right) - \frac{1}{R_y}\left(\frac{\partial^2 W}{\partial X^2}\right) - \frac{\partial^2 W}{\partial X^2}\frac{\partial^2 W}{\partial Y^2} - \left(\frac{\partial^2 W}{\partial X \partial Y}\right)^2 = 0 \qquad (5.68)$$

114

where W and F are the displacement and stress functions respectively, N_x, N_y, N_{xy} are the membrane stress resultants (equal to the second derivatives of the stress function F), $1/R_x$, $1/R_y$ are the local curvatures of the deformed cylinder, and following the linearization procedure described in [85], the linearized form of Equations (5.67) and (5.68) is obtained as follows

$$
\begin{aligned}
\big[(\partial_x{}^2 + \partial_y{}^2)^4 + \frac{1}{Eth^0}(N_x\partial_x{}^2 + N_y\partial_y{}^2 - 2N_{xy}\partial_x\partial_y)(\partial_x{}^2 + \partial_y{}^2)^2 \\
+ (k_x\partial_y{}^2 + k_y\partial_x{}^2 - 2k_t r_{\theta 0}\partial_x\partial_y)^2 \big]\tilde{w} = 0
\end{aligned}
\tag{5.69}
$$

where $\tilde{w}(x,y)$ is a small deviation of the radial displacement from the pre-buckling state, x and y are dimensionless local coordinates, so that

$$
x = X/c, \quad y = Y/c, \quad c = \sqrt{r_{\theta 0}t}\big/\sqrt[4]{12(1-v^2)}
\tag{5.70}
$$

∂_x, ∂_y denote partial derivatives with respect to x and y,

$$
h^0 = \frac{t}{r_{\theta 0}\sqrt{12(1-v^2)}} \ , \quad k_x = \frac{r_{\theta 0}}{R_x} \ , \quad k_y = \frac{r_{\theta 0}}{R_y}
\tag{5.71}
$$

k_t is the ''torsion'' of the deformed cylinder surface and $r_{\theta 0}$ is the deformed cross-sectional radius at the middle of the buckling zone ($x = y = 0$).
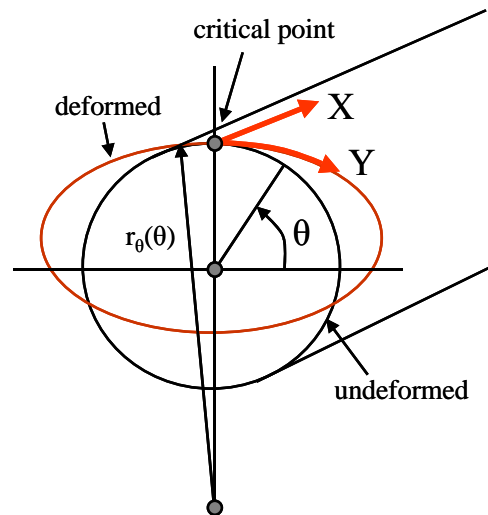

Fig. 72 Local coordinates X and Y are defined on the buckling zone area

Assuming constant deformation and stress within the buckling zone, as well as symmetry of the pre-buckling state with respect to the plane of bending, N_x, N_y, k_x are constant, $k_y = 1$, $N_{xy} = 0$

115

and $k_t = 0$. In addition, a wave-type solution of (5.69) is considered, with no variation in the hoop direction:

$$\tilde{w} = \tilde{w}(x) = A \cos mx \qquad (5.72)$$

where A is an arbitrary constant and m is a dimensionless wavelength parameter. Substituting expression (5.72) into (5.69), the requirement of non-trivial solution dictates that the following expression should hold at the bifurcation stage within the buckling zone,

$$N_x = \frac{Et^2}{r_{\theta 0}\sqrt{12(1-v^2)}}\left[m^2 + \frac{1}{m^2}\right] \qquad (5.73)$$

It is noted that a more general form of (5.73), considering trigonometric variation in both directions x and y, is reported in [85]. Minimization of N_x in (5.73) with respect to m gives $m = 1$, or equivalently,

$$L_{hw} = \frac{\pi c}{m} = \frac{\pi}{[12(1-v^2)]^{1/4}}\sqrt{r_{\theta 0}t} \qquad (5.74)$$

and (5.73) becomes:

$$\sigma_{x0} = \frac{E}{\sqrt{3(1-v^2)}}\left(\frac{t}{r_{\theta 0}}\right) \qquad (5.75)$$

where σ_{x0} is the longitudinal buckling stress within the buckling zone. Equation (5.75) resembles (5.65), and implies that the cylinder buckles at the location where stress σ_{x0} becomes equal to the buckling stress of a uniformly compressed circular cylinder, with radius equal to the current hoop radius $r_{\theta 0}$ at the critical location.

Closed-form Bifurcation Solution

In the present study, (5.75) is further elaborated to obtain a closed-form expression for the bifurcation curvature. The analysis is limited to cylinders with relatively small initial curvature and initial ovality, so that buckling occurs at $\theta = \pi/2$. The key step in the development of the closed-form solution is consideration of the simplified ovalization solution presented in a previous paragraph, to describe the prebuckling state. In particular, the local hoop curvature $1/r_{\theta 0}$ and the longitudinal stress σ_{x0} at $\theta = \pi/2$ at the ovalized prebuckling configuration can be approximated from (5.55) and (5.56) as follows:

$$\frac{1}{r_{\theta 0}} = \frac{1}{r_\theta(\pi/2)} = \frac{-3\zeta_0 + 1 - f - 3\kappa(\kappa + \kappa_{in})}{r(1-f)} \qquad (5.76)$$

$$\sigma_{x0} = \sigma_x(\pi/2) = \frac{E}{\sqrt{1-v^2}}\left(\frac{t}{r}\right)\left[-\zeta_0\frac{\kappa + f\kappa_{in}}{1-f} + \kappa\left(1 - \frac{(\kappa + \kappa_{in})^2}{1-f}\right)\right] \qquad (5.77)$$

116

Substituting the above expressions for $1/r_{\theta 0}$ and σ_{x0} in (5.75), a third-order algebraic equation is obtained in terms of the critical curvature κ_{cr}:

$$\kappa_{cr}\left(1 - \frac{(\kappa_{cr} + \kappa_{in})^2}{1-f}\right) - \frac{1}{\sqrt{3}}\left(1 - \frac{3\kappa_{cr}(\kappa_{cr} + \kappa_{in})}{1-f}\right) - \zeta_0\frac{\kappa_{cr} + f\kappa_{in}}{1-f} + \sqrt{3}\frac{\zeta_0}{1-f} = 0 \quad (5.78)$$

which has the following closed-form solution

$$\kappa_{cr} = \frac{1}{\sqrt{3}} - \frac{2\kappa_{in}}{3} - \frac{2}{3}\sqrt{abs[3(2-f) - \sqrt{3}\kappa_{in} + \kappa_{in}^2 - 3\zeta_0]} \times$$

$$\times \cos\left(\frac{\pi}{3} + \frac{1}{3}\arccos\left[\frac{1}{2}\frac{3\sqrt{3}\kappa_{in}^2 - 2\kappa_{in}^3 + 6\sqrt{3}(1 - 6\zeta_0) + 9\kappa_{in}(3 - 2\zeta_0 + f(3 - 2\zeta_0))}{abs[3(2-f) - \sqrt{3}\kappa_{in} + \kappa_{in}^2 - 3\zeta_0]^{3/2}}\right]\right) \quad (5.79)$$

where $abs[\ ]$ is the absolute value of $[\ ]$. Subsequently, the bifurcation moment m_{cr} is obtained from (5.54) as follows:

$$m_{cr} = -\frac{3}{4}\zeta_0\pi\left(\frac{2\kappa + f\kappa_{in}}{1-f}\right) + \kappa_{cr}\pi\left(1 - \frac{3(\kappa_{cr} + \kappa_{in})(2\kappa_{cr} + \kappa_{in})}{4(1-f)}\right) \quad (5.80)$$

Expressions (5.79) and (5.80) define the bifurcation point on the primary $m - \kappa$ path of (5.54). Furthermore, (5.74) and (5.76) lead to the following expression for the normalized half wavelength:

$$s = \sqrt{\frac{(1-f)}{-3\zeta_0 + (1-f) - 3\kappa_{cr}(\kappa_{cr} + \kappa_{in})}} \quad (5.81)$$

For the particular case of initially straight pressurized cylinders without initial ovality ($\kappa_{in} = 0$ and $\zeta_0 = 0$), (5.78) becomes:

$$\kappa_{cr}\left(1 - \frac{1}{1-f}\kappa_{cr}^2\right) - \frac{1}{\sqrt{3}}\left(1 - \frac{3}{1-f}\kappa_{cr}^2\right) = 0 \quad (5.82)$$

and its solution is written in closed form as follows:

$$\kappa_{cr} = \frac{1}{\sqrt{3}} - \frac{2}{3}\sqrt{abs[3(2-f)]}\,\cos\left(\frac{\pi}{3} + \frac{1}{3}arc\cos\left[\frac{3\sqrt{3}}{abs[3(2-f)]^{3/2}}\right]\right) \quad (5.83)$$

Furthermore, the expression for the corresponding normalized half-wave length becomes:

$$s = \frac{L_{hw}}{L_0} = \sqrt{\frac{r_{\theta 0}}{r}} = \sqrt{\frac{(1-f)}{1 - f - 3\kappa_{cr}^2}} \quad (5.84)$$

If no pressure is applied ($f = 0$) the above expressions are reformed as:

$$\kappa_{cr}\left(1 - \kappa_{cr}^2\right) - \frac{1}{\sqrt{3}}\left(1 - 3\kappa_{cr}^2\right) = 0 \quad (5.85)$$

$$\kappa_{cr} = \frac{1}{\sqrt{3}} - \frac{2\sqrt{2}}{\sqrt{3}}\,\cos\left(\frac{\pi}{3} + \frac{1}{3}arc\cos\left[\left(\sqrt{2}\right)^{-3}\right]\right) = 0.381122 \quad (5.86)$$

117

$$s = \frac{L_{hw}}{L_0} = \sqrt{\frac{r_{\theta 0}}{r}} = \sqrt{\frac{1}{1 - 3\kappa_{cr}^2}} = 0.33128 \qquad (5.87)$$

The accuracy of κ_{cr} and m_{cr} values, obtained from the above analytical equations, are shown in Fig. 73-Fig. 75 for circular initially straight cylinders, considering pressure effects, together with numerical results, indicating a remarkable accuracy. The agreement is better in the case of thin-walled cylinders (large values of r/t ratio), because those cylinders exhibit a smaller size of buckling zone, as discussed in the previous section. The comparison between the numerical results with the analytical solution shows that the above closed-form expressions are quite accurate for relatively small values of κ_{in} and ζ_0, as shown in Fig. 76 and Fig. 77. In those figures, (5.54) is used to express the prebuckling analytical solution, and the bifurcation point, (denoted by the arrows ↓↑) as it is obtained from (5.79) and (5.80). For the particular case of zero initial ovality ($\zeta_0 = 0$) the obtained numerical results result in the observation that these analytical expressions provide very good accuracy when $-0.4 \le \kappa_{in} \le 0.2$.
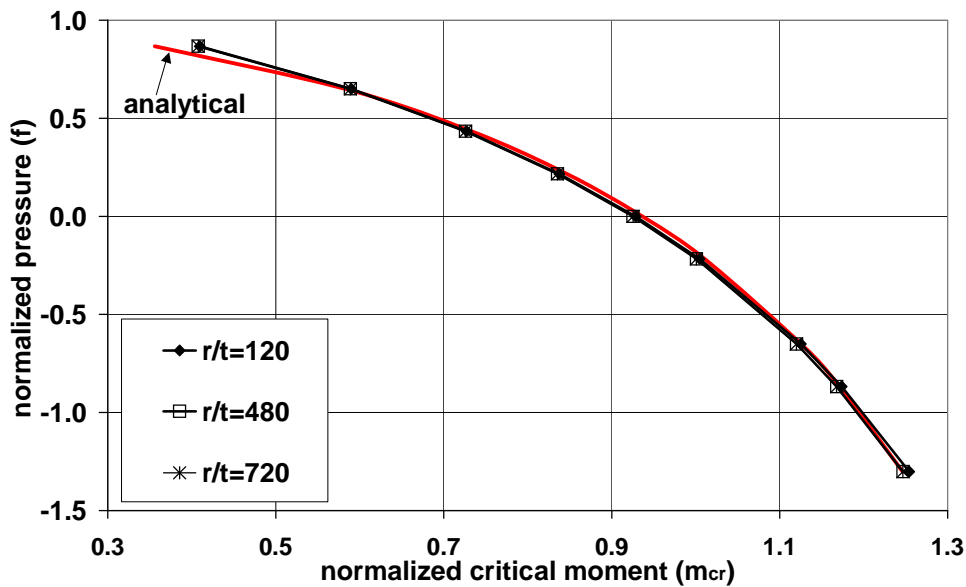

Fig. 73 Variation of m_{cr} with respect to pressure level f ; comparison of numerical and analytical results (5.80)
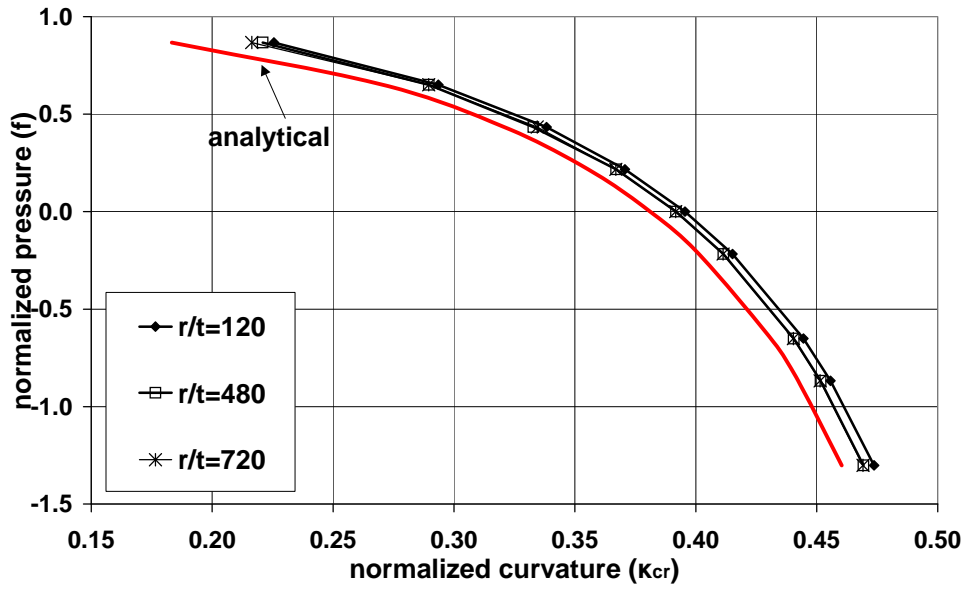
118

Fig. 74 Variation of κ_{cr} with respect to pressure level f ; comparison of numerical and analytical results(5.83)
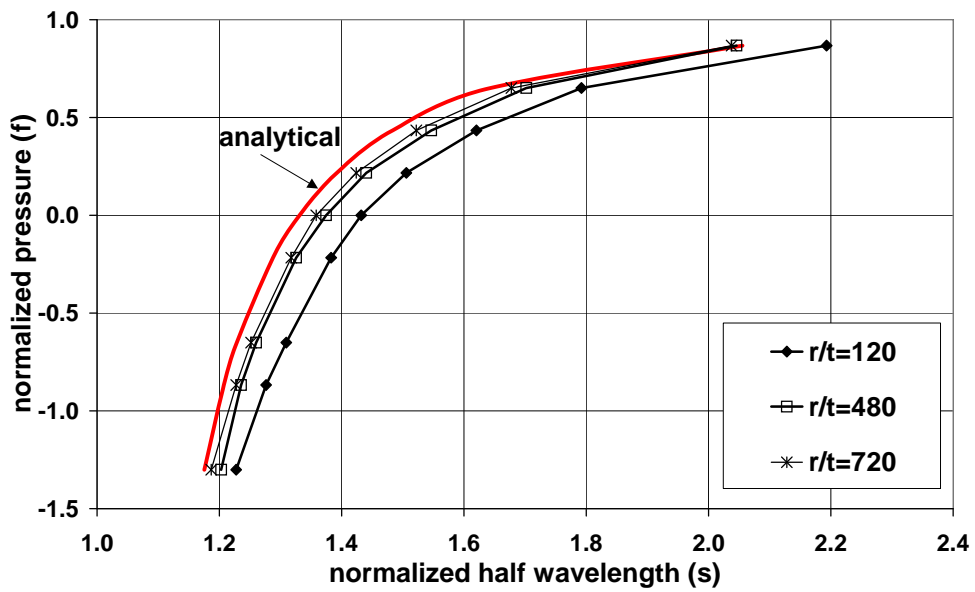

Fig. 75 Variation of s with respect to pressure level f ; comparison of numerical and analytical results (5.84)
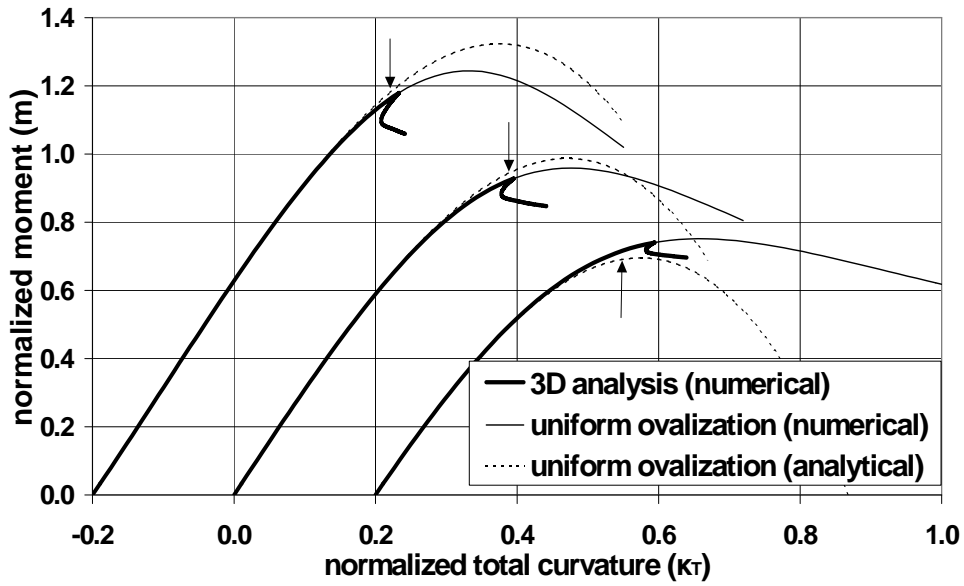
119

Fig. 76 Comparison of numerical results and analytical solutions for non-pressurized cylinders (r/t =120) and for three different values of initial curvature (κ_{in} =0, κ_{in} =±0.2); arrows (↓↑) denote the critical points obtained from the analytical solution.
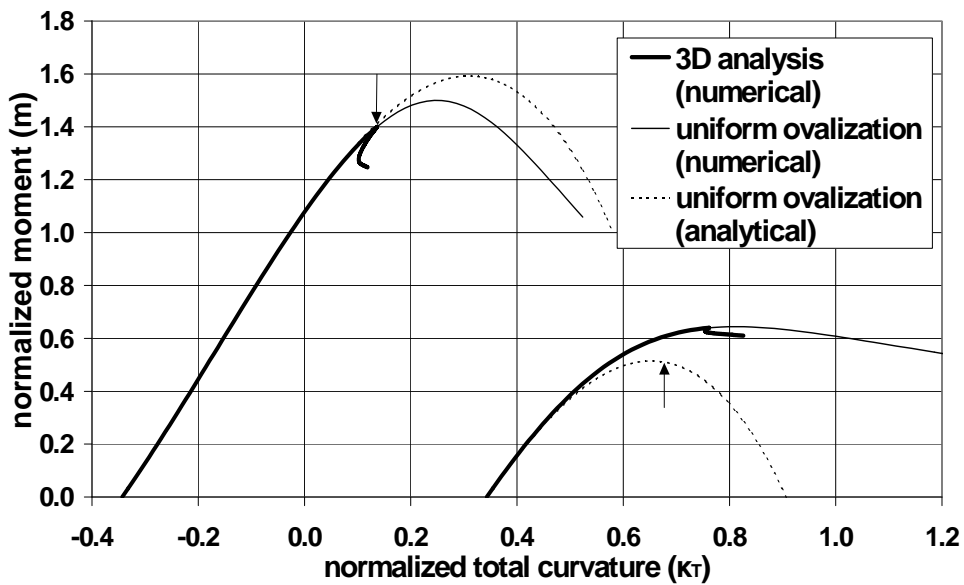

Fig. 77 Comparison of numerical results and analytical solutions for non-pressurized cylinders (r/t =120) and for two different values of initial curvature (κ_{in} =±0.343); arrows (↓↑) denote the critical points obtained from the analytical solution

120

5.2.4 Mechanical Model

A simple model, depicted in Fig. 78a, provides a physical explanation of the numerical and analytical results, reported in the previous paragraphs. The model was proposed in an early publication [1] for cylindrical shells under uniform, axial compression. According to this model, the cylinder is considered as a ''bundle'' of compressed longitudinal strips in the longitudinal direction, each one supported by a series of springs, so that the problem under consideration is similar to the buckling problem of a beam on elastic foundation. The ''foundation springs'' are elastic arches, representing the stiffness provided by the hoop deformation of the shell.

In the present study, the model is used to illustrate some bifurcation aspects of pressurized cylinders under bending. More specifically, the compressed strip is considered in the middle of the buckling zone, and the arch may be ovalized, representing the shape of the cylindrical cross-section just prior to buckling. Arch stiffness plays a key role on the buckling stress and the corresponding wavelength, and depends on the amount of ovalization. In Fig. 78b, the response of such elastic arches under concentrated load on its crest is plotted. Three cases are considered, corresponding to initially non-ovalized (circular), initially ''flattened'' and initially ''bulged'' cylinders denoted as cases A, B and C, respectively. The results are obtained numerically, using a non-linear degenerated shell finite element analysis [86]. In those results, the ''flattening'' direction of the load is considered positive. In all three cases, the response is nonlinear ''softening/hardening'', resulting in an unstable post-buckling path for the compressed strip, as discussed in [1]. Fig. 78b also shows that the support-arch stiffness is significantly reduced in the initially ''flattened'' arch (case B), but it is quite higher in the initially ''bulged'' arch (case C).

The above model can illustrate some aspects of cylinder bifurcation under the combined action of bending and pressure. In the case of closing bending moments, the cross-section flattens around the critical location, reduces the stiffness of the supporting arches, and results in a decrease of the critical moment, as shown in Fig. 58 and Fig. 62. The reduction of support stiffness is accentuated in the presence of external pressure, whereas internal pressure reduces flattening, increasing the stiffness of the supports and the corresponding critical longitudinal stress. Similarly, the presence of initial curvature opposite to the direction of bending (opening moments), increases the local hoop curvature, resulting in larger support stiffness, and therefore, it corresponds to a shorter wavelength and a higher critical moment, also depicted in Fig. 60 and Fig. 66.
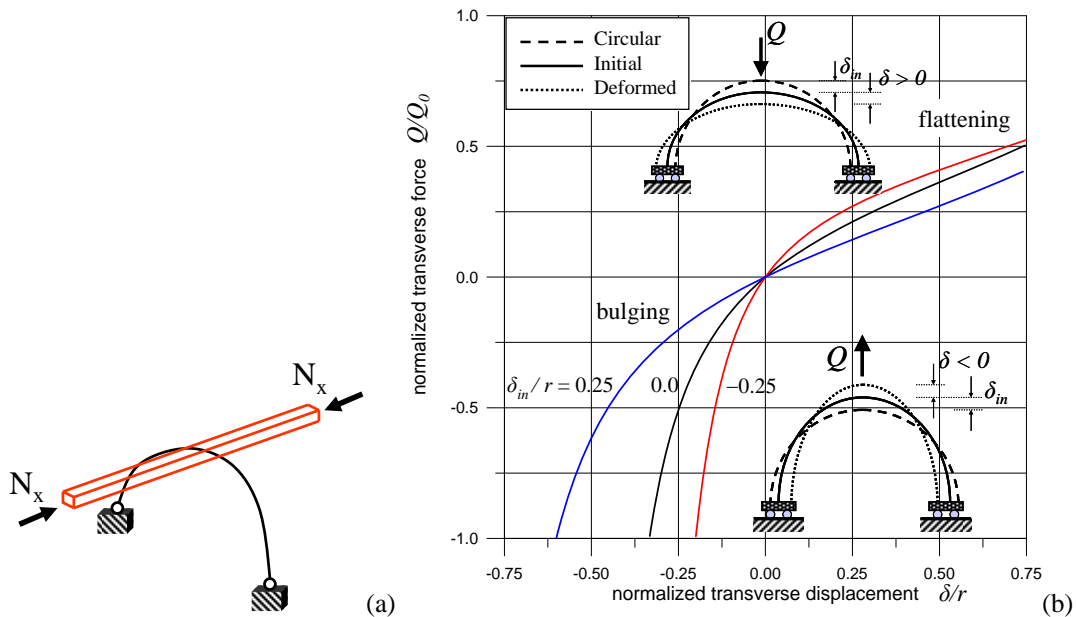
121

Fig. 78 (a) Simple mechanical model, simulating buckling of cylindrical shells under axial compression [1] (b) Response of circular and initially oval arches under a concentrated load on the crest; results from shell finite element analysis [86]. Negative values of δ_{in} indicate initial ovality opposite to the one shown in the sketches.

5.3 Imperfection Sensitivity

Buckling of shells is generally characterized by significant sensitivity with respect to initial imperfections. This was originally investigated in the early works by von Karman et al [1] and Koiter [3] for axially loaded cylinders. Both works were aimed at "bridging the gap" between the high values of analytical predictions and the low values from experimental data. Koiter's general theory of elastic stability is shortly presented in Appendix. The main issue clarified by Koiter was that imperfection sensitivity of a structure is directly related to its initial post-buckling behavior.

Herein, imperfection sensitivity of elastic circular cylinders under bending loads is examined numerically, and the results are compared with asymptotic solutions reported elsewhere. Towards this purpose, an initial periodic imperfection is assumed in the shape of the first instability mode corresponding to the buckling (bifurcation) moment. This buckling mode is obtained through an eigenvalue analysis of the deformed (ovalized) cylinder's configuration. More specifically, at the end of each increment of the step-by-step Newton-Raphson procedure, the tangent stiffness is calculated and its eigenvalues are computed. Bifurcation occurs at the stage where the tangent stiffness becomes singular. This eigenvalue analysis provides the buckling mode (Fig. 79), which is the one corresponding to the zero eigenvalue. It is emphasized that bifurcation of a cylinder under bending loads is characterized by a single

122

buckling mode similar to the case of non-circular cylinders under axial compression. This is a significant differentiation with the infinite number of buckling modes that characterize circular cylinders axially compressed. This single instability mode is imposed in the initial configuration as an imperfection. Furthermore, the imperfection parameter ξ is introduced, defined as the total wave height W_0 normalized by the cylinder thickness t ($\xi = W_0/t$), and it is similar to the imperfection parameter introduced in the cases of axial compression examined in the previous two Chapters.

Results for the imperfection sensitivity of initially straight isotropic elastic cylinders with $r/t = 100$ under bending are obtained considering the ''imperfect'' geometry of the cylinder. The numerical results in Fig. 80 show that the ultimate bending load of the elastic cylinder is reduced with increasing imperfection amplitude and this drop is shown in detail in Fig. 80b. It is interesting to note that as the imperfection amplitude increases, the response becomes smoother, as indicated in Fig. 80.

Pressure effects are also considered. The numerical results reveal a similar response regarding initial post-buckling equilibrium. As external pressure is increased a significant reduction of the moment capacity of the cylinder is observed (Fig. 81 and Fig. 82). This effect can be readily interpreted as external pressure increases cross-sectional ovalization.

Imperfection sensitivity of elastic cylinders with the $r/t = 100$ has also been investigated by Fabian [41]. In that study, Fabian applied Koiter's initial post-buckling theory, enhanced by Fitch's [40] considerations to account for a non-linear pre-buckling state. The resulting first-order and second-order boundary-values problems were solved through a finite difference technique, choosing η as the perturbation parameter, as described in Appendix, the following asymptotic expression for the post-buckling path was obtained

$$\frac{m}{m_{cr}} = 1 + b\eta^2 + ...$$ (5.88)

where b is a negative constant, that depends on the r/t ratio and the level of pressure. The negative value of b indicates an unstable post-buckling behaviour, which is verified by the present numerical results. Furthermore, assuming an initial imperfection in the form of the first buckling mode, Fabian [41] obtained a relation of the following form for the maximum moment $m_{\max}$ in terms of the imperfection amplitude ξ:

$$\frac{m_{\max}}{m_{cr}} = 1 - C\xi^{2/3}$$ (5.89)

where C is a constant that depends on r/t ratio and the level of pressure f. The present numerical results are found to agree very well with the exponential relation (5.89), as shown in Fig. 83.

Both numerical and asymptotic results confirm that even small geometrical imperfections may reduce the maximum moment that the cylinder can sustain. Moreover, the presence of external pressure results in an increase of m_{max}/m_{cr} ratio for the same imperfection amplitude (Fig. 83), whereas internal pressure has the opposite effects, which is in accordance with Fabian's asymptotic results [41]. This means that imperfection sensitivity is more severe as the level of internal pressure increases.

Numerical results for the imperfection sensitivity of very thin cylinders (r/t =720) are also obtained. It is found that the variation of maximum moment m_{max} with respect to the imperfection amplitude ξ follows an exponential expression similar to (5.89), where the value ''2/3'' for the exponent is verified (Appendix). Finally, Fig. 84 indicates that the m_{max}/m_{cr} curve for the thinner cylinders (r/t =720) lies below the one obtained for the thicker ones (r/t =100), which leads to the conclusion that thinner cylinders are more sensitive to initial imperfections.
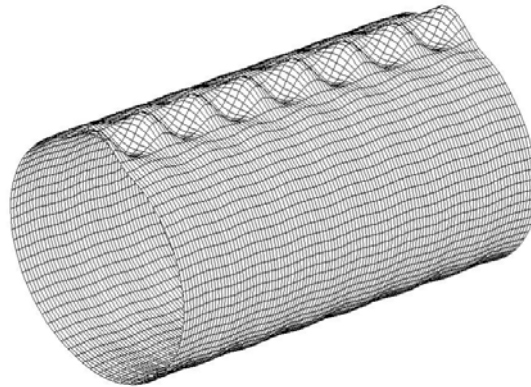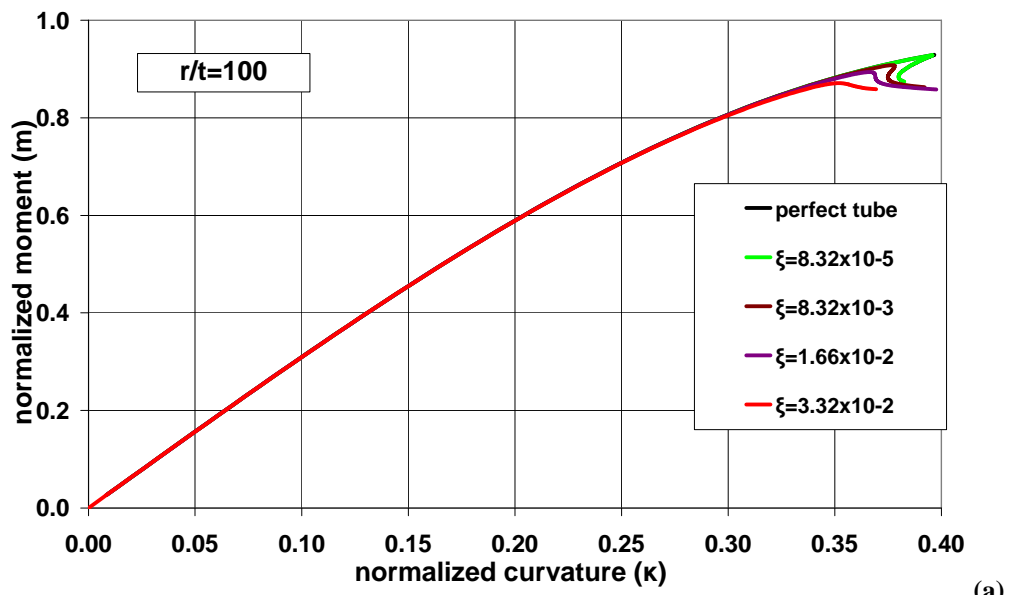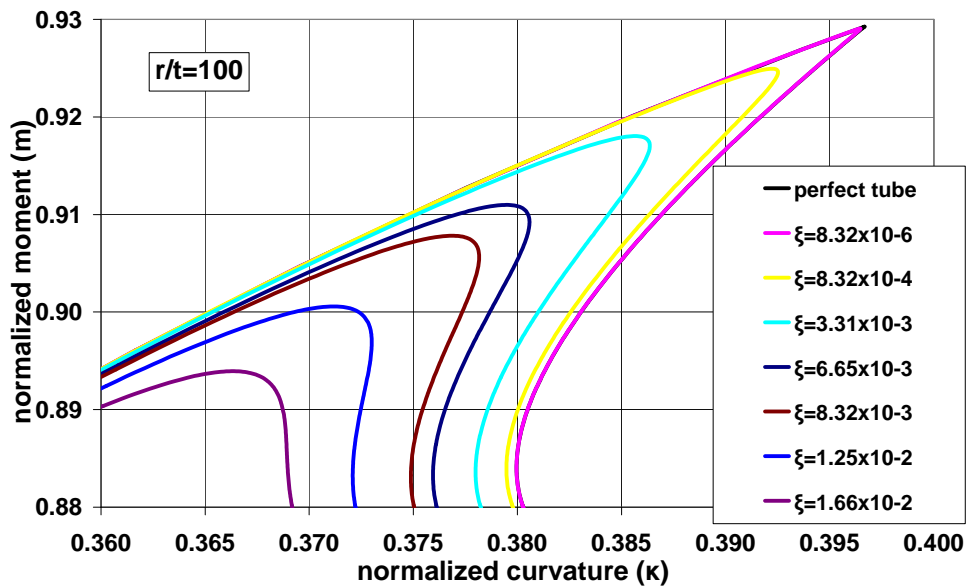

Fig. 79 Buckling mode of elastic cylinder under bending moments

124

Fig. 80 Imperfection sensitivity of an unpressurized elastic cylinder; (a) entire $m - \kappa$ **path and (b) detail at bifurcation (numerical results)**
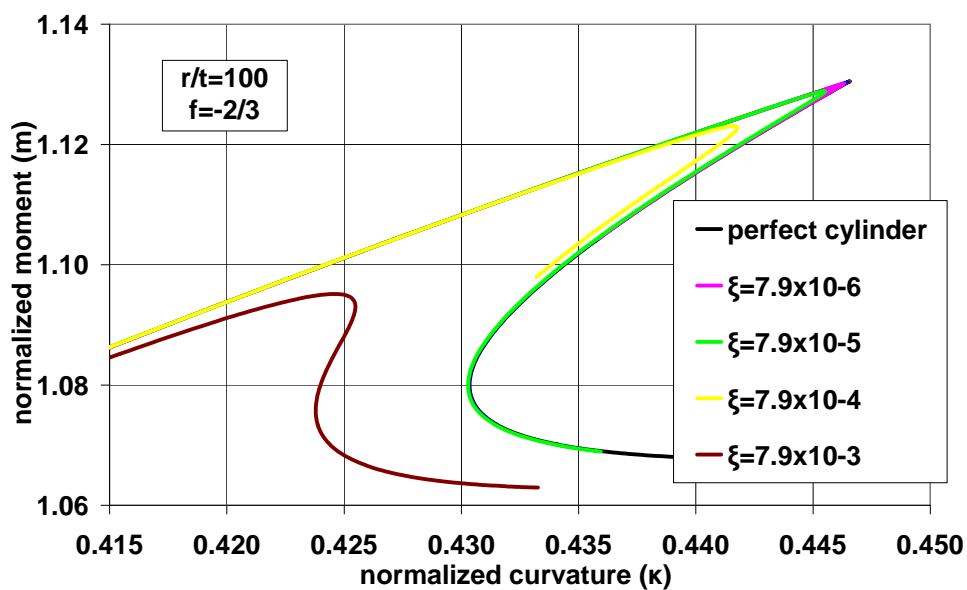
125

Fig. 81 Imperfection sensitivity for a pressurized cylinder under bending (numerical results)
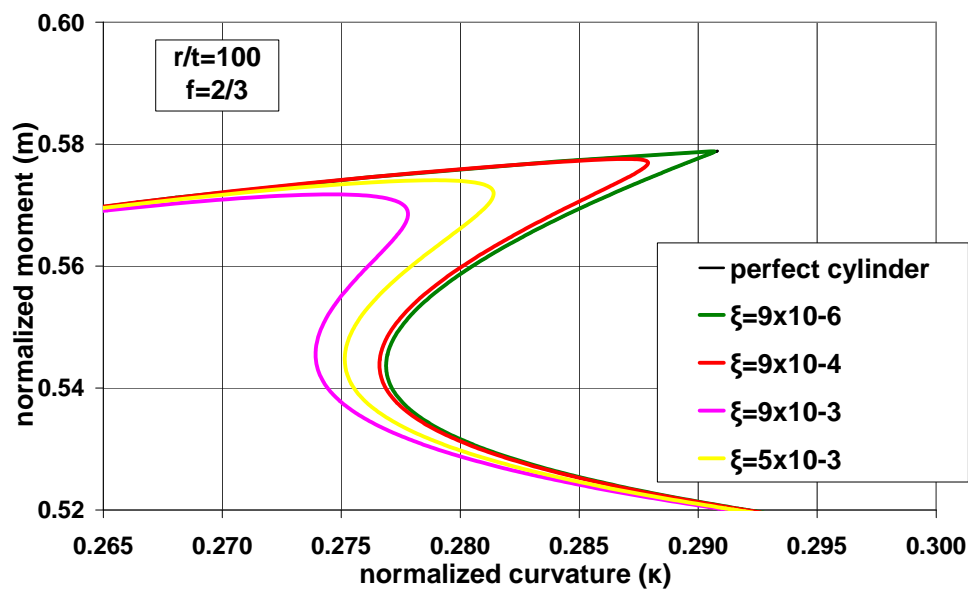
Fig. 82 Imperfection sensitivity for a pressurized cylinder under bending (numerical results)
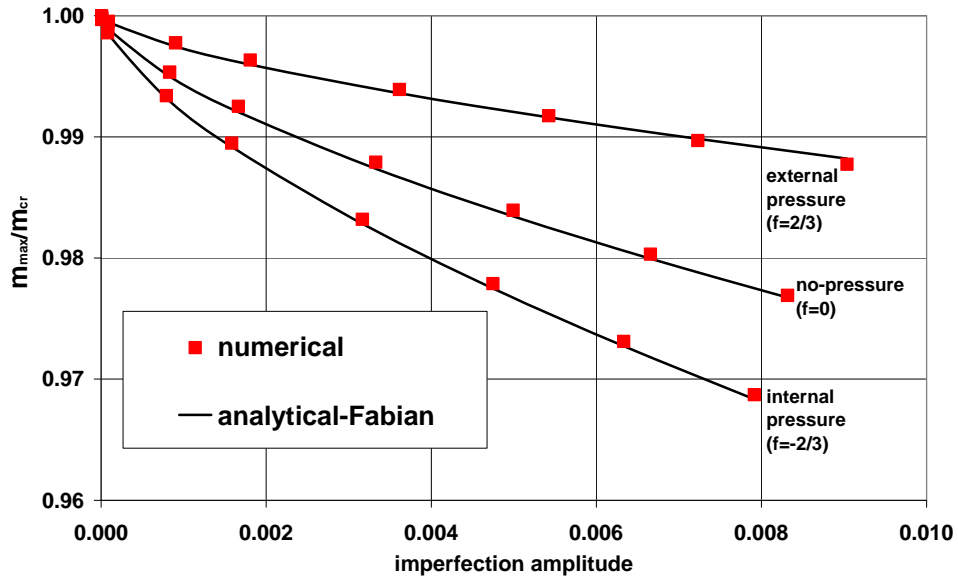
126

Fig. 83 m_{max}/m_{cr} **vs imperfection amplitude for three different pressure levels; direct comparison of the present numerical results and the asymptotic solution [41]** (r/t **=100)**
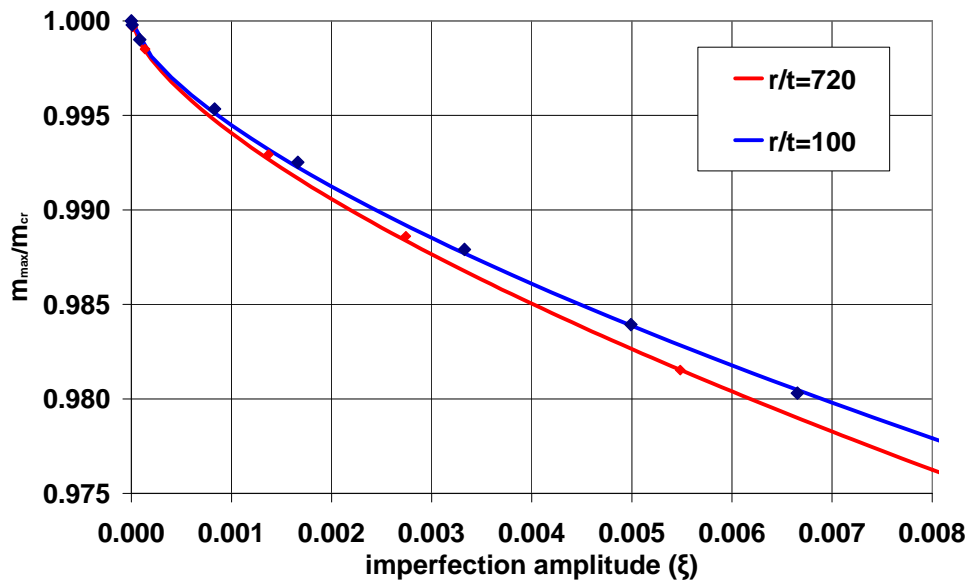

Fig. 84 m_{max}/m_{cr} **vs imperfection amplitude for two different** r/t **ratios in the absence of pressure (numerical results)**

127

Chapter 6

THIN-WALLED TRANSVERSELY-ISOTROPIC ELASTIC CYLINDERS UNDER BENDING AND PRESSURE

The present Chapter investigates the stability of long thin-walled transversely-isotropic elastic cylinders subjected to bending and uniform pressure, extending the work presented in the previous Chapter for isotropic cylinders. This subject of anisotropic materials has received significant attention in the last three decades due to its applications in analysis and design of composite-material structures. Issues of bifurcation, postbuckling response and imperfection sensitivity of circular cylinders with respect to the level of anisotropy are discussed. Furthermore, an extension of the simplified analytical formulation for isotropic cylinders in the case of anisotropic cylinders is presented, to describe the gradual progress of ovalization of the cross-section and predict the uniform wrinkling bifurcation on the primary path.

Equation Chapter 6 Section 6

6.1 Introduction

Similar to the case of isotropy, the bending response of anisotropic cylinders is initially characterized by cross-sectional ovalization followed by bifurcation into a wrinkled state. Kedward [87] reported a first attempt to enhance Brazier's solution [62] considering a different modulus for the longitudinal and the hoop direction, and resulted in a closed-form expression for the ovalization and the primary moment-curvature path. Spence and Toh [88] extended Reissner's formulation [64] to account for orthotropic material behavior, using nonlinear finite deflection thin shell theory. The numerical results were compared with experimental test data from steel and ''melenex'' cylinders. Stockwell and Cooper [89] presented a direct extension of Reissner's [64] isotropic cylinder formulation to obtain a closed-form expression for the moment-curvature relationship, and the analytical results were compared with numerical results from a commercial finite element program. Libai and Bert [90] used thin-shell theory and a mixed variational principle to investigate the nonlinear ovalization behavior of anisotropic cylinders, and reported solutions for long, medium-length and short cylinders, including the effects of end boundary conditions. Furthermore, a closed-form expression for the moment-curvature ovalization path was derived for infinitely long cylinders. Corona and Rodrigues [91] presented numerical results for orthotropic cylinders with cross-ply layers. Using nonlinear ring

128

theory, the prebuckling ovalization solution was determined. Uniform wrinkling was also examined in [91] through a perturbation technique, based on non-shallow cylindrical shell kinematics. Tatting et al [92] analyzed long anisotropic cylinders with symmetric lay-ups through a finite-difference solution of semi-membrane shell equations. The final moment-curvature expression was identical to the one reported by Reissner [64] for isotropic cylinders, and its solution was found to compare well with the simplified Kedward solution [87]. In this study [92], local buckling was examined, using the Kedward solution for the pre-buckling equilibrium path, and considering the simplified engineering hypothesis, as proposed by Axelrad [78]. Furthermore, the effects of pressure and the influence of laminate stacking sequence were examined. It was found that bifurcation occurs before a limit point is reached on the ovalization path. Harursmapath and Hodges [93] developed an enhanced beam model accounting for cross-sectional deformation, in terms of trigonometric series expansion, to analyze long, thin-walled cylinders of anisotropic materials. Employing one term of series expansion, they provided closed form expressions for the ovalization path and the corresponding stresses. Using this simplified solution, limit-moment instability, local buckling and material ply failure were examined. Recently, Wadee et al [94], using an analytical formulation and a second-degree trigonometric series solution in the hoop direction obtained results for anisotropic cylinders, in terms of the ultimate moment and buckling wavelength. Furthermore, it is mentioned that several attempts (e.g. [82], [83]) have been reported to apply shell stability concepts to simulate the bending response of carbon nanotubes.

6.2 Ovalization Instability

A simplified ovalization solution for transversely-isotropic cylinders under bending and pressure can be obtained, employing an energy formulation similar to the one presented in section 5.2.3. This time, the values of pressure p, bending moment M and longitudinal stress σ are normalized by $\overline{p}_{cr}$, $\overline{M}_e$ and $\overline{\sigma}_e$, respectively:

$$\overline{p}_{cr} = \frac{E_{11}t^3}{4r^3(1-v_{12}v_{21})} \tag{6.1}$$

$$\overline{M}_e = \frac{E_{22}rt^2}{q\sqrt{1-v_{12}v_{21}}} \tag{6.2}$$

$$\overline{\sigma}_e = \frac{E_{22}t}{rq\sqrt{1-v_{12}v_{21}}} \tag{6.3}$$

where E_{11} and E_{22} are the elastic uniaxial modulus for the hoop and longitudinal direction, v_{12} and v_{21} are Poisson's ratio and $\overline{q} = \sqrt{E_{22}/E_{11}}$ (Note in section 2.2.2). Curvature k, which is

129

expressed as the ratio of the relative rotation between the two end sections of the cylinder segment over their initial distance, is normalized by:

$$\bar{k}_N = \frac{t}{r^2 q \sqrt{1 - \nu_{12}\nu_{21}}} \tag{6.4}$$

It is noted that, when $\bar{q} = \sqrt{E_{22}/E_{11}} = 1$ (isotropic material) the values of $\bar{p}_{cr}$, $\bar{M}_e$, $\bar{k}_N$ and $\bar{\sigma}_e$ are equal to the normalization values p_{cr}, M_e, k_N and σ_e used in Chapter 5 for isotropic cylinders, respectively.

Following the energy formulation, presented in section 5.1.2, and including the effects of pressure in ovalization instability, the potential energy, in the case of pressurized bending, can be described as:

$$\Pi = U_L + U_C + V_P - W_P - M\,k \tag{6.5}$$

where, U_L is the longitudinal bending strain energy, U_C is the cross-sectional (hoop) deformation strain energy, V_P is the pressure potential and W_p is the second-order of hoop pressure stress $\sigma_p = pr/t$.

Enforcing minimization of Π in terms of a ($\partial\Pi/\partial a = 0$) and employing the normalization values $\bar{p}_{cr}$, $\bar{M}_e$, $\bar{k}_N$ and $\bar{\sigma}_e$, the following ovalization-curvature relationship is obtained:

$$a = \frac{\kappa^2 r}{1 - f} \tag{6.6}$$

$$\zeta = \frac{a}{r} = \frac{\kappa^2}{1 - f} \tag{6.7}$$

Inserting the value of ovalization amplitude α, as described in (5.42), in the expression of potential energy and enforcing equilibrium ($\partial\Pi/\partial k = 0$), an expression for the bending moment is obtained:

$$m = \kappa\pi\left(1 - \frac{3\kappa^2}{2(1 - f)}\right) \tag{6.8}$$

Furthermore, closed-form expressions for the longitudinal stress σ_x as well as the radii of curvature at the deformed configuration $1/r_\theta(\theta)$ are obtained:

$$\frac{\sigma_x}{\bar{\sigma}_e} = \kappa\left((1 - \frac{3\kappa^2}{4(1 - f)})\sin\theta + \frac{\kappa^2}{4(1 - f)}\sin 3\theta\right) \tag{6.9}$$

$$\frac{1}{r_\theta(\theta)} = \frac{1}{r}\left(1 + \frac{3\kappa^2}{1 - f}\cos 2\theta\right) \tag{6.10}$$

The dimensionless expressions (6.6)-(6.10) are identical to the ones obtained in Chapter 5 for isotropic cylinders.

130

In the sequence, the analytical expressions for the ovalization path presented in earlier studies can now be written, using the present normalization, which allows their direct comparison with (6.8). These expressions are:

■ Kedward [87]:

$$m = \kappa \pi \left(1 - \frac{3\kappa^2}{2} \right) \tag{6.11}$$

■ Stockwell and Cooper [89]:

$$m = \kappa \pi \left(1 - \frac{3}{2}\kappa^2 - \frac{3}{2}\kappa^4 \right) \tag{6.12}$$

■ Libai and Bert [90]:

$$m = \kappa \pi \left(1 - \frac{3}{2}\kappa^2 + \frac{5}{8}\kappa^4 \right) \tag{6.13}$$

■ Harursampath and Hodges [93]:

$$m = \kappa \pi \left(1 - \frac{3}{2}\kappa^2 + \frac{15}{8}\kappa^4 \right) \tag{6.14}$$

In Fig. 85 the ovalization path obtained from the present finite element technique is compared with expressions (6.11)-(6.14) for the case of unpressurized bending. The comparison shows that despite its simplicity, Kedward's expression (6.11), which is basically the Brazier solution [62], provides a better prediction than the more elaborate formulae proposed in [89], [90], [93]. The fact that this simple expression (6.11) provides very good predictions has also been noted in previous studies [76].
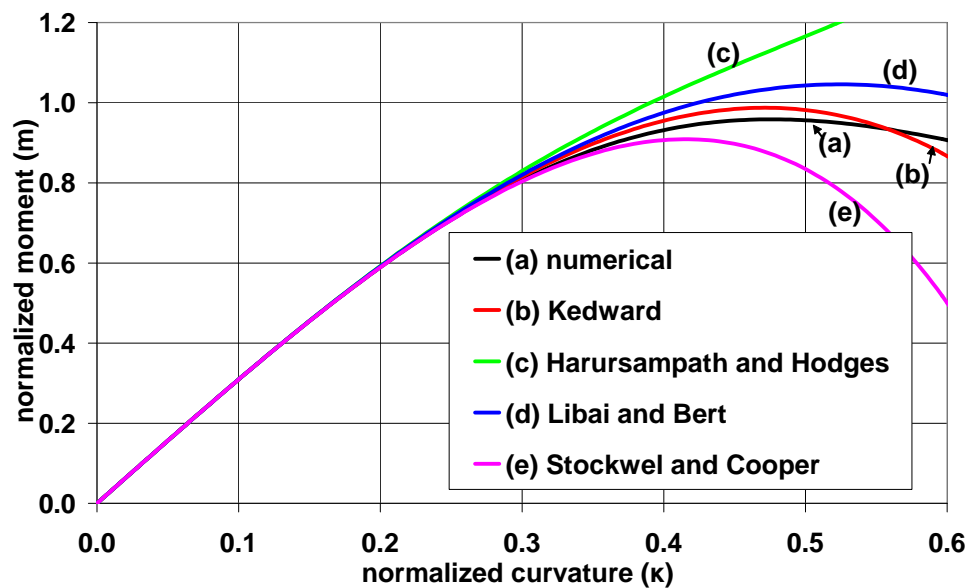

Fig. 85 Ovalization pre-buckling path; numerical results compared to analytical expressions ([87], [93], [90], [89])

131

6.3 Bifurcation Instability

In this section uniform wrinkling instability of transversely-isotropic cylinders is examined numerically. Regarding numerical implementation issues, a 16th degree expansion in equations (2.150) is found adequate for the cases of interest as it is illustrated in Fig. 86, and a spherical arc-length procedure that monitors selected degrees of freedom of the ''tube-element'' was employed (section 2.7). Furthermore, an initial series of numerical results with both hypoelastic and hyperelastic constitutive modeling was conducted and no difference in terms of the calculated buckling and post-buckling response was found. It is mentioned that, for the majority of the results the λ/μ ratio is considered equal to 3/2, unless mentioned otherwise, whereas the anisotropy parameter S value ranges between 1 and 10.
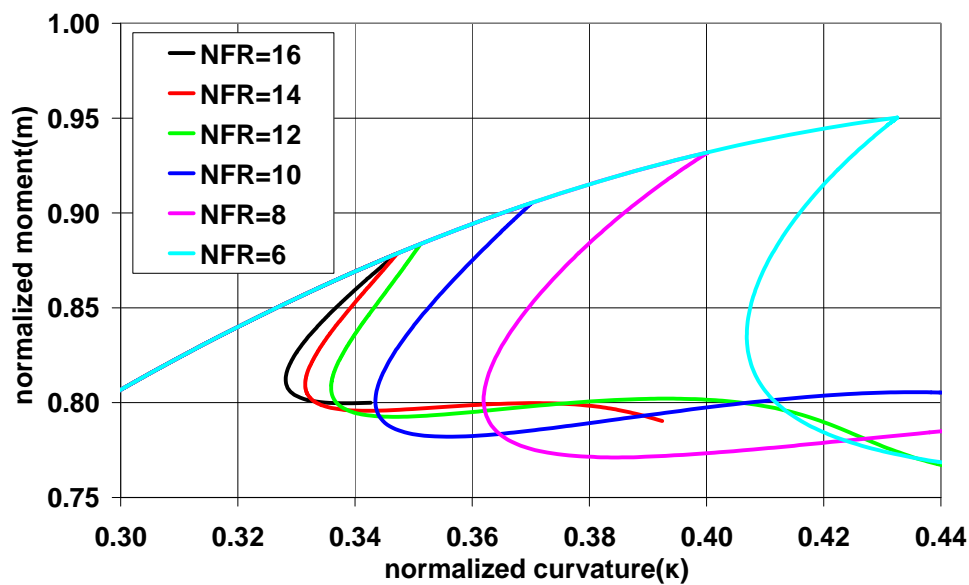

Fig. 86 Effect of the degree of trigonometric expansion used in equation (2.150) (r/t =100, S =3)

A comparison between results from the present numerical formulation and numerical results reported in [91], is offered in Fig. 87 for a cylinder with AS3501 material, 0^0 layers and diameter-to-thickness ratio D/t equal to 100, in terms of buckling moment and curvature. The comparison of these two numerical procedures, as shown in Fig. 87, is very good and validates the efficiency of the present formulation. It is noted that according to the analysis conducted in [91], ovalization instability occurs at curvature κ_{ov} =0.486 and moment m_{ov} =0.976, whereas buckling occurs at lower values of curvature and moment (κ_{cr} =0.369 and m_{cr} =0.915), as indicated by the symbol '↑' in Fig. 87. The present numerical results indicate similar behavior with ovalization limit point at κ_{ov} =0.480, m_{ov} =0.954, and bifurcation at κ_{cr} =0.354, m_{cr} =0.882, denoted by the symbol '↓'.
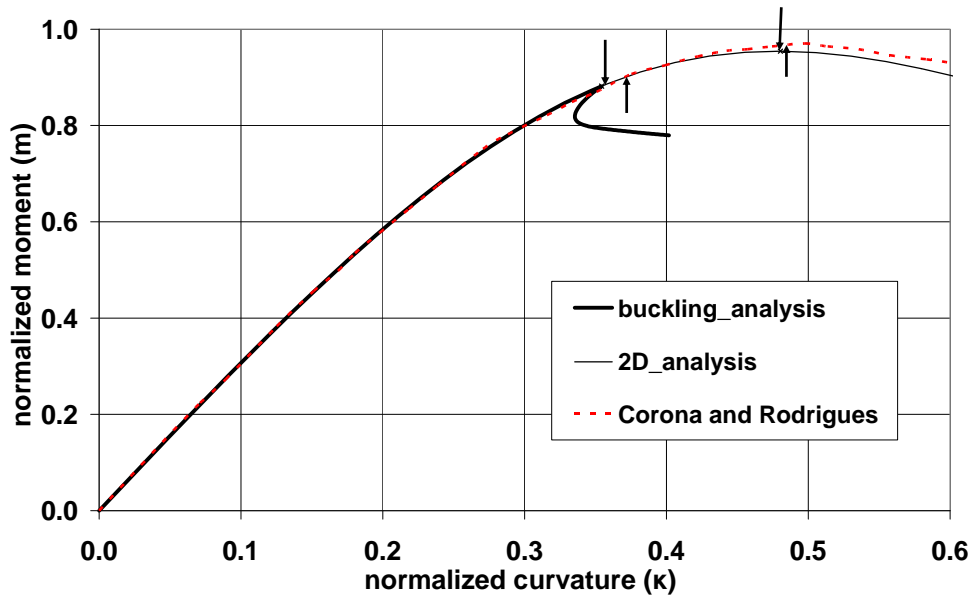
132

Fig. 87 Comparison of numerical results, arrows (↑) denote the critical and ovalization points obtained from [91] and arrows (↓) denote the corresponding points calculated herein

Subsequently, the bifurcation and post-buckling response of transversely-isotropic cylinders with radius-to-thickness ratio between r/t 10 and 720 is examined for different levels of anisotropy. The response of thin-walled cylinders with r/t equal to 100 and 720 with emphasis on the bifurcation point is depicted in Fig. 88 and Fig. 89, respectively, for different values of the anisotropy parameter S. In all cases, bifurcation occurs before a limit point is reached and the initial post-buckling behavior is unstable, characterized by a ''snap-back'' of the $m-\kappa$ path. Furthermore, the results show that the location of bifurcation on the $m-\kappa$ primary path, as well as the post-buckling behavior depend on the level of anisotropy S. More specifically, increasing the level of anisotropy, bifurcation occurs earlier on the normalized prebuckling path. For the case of thin-walled cylinder (r/t =720) the buckling curvature κ_{cr} ranges from 0.390 for the isotropic case (S =1, E_{22}/E_{11} =1), to 0.343 for S =10 (E_{22}/E_{11} =12.03).

Subsequently, the bifurcation and post-buckling response of transversely-isotropic cylinders with radius-to-thickness ratio between r/t 10 and 720 is examined for different levels of anisotropy. The response of thin-walled cylinders with r/t equal to 100 and 720 with emphasis on the bifurcation point is depicted in Fig. 88 and Fig. 89, respectively, for different values of the anisotropy parameter S. In all cases, bifurcation occurs before a limit point is reached and the initial post-buckling behavior is unstable, characterized by a ''snap-back'' of the $m-\kappa$ path. Furthermore, the results show that the location of bifurcation on the $m-\kappa$ primary path, as well as the post-buckling behavior depend on the level of anisotropy S. More specifically, increasing the level of anisotropy, bifurcation occurs earlier on the normalized prebuckling

133

path. For the case of thin-walled cylinder (r/t =720) the buckling curvature κ_{cr} ranges from 0.390 for the isotropic case (S =1, E_{22}/E_{11} =1), to 0.343 for S =10 (E_{22}/E_{11} =12.03).

Numerical results from a thick cylinder (r/t =10) are shown in Fig. 90 and Fig. 91. A significant shift of the location of the bifurcation point is observed, as the anisotropy parameter S increases. It is noted that the material properties of the cylinder in Fig. 91 are obtained from the paper of Wang et al [95], and are the properties of single-walled carbon nanotubes, calculated from molecular dynamics.
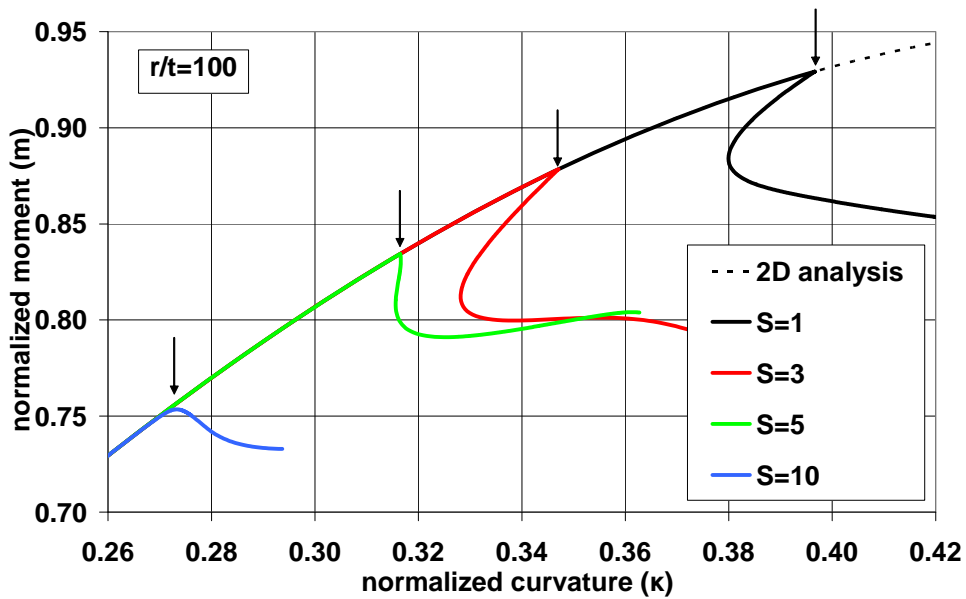

Fig. 88 Numerical results for different values of anisotropy parameter S (r/t =100)
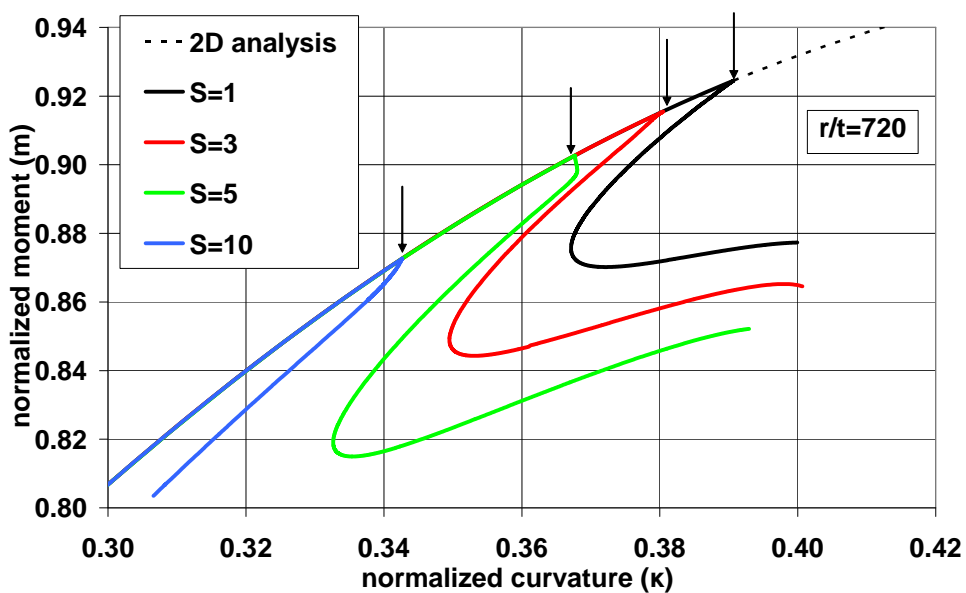

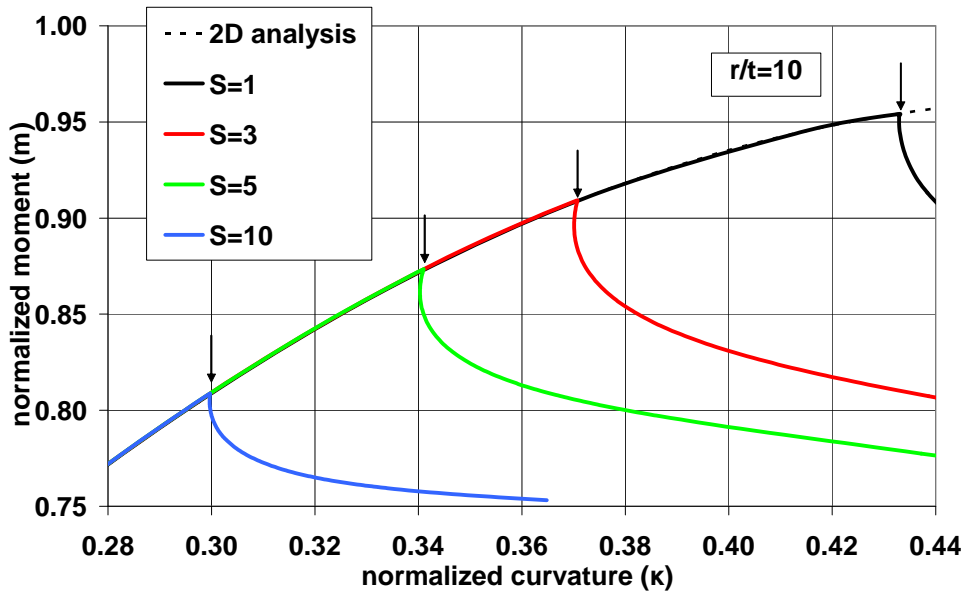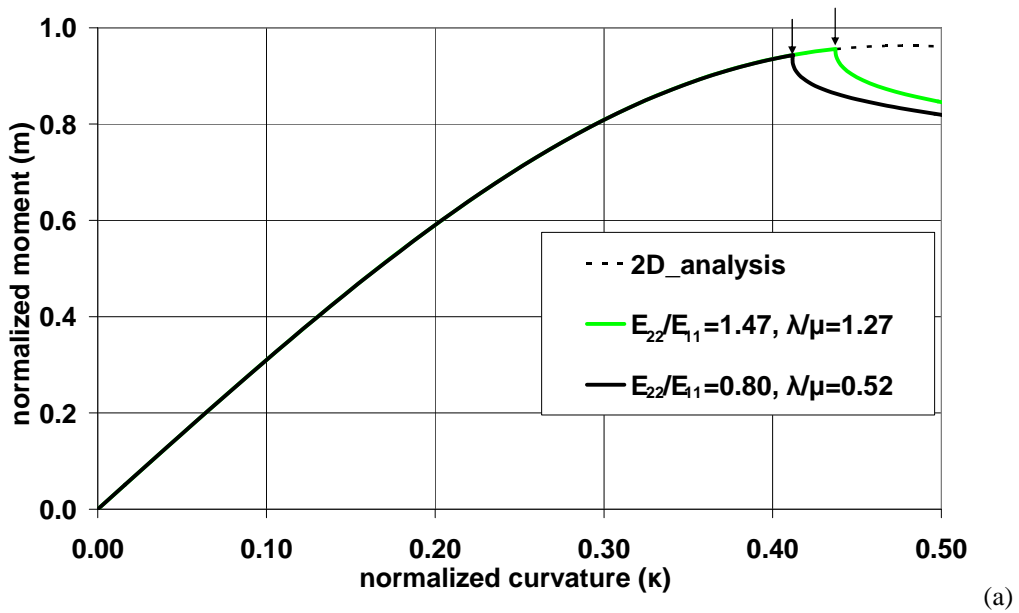**Fig. 89 Numerical results for different values of anisotropy parameter S (r/t =720)**

134

Fig. 90 Finite element results of the response of a non-pressurized cylinder for different values of anisotropy parameter S (r/t =10), arrows '↓' stand for bifurcation points

(a)

135

(b)
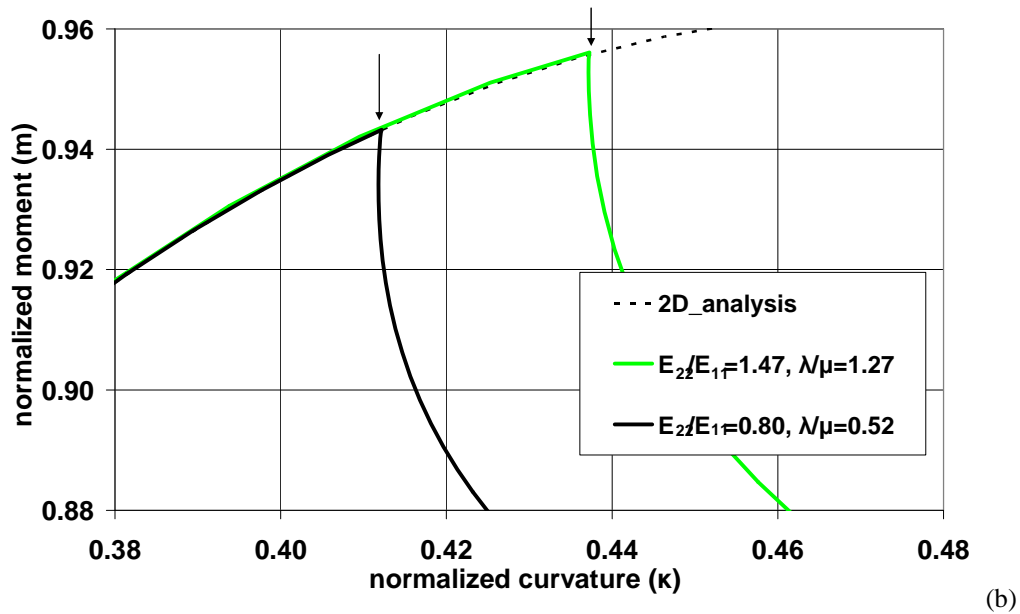
Fig. 91 Buckling analysis of cylinders with mechanical properties as described in [95]; arrows '↓' indicate buckling points (r/t =10); (a) entire $m-\kappa$ path and (b) detail at bifurcation
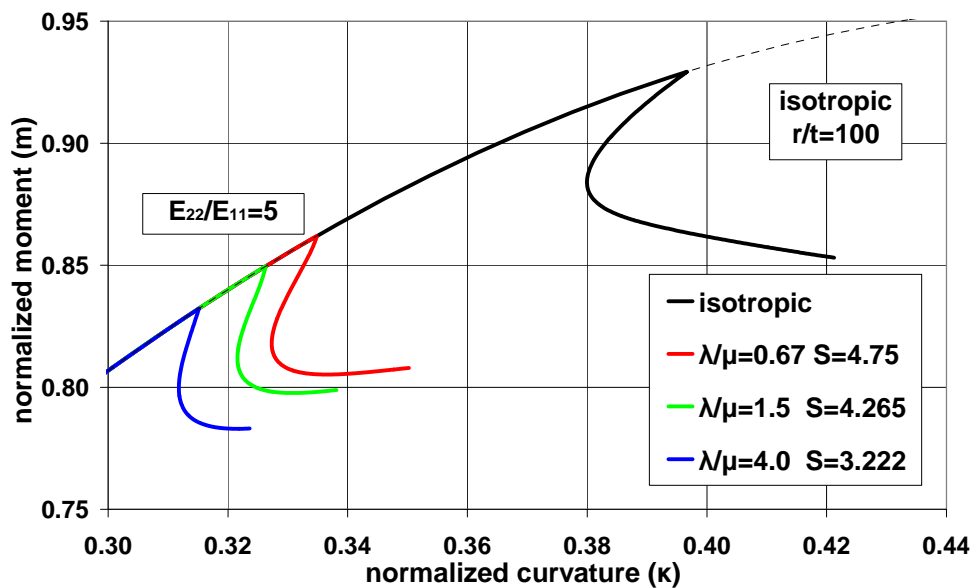
Fig. 92 Buckling analysis for three different λ/μ values keeping the $\bar{q}^2 = E_{22}/E_{11}$ parameter constant

Fig. 85 shows the dependence of the buckling (bifurcation) point on the value of the λ/μ ratio, keeping the E_{22}/E_{11} ratio constant (constant parameter $\bar{q}^2$). These results indicate that the λ/μ ratio has no effect on the bending response of isotropic cylinders. However, when the longitudinal direction is reinforced with respect to the hoop direction, buckling occurs at lower values of κ_{cr} as the value of the λ/μ ratio increases. It is worth mentioning that the λ/μ ratio

136

is controlled by the Poisson's ratio ν_{21}, as shown by equation (2.90), and can be expressed as follows:

$$\frac{\lambda}{\mu} = \frac{2\nu_{21}}{1 - 2\nu_{21}} \qquad (6.15)$$

Next, a simple analytical formulation, as in Chapter 5, is employed, adopting the ''equivalent cylinder'' concept, initially proposed in [96]. This analytical methodology is extended herein to analyze uniform wrinkling bifurcation of transversely isotropic cylinders. The prebuckling state of stress and deformation are expressed by (6.9)-(6.10). Furthermore, the buckling zone location is assumed in the vicinity of $\theta = \pi/2$. Following the same procedure adopted for isotropic cylinders, one readily obtains the same third-order algebraic equation for the critical curvature κ_{cr}:

$$\kappa_{cr}\left(1 - \frac{1}{1-f}\kappa_{cr}^2\right) - \frac{1}{\sqrt{3}}\left(1 - \frac{3}{1-f}\kappa_{cr}^2\right) = 0 \qquad (6.16)$$

which has the following closed-form solution:

$$\kappa_{cr} = \frac{1}{\sqrt{3}} - \frac{2}{3}\sqrt{abs[3(2-f)]}\ \cos\left(\frac{\pi}{3} + \frac{1}{3}\arccos\left[\frac{3\sqrt{3}}{abs[3(2-f)]^{3/2}}\right]\right) \qquad (6.17)$$

It is noted that the critical value of the normalized curvature κ_{cr} predicted by (6.17) is independent of the level of anisotropy S. Fig. 88 and Fig. 89 show that this critical curvature is a good prediction of the corresponding critical value calculated from the nonlinear finite element technique for isotropic or nearly isotropic cylinders. The prediction is particularly good for thin-walled cylinders. These figures indicate that, in the absence of pressure $f = 0$, the value $\kappa_{cr} = 0.3811$ obtained from analytical formula (6.17) is a reasonable estimate for relatively low levels of anisotropy ($S < 3$) and thin-walled cylinders. On the other hand, for higher levels of anisotropy and for thick cylinders (Fig. 90) $\kappa_{cr} = 0.3811$ provides a rather poor prediction of the critical curvature.

These observations lead to the conclusion that for high values of anisotropy the concept of ''local buckling'' hypothesis, which assumes no variation of stresses and strains in the hoop direction within the buckling zone, loses its applicability. Fig. 93 and Fig. 94 provide good evidence for this argument, showing the buckling modes of an isotropic cylinder ($S = 1$) and two cases of anisotropy ($S = 3$ and 10) for two r/t ratios ($r/t = 10$ and 720). The mode for the isotropic case is characterized by a smooth buckle in the hoop direction located around $\theta = \pi/2$ location, that ''dies out'' rather quickly (especially for thin-walled cylinders). On the other hand, the buckling modes for the anisotropic cases have the form of multiple waves within the compression zone. Those waves become more pronounced when the value of the

137

anisotropy parameter S increases and therefore the variation in the hoop direction is more significant.

(s =1, r/t =10)

(s =3, r/t =10)

(s =10, r/t =10)

Fig. 93 Buckling modes for a thick cylinder (r/t =10); higher values of anisotropy parameter

S **result in greater variation in the hoop direction**

138

(s =1, r/t =720)

(s =3, r/t =720)
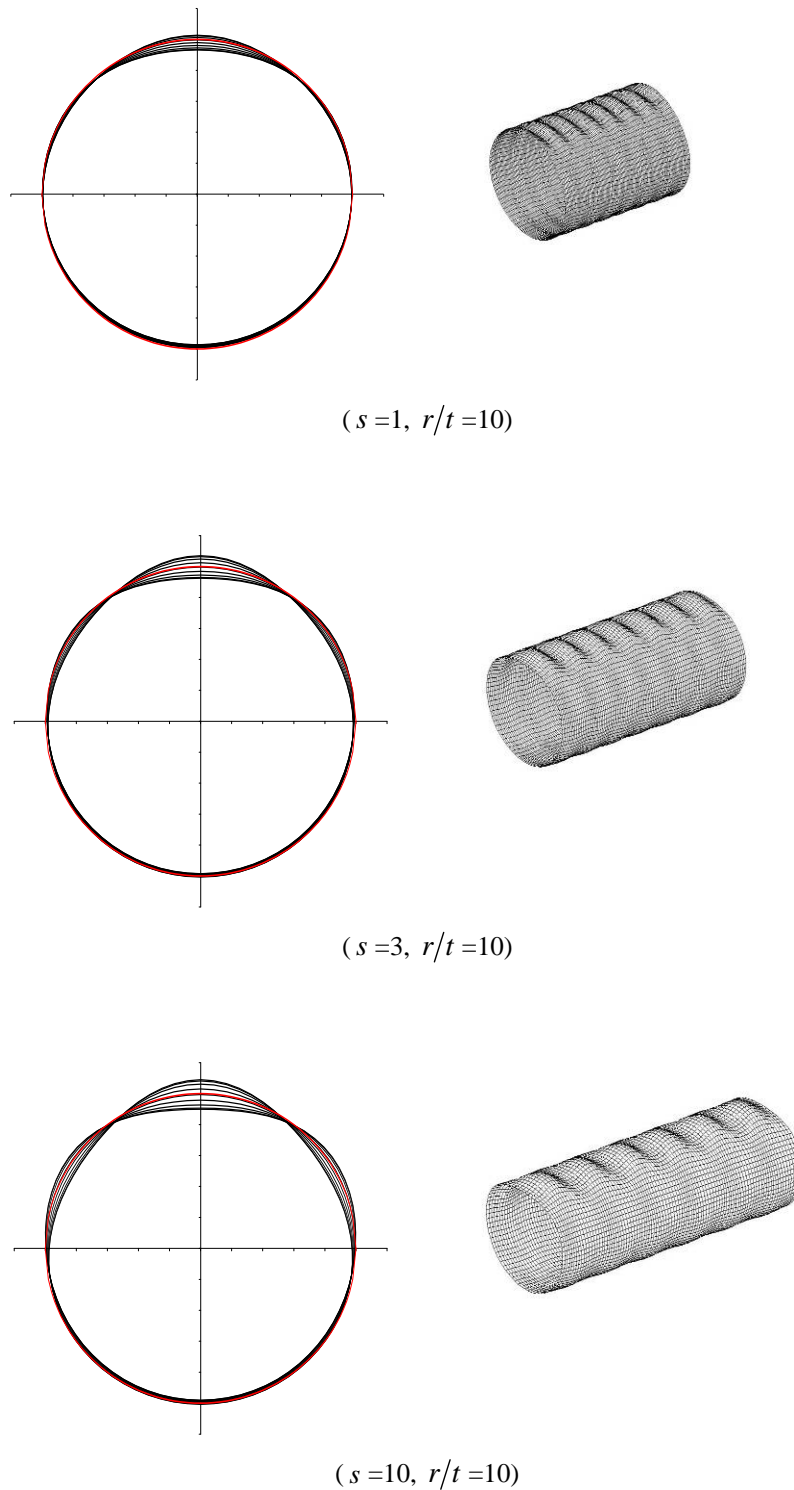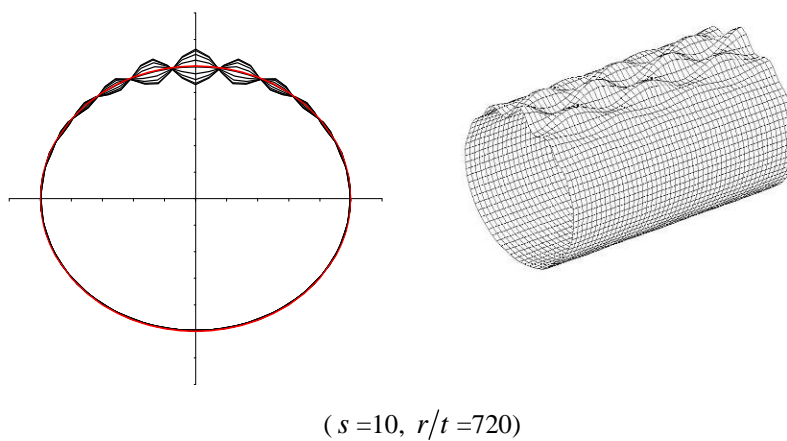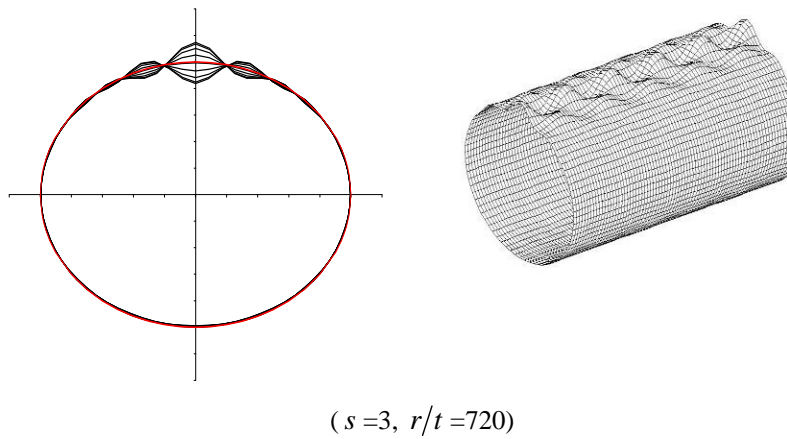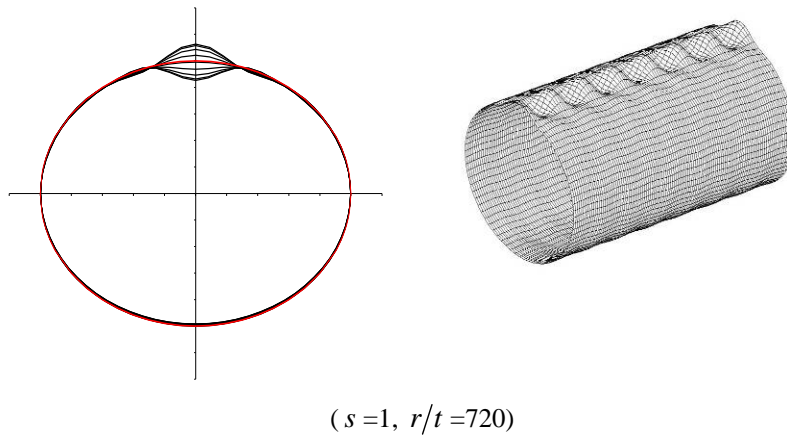

(s =10, r/t =720)

Fig. 94 Buckling modes for a thin cylinder r/t =10, higher values of anisotropy parameter S result in greater variation in the hoop direction

Furthermore, the variation of the buckling wavelengths, with respect to the level of anisotropy, is shown in Fig. 95. A significant dependence of the value of L_{hw} in terms of anisotropy level is observed. This variation is more significant for thicker cylinders and especially when anisotropy effects are more pronounce. In these cases the ''local-buckling'' hypothesis is longer applicable, as it can be confirmed by Fig. 93 and Fig. 94. It is noted that the buckling half-wavelength L_{hw} is normalized by the cylinder diameter D.
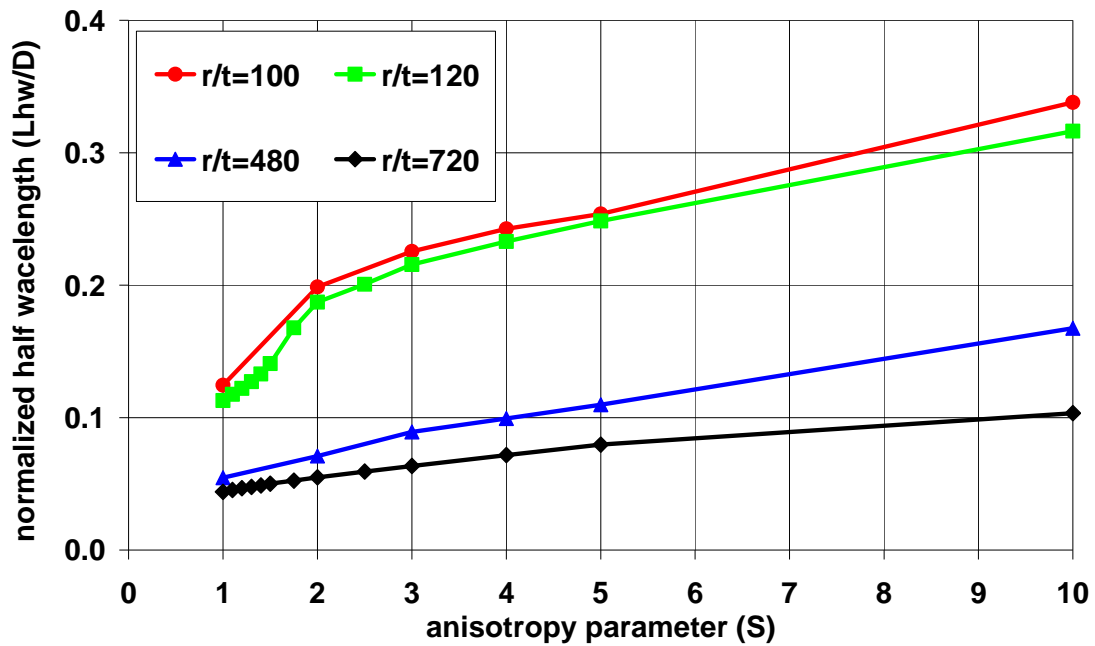
Fig. 95 Numerical results of the buckling half-wavelengths with respect to anisotropy level S

6.4 Imperfection Sensitivity

The influence of initial imperfections is examined on the bending response of initially straight transversely-isotropic cylinders. The initial imperfections are assumed periodic, in the form of the buckling mode, obtained from an eigenvalue analysis on the pre-buckling path at the stage where bifurcation occurs. These instability modes were presented in Fig. 93 and Fig. 94. The imperfection amplitude ξ is defined as previously by the ratio of the total wave height W_0 over the cylinder thickness t ($\xi = W_0/t$).

As shown in an earlier section, the post-buckling behavior of perfect transversely-isotropic cylinders is analogous to the behavior of isotropic cylinders, which exhibit a snap-back behavior and this indicates a sensitivity of the behavior in the presence of initial imperfections. Therefore, a sensitivity of the behavior is expected in the presence of initial imperfections. Numerical results on transversely isotropic cylinders subjected to bending show that the value

140

of the ultimate bending moment $m_{\max}$ is reduced as the imperfection amplitude increases and the buckling response becomes smoother.

The bending behavior of cylinders with r/t equal to 100 and 720 is shown in Fig. 96 and Fig. 97, respectively, in the presence of initial imperfections. It is numerically confirmed that very small geometric imperfections (i.e. imperfections with amplitude equal to a small fraction of the cylinder wall thickness) may influence the maximum bending capacity.

The maximum moment reduction in these cases is depicted in Fig. 98 and Fig. 99, in terms of initial imperfection amplitude. Assuming that the variation of the $m_{\max}/m_{cr}$ ratio in terms of ξ follows an exponential expression of the form:

$$m_{\max}/m_{cr} = 1 - C\xi^n \tag{6.18}$$

it can be easily shown that the value of the exponent n that fits the numerical results is equal to 2/3, whereas the value of C depends on the r/t ratio and the value of anisotropy level S. The value of the exponent $n=2/3$ is in complete accordance with the corresponding value from the asymptotic theory [41].

(a)

141

(b)
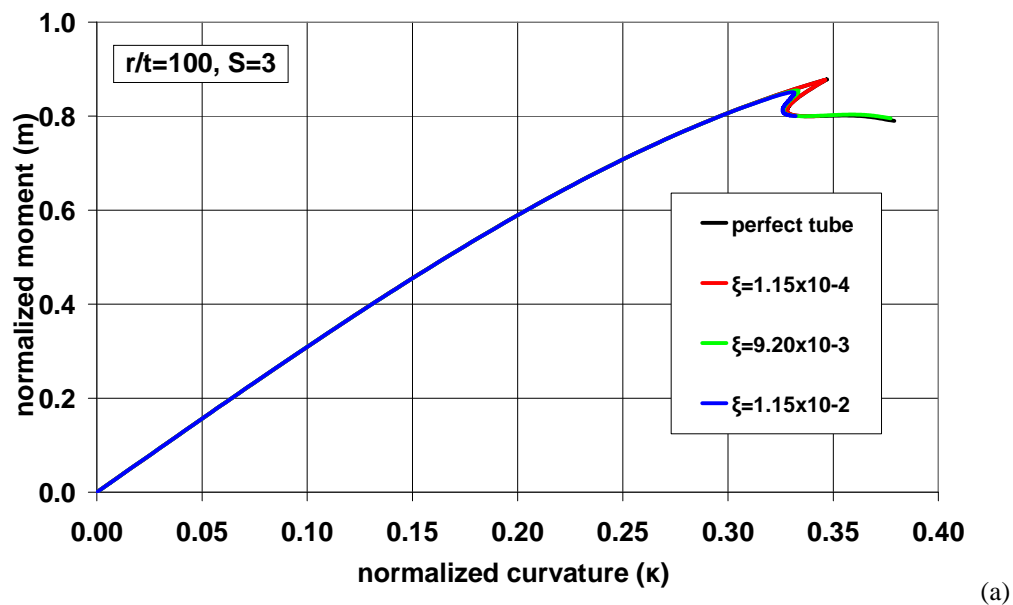
Fig. 96 Imperfection sensitivity of a transversely-isotropic cylinder; (a) entire $m - \kappa$ path and (b) detail at bifurcation

Fig. 97 Detail of the imperfection sensitivity of a transversely-isotropic cylinder (r/t =720, S =3)

142

Fig. 98 Imperfection sensitivity versus imperfection amplitude (r/t **=100)**

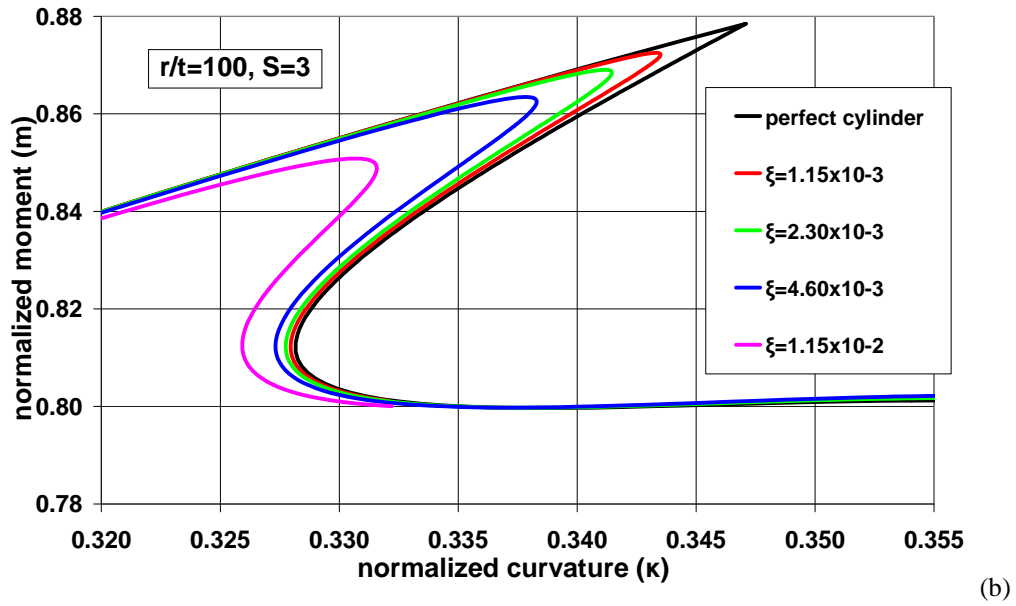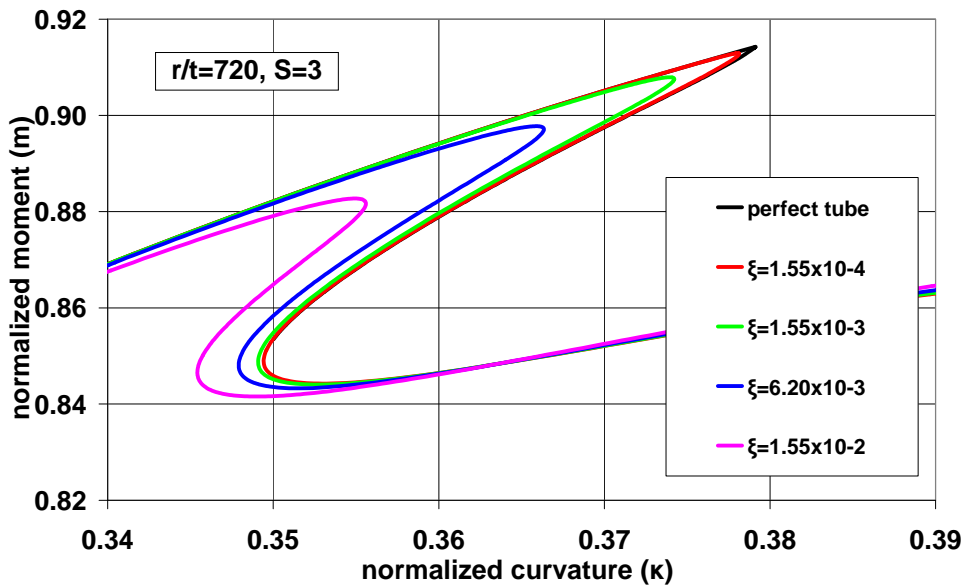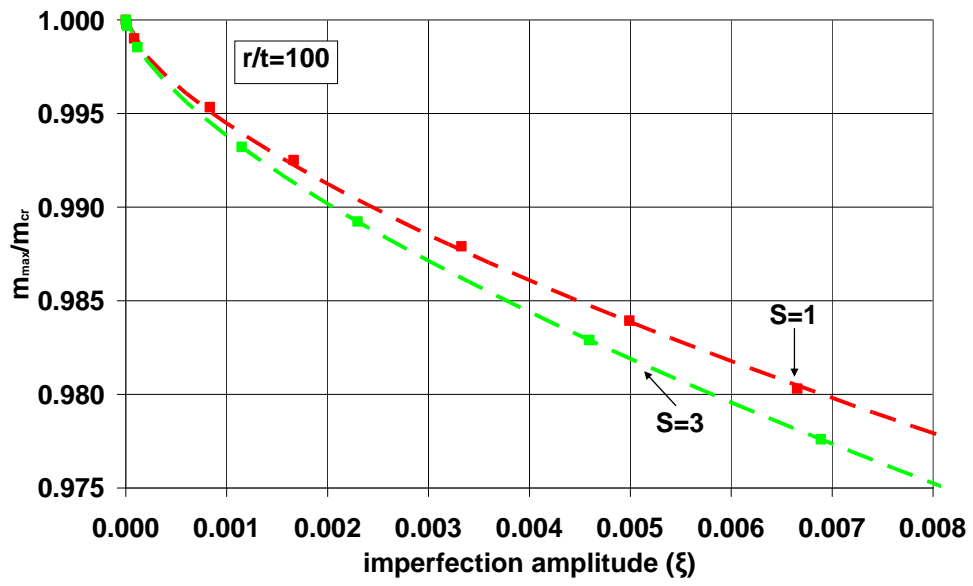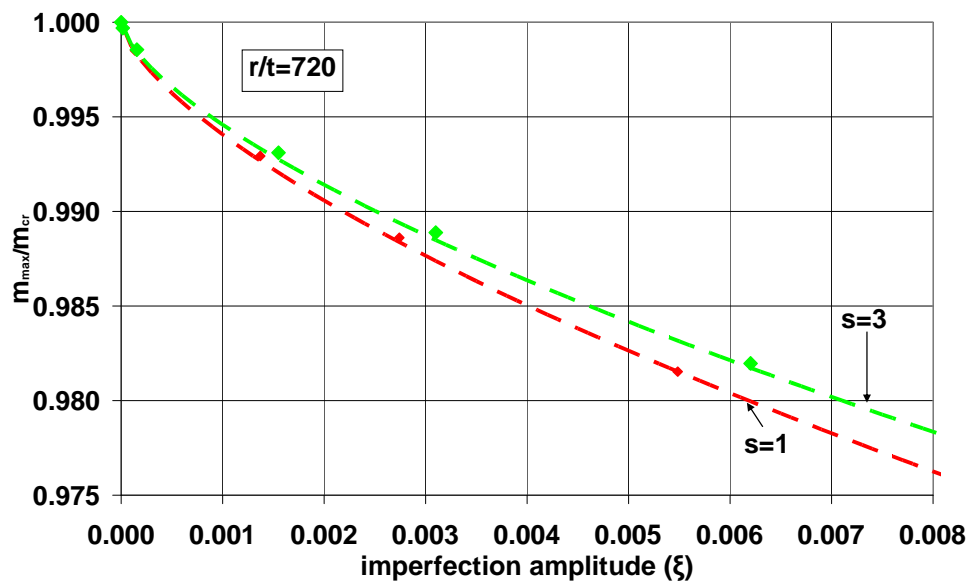**Fig. 99 Imperfection sensitivity versus imperfection amplitude (** r/t **=720)**

143

Chapter 7

BENDING OF THIN-WALLED CYLINDERS IN THE INELASTIC RANGE

Bending instabilities in long metal thin-walled cylinders, bent beyond the elastic regime, are examined in the present Chapter, extending the results of Chapters 5 and 6 for elastic cylinders. This constitutes a problem with significant applications for the structural integrity of chimneys, tubular towers and low-pressure water pipelines. The bending response is analyzed numerically, using the ''tube-element'' technique and appropriate constitutive models to account for inelastic material behavior. The numerical results, initially, refer to the prediction of plastic bifurcation loads into a uniform wrinkling state, and the corresponding post-buckling response. Subsequently, the phenomenon of buckling localization in metal cylinders is examined.

Equation Section 7

7.1 Introduction

The problem of inelastic bending involves both material and geometric nonlinearities. Material nonlinearities are due to the elastic-plastic behavior of the material, whereas geometric nonlinearity arises since the early loading steps from the distortion of the cross-section along the cylinder (ovalization-Brazier effect [62]). As bending proceeds, the geometric nonlinearity becomes stronger with the appearance and growth of ripples on the compression zone. Eventually, the combination of material inelastic behavior and wrinkle formulation leads to the catastrophic collapse of the cylinder in the form of localized buckling deformation. The present work focuses on the simulation of the mechanical behavior of thin-walled cylinders, accounting for the above phenomena.

Previous experimental works have confirmed that upon buckling, thinner cylinders develop short wavelength periodic wrinkles on the compressed side of the shell, which very soon result in local buckling and sudden collapse of the shell [97], [98], [99]. In thin-walled cylinders, this buckling collapse mechanism usually takes place before a limit moment is reached on the ovalization path and, therefore, bifurcation instability is considered to be the critical failure mode, as opposed to relatively thick cylinders, such as those employed in marine pipelines, where an ovalization limit point is reached before cylinder wall wrinkles and ovalization constitutes the governing instability type [97], [100].

144

A numerical methodology for analyzing the ovalization process in the plastic range was first introduced by Ades [101]. In this study the limit (ovalization) moment of an elastic-plastic long cylinder was obtained, assuming that the cross-section ovalizes into an elliptical shape, and considering the J_2 deformation theory of plasticity to describe inelastic material behavior. This study can be considered as a simple and approximate extension of Brazier's [62] solution in the inelastic range. The limit point obtained in [101] was found to occur at lower levels compared to the corresponding values of limit moment and curvature in the elastic case. Gellin [102] considered J_2 deformation theory of plasticity to determine the limit moment and the corresponding curvature. The basic model was related to a uniform ovalization along the cylinder axis, where nonlinear kinematic relations from ring deformation theory were employed, enforcing the condition of inextentionality. Analogous formulations for ovalization instability were considered by Fabian [103], with the J_2 flow theory to be incorporated in the solution methodology. Motivated by the mechanical behavior of offshore pipelines, ovalization instability in relatively thick cylinders ($7.5 < r/t < 40$) was extensively examined by Shaw and Kyriakides [104], considering extentional ring kinematics and incremental (flow) plasticity models. The results obtained in [104] were presented in the form of interaction diagrams of pressure versus curvature. This work was further extended by Corona and Kyriakides [105] and the interaction diagrams presented in [105] were supported by experimental data ($r/t = 12.3$ and 17.4). Analogous interaction curves and conclusions were drawn in the finite-element investigation of Karamanos and Tassoulas [106]. The numerical results of this study were found to be in very good agreement with the experimental data reported in [105]. Theoretical models for the ovalization mechanism in circular cylinders under bending were also depicted by Elchalakani et al. [99], where the validity of these models was confirmed with experiments ($10 < r/t < 20$). These studies have shown that the instability of ovalization in the inelastic region has a nonlinear behavior, which can not be described by closed-form analytical expressions.

This bifurcation from the ovalization primary path occurs either before or beyond reaching a maximum (ovalization) load, depending on cylinder thickness. This results in the development of axial ripples in the compression zone, and expresses another governing instability mode, referred to as buckling. Due to the presence of material and geometric nonlinearities this instability requires a numerical investigation. A tool for detecting bifurcation and uniqueness of solution in the plastic range is offered by the theory of Hill [32], [107], which employs the concept of the so-called ''comparison solid'' as described in section 2.8. However, it has been shown that, in general, buckling predictions based on this theory are sensitive to the choice of plasticity constitutive equation. Generally, bifurcation loads in thin-walled structures calculated using flow theories of plasticity consistently overestimated buckling loads obtained in tests. On the other hand, buckling predictions based on deformation theories have been shown consistent

145

with test results for a range of loading paths in the vicinity of proportional loading. In the early studies of Batdorf [35] and Sanders [108] it was suggested that this difficulty could overcome if the smooth yield surface was discarded, and a sharp corner was developed in the yield surface at the loading point. A more sophisticated flow theory that permits corner formation, namely the slip theory, was suggested by Batdorf and Budiansky [109]. Furthermore, Christoffersen and Hutchinson [110] proposed a new ''corner yield surface'' theory, which has been applied for shell bifurcation calculations, post-buckling response and imperfection sensitivity (e.g. [111], [112]).

Numerical studies on the uniform wrinkling of bent cylinders were reported by Gellin [102], where bifurcation in the inelastic range was detected at loads lower than the limit point ($30 < r/t < 100$). Bifurcation was investigated in a way similar to the elastic study of Fabian [41] but no further details on the numerical technique were given in [102]. The numerical model was based on the implementation of J_2 flow theory for the moment-curvature path, while J_2 deformation theory was adopted for bifurcation calculations. A more detailed study for the inelastic cylinder stability under the combined action of bending and pressure was presented in a subsequent study of Fabian [103], based on an asymptotic analysis for smooth yield surfaces and following a J_2 flow theory

Experiments on plastic buckling of thick steel and aluminium cylinders ($30 < D/t < 80$) were presented by Reddy [113] to elucidate the buckling process for the case of monotonic pure bending. It was found that for this range buckling takes place well into the inelastic range. In those tests, a considerable scatter was observed in terms of critical strains. An attempt was made to compare the corresponding wavelengths with Batterman's [34] analytical expressions for axially loaded inelastic tubes under uniform compression, using both J_2 deformation and J_2 flow theories of plasticity.

An extensive experimental investigation on uniform wrinkling of thick-walled metal cylinders was reported by Kyriakides and Ju [97]. Carefully controlled and monitored bending experiments were conducted with aluminium cylinders of r/t ratios ranging between 9.8 and 30, bent up to failure. Bifurcation instability was found to occur in the plastic regime before or after the ovalization limit point, dependent on the D/t ratio, and confirming Reddy's [113] observations regarding the values of buckling wavelengths. In a subsequent work of Ju and Kyriakides [81], a semi-numerical technique was presented and the results were compared directly with the experimental results reported in [97]. It is interesting to note that, in that study, the inelastic material behavior was modelled through the J_2 flow plasticity theory with isotropic hardening, whereas the detection of bifurcation was examined using the J_2 deformation plasticity moduli. The overprediction of the calculated wrinkle wavelengths reported in [81] was recently re-examined in the work of Corona et al. [114], and was attributed to the effects of

146

anisotropy. The book of Kyriakides and Corona [115] constitutes a notable publication that addresses the problem of buckling and collapse of inelastic cylinders, and summarises the above experimental and semi-numerical studies.

Karamanos and Tassoulas [116], [117] also investigated the inelastic buckling response of cylindrical shells (r/t =9 and 17.4) introducing a nonlinear finite element, referred to as ''tube-element'', in its original form. The ''tube-element'' is also employed and further enhanced for the purposes of the present study. To verify the validity of this numerical formulation, computational results were compared with experimental data from both long and stub tubular beam-column tests [118], [119], [120]. The study was motivated by the structural integrity of relatively thick deep offshore tubular members. It was shown that, beyond the limit point, the tube response was characterized by a localization of ovalization, which upon formation grows rapidly, reducing the moment capacity of the member and resulting in its failure.

In addition to limit load and uniform wrinkling instabilities, experiments have demonstrated that shell bending failure is ultimately characterized by another mode; distinct localization of deformations has been observed in a number of experiments [97], [98], [99] especially for thin-walled cylinders, where the final collapse configuration involves one main buckle, rather than periodic wavy-type buckle patterns. This collapse mechanism can be considered as an abrupt deviation from the periodic buckling patterns. Upon localization, cylinder deformation concentrates in one small region, resulting in the structural failure of the shell. Several approaches to analyze the development of localization can be found in [112] for the case of inelastic cylinders under uniform axial compression and in [111], [121] for cylindrical panels. Moreover, in [121] simple models have been presented in an attempt to associate load maximum and the localization of buckling patterns.

To determine initial post-bifurcation behavior of structures undergoing inelastic deformations an extension of Koiter's theory [3] is a rather complicated task because of elastic-plastic material behavior. An attempt to develop such an asymptotic theory in the plastic range has been proposed by Hutchinson [33] for the particular case of smooth yield surfaces and for a single-mode buckling. In particular, Hutchinson presented an asymptotic expression for the load parameter λ in terms of the amplitude η is a perturbation parameter of the eigenmode, associated with the lowest bifurcation load λ_{cr}, as follows:

$$\lambda = \lambda_{cr} + \lambda_1 \eta + \lambda_2 \eta^{1+\beta} + ... \tag{7.1}$$

In this relation, written in the framework of Koiter's theory (Appendix), λ_1 has been shown to be a positive constant in general, showing that bifurcation takes place under increasing load, whereas λ_2 is found to be a negative constant. The term containing coefficient λ_2 and exponent

147

β makes a contribution only within the elastically unloaded zone. Coefficients λ_1, λ_2 and exponent β are to be determined for each specific problem.

In the framework of the present study, the problem of inelastic tube bending is examined using the numerical technique presented in Chapter 2. Various aspects of bent cylinder response are discussed including buckling moment, post-buckling behavior, imperfection sensitivity and buckling localization. The ''tube-element'' is employed so that this problem and the mechanisms that govern it become more accessible. In particular, the numerical approach is based on a large-strain hypoelastic J_2 flow plasticity model; whereas bifurcation on the primary $m - \kappa$ path to a uniform wrinkling deformation pattern is detected using the comparison solid concept and employing the J_2 deformation theory moduli (section 2.8). Furthermore, uniform wrinkle growth and localization of buckling patterns are investigated numerically.

7.2 Ovalization Instability

The first problem examined in this study concnerns a long thin-walled cylinder (r/t =120) bent in the inelastic range with no variation of deformation along the length, so that end effects are neglected.. Under this assumption the cylinder exhibits ovalization and limit-moment instability, whereas wrinkling bifurcation is not possible. Therefore, a two-dimensional analysis is conducted, restraining the out-of-plane (warping) cross-sectional deformation parameters c_n, γ_n (defined in section 2.6). The ovalized pre-buckling equilibrium path is calculated using the J_2 flow theory to account for inelastic effects.

Normalization values similar to the ones used in the analysis of elastic cylinders are employed for moment, curvature and stress. The values of moment M , curvature k and stress σ are normalized by $M_e = Ert^2/\sqrt{1-v^2}$, $k_N = t/(r^2\sqrt{1-v^2})$ and $\sigma_e = Et/(r\sqrt{1-v^2})$ respectively.

Using the closed-form expressions obtained in Chapter 5 for elastic cylinders, it is possible to estimate the curvature κ_y at which first yield occurs, considering ovalization and pressure effects. In particular, longitudinal and hoop stresses in the absence of pressure are described by (7.2) and (7.3) (given in section 5.1.2):

$$\frac{\sigma_x(\theta)}{\sigma_e} = \kappa\left[\left(1 - \frac{3}{4}\kappa^2\right)\sin\theta + \frac{1}{4}\kappa^2\sin 3\theta\right] \tag{7.2}$$

$$\frac{\sigma_\theta(\theta, \rho)}{\sigma_e} = \frac{3}{\sqrt{1-v^2}}\left(\frac{\rho}{t}\right)\kappa^2\cos 2\theta \tag{7.3}$$

Taking into account that the maximum stresses $\sigma_x(\theta)$ and $\sigma_\theta(\theta, \rho)$ are located at $\theta = \pi/2$ and $\rho = \pm t/2$, the above expressions can be written as:

148

$$\sigma_x = \sigma_e \kappa \left(1 - \kappa^2\right) \tag{7.4}$$

$$\sigma_\theta = \pm \sigma_e \frac{1}{\sqrt{1-v^2}} \frac{3\kappa^2}{2} \tag{7.5}$$

Assuming a von Mises yield criterion, as described below:

$$\sigma_x^2 + \sigma_\theta^2 - \sigma_x \sigma_\theta = \sigma_y^2 \tag{7.6}$$

and inserting (7.4)-(7.5) into (7.6) one results in an algebraic equation in terms of the first-yield curvature κ_y can be calculated in terms of the value of yield stress σ_y. In Fig. 100 the first-yield curvature κ_y is shown graphically for an unpressurized cylinder, in terms of the geometric/material parameter $S = (\sigma_y r / Et)\sqrt{1-v^2}$. The dotted line corresponds to the yield curvature κ_y calculated from (7.6), accounting for ovalization, whereas the continuous red line represents the yield curvature when ovalization is neglected. In the latter case, employing simple strength of materials formulae ($\sigma = Mr/I$, $M = EIk$) one readily obtains $\kappa_y = S$. For a yield stress σ_y equal to 300 MPa the values of S considered in the horizontal axis of Fig. 100 correspond to r/t ratios ranging between 50 and 300. Therefore, in the absence of a closed formula describing first yield curvature considering ovalization effects, expressions (7.4)-(7.6) can be conservatively used to give an estimate of κ_y.

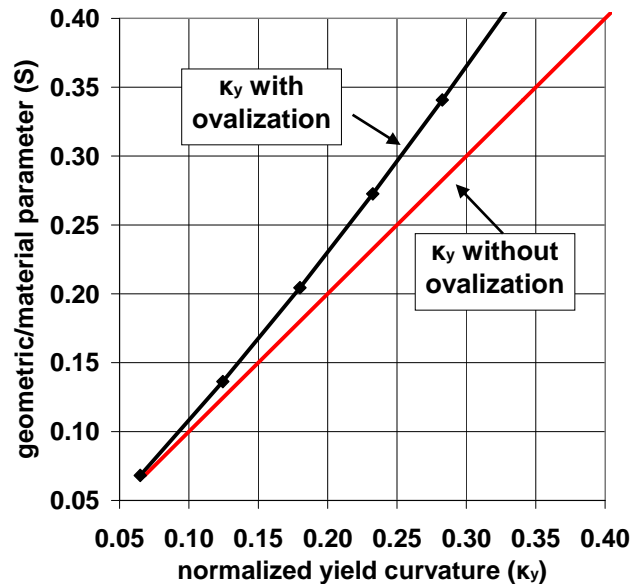**Fig. 100 Variation of yield curvature κ_y with respect to the geometric/material parameter**

$S = (\sigma_y r / Et)\sqrt{1-v^2}$ **, considering or not ovalization effects, represented by dotted and continuous**

lines respectively

149

In Fig. 101, the ovalization $m - \kappa$ path for thin-walled long inelastic cylinders is shown in terms of the applied curvature, for three different values of the S parameter. These results show that beyond yielding the moment ovalization capacity of the cylinders is decreased, resulting in a limit moment, which is lower than the limit moment of the corresponding elastic cylinder.
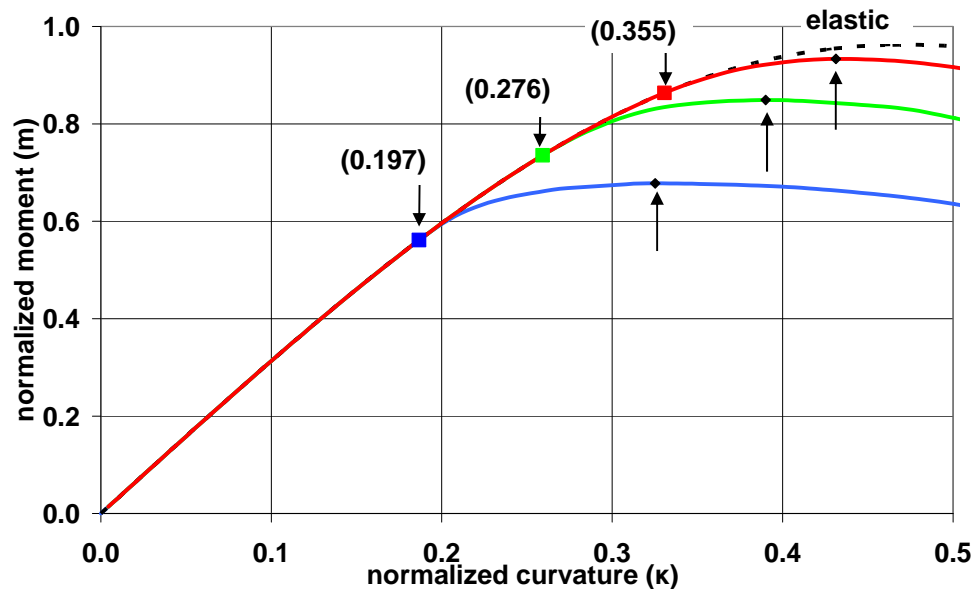

Fig. 101 Ovalization primary path of inelastic cylinders for different values of parameter S under bending loads and comparison with elastic cylinder solution; arrows (↓) denote the first yielding points and arrows (↑) denote limit points, both obtained by the finite elements technique ($r/t = 120$)

7.3 Uniform Wrinkling

In this section the possibility of bifurcation on the ovalization prebuckling $m - \kappa$ path is investigated for thin-walled cylinders. In this analysis, only one half-wavelength L_{hw} of the cylinder is considered, discretized with four ''tube-elements'', and appropriate periodic boundary conditions are imposed. The half-wavelength L_{hw} value is not known a priori and, therefore, a sequence of analyses is conducted for each case so that the actual wavelength corresponds to the 'earliest' bifurcation point on the primary path.

As discussed in section 2.8 the detection of bifurcation from the uniform-ovalized pre-buckling state to a uniform wrinkling state is based on the consideration of the positive definiteness of the quadratic functional F given by (2.177), and discretized as described in section 2.5. Previous studies have demonstrated the predicament of flow theory compared to the deformation theory in predicting reasonable bifurcation loads for various buckling problems.

150

Therefore, material moduli based in J_2 deformation theory are employed for the purposes of the present study.

The eigenmode associated with the zero eigenvalue of the discretized functional referred to as ''buckling mode'' (Fig. 102a) can be imposed as an initial geometric imperfection. The imperfection amplitude ξ is defined, similar to the previous Chapters, by the total wave height W_0 normalized by the cylinder thickness t, so that $\xi = W_0 / t$ (Fig. 102b). In the sequence, the initially imperfect cylinder can be analyzed, using a nonlinear step-by-step analysis that employs an arc-length algorithm. Regarding the numerical implementation of this procedure, a spherical arc-length algorithm is employed that monitors the increments of translational degrees of freedom $\Delta u_2^{(k)}, \Delta u_3^{(k)}$ at each node. Moreover, a 16th degree expansion for the discretized in-plane and out-of-plane displacements of the reference line $w(\theta), v(\theta), u(\theta)$ and $\gamma(\theta)$, with 23 equally spaced integration points around the half-circumference, is adopted.

(a)   **(b)**
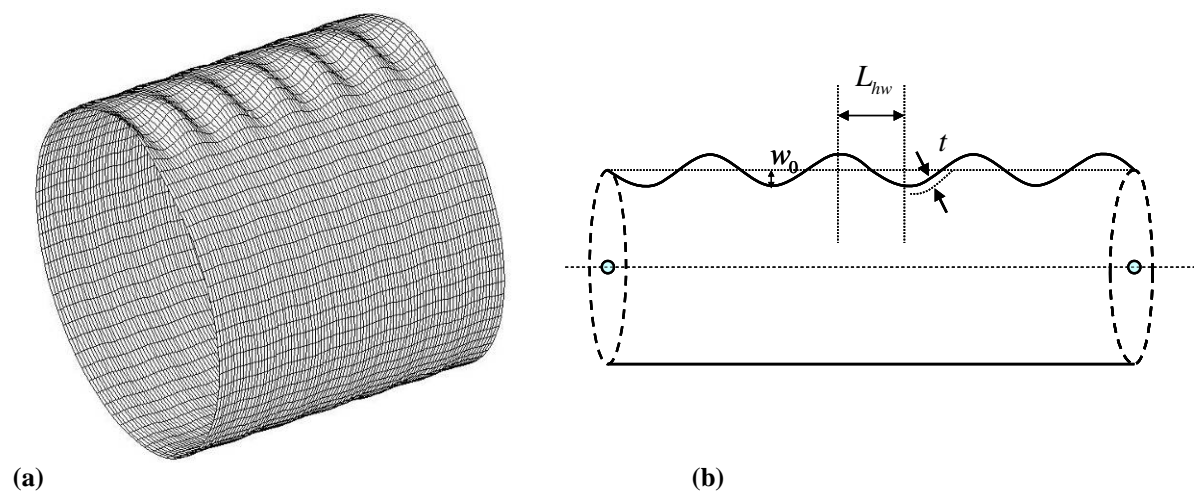
Fig. 102 Buckling mode of an elastic-perfectly plastic cylinder; (a) buckling mode that corresponds to uniform wrinkling, (b) amplitude of the initial imperfection (r / t =120, σ_y / E =0.0023)

In Fig. 103 the primary ovalization path is plotted with dashed lines, and the bifurcation point on this path is denoted. Uniform wrinkling bifurcation precedes ovalization limit point and governs the structural behavior and this is in accordance with previous results (e.g. [81]) in thin-walled cylinders. The effect of initial geometric imperfections on the bending response is also given in Fig. 103. A first important observation is that the presence of very small initial wrinkling imperfections (i.e. imperfections of magnitude that corresponds to a small fraction of the wall thickness t) cause a significant decrease of bending stiffness of the cylinder.

151

Imperfection sensitivity in the inelastic range for a specific case is also examined, and the numerical results are shown in Fig. 104 (r/t=120 and σ_y/E=0.0023). The results indicate a reduction of the maximum moment for the case considered.
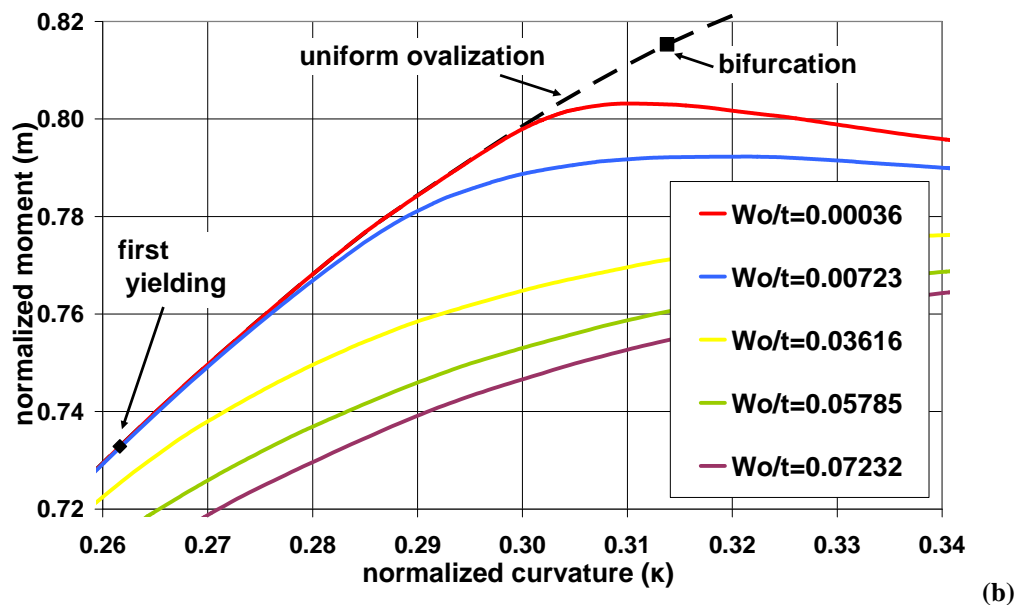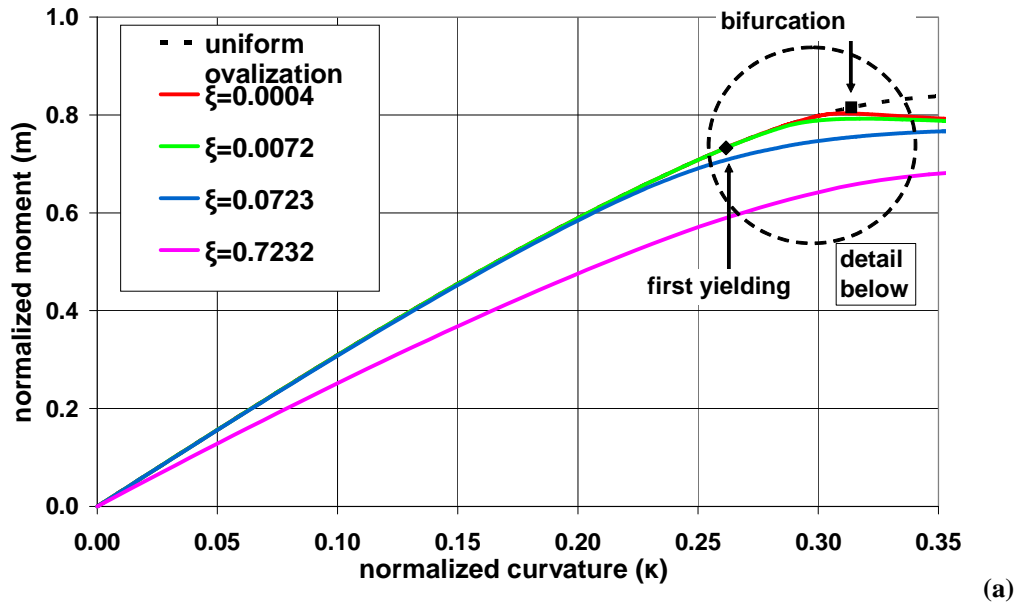

Fig. 103 Bending response of an elastic-perfectly plastic cylinder; (a) complete $m-\kappa$ path (b) detail at bifurcation point (r/t=120, σ_y/E=0.0023)
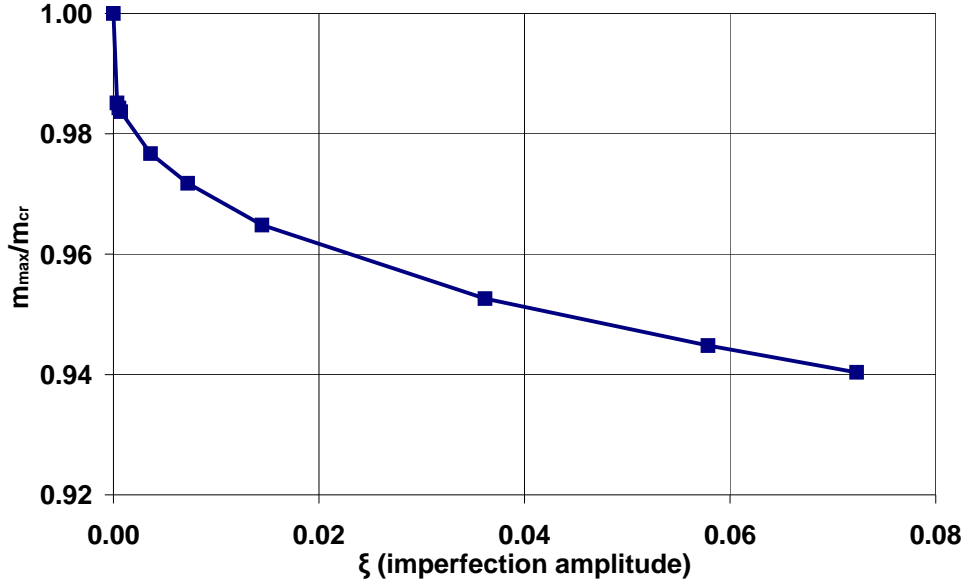
152

Fig. 104 Variation of m_{max}/m_{cr} **vs imperfection amplitude** ξ **(** r/t **=120,** σ_y/E **=0.0023)**

7.4 Localization of Buckling Patterns

In the previous results, bifurcation from a uniform ovalized configuration into a state of uniform axial wrinkling has been investigated. It was shown that thin-walled cylinders of high r/t ratios initially ovalize and, subsequently, short wavelength wrinkles are developed in the compression zone. However, these thin-walled cylinders soon after uniform wrinkles appear, exhibit localization of the buckling patterns and buckle locally in the form of a kink at a suddenly dropping moment.

In previous studies, localization of buckling deformation has been investigated for thick-walled tubular members under bending [114] and curved panels under axial compression [121]. In those studies a longer cylinder segment has been considered, which is m times multiple of the half wavelengths, and appropriate periodic end conditions are applied. In this initial configuration, an additional imperfection is imposed in the shape of the uniform wrinkling buckling mode, as described in the previous section, multiplied by the following factor that expresses localization:

$$f = 1 + \xi_L \cos\left(\frac{\pi z}{mL_{hw}}\right) \qquad (7.7)$$

where z is the coordinate along the cylinder axis of the three-wavelength cylinder, m is the number of half wavelengths considered within the segment and ξ_L is the imperfection parameter associated with localization mechanism, affecting the amplitude of the waves.

153

Clearly, if $\xi_L = 0$, uniform wrinkling conditions are imposed. It is noted, that the above approach is also adopted in the present work.

In Fig. 105 the non-uniform initial shape of the buckling mode, as expressed by (7.7), is illustrated. In this Figure, the cross-sectional displacements are magnified for visualization purposes. In Fig. 106 the $m - \kappa$ equilibrium curve for a steel cylinder with $r/t = 120$ and $\sigma_y / E = 0.0023$ are shown. A uniform initial imperfection with amplitude $\xi = 0.072$ in the form of the uniform wrinkling buckling mode is considered with two values of the localized imperfection parameter ξ_L ($\xi_L = 10^{-1}$ and 10^{-2}). The numerical results indicate that buckling patterns do localize. The presence of small amplitudes of the localization factor ξ_L affect significantly the bending response of the cylinder, and verify the experimental observations that localization of deformation is responsible for the sudden and catastrophic failure of the cylinder. The deformed configuration of the cylinder, at the development of localization, is given in Fig. 107 for $\xi_L = 10^{-2}$. The cylinder shape shows that a wrinkle, which is initially slightly larger than the other wrinkles, grows significantly more than the others, resulting in localization of the buckling pattern and sudden reduction of moment capacity.
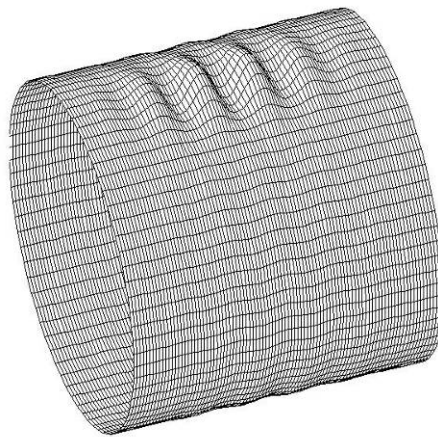
Fig. 105 The localized buckling mode for $\xi_L = 1$, where a magnification of the buckling patterns is applied for visualization purposes ($r/t = 120$, $\sigma_y / E = 0.0023$)

154

(a)

(b)
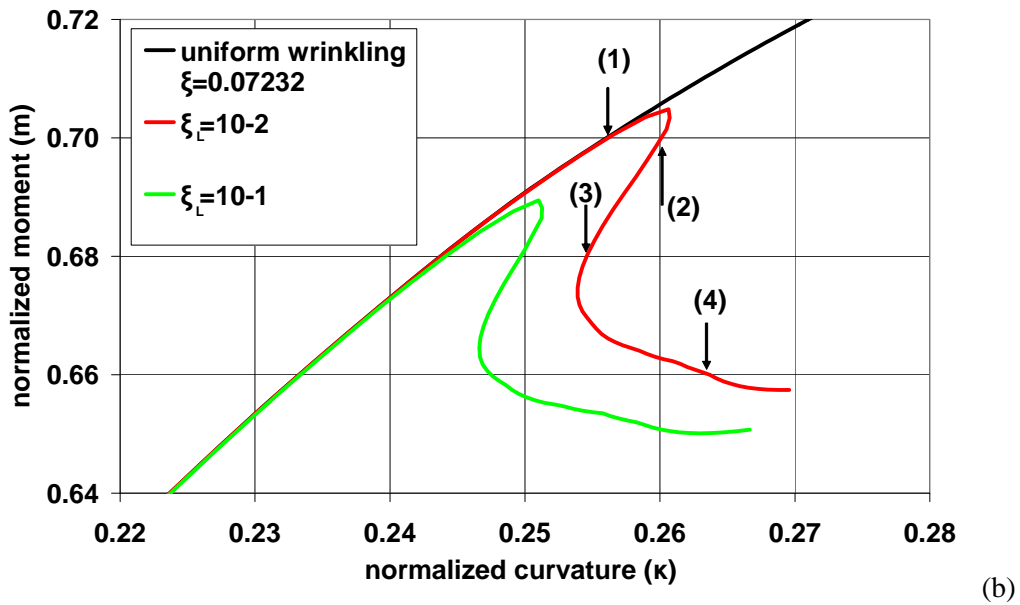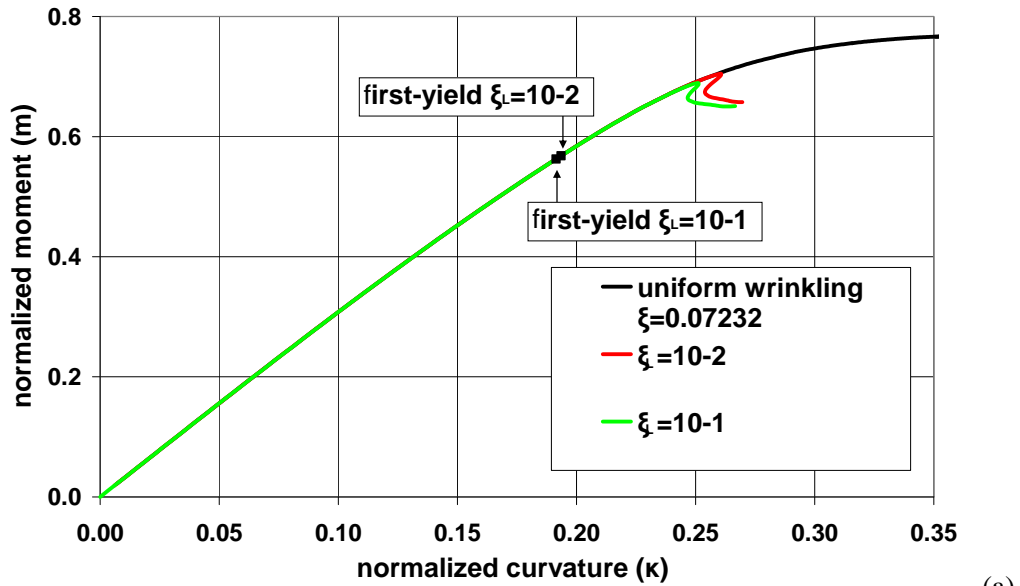
Fig. 106 Localization of deformation in a bent steel cylinder considering uniform ($\xi = 0.07$, $\xi_L = 0$) and localized ($\xi = 0.07$, $\xi_L = 10^{-1}$ and $\xi_L = 10^{-2}$) initial imperfections; (a) entire $m - \kappa$ paths and (b) detail at bifurcation point. ($r/t = 120$, $\sigma_y / E = 0.0023$)

155
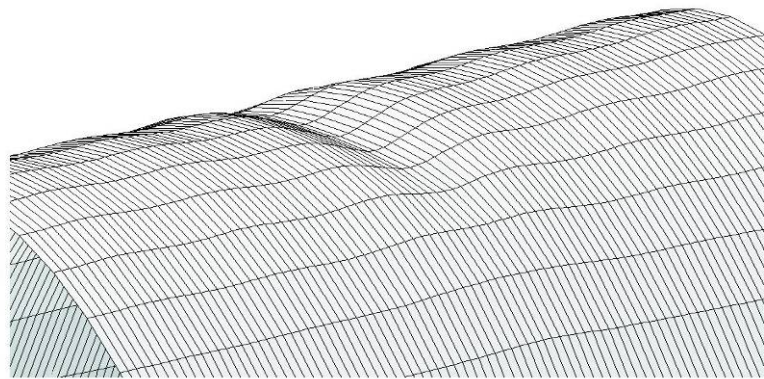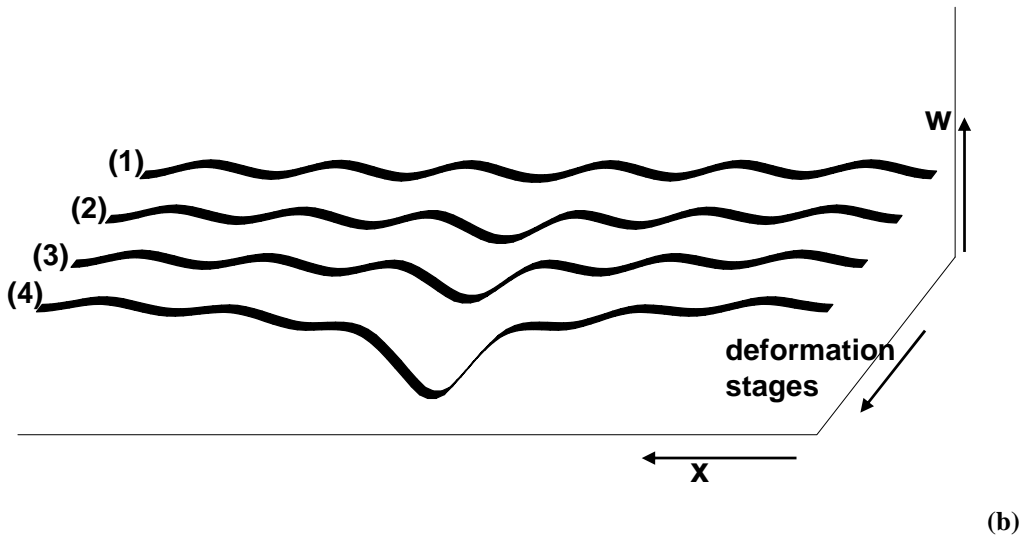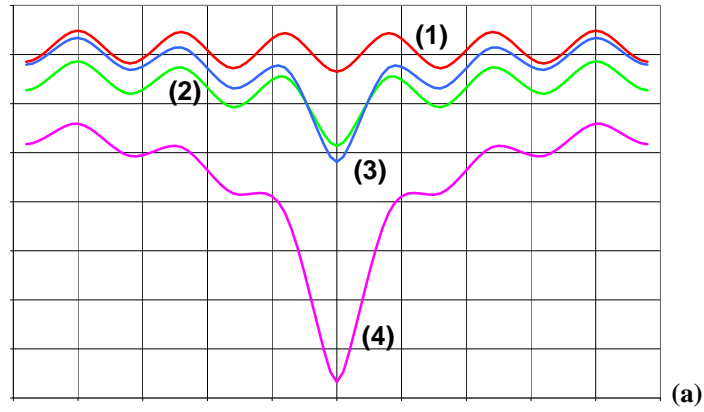
Fig. 107 Development of inelastic localization;(a) and (b) longitudinal strips at various deformation steps (c) deformed configuration at state (4) (r/t =**120,** σ_y/E =**0.0023,** ξ_L =**10^{-2}**)

156

Chapter 8

<u>CONCLUSIONS</u>

The present study concerns the stability analysis of long thin-walled cylinders, under structural loads and pressure. Bending loading was mainly investigated, whereas uniform axial compression was also analyzed. The work was motivated by the need for a better understanding and more accurate prediction of bifurcation and postbuckling response of thin-walled structures.

A numerical investigation of the problem was adopted, using a nonlinear finite element formulation, and adopting a modified Newton-Raphson solution scheme, in the framework of an "arc-length" continuation algorithm, as presented in Chapter 2. The main feature of the numerical technique is the use of a special-purpose finite element, called "tube-element", which combines longitudinal (beam-type) deformation with cross-sectional (shell-type) deformation in an efficient manner. This element has been employed elsewhere for the analysis of relatively thick tubes; in the present work it was properly enhanced for the buckling and postbuckling response of thin-walled cylinders.

Elastic cylinders have been modelled through both hypoelastic and hyperelastic large-strain material models, which include the effects of transversely anisotropic material behavior. The hypoelastic model, developed for the purposes of the present study, relates a stress rate, co-rotational with the local anisotropy axis, with the rate-of-deformation tensor. The hyperelastic constitutive equation, based on a quadratic free energy function, allows a straightforward representation of anisotropy. Both models were numerically implemented and incorporated in the finite element technique. Inelastic material behavior was considered through a large-strain J_2 flow plasticity model, whereas bifurcation on the primary equilibrium path is detected through Hill's comparison solid concept and using the J_2 deformation plasticity instantaneous moduli.

Favorable conclusions, as to the accuracy and efficiency of the numerical technique, to simulate the nonlinear response and buckling of thin-walled cylinders were drawn in Chapter 3, where excellent agreement with available results from a semi-analytical solution was found for the case of an uniformly compressed circular cylinder in the presence of initial axisymmetric imperfections. Furthermore, in Chapter 4, uniformly compressed oval cylinders were analyzed. The numerical results compare very well with existing semi-analytical asymptotic results on the

157

initial postbuckling response and the initial imperfection sensitivity. Furthermore, the present numerical results indicated a "snap-back" postbuckling path, and verified rigorously experimental observations on the load carrying capacity reserves of an oval cylinder, beyond the bifurcation point. It was also shown that hypoelastic and hyperelastic models provided very similar results.

The bending response of elastic isotropic cylinders was excessively examined in Chapter 5. This constitutes a challenging problem that combines ovalization and bifurcation instability, and is characterized by a highly nonlinear prebuckling state. The effects of pressure, initial curvature and initial ovality, as well as the influence of the radius-to-thickness ratio were investigated. The results showed that the response is governed by the strong interaction of cross-sectional prebuckling ovalization, and bifurcation instability, in the form of uniform periodic wrinkles along the cylinder. On the other hand, buckling was found to occur within a limited region around the cross-section, called "buckling zone". It was demonstrated that the presence of relatively small initial longitudinal curvature may have significant influence on the buckling behavior and the location of the buckling zone.

Assuming a constant state of stress and deformation within the buckling zone (referred to as "local buckling hypothesis"), a simplified analytical bifurcation solution was also developed, which resulted in closed-form expressions for the critical curvature, the critical moment and the corresponding buckling wavelength of thin-walled elastic isotropic cylinders subjected to pressurized bending, including the effects of initial longitudinal curvature and initial ovality. The closed-form analytical expressions provide results of remarkable accuracy with respect to the finite elements results, for relatively small values of initial curvature. Furthermore, the analytical predictions were found closer to the numerical results for thin-walled cylinders. Finally, the post-buckling behavior of elastic cylinders was illustrated in an elegant manner, using a simple mechanical model, pinpointing the effects of ovalization and pressure (internal or external).

The bending results of Chapter 5 were extended in Chapter 6, to investigate the nonlinear response of transversely isotropic cylinders, with special emphasis on the influence of anisotropy level. The response is governed by the interaction of ovalization and bifurcation instabilities. Using the "local buckling hypothesis", analogous analytical bifurcation expressions are derived. However, as the anisotropy level increases, buckling did no longer occur in a limited region, and the above hypothesis is no longer valid. By consequence, in such cases, the analytical expressions do not always compare well with numerical results. Finally, issues of imperfection sensitivity were examined numerically and the initial post buckling path was found unstable, verifying the sensitivity of maximum moment on the presence of initial imperfections.

158

Finally, in Chapter 7 numerical results were obtained for long metal cylinders, which buckle in the inelastic range. The present study refers to thin-walled cylinders, which may be used as chimneys or water transmission pipelines, and is aimed at determining bifurcation in the plastic range as well as simulating the formation of periodic buckling patterns along the cylinder axis, and the development of localized buckling deformations (local buckling mechanism). Using the numerical technique, which implements the comparison solid concept, discretized through the ''tube-element'', the buckling moment and the corresponding uniform buckling mode were obtained. Moreover, using this numerical formulation the transition of uniform to localized wrinkling was demonstrated resulting in the sudden collapse of thin-walled cylinders.

REFERENCES

[1] Von Karman, Th., Dunn, G., Tsien, H., 1940. *The influence of curvature on the buckling characteristics of structures*. Journal of Aeronautical Science, 7, 7, 276-289

[2] Von Karman, Th., 1941. *The buckling of thin cylindrical shells under axial compression*. Journal of Aeronautical Sciences, 8, 303-312

[3] Koiter, W.T., 1945. *On the stability of elastic equilibrium*, Thesis, Delft, Netherlands. H.J. Paris, Amsterdam, English translation: NASA Technical Translation F10, 1967

[4] Koiter, W.B., 1963. The *effect of axisymmetric imperfections on the buckling of cylindrical shells under axial compression*, Proceedings: Koninklijke Nederlandse Akademie van Wetenschappen, B66, 265-279

[5] Koiter, W.T., 1963. *Elastic stability and post-buckling behaviour*, Proceeding of the Symposium in Nonlinear Problems, 257-275, University of Wisconsin Press, Madison

[6] Kempner, J., 1954. *Postbuckling behavior of axially compressed circular cylindrical shells*, Journal of Aeronautical Sciences, 21, 5, 329

[7] Kempner, J., 1962. *Some results on buckling and postbuckling of cylindrical shells*, In Collected Papers on Instability of Shell Structures, NASA TND 1510, 173-186

[8] Kempner, J., Chen, Y.N., 1968. *Postbuckling of an axially compressed oval cylindrical shell*, Proceeding of the 12th International Congress in Applied Mechanics, 246-256, Standford University

[9] Amazigo, J.C., Budiansky, B., Carrier, G.F., 1970. *Asymptotic analyses of the buckling of imperfect columns on nonlinear elastic foundations*, International Journal of Solids and Structures, 6, 10, 1341-1356

[10] Budiansky, B. and Hutchinson, J.W., 1964. *Dynamic buckling and imperfection-sensitive structures*, Proceedings of the 11th International Congress of Applied Mechanics , Munich, Springer-Verlag, Berlin, 636-651

[11] Brush, D.O., Almroth, B.O., 1975. *Buckling of bars, plates and shells*, McGraw-Hill, New York

[12] Wempner, G., Talaslides, D., 2003. *Mechanics of solids and shells*, CRC Press

[13] Teng, J.G., 1996. *Buckling of thin shells: Recent advances and trends*, Applied Mechanics Reviews, 49, 4, 263-274

[14] Singer, J., 2002. *Buckling Experiments: Experimental Methods in Buckling of Thin-walled Structures*, John Wiley and Sons

[15] Needleman, A., 1982. *Finite elements for finite strain plasticity problems* in *Plasticity of Metals at Finite Strain: Theory, Experiment and Computation*, edited by E.H. Lee and R.L. Mallett, Rensselaer Polytechnic Institute, Troy, New York, 387-436

[16] Karamanos, S.A., Tassoulas, J.L., 1996. *Tubular members I: stability analysis and preliminary results*, Journal of Engineering Mechanics, ASCE, 122, 1, 64-71

[17] Green, A.E., Zerna, W., 1992, *Theoretical Elasticity*, Dover Publications Inc.

[18] Christensen, R.M., 1979. *Mechanics of composite materials*, Wiley, New York

[19] Aravas, N., 1992. *Finite elastoplastic transformations of transversely isotropic metals*. International Journal of Solids and Structures, 29, 2137–2157

[20] Spencer, A.J.M., 1972. *Deformations of fiber-reinforced materials*. Oxford University Press, Oxford

[21] Spencer, A.J.M., 1984. *Constitutive theory for strongly anisotropic materials* in Continuum Theory of the Mechanics of Fiber-Reinforced Composites (Edited by A.J.M. Spencer), Courses and Lectures, 282, 1-32, International Center for Mechanical Sciences, Udine. Spinger, Berlin

[22] Bathe, K.J., Almeida, C.A., 1980. *A simple and effective pipe elbow element–linear analysis*, J. Applied Mechanics, ASME, 47, 93-100

[23] Bathe, K.J., Almeida, C.A., 1982. *A simple and effective pipe elbow element–intreraction effects*, J. Applied Mechanics, ASME, 49, 165-171

[24] Bathe, K.J., Almeida, C.A., Ho, L.W., 1983. *A simple and effective elbow element–some nonlinear capabilities*, Computers and Structures, 17, 5-6, 659-667

[25] Millittelo, C., Huespe, A.E., 1988. *A displacement-based pipe elbow element*, Computers and Structures, 29,.2, 339-343

[26] Yan, A.M., Jospin, R.J. and Nguyen, D.H., 1999. *An enhanced pipe elbow element–application in plastic limit analysis of pipe structures*, International Journal For Numerical Methods in Engineering, 46, 409-431

[27] Hibbit, Karlsson and Sorensen Inc. (HKS), 2004. *ABAQUS Theory Manual*, version 6.4, Pawtucket, RI.

[28] Riks, E., 1972. *The application of Newton's method to the problem of elastic stability*, Journal of Applied Mechanics, 39, 1060-1066

[29] Riks, E., 1979. *An incremental approach to the solution of snapping and buckling problems*, International Journal of Solids and Structures, 15, 529-551

[30] Wempner, G.A., 1971. *Discrete approximations relate to nonlinear theories of solids*, International Journal of Solids and Structures, 7, 1581-1599

[31] Crisfield, M.A., 1991. *Non-linear finite element analysis of solids and structures I*, John Wiley and Sons

[32] Hill, R., 1958. *A general theory of uniqueness and stability of elastic-elastic solids*, Journal of the Mechanics and Physics of Solids, 6, 236-249

[33] Hutchinson, J.W., 1974. *Plastic buckling*, Advances n Applied Mechanics, 14, 67-144.

[34] Batterman, S. C., 1965. *Plastic buckling of axially compressed cylindrical shells*, AIAA Journal, 3, 316-325

[35] Batdorf, S.B., 1949. T*heories of plastic buckling*, Journal of Aeronautical Sciences, 16, 405-408

[36] Bardi, F.C., Kyriakides, S., 2006. *Plastic buckling of circular tubes under axial compression-part I: Experiments,* International Journal of Mechanical Sciences, 48, 830-841

[37] Von Karman, Th., Tsien H.S., 1941. *The buckling of thin cylindrical shells under axial compression*, Journal of Aeronautical Sciences, 8, 303-312

[38] Budiansky, B., 1965. *Dynamic buckling of elastic structures: criteria and estimates*, Proceeding of the International Conference in Dynamic Stability of Structures, 83-106

[39] Cohen, G.A., 1968. *Effect of a nonlinear prebuckling state on the postbuckling behavior and imperfection-sensitivity of elastic structures*, AIAA Journal, 6, 1616-1620

[40] Fitch, J.R., 1968. T*he buckling and postbuckling behavior of spherical caps under concentrated load*, International Journal of Solids and Structures, 4, 421-446

[41] Fabian, O., 1977. *Collapse of cylindrical, elastic tubes under combined bending, pressure and axial loads*, International Journal of Solids and Structures, 13, 1257-1270

[42] Hutchinson, J.W., Koiter, W.T., 1970. *Postbuckling theory*, Applied Mechanics Reviews, 23, 1353-1366

[43] Timoshenko, S., Gere, J, 1961. *Theory of elastic stability*, 2nd edition, McGraw-Hill, New-York

[44] Donnell, L.H., 1933. *Stability of thin-walled tubes under torsion*, NACA Rep. 479

[45] Donnell, L.H., 1934. A new theory for the buckling of thin cylindrical shells under axial compression and bending, ASME Transactions., 56, 795-806

[46] Feinstein, G., Erickson, B., Kempner, J.,1971, *Stability of oval cylindrical shells*, Experimental Mechanics, 11, 514-520

[47] Tennyson, R.C., Booton, M., Caswell, R.D., 1971. *Buckling of imperfect elliptical cylindrical shells under axial compression*, AIAA Journal, 9, 250-255

[48] Kempner, J., Chen, Y.N., 1964. *Large deflections of an axially compressed oval cylindrical shell,* Proceedings of the 11th International Congress of Applied Mechanics, 299-306, Munich, Springer Verlag, Berlin

[49] Kempner, J., Chen, Y.N., 1967. *Buckling and postbuckling of an axially compressed oval cylindrical shell*, Proceedings of the Symposium on Theory of Shells to Honor Lloyd Hamilton Donnell, 141-183, University of Houston, McCutchaw Publications

[50] Hutchinson J.W., 1968. *Buckling and postbuckling behavior of oval cylindrical shells under axial compression*, Journal of Applied Mechanics, 35, 66-72

[51] Kempner, J., Chen, Y.N., 1968. *Postbuckling of an axially compressed oval cylindrical shell*, Proceedings of the 12th International Congress of Applied Mechanics, 246-256, Standford University

[52] Kempner, J., Chen, Y.N., 1974. *Buckling and initial postbuckling of oval cylindrical shells under combined axial compression and bending*, Transactions New York Academy of Sciences, Ser. 11, 36, 171-191

[53] Almroth, B.O., Brogan, F.A., Marlowe, M.B., 1971. *Collapse analysis of elliptic cones*, AIAA Journal, 9, 32-37

[54] Busnell, D., 1971. *Stress, buckling and vibration of prismatic shells*, AIAA Journal, 9, 401-410

[55] Semenyuk, N.P., 1984. *Stability of non-circular cylindrical shells under axial compression*, Soviet Applied Mechanics, 20, 813-818

[56] Sun, G., 1991. *Buckling and postbuckling behavior of laminated oval cylindrical shells under axial compression*, Journal of Applied Mechanics, 58, 848-851

[57] Sheinman, I., Firer, M., 1994. Buckling analysis of laminated cylindrical shells with arbitrary noncircular cross section, AIAA Journal, 32, 648-654

[58] Firer, M., Sheinman, I., 1995. *Nonlinear analysis of laminated non-circular cylindrical shell*s, International Journal of Solids and Structure, 32, 1405-1416

[59] Soldatos, K.P., 1992. *Non-linear analysis of transverse shear deformable laminated composite cylindrical shells part I: Derivation of the governing equations*, ASME Journal of Pressure Vessels Technology, 114, 105-109

[60] Soldatos, K.P., 1992. *Non-linear analysis of transverse shear deformable laminated composite cylindrical shells part II: Buckling of axially compressed cross-ply circular and oval Cylinders*, ASME Journal of Pressure Vessels Technology, 114, 110-114

[61] Soldatos, K.P., 1999. *Mechanics of cylindrical shells with non-circular cross-sections: A Survey*, Applied Mechanics Review, 52, 8, 237-274

[62] Brazier, L.G., 1927. *On the flexure of thin cylindrical shells and other "thin" sections*, Proceedings of The Royal Society, A116, 104-114

[63] Wood, J. D., 1958. *The flexure of a uniformly pressurized, circular, cylindrical shell*, Journal of Applied Mechanics, ASME, 25, 453-458

[64] Reissner, E., 1959. *On finite bending of pressurized tubes*, Journal of Applied Mechanics, ASME, 26, 386-392

[65] Karman, Th. von, 1911. *Uber die Formuanderung dunnwandiger Rohre* [in German], Zeit. Des Vereines deutcher Ingenieure, 55, 1889-1895

[66] Reissner, E., 1961. *On finite pure bending of cylindrical tubes*, Osterr. Ing. Arch., 15, 165-172

[67] Reissner, E., Weinitschke, H. J., 1963. *Finite pure bending of circular cylindrical tubes*, Quarterly of Applied Mathematics, XX, 4, 305-319

[68] Aksel'rad (Axelrad), E. L., 1961. *Flexure of thin-walled beams under large elastic displacements*. [in Russian]. Izvestiya Akademii Nauk SSSR, Otdelenie Tekhnicheskikh Nauk, Mekhanika i Mashinostroenie, 3, 124-132

[69] Aksel'rad (Axelrad), E. L., 1962. *Flexure and instability of thin-walled pressurized tubes*. [in Russian]. Izvestiya Akademii Nauk SSSR, Otdelenie Tekhnicheskikh Nauk, Mekhanika i Mashinostroenie, 1, 98-114

[70] Axelrad, E. L. 1980. *Flexible shells,* Proceedings of 15th IUTAM Congress, Toronto, 45-56

[71] Axelrad, E. L., 1987. *Theory of Flexible Shells*, North-Holland, Amsterdam, The Netherlands

[72] Axelrad, E. L., Emmerling, F. A., 1984. *Elastic tubes*, Applied Mechanics Reviews, 37, 7, 891-897

[73] Thurston, G. A., 1977. *Critical bending moment of circular cylindrical tubes*, Journal of Applied Mechanics, Transactions of the ASME, Series E 44, 173-175

[74] Boyle, J. T., 1981. *The finite bending of curved pipes*, International Journal of Solids and Structures, 17, 515-529

[75] Karamanos, S.A., 2002, *Bending instabilities of elastic tubes*, International Journal of Solids and Structures, 39, 2059-2085

[76] Calladine, C.R. , 1983. *Theory of shell structures*, Cambridge University Press, Cambridge, UK.

[77] Seide, P., Weingarten V. I., 1961. *On the buckling of circular cylindrical shells under pure bending*, Journal of Applied Mechanics, ASME, 28, 112-116

[78] Axelrad, E. L., 1965. *Refinement of buckling-load analysis for tube flexure by way of considering precritical deformation*. [in Russian]. Izvestiya Akademii Nauk SSSR, Otdelenie Tekhnicheskikh Nauk, Mekhanika i Mashinostroenie, 4, 133-139

[79] Emmerling, F.A., 1982. Nichtlineare *Biegung und Beulen von Zylindern und krummen Rohren bei Normaldruck* [in German], Ingenieur – Archiv, 52, 1-16

[80] Stephens, W.B., Starnes Jr.,J.H., Almroth, B.O., 1975. *Collapse of long cylindrical shells under combined bending and pressure loads*, AIAA Journal, 13, 1, 20-25

[81] Ju, G.T., Kyriakides, S., 1992. *Bifurcation and localization instabilities in cylindrical shells under bending II: Predictions*, International Journal of Solids and Structures, 29, 1143-1171

[82] Ijima, S., Bradec, C., Maiti, A., Bernholc, J., 1996. *Structural flexibility of carbon nanotubes*. Journal of Chemical Physics, 104, 5, 2089–2092

[83] Vodenitcharova, T., Zhang, L.C., 2004. *Mechanism of bending with kinking of single-walled carbon nanotubes*. Physical Review B, 69, 115410

[84] Yacobson, B.I., Bradec, C.J., Bernholc J., 1996. *Nanomechanics of carbon tubes: instabilities beyond linear response*. Physical Review Letters, 79, 14, 2511-2514

[85] Axelrad, E.L., 1985. *On local buckling of thin shells*, International Journal of Non-linear Mechanics, 20, 4, 249-259

[86] Karamanos, S. A., 1996. Stability of Pressurized long inelastic cylinders under radial transverse loads, Computational Mechanics, 18, 6, 444-453

[87] Kedward, K. T., 1978. *Nonlinear collapse of thin-walled composite cylinders under flexural loading*, Proc. 2nd International Conference on Composite Materials (Toronto), Metallurgical Society of AIME, Warrendale, PA, 353-365

[88] Spence, J., Toh, S.L., 1979. *Collapse of thin orthotropic elliptical cylindrical shells under combined bending and pressure loads*, Journal of Applied Mechanics, 46, 2, 363-371

[89] Stockwell, A., Cooper, P.A., 1992. *Collapse of composite tubes under end moments*, Proceedings of the 33rd Structures, Structural Dynamics and Materials Conference, Dallas, TX, AIAA Journal paper 92-2389, 1841-1850

[90] Libai, A., Bert, C.W., 1994. *A mixed variational principle and its application to the nonlinear bending problem of orthotropic tubes - II. Application to nonlinear bending of circular cylindrical tubes*, International Journal of Solids and Structures, 31,1019-1033

[91] Corona, E., Rodrigues, A., 1995. *Bending of long cross-ply composite circular cylinder*, Composites Engineering, 5, 2, 163-182

[92] Tatting, B.F., Gürdal, Z., Vasiliev, V.V., 1996. *Nonlinear response of long orthotropic tubes under bending including the Brazier effect*, AIAA Journal, 34, 9, 1934-1940

[93] Harursampath, D., Hodges, D.H., 1999. *Asymptotic analysis of the non-linear behavior of long anisotropic tubes*, International Journal of Non-Linear Mechanics, 34, 6, 1003-1018

[94] Wadee, M.K., Wadee, M.A., Bassom, A.P., 2007. *Effects of orthotropy and variation of Poisson's ratio on the behavior of tubes in pure flexure*, Journal of Mechanics and Physics of Solids, 55, 1086-1102

[95] Wang, L., Zheng, Q., Liu, J.Z., Jiang, Q., 2005. *Size dependence of the thin-shell model for carbon nanotubes*, Physical Review Letters, 95, 105501

[96] Houliara, S. and Karamanos, S.A., 2006. *Buckling and post-buckling of pressurized thin-walled elastic tubes under in-plane bending*, International Journal of Nonlinear Mechanics, 41, 4, 491-511

[97] Kyriakides, S., Ju, G.T., 1992. *Bifurcation and localization instabilities in cylindrical shells under bending I: Experiments*, International Journal of Solids and Structures, 29, 9, 1117-1142

[98] Mathon, C., Limam, A., 2006. *Experimental collapse of thin cylindrical shells submitted to internal pressure and pure bending*, Thin-Walled Structures, 44, 39-50

[99] Elchalakani, M., Zhao, X.L., Grzebieta, R.H., 2002. *Bending tests to determine slenderness limits for cold-formed circular hollow sections*, Journal of Constructional Steel Research, 58, 1407-1430

[100] Elchalakani, M., Zhao, X.L., Grzebieta, R.H., 2002. *Plastic mechanism analysis of circular tubes under pure bending*, International Journal of Mechanical Sciences, 44, 1117-1143

[101] Ades, C.S., 1957. *Bending strength of tubing in the inelastic range*, Journal of Aeronautical Sciences, 2, 605-610

[102] Gellin, S., 1980. *The plastic buckling of long cylindrical shells under pure bending*, International Journal of Solids and Structures, 10, 397-407

[103] Fabian, O., 1981. *Elastic-plastic collapse of long tubes under combined bending and pressure load*, Ocean Engineering, 8, 295-330

[104] Kyriakides S., Shaw, P.K., 1982. Response and stability of elastoplastic circular pipes under combined bending and external pressure, International Journal of Solids and Structures, 18, 11, 957-973

[105] Corona, E., Kyriakides, S., 1988. *On the collapse of inelastic tubes under combined bending and pressure*, International Journal of Solids and Structures, 24, 505-535

[106] Karamanos, S.A., Tassoulas. J.L., 1991. *Stability of inelastic tubes under external pressure and bending*, Journal of Engineering Mechanics. ASCE 117, 2845-2861

[107] Hill, R., 1961. *Bifurcation and uniqueness in nonlinear mechanics of continua* in Problems of Continuum Mechanics, 155-164, SIAM, Philadelphia

[108] Sanders Jr., J.L., 1954. *Plastic stress-strain relations based on linear loading functions*, Proceedings: 2nd U.S. National Congress of Applied Mechanics, 455-460

[109] Batdorf, S.B., Budiansky, B., 1949. *A mathematical theory of plasticity based on the concept of slip*, NACA TN No. 1871

[110] Christoffersen, J., Hutchinson, J.W., 1979. *A class of phenomenological corner theories of plasticity*. Journal of Mechanics and Physics of Solids, 27, 445-487

166

[111] Needleman, A., Tvergaard, V., 1982. *Aspects of plastic postbuckling behavior*, in Mechanics of Solids. The Rodney Hill 60th Anniversary Volume, H.G. Hopkins and M.J. Sewell (eds.), 453-498, Pergamon Press, Oxford

[112] Tvergaard, V., 1983. *Plastic buckling of axially compressed circular cylindrical shells*. Thin-Walled Structures, 1, 139-163

[113] Reddy , B.D., 1979. *An experimental study of the plastic buckling of circular cylinders in pure bending*, International Journal of Solids and Structures, 15, 9, 669-683

[114] Corona, E., Lee, L.H., Kyriakides S., 2006. *Yield anisotropy effects on buckling of circular tubes under bending*, International Journal of Solids and Structures, 43, 7099-7118

[115] Kyriakides S., Corona, E., 2007. *Mechanics of offshore pipelines, vol. 1: Buckling and collapse*. Elsevier Publications

[116] Karamanos, S.A., Tassoulas, J.L., 1996a. *Tubular members I: Stability analysis and preliminary results*, Journal of Engineering Mechanics, ASCE, 122, 1, 64-71

[117] Karamanos, S.A., Tassoulas, J.L., 1996b. *Tubular members II: Local buckling and experimental verification*, Journal of Engineering Mechanics, ASCE, 122, 1, 72-78

[118] *Collapse tests of short tubular columns subjected to combined loads*, 1985. Final Report Prepared by Penzoil/Joint Industry Project, Chicago Bridge and Iron, Plainfield, III

[119] *Effects of external hydrostatic pressure on tubular beam-columns*, 1988. Final Report, Project No. 06-1184, American Petroleum Institute Project No. 86/87-56, Southwest Research Institute, San Antonio, Texas

[120] *Hydrostatic beam-column tests (phase II)*, 1989. Final Report, Contract No. C92731, American Petroleum Institute Project No. 87-56, Chicago Bridge and Iron, Plainfield, III

[121] Tvergaard, V., Needleman, A., 2000. *Buckling localization in a cylindrical panel under axial compression*, International Journal of Solids and Structures, 37, 6825-6842

[122] Tvergaard, V., 1999. *Studies of elastic-plastic instabilities*, Journal of Applied Mechanics, 66, 3-9

APPENDIX

Initial Post-Buckling Theory of Elastic Structures

Equation Chapter 9 Section 9

The initial post-buckling theory was initially introduced by Koiter [3], [4] and Budiansky [38]. In this initial form, the theory was limited to structures with linear pre-buckling behavior. This is a quite usual case in structural mechanics, such as the cylinder under axial compression or the sphere under uniform pressure. On the other hand, cylinder bending is characterized by a non-linear pre-buckling state. An enhancement of the general theory to account for nonlinear prebuckling behavior has been presented in the works of Cohen [39] and Fitch [40]. This theory is briefly presented in this Appendix. The concepts of initial post-buckling and imperfection sensitivity are summarized. It is noted that discussion is restricted to the case of a single buckling mode.

It is supposed that under the loading $\mathbf{q}$ the elastic structure acquires displacements $\mathbf{u}$, strains $\boldsymbol{\varepsilon}$ and stresses $\boldsymbol{\sigma}$. These field variables are required to satisfy the strain-displacement relation:

$$\boldsymbol{\varepsilon} = L_1(\mathbf{u}) + \frac{1}{2} L_2(\mathbf{u}) \tag{1}$$

where L_1 and L_2 are linear and quadratic functionals respectively.

The stress-strain relation is given by:

$$\boldsymbol{\sigma} = H(\boldsymbol{\varepsilon}) \tag{2}$$

where H is a linear functional.

The variational equation of equilibrium is:

$$\int_V \boldsymbol{\sigma} \cdot \delta\boldsymbol{\varepsilon} \, dV = \int_B \mathbf{q} \cdot \delta\mathbf{u} \, dB \tag{3}$$

Expression (3) is a statement of the principle of virtual work and should hold for any admissible variation displacement function $\delta\mathbf{u}$. Furthermore, the strain variation $\delta\boldsymbol{\varepsilon}$ follows from (1). The principle of virtual work guarantees equilibrium of the stress $\boldsymbol{\sigma}$ and loads $\mathbf{q}$.

The occurrence of buckling can be detected considering a perturbation in the pre-buckling solution $\mathbf{u}_0$, $\boldsymbol{\varepsilon}_0$ and $\boldsymbol{\sigma}_0$:

$$\begin{aligned} \mathbf{u} &= \lambda_{cr}\mathbf{u}_0 + \eta\mathbf{u}_1 \\ \boldsymbol{\varepsilon} &= \lambda_{cr}\boldsymbol{\varepsilon}_0 + \eta\boldsymbol{\varepsilon}_1 \\ \boldsymbol{\sigma} &= \lambda_{cr}\boldsymbol{\sigma}_0 + \eta\boldsymbol{\sigma}_1 \end{aligned} \tag{4}$$

where η is a perturbation parameter. Substitution into the field equations, and keeping terms linear with respect to η results in an eigenvalue problem. Solution of the eigenvalue problem provides the buckling load λ_{cr} (lowest eigenvalue) and the corresponding buckling mode. It is assumed that there is a single mode associated with the buckling load.

In order to investigate the behavior of the structure beyond bifurcation, the following relations for the displacement, strain and stress are written:

$$
\begin{aligned}
\mathbf{u} &= \lambda \mathbf{u}_0 + \eta \mathbf{u}_1 + \eta^2 \mathbf{u}_2 + \eta^3 \mathbf{u}_3 + ... \\
\boldsymbol{\varepsilon} &= \lambda \boldsymbol{\varepsilon}_0 + \eta \boldsymbol{\varepsilon}_1 + \eta^2 \boldsymbol{\varepsilon}_2 + \eta^3 \boldsymbol{\varepsilon}_3 + ... \\
\boldsymbol{\sigma} &= \lambda \boldsymbol{\sigma}_0 + \eta \boldsymbol{\sigma}_1 + \eta^2 \boldsymbol{\sigma}_2 + \eta^3 \boldsymbol{\sigma}_3 + ...
\end{aligned}
\tag{5}
$$

Furthermore, the following asymptotic expression relating the load in the post-buckling regime with the value of η with λ is assumed:

$$
\frac{\lambda}{\lambda_{cr}} = 1 + a\eta + b\eta^2 + ...
\tag{6}
$$

Substituting equations (5) into the principle of virtual work (3), and considering expression (6), the values of a and b can be determined. The variation of λ / λ_{cr} with respect to η immediately after bifurcation is shown by the solid curves in Fig. 108 for three cases, $a \neq 0$, $a = 0, b > 0$ and $a = 0, b < 0$.
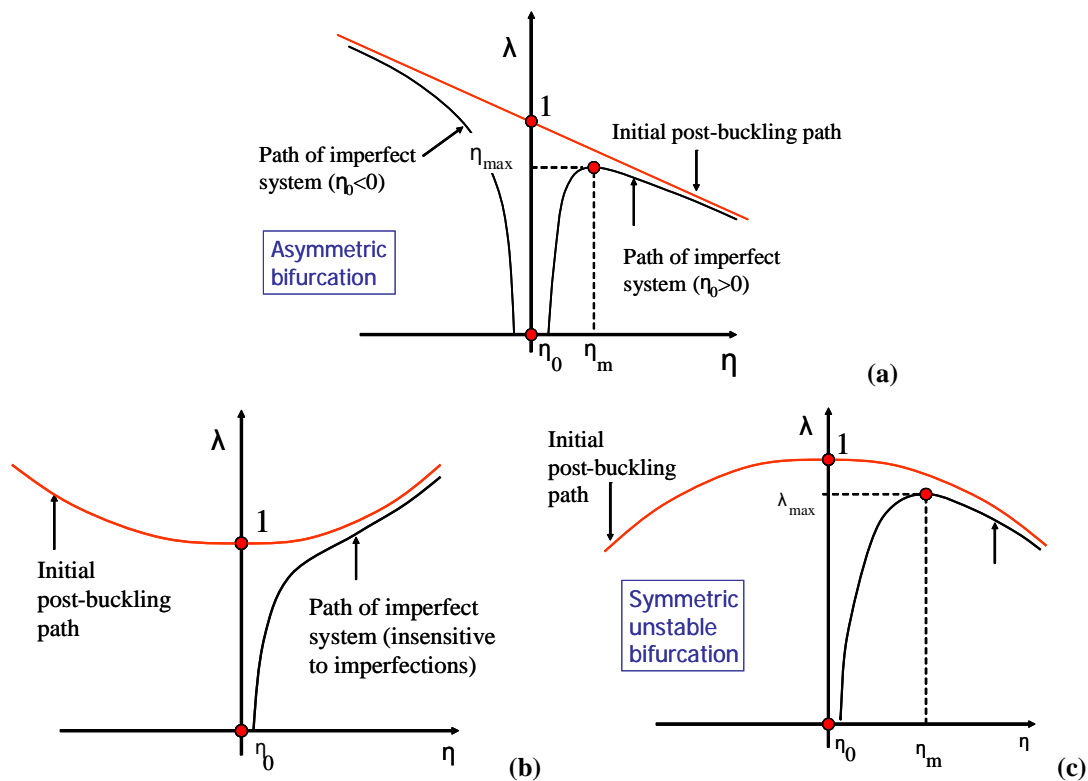

Fig. 108 Load-deflection curves for the post-buckling path (a) $a \neq 0$ **, (b)** $a = 0, b > 0$ **and (c)**

$$a = 0, b < 0.$$

169

Quite often, the case where $a = 0$ occurs. In such a case, "symmetric" buckling is examined, so that equation (6) is rewritten as follows:

$$\frac{\lambda}{\lambda_{cr}} = 1 + b\eta^2 \tag{7}$$

In equation (7), b is the known Koiter's initial post-buckling coefficient (sometimes referred to as b-coefficient). If $b > 0$ then the initial post-buckling path is stable (Fig. 108b) whereas the case where $b < 0$ corresponds to unstable initial post-buckling path (Fig. 108c).

To study the influence of initial imperfections, an initial displacement $\bar{\mathbf{u}}$ is supposed to characterize the unloaded, stress-free structure. It is assumed that the initial imperfection is in the form of the first buckling mode

$$\bar{\mathbf{u}} = \eta \mathbf{u}_1 \tag{8}$$

Using this imperfection, it is possible to obtain the following asymptotic expression between the load λ, the imperfection amplitude ξ, and the value of η:

$$\left(1 - \frac{\lambda}{\lambda_{cr}}\right)\eta + a\eta^2 + b\eta^3 + \dots = \frac{\lambda}{\lambda_{cr}}\xi \tag{9}$$

In the case of $a \neq 0$, there exists a maximum on the load–displacement path. Differentiation of the above expression provides the maximum load λ_{max} as a function of the imperfection amplitude ξ:

$$\left(1 - \frac{\lambda_{max}}{\lambda_{cr}}\right)^2 + 4a\xi\rho\left(\frac{\lambda_{max}}{\lambda_{cr}}\right) = 0 \tag{10}$$

where ρ is a parameter that depends on the nonlinearity of the prebuckling state. For linear pre-buckling state ρ is equal to unity. When $\alpha = 0$ the existence of local maximum on the load–displacement path depends on the value of b. If $b < 0$ a maximum load exists, and it is given by the following asymptotic expression

$$\left(1 - \frac{\lambda_{max}}{\lambda_{cr}}\right)^{3/2} - \frac{3\sqrt{3}}{2}(-b\rho)^{1/2}|\xi|\left(\frac{\lambda_{max}}{\lambda_{cr}}\right) = 0 \tag{11}$$

On the other hand, no maximum exists when $a = 0$ and $b < 0$. In that case, the response of the imperfect structure is monotonically increasing.

It is convenient, to refer to ''quadratic structures'' and ''cubic structures'' as those governed by the cases $a \neq 0$ and $a = 0$, $b < 0$, respectively. It is also noted that for ''quadratic structures''

$$(1 - \lambda_s / \lambda_{cr}) = 0\{|\xi|^{1/2}\} \tag{12}$$

whereas in imperfection ''cubic structures''

170

$$(1 - \lambda_s / \lambda_{cr}) = 0\{|\xi|^{2/3}\} \qquad (13)$$

$$(1 - \lambda_s \quad {}_{cr} 171$$